Modelling Dust Processing and Evolution in Extreme Environments as seen by Herschel Space Observatory

Marco Bocchio

Université Paris-Sud

ED Astronomie et Astrophysique d'Ile de France
Institut d'Astrophysique Spatiale

Discipline : Science de l'Univers

Thèse de doctorat

Soutenue le 16 Septembre 2014 par

Marco Bocchio

Modelling Dust Processing and Evolution in Extreme Environments as seen by *Herschel* Space Observatory

Directeur de thèse :	Anthony Jones	Directeur de recherche (IAS)
Composition du jury :		
Rapporteurs :	Eli Dwek	NASA / GSFC, USA
	Hugues Leroux	Professeur (Université Lille 1)
Examinateurs :	Haley Gomez	School of Physics and Astronomy (Cardiff University, UK)
	Guillaume Pineau des Forêts	Professeur (Université Paris-Sud, Orsay)

This manuscript is downloadable from the site of the Institut d'Astrophysique Spatiale: `www.ias.u-psud.fr/`

The page layout is optimized for A5 format.

For any questions or comments please contact me at:
`marco.bocchio@ias.u-psud.fr` or `mbocchio87@gmail.com`

Acknowledgements

Here we are, the journey is over and three years have passed so quickly. It is not something new, doing a PhD requires a big effort and most likely it is full of moments when you think that you are going the wrong way. However, a PhD is also full of exciting moments! ...because you finally found what you have been looking for weeks or even months, you were right! you just needed to keep pushing... But you do not do a PhD by yourself, it is all about the people you are surrounded by!

First of all I would like to warmly thank my PhD supervisor, Ant Jones, for his big support and patience during these three years. I really enjoyed the long hours talking about science with you, day after day you were teaching me something new, making me feeling curious to learn even more, you were transmitting your big passion. Whenever there were unexpected problems, you always had nice words to lift my spirits motivating myself again to go back to the issue with a positive attitude. You always impressed me for you wide view in Astrophysics and the way you can command an audience in large conferences. I learned so much from you, science-wise but more importantly from the human point of view. Keep on climbing, Ant!

Then I thank Alain Abergel. I spent many afternoons in his office, and it was worth it. I particularly appreciate your meticulous and stable way to proceed in a reasoning. It was a pleasure to have an expert on *Herschel* data by my side. You were pushing my curiosity further and further, we were making great progress.

I would like to thank Laurent Verstraete. It was a pleasure to publish my first paper with you. We spent quite some time making calculations together in your office and I was always impressed by the way, with only a paper and a pen, you were able to explain me what I was asking for.

I am also grateful to Vincent Guillet for good discussions about science, for your insightful advice and for pushing me to look at the *Herschel* data searching for a correspondence to the performed modelling.

I thank Guillaume Pineau des Forêts for having supported me for these three years as the person in charge of the École Doctorale A&A and for having been the director of my jury. I also extend my thanks to Eli Dwek and Hugues Leroux for having carefully read my thesis and I acknowledge them together with Haley Gomez for having accepted to be part of my jury.

A particular thanks goes to Mathieu Langer for his support during my M2 thesis and during the choice of my PhD project.

A big thanks to the PhD students and PostDoc fellows at the IAS. Thanks to Agnès, Nathalie, Pierre, Melanie, Lapo, Davide, Stéphane, Fabien, Elisabetta, Guillaume, Chloé, Claudia, JB, Clement, Heddy, Éléonore, Raoul, Andrea, Alex, David, Anna, Cynthia, Cédric, Marta, Gonzalo, ... for breakfasts, coffee breaks, lunches, seminars, scientific discussions and beers together! They were three nice years!

I thank also my NPAC classmates Agnès, Vince, Guillaume, Asenath, Estelle, Jérémy, Pierre, Samuel, Marie for good lunches and soirées together. I also owe you a dept of gratitude for the patience you put in teaching me French.

I would like to say a big thank you to my family for having supported me during these tough years far from home. You always gave me good advice and encouraged me, whatever my decision was, to pursue my dreams. Thanks for your unconditioned affection.

Last but not least, I would like to thank Irene. It is not always easy to deal with a stressed and tired PhD student. It was also not easy to be miles away from each other... but we managed it. Now it is all downhill from here (well, at least flatter than before) and we can enjoy the beautiful Tuscany. Thanks for you love and your renovated support day by day.

I dedicate this thesis to
my family and my girlfriend, Irene
for their support and wholehearted love.

Abstract

The main goal of my PhD study is to understand the dust processing that occurs during the mixing between the galactic interstellar medium and the intracluster medium. This process is of particular interest in violent phenomena such as galaxy-galaxy interactions or the "Ram Pressure Stripping" due to the infalling of a galaxy towards the cluster centre.

Initially, I focus my attention to the problem of dust destruction and heating processes, re-visiting the available models in literature. I particularly stress on the cases of extreme environments such as a hot coronal-type gas (e.g., IGM, ICM, HIM) and supernova-generated interstellar shocks. Under these conditions small grains are destroyed on short timescales and large grains are heated by the collisions with fast electrons making the dust spectral energy distribution very different from what observed in the diffuse ISM.

In order to test our models I apply them to the case of an interacting galaxy, NGC 4438. Herschel data of this galaxy indicates the presence of dust with a higher-than-expected temperature. With a multi-wavelength analysis on a pixel-by-pixel basis we show that this hot dust seems to be embedded in a hot ionised gas therefore undergoing both collisional heating and small grain destruction.

Furthermore, I focus on the long-standing conundrum about the dust destruction and dust formation timescales in the Milky Way. Based on the destruction efficiency in interstellar shocks, previous estimates led to a dust lifetime shorter than the typical timescale for dust formation in AGB stars. Using a recent dust model and an updated dust processing model we re-evaluate the dust lifetime in our Galaxy.

Finally, I turn my attention to the phenomenon of "Ram Pressure Stripping". The galaxy ESO 137-001 represents one of the best cases to study this effect. Its long H_2 tail embedded in a hot and ionised tail raises questions about its possible stripping from the galaxy or formation downstream in the tail. Based on recent hydrodynamical numerical simulations, I show that the formation of H_2 molecules on the surface of dust grains in the tail is a viable scenario.

Resumé

L'objectif principal de mon travail de thèse est de comprendre les processus qui agissent sur la poussière pendant le couplage entre le milieu interstellaire galactique et le milieu intra-amas. Ce processus est d'intérêt particulier dans les phénomènes violents comme les interactions galaxie-galaxie ou le "Ram Pressure Stripping" causé par la chute d'une galaxie vers le centre de l'amas.

Initialement, je me suis concentré sur le problème de la destruction de la poussière et le processus de chauffage, en re-visitant les modèles présents en littérature. J'ai particulièrement insisté sur les cas des environnements extrêmes comme le gaz chaud de type coronale (e.g., IGM, ICM, HIM) et les chocs interstellaires générés par les supernovae. Sous ces conditions les petits grains sont détruits rapidement et les gros grains sont chauffés par les collisions avec les électrons énergétiques, en rendent la distribution spectral d'énergie de la poussière très différente de ce qu'on observe dans le milieu interstellaire diffus.

Pour tester nos modèles j'ai les appliqués au cas d'une galaxie en interaction, NGC 4438. Les données Herschel de cette galaxie indiquent la présence de la poussière avec une température plus élevée de ce qu'on s'attendait. Avec une analyse à plusieurs longueurs d'onde on montre que cette poussière chaude semble être dans un gaz ionisé et chaud et donc subir à la fois le chauffage collisionnel et la destruction des petits grains.

De plus, je me suis focalisé sur l'énigme de longue date à propos de la différence entre les échelles de temps de destruction et formation de la poussière dans la Voie Lactée. Basées sur l'efficacité de destruction de la poussière dans les chocs interstellaires, les estimations précédentes portent à une durée de vie de la poussière plus courte que l'échelle de temps typique de sa formation dans les étoiles AGB. En utilisant un modèle de poussière récent et les dernières estimations pour l'évolution de la poussière, on a réévalué la durée de vie de la poussière dans notre Galaxie.

Finalement, j'ai tourné mon attention au phénomène de "Ram Pressure Stripping". La galaxie ESO 137-001 représente un des meilleurs cas pour étudier cet effet. Sa longue queue H_2 intégrée dans une queue de gaz chaud et ionisé soulève des questions sur son possible arrachement de la galaxie ou sa formation en aval dans la queue. Basé sur des récentes simulations numériques, j'ai montré que la formation des molécules de H_2 sur la surface des grains dans la queue est un scénario viable.

Contents

Chapter 1

A journey through the interstellar medium

Pumbaa: Hey, Timon, ever wonder what those sparkly dots are up there?
Timon: Pumbaa, I don't wonder; I know.
Pumbaa: Oh. What are they?
Timon: They're fireflies. Fireflies that, uh... got stuck up on that big bluish-black thing.
Pumbaa: Oh, gee. I always thought they were balls of gas burning billions of miles away.
Timon: Pumbaa, with you, everything's gas.

The Lion King (1994)

A galaxy is a massive, gravitationally bound system composed of stars, interstellar medium and dark matter. With the term interstellar medium we refer to the matter in between stars. This medium is mostly composed of gas (neutral, molecular or ionised), dust (tiny solid particles) and cosmic rays. This introductory chapter first describes the classical three-phase composition of the interstellar medium and then will take you on the journey a dust grain would follow through the interstellar medium in our Galaxy.

1.1 The three-phase model of the interstellar medium

Following the classical theory of the interstellar medium (McKee and Ostriker 1977; Cox 2005; Tielens 2010), we can assume it to be divided into three phases: the cold neutral medium (CNM), the warm neutral/ionised medium (WNM/WIM) and the hot ionised medium (HIM).

In the 1970s, for the first time, McKee and Ostriker (1977) showed how starting from a two phase primitive galaxy, the system can evolve to the present three-phase medium. They supposed that the initial system was mainly composed by cold neutral clouds and an intercloud phase (WNM and WIM, which represent the most extended phase). The explosion of a massive ($M \gtrsim 8M_\odot$) star (supernova, SN) releases a large amount of energy ($E_{\rm SN}$) and matter ($1 - 5M_\odot$) and generates turbulence in the ISM. As a consequence, the shocked gas will be ionised and its temperature will

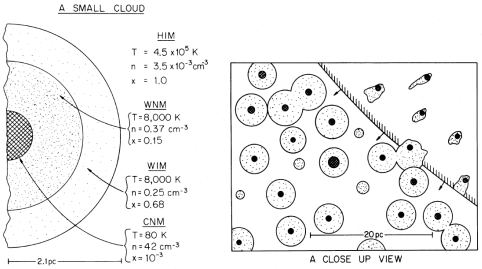

Figure 1.1: Left: diagram of the different phases of a small dense cloud. Right: the global view of the interstellar medium. A few clouds are represented as they are invaded by a supernova, expanding from the upper right part. McKee and Ostriker (1977).

rise to $T_{\rm HIM} \gtrsim 10^6\,{\rm K}$. At these temperatures, the radiative cooling timescale is long ($\tau_{\rm th} \gtrsim 10^8\,{\rm yr}$, see Section 5.B) and therefore this gas will coexist with the two other phases.

Once the pressure equilibrium between the different phases is reached, the volume occupied by the hot gas at the galactic scale is related to the volume, $V_{\rm SNR}$, and cooling timescale, $\tau_{\rm SNR}$, of the single supernova remnants. These two latter quantities can be express as (Tielens 2010):

$$V_{\rm SNR} = 1.7 \times 10^{-3} \left(\frac{E_{\rm SN}}{10^{51}\,{\rm erg}} \right)^{11/15} n_0^{-11/15}\,{\rm kpc}^3 \tag{1.1.1}$$

and

$$\tau_{\rm SNR} = 1.7 \times 10^{6} \left(\frac{E_{\rm SN}}{10^{51}\,{\rm erg}} \right)^{11/45} n_0^{-11/45}\,{\rm years}, \tag{1.1.2}$$

where n_0 is the density of the medium where the SN expands. For a typical SN, the energy released is $E_{\rm SN} \sim 10^{51}$ erg (e.g. McKee 1989). Furthermore, since the filling factor of the CNM is low ($\sim 1-5\%$), we can assume that a shock wave mainly expands in the WIM, where the density is $n_0 \sim 0.25\,{\rm cm}^{-3}$. The SNR volume and timescale then result $V_{\rm SNR} \sim 4.7\times10^{-3}\,{\rm kpc}^3$ (i.e. a sphere of radius $\sim 100\,{\rm pc}$) and $\tau_{\rm SNR} \sim 2.4\times10^6\,{\rm yr}$.

Given the rather large volume of the ISM affected by a SNR and its long timescale, we can therefore imagine that, a series of several supernovae in a galaxy may create interconnections between the shocked regions. We can define a porosity parameter, Q, as (Cox and Smith 1974):

$$Q = k_{\rm SN} V_{\rm SNR} \tau_{\rm SNR}, \tag{1.1.3}$$

where the supernova rate per unit volume, $k_{\rm SN}$, is estimated to be (Tielens 2010):

$$k_{\rm SN} = 6.7 \times 10^{-5} N_{\rm SN}\,{\rm years}^{-1}{\rm kpc}^{-3}, \tag{1.1.4}$$

with $N_{\rm SN}$ the number of SN per 100 years in the our Galaxy, i.e. $N_{\rm SN} \sim 1$. The porosity parameter then results

$$Q \simeq 0.12 N_{\rm SN} \left(\frac{E_{\rm SN}}{10^{51}\,{\rm erg}}\right)^{44/45} n_0^{-44/45}, \tag{1.1.5}$$

and for the assumed values of energy, density and rate we obtain $Q \simeq 0.73$.

According to the percolation theory, the filling factor of the HIM is related to the porosity as (Shull and Draine 1987; Ferriere 1995)

$$f_{\rm HIM} = \frac{Q}{1+Q}. \tag{1.1.6}$$

Thus, for the estimated porosity parameter, the HIM filling factor results $f_{\rm HIM} = 0.42$. This means that, if we assume randomly distributed supernovae, there is a probability of 42% that a supernova explodes in a hot cavity. Furthermore, if we take into account that the supernova will expand for $\sim 100\,{\rm pc}$, then the probability that there will be an overlap between the hot cavities generated by the newly exploded and past supernovae is very high ($p = 1 - exp(-8Q) \simeq 0.99$, Tielens 2010; Quintanilla and Torquato 1996).

This is a runaway process: because of the large overlap between the hot cavities, the pre-shock density of the gas swept up by a SN will be increasingly lower and the SN will expand further, reaching a larger filling factor. However, despite numerous theoretical studies since the first works, the HIM filling factor is still highly uncertain (see Table 1.1).

This is the classical three-phase model of the ISM. Supernova explosions regulate the filling factor of the three phases and asymptotically they will coexist in pressure equilibrium. However, in the ISM there is a continuous transition between the different phases and as we will see in the next section, these transition regions are of particular interest and contribute to the global picture that we have of the Galaxy.

Table 1.1: Parameters of the different phases of the interstellar medium. f is the filling factor, $T_{\rm gas}$ and $n_{\rm H}$ are the gas temperature and density respectively.

Phase	f	$T_{\rm gas}$ (K)	$n_{\rm H}$ (cm^{-3})
CNM	$0.01-0.05$	$50-100$	$20-50$
WNM	$0.1-0.2$	8×10^3	$0.2-0.5$
WIM	$0.2-0.5$	8×10^3	$0.2-0.5$
HIM	$0.3-0.7$	10^6-10^7	$10^{-2}-10^{-4}$

1.2 The lifecycle of dust

Dust is an important component of the interstellar medium and its dynamics is key to understand the star and planet formation. In the framework described above, you will be taken on a journey through the interstellar medium following the lifecycle of the dust in our Galaxy (see Fig. 1.2).

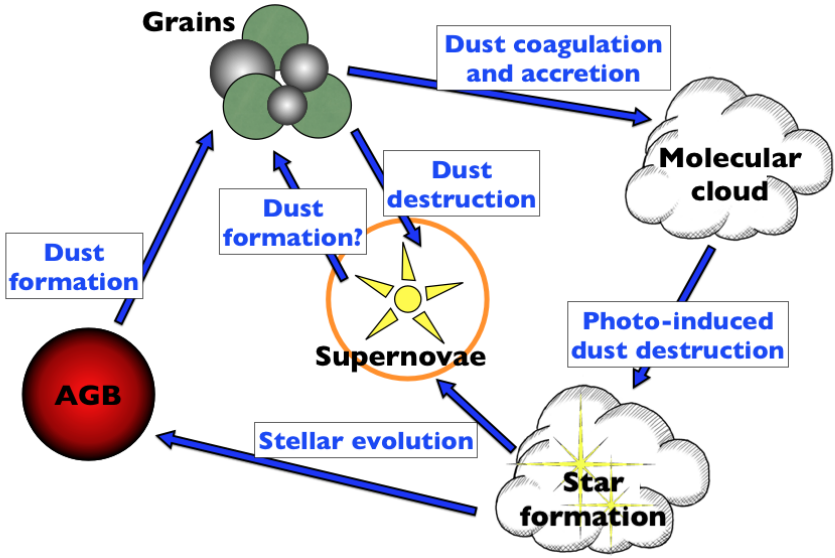

Figure 1.2: The Lifecycle of dust.

1.2.1 Dust formation

Dust is believed to be formed mainly in the external layers of evolved metal-rich stars. From their formation, stars burn huge quantities of hydrogen in their core leading to the exhaustion of their supply of hydrogen in the late stages of their lives. For a low- to intermediate-mass star ($0.6 - 10\,M_{\odot}$), this process leads to an increase in the temperature and density in the core, while the outer layers expand and cool. At a sufficiently high core temperature ($\sim 3 \times 10^8\,\mathrm{K}$) the fusion of helium nuclei begins. The cooling of the star halts and its luminosity increases again leading to a phase known as the early asymptotic giant branch (E-AGB). When the star has burned all the helium supply, a phase of thermal pulsations begins (TP-AGB). At the early stages of this phase, the star derives its energy from a very thin layer of hydrogen. As the hydrogen burns, more and more helium is produced leading to an explosive reaction known as a helium shell flash. The increase in temperature and luminosity then leads to a sufficiently high energy to ignite hydrogen burning, leading the cycle to start again. Because of these thermal pulsations the star expels large amount of material that forms the circumstellar envelope. This is the place where most of the cosmic dust is formed and finally released into the ISM with a timescale of $\sim 3 \times 10^9\,\mathrm{yr}$ (Dwek and Scalo 1980; Gehrz 1989; Jones and Tielens 1994). In particular, carbon-rich and oxygen-rich stars are believed to mainly form carbonaceous and silicate grains, respectively.

Furthermore, analyses of presolar grains within primitive meteorites seem to indicate evidence for SiC and graphite grains formed in Type II SNe (e.g. Hoppe et al. 2009, 2010; Lodders 2006). However, whether this mechanism is able to efficiently form large amount of dust is a debated topic. For example, observations of type II SNe such as Cas A or Supernova 1987A reveal the presence of newly formed dust ($\sim 0.1 M_{\odot}$ for CasA, Arendt et al. 2014, $\sim 0.4 - 0.7 M_{\odot}$ for Supernova 1987A, Matsuura et al. 2011). However, these SNe have not yet reached the phase where the reverse-shock would destroy part of the observed dust. If a significant amount of dust were formed in SN ejecta, this could considerably reduce the dust injection timescale but as yet the evidence is inconclusive.

Once ejected into the ISM by stellar winds (or shocks), and depending on the environment, dust undergoes different processes leading to an evolution of its physical properties, size distribution and chemical composition.

1.2.2 Dust destruction

As mentioned in the previous section, supernova remnants cool down with a very long timescale ($\tau_{\mathrm{SNR}} \sim 10^8\,\mathrm{yr}$) therefore leading to a large HIM filling factor ($f_{\mathrm{HIM}} \sim 0.3 - 0.7$). This medium is highly ionised and because of its high gas temperature ($T_{\mathrm{g}} \sim 10^6 - 10^7\,\mathrm{K}$) ions and electrons are in thermal motion at high velocities ($v_{\mathrm{e}} \sim 5 - 10 \times 10^3\,\mathrm{km\,s^{-1}}$ and $v_{\mathrm{p}} \sim 1 - 4 \times 10^3\,\mathrm{km\,s^{-1}}$ for electrons and protons, respectively). This represents a harsh environment for the dust. Fast ions and electrons, interacting with dust grains (Section 3.2 and 3.3) are able to efficiently erode them (Draine and Salpeter 1979a; Jones 2004; Micelotta et al. 2010b; Bocchio et al. 2012). This process, known

as sputtering, leads to the complete destruction of grains on rather short timescales ($t_{\rm dest} \sim 10^7$ yr for a 100 nm carbonaceous grain embedded in the HIM, Bocchio et al. 2012, Chapter 4).

Furthermore, during a supernova explosion, the propagation of shock waves in the ISM, leads to the destruction of large amounts of dust (Chapter 6) on a timescale of the order of $10^8 - 10^9$ years (Barlow 1978a,b; Draine and Salpeter 1979a,b; Dwek and Scalo 1980; Seab and Shull 1983; McKee et al. 1987; Jones et al. 1994, 1996). In the framework of the three-phase model, the dust destruction is estimated to be dominant in the WIM (McKee 1989). In fact, the HIM is too tenuous for the sputtering to be an efficient mechanism while the CNM has a too low filling factor to give a major contribution to the dust destruction. During the coupling to the shocked gas, dust undergoes interactions with ions/atoms and electrons (Section 3.2 and 3.3) and other grains (Section 3.5). This mechanism is the main source of dust destruction in the ISM and will therefore determine its lifetime in the Galaxy. The timescale for the complete destruction of dust due to SNe in the Galaxy was estimated by McKee (1989) as

$$t_{\rm SNR} = \frac{9.7 \times 10^7}{\int \epsilon(v_{\rm s7}) v_{\rm s7}^{-3} dv_{s7}}, \tag{1.2.1}$$

where $v_{\rm s7}$ is the shock velocity in units of 100 km s^{-1} and $\epsilon(v_{\rm s7})$ is the dust destruction efficiency for a shock of that velocity. The more recent estimates of dust destruction efficiency were calculated by Jones et al. (1994, 1996) for different shock velocities and taking into account both ion/atom - grain interactions and grain - grain collisions, finding a lifetime of 4×10^8 yr and 6×10^8 yr for silicate and carbonaceous grains, respectively. These estimates have now been re-visited by Bocchio et al. (2014) with the use of a new dust model (Jones et al. 2013) and updated dust processing models (Serra Díaz-Cano and Jones 2008; Micelotta et al. 2010a,b; Bocchio et al. 2012, 2013b, see Chapter 6), resulting in even shorter lifetimes for both silicate ($t_{\rm dest} \sim 3 \times 10^8$ yr) and carbonaceous grains ($t_{\rm dest} \sim 6 \times 10^7$ yr). Thus, the issue of dust lifetime is still a major conundrum (e.g., Jones and Nuth 2011).

1.2.3 Dust in the CNM

As the dust continues its journey, it enters denser regions, the CNM. The CNM appears to contain essentially three types of clouds: the diffuse, translucent and molecular clouds. While the diffuse clouds are rather tenuous ($n_{\rm H} \sim 10 - 100\,{\rm cm}^{-3}$) and exposed to starlight, the molecular clouds are much denser ($n_{\rm H} > 10^4\,{\rm cm}^{-3}$) and protected from stellar UV radiation. Translucent clouds have properties in between these two extremes and represent a transition between these two phases.

In diffuse clouds, dust is mainly heated by the absorption of UV-visible starlight (Section 3.1). This absorbed light is then re-emitted in the IR-mm, making dust detectable by IR-mm telescopes (Section 2.2). Furthermore, the absorption of UV photons is expected to modify the internal structure of grains (Jones et al. 2014). For

example, the absorption of UV photons by carbonaceous grains leads to the destruction of C-C bonds then making the outer layer of these grains aromatic-rich (see Section 3.1).

On the other hand, during the transition between diffuse and molecular clouds, as the gas density increases, the starlight is dimmed and the process of aromatization of the outer layer of carbonaceous grains is quenched and another process, their re-hydrogenation, can be efficient and carbonaceous dust is then expected to be aliphatic-rich (Section 3.1, Jones et al. 2014).

Finally, once the grains are incorporated into molecular clouds, the gas density is high enough to allow for gas phase species (e.g., C, O, N) to accrete onto grain surfaces (Jones 2013; Jones et al. 2013, 2014; Köhler et al. 2014). This process is expected to be efficient in the ISM of the Milky Way but, on the contrary, seems not to be at work in low metallicity galaxies (Rémy-Ruyer et al. 2014). Then, moving to the cold core of molecular clouds, the dust temperature drops ($T \lesssim 10\,\mathrm{K}$) and molecules hitting the surface grains are expected to form icy mantles (see e.g. Gibb et al. 2004).

Molecular clouds also represent the perfect environment for the formation of stars and are sometimes called "stellar nurseries". A newly born star is luminous and, because of its energetic radiation, will form a large, low-density and mostly ionised cloud (HII region). The surrounding molecular cloud is also affected by the strong radiation field, which acts as main source of gas heating (photodissociation region, PDR). Dust grains in PDRs almost immediately release the ice locked in their mantles to the gas phase and the absorption of high energy photons by small grains can lead to their destruction by evaporation (e.g. Pilleri et al. 2013).

Finally, the star follows its standard evolution, dust grains will gather to form planets and the system may look like our Solar System. Finally, low- to intermediate-mass stars, later in their lives will quit the main sequence and will end up in the AGB phase. The life-cycle of dust will then re-start again from the beginning.

1.3 Thesis organization

The main goal of my PhD study is to understand the dust processing that occurs during the mixing between the galactic interstellar medium and the intracluster medium. This process is of particular interest in violent phenomena such as galaxy-galaxy interactions or the "ram pressure stripping" due to the infalling of a galaxy towards the cluster centre.

In particular we want to understand what are the mechanisms of destruction and heating of dust outside the boundaries of galaxies. Is dust destroyed? Can it emit enough to be observed? These are the main questions that we asked ourselves since the beginning of this PhD study.

Since the discovery of dust, observational constraints have given the possibility to retrieve information about its chemical composition and size distribution in different environments. Chapter 2 presents different observations (ranging from UV/vis to FIR) in chronological order and shows how they contributed to our present knowledge of the

dust properties. We then describe the main dust models developed since the discovery of the dust and how they have been able to explain the main observables.

As seen in this chapter, the ISM is not uniform but rather presents a variety of phases. During its journey through the interstellar medium, depending on the environment, dust undergoes different physical interactions. We describe these processes in Chapter 3 dividing them into three main categories:

- photon - grain interactions,
- ion/atom - grain or electron - grain interactions,
- grain - grain interactions.

Each of these processes will then be responsible for the observation of different features and only a proper modelling of these interactions may explain our observations.

In Chapter 4 we present and discuss the details of the interaction between grains and energetic ions and electrons. In particular, we quantify the destruction and heating that a grain undergoes as a consequence of collisions with gas ions and electrons when embedded in a hot coronal-type gas and we calculate the expected dust emission spectrum. Furthermore, in order to validate our modelling work, we compare the expected dust emission spectrum with extragalactic sources as observed by the *Herschel* Space Observatory. However, because of the short lifetime of dust in a hot gas, the observation of collisionally heated dust turns out to be a particularly difficult task, therefore forcing us to a better understanding of the *Herschel* instruments.

Chapter 6 focuses on the dust processing in interstellar shock waves. In particular, we updated the code presented by Jones et al. (1994, 1996) in order to estimate the dust destruction efficiency for different shock velocities. We now use the recent Jones et al. (2013) dust model and implement all the recent modelling on dust destruction (Serra Díaz-Cano and Jones 2008; Micelotta et al. 2010a,b; Bocchio et al. 2012, 2013b). We then calculate the dust lifetime in our Galaxy and, comparing it to the dust formation timescale, we draw some general conclusions on the grain growth in the ISM.

Finally, in Chapter 7 we focus on the phenomenon of "Ram Pressure Stripping". Multiwavelength observations of different infalling galaxies can tell us much about this process. We select particularly significant observations and we show them in this chapter. However, only a good balance between observations and numerical simulations may lead to a full understanding of this process. We focus on the well studied galaxy ESO 137-001 and, using both the results of AMR numerical simulations and our modelling work, we propose a viable mechanism to explain the presence of dust and molecular gas in the tail of this galaxy.

Chapter 2

Evidence for Dust in the Universe

> If there is anything that can bind the mind of man to this dreary exile of our earthly home and can reconcile us with our fate so that one can enjoy living, then it is verily the enjoyment of the mathematical sciences and astronomy.
>
> Johannes Kepler

Contents

THIS chapter focuses on one of the major components of the interstellar medium: the dust. During the last century, many observations suggested the presence of dust in the Universe. Since the discovery of dust, observational constraints provide information about its chemical composition and size distribution in different environments. We will follow the different stages and major discoveries that led to our present knowledge of the constituents of dust in our Galaxy.

2.1 Dust extinction

During the first years of the XX century, for the first time Barnard (1907, 1910) and later Trumpler (1930) found that the light emitted by some stars was dimmed by an "absorbing medium" present between us and the source. This was the beginning of our study of the cosmic dust. However, despite more than half a century of research, there are still large uncertainties on the dust chemical composition and its size distribution.

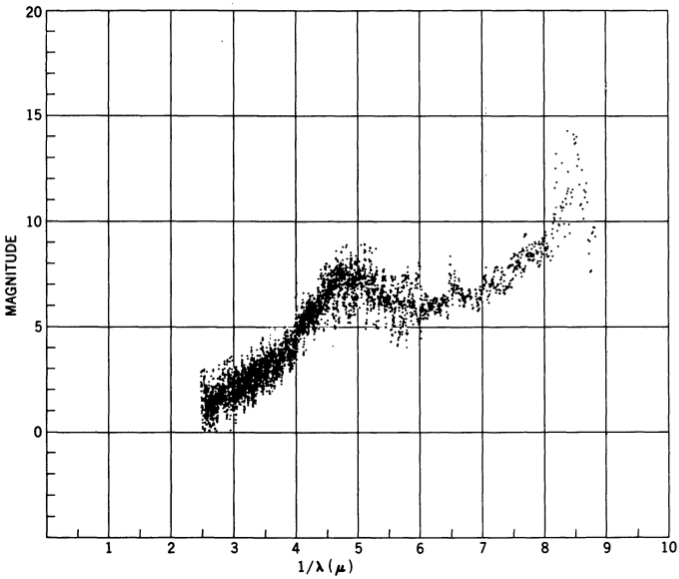

Figure 2.1: Interstellar extinction in magnitudes as determined from ζ and ϵ Persei. Stecher (1969).

We now know that the "absorbing medium" hypothesized by Barnard and Trumpler is actually interstellar dust. The phenomenon of the attenuation of starlight can be explained as the combined effect of absorption and scattering of light from dust grains. For example, observing stars at low galactic latitudes, the detection of light from the UV band to the IR band is significantly affected by the presence of dust. If we consider an infinitesimal path length, ds, along the line of sight, the variation of the light intensity, dI_λ is then given by:

$$dI_\lambda = -I_\lambda \kappa_{\mathrm{e},\lambda} ds + j_\lambda ds, \tag{2.1.1}$$

where $\kappa_{\mathrm{e},\lambda}$ is the extinction coefficient at the wavelength λ and j_λ is the emissivity of the material present in the element ds. The extinction coefficient is expressed as:

$$\kappa_{\mathrm{e},\lambda} = \kappa_{\mathrm{a},\lambda} + \kappa_{\mathrm{s},\lambda}, \tag{2.1.2}$$

where $\kappa_{a,\lambda}$ and $\kappa_{s,\lambda}$ are the absorption and scattering coefficients at the wavelength λ. A quantitative study of the wavelength dependence of the dust extinction coefficient can give us important information on the chemical composition of the grains.

In the 1960s, Stecher (1965, 1969), observing the spectrum of different stars, noticed a characteristic bump in the UV extinction between 115 nm and 400 nm (corresponding to $1/\lambda \simeq 2.5 - 8.7\,\mu\text{m}^{-1}$, see Fig. 2.1). This discovery opened up the field of study, allowing scientists to have a better understanding of the dust, and a few years later led to the formulation of the first dust models (see Section 2.4). However, the identification of this "UV bump" is still somewhat controversial.

Nowadays, we have precise measurements of the dust extinction in the diffuse interstellar medium of our Galaxy from UV to IR bands (see Fig. 2.2, Mathis 1990). We can define the parameter $R_V \equiv A_V/E(B-V)$, where $E(B-V) \equiv A_B - A_V$ and

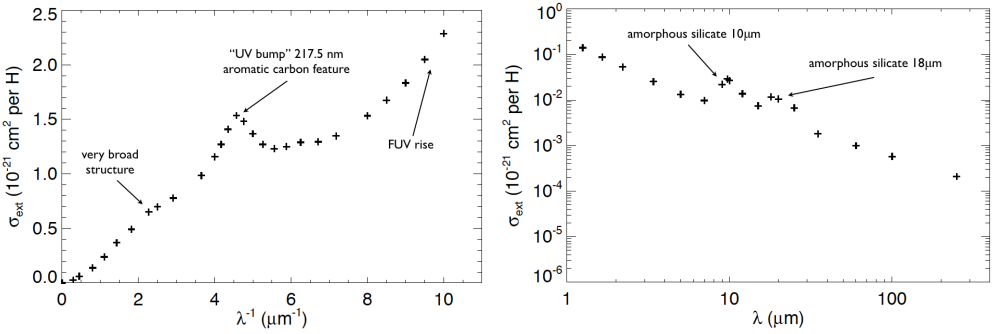

(a) (b)

Figure 2.2: Observed extinction in the UV (left) and IR (right) bands as per Mathis (1990).

A_λ is the extinction at a wavelength λ (B and V bands are centered at 435 and 555 nm, respectively). It has been noted that through different sight lines in the diffuse medium of our Galaxy the value of $R_V \approx 3.1$. On the other hand, moving towards denser regions in the interstellar medium, the observed value of R_V increases leading to a flattening of the extinction curve at short wavelengths (e.g. Cardelli et al. 1989; Fitzpatrick and Massa 2007).

From the observed extinction spectrum we can constrain the width and peak position of the bump at 917.5 nm, observed by Stecher (1965, 1969). This feature seems to originates from carbonaceous dust. Furthermore, we observe a rise in the FUV wavelength range most likely also associated with carbonaceous grains. Finally, we clearly see silicate features in the IR extinction data at 10 and 18 μm. These observations, together with the observed IR emission and the cosmic abundance of elements, represent strong constraints that any viable dust model should satisfy.

2.2 Dust emission

During the 1960s, different observations of planetary nebulae[1] highlighted a larger-than-expected emission at 10 μm (Gillett et al. 1967; Woolf 1969). A first interpretation was given by Krishna Swamy and O'dell (1968). They developed a model where Lyα photons in the nebula were absorbed by graphitic grains and then re-emitted in the IR therefore explaining the excess. A few years later, Gillett et al. (1973) for the first time showed the MIR emission spectrum of a planetary nebula (see Fig. 2.3). The

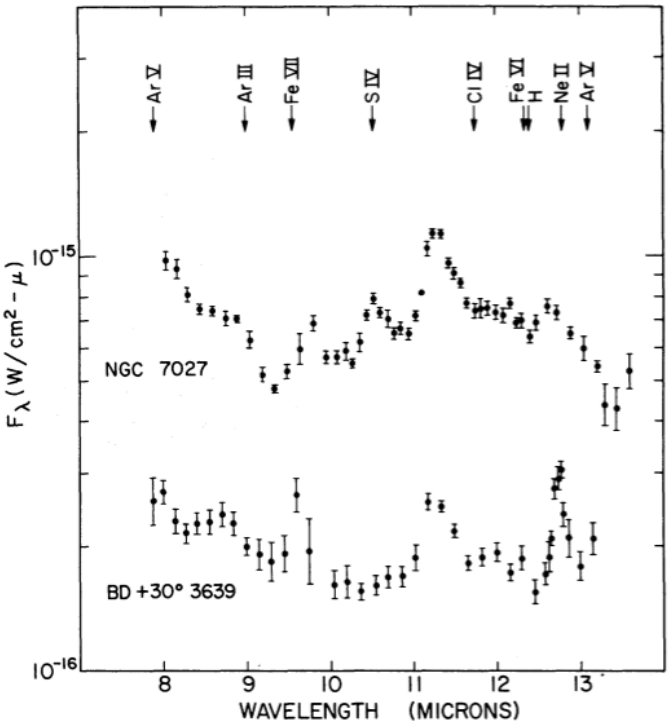

Figure 2.3: 8 - 13 μm spectrum of NGC 7027 and BD +30°3639. Wavelengths of predicted fine-structure lines are indicated. Gillett et al. (1973).

spectrum presents features that cannot be attributed to the emission from graphitic grains, therefore proving that the interpretation by Krishna Swamy and O'dell (1968)

[1] A planetary nebula is a relatively short phase (a few 10^4 yr) towards the end of the life of a star when the external layers of ionised gas are expelled from an old red giant star. The term "planetary nebula" was introduced by William Herschel in the 1780s when looking at these objects, he interpreted them as forming planetary systems.

was not able to account for that emission. At that time nobody was able to identify those features and it remained an unsolved puzzle in infrared astronomy for a long time.

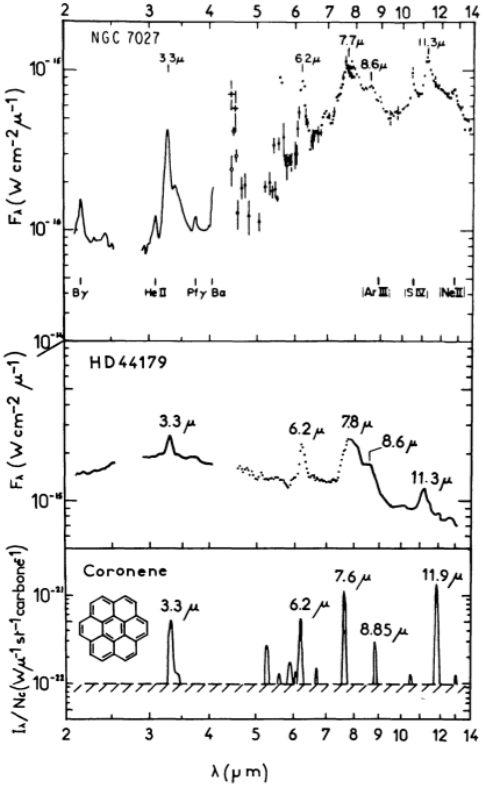

Figure 2.4: The first two panels show the observed spectrum towards two planetary nebulae, while the bottom panel shows laboratory measurements of the coronene spectrum. Leger and Puget (1984).

Almost a decade later, Duley and Williams (1981) proposed that these features could be attributed to the emission and absorption of surface functional groups on small carbon particles. The proposed functional groups are rich in hydrogen and encompass aromatic $-CH$, $-CH_3$, $-OH$, $-CHO$ and $-NH_2$. The stretching, wagging and deformation modes of these groups could explain the absorption at 3.4 μm and the emission seen at other wavelengths. However, Leger and Puget (1984) pointed out that hydrogenated graphitic grains were able to explain the 3.28 μm emission band but that their spectrum presented a strong continuum with weak bands at 6.3 μm 11.5

μm. They suggested instead that all these IR features can be associated with the emission/absorption of one kind of molecule: polycyclic aromatic hydrocarbons (PAHs). In Fig. 2.4 we report a figure from Leger and Puget (1984). The top two panels show the observed IR emission features in NGC 2027 and HD 44179. The bottom panel shows the calculated emission of a coronene molecule (a PAH, $C_{24}H_{12}$) heated to 600 K. Comparing the laboratory measurements to the observations, it is clear that the observed emission features in these objects could be well explained by the presence of PAHs. The only weak point at that time was that the 11.9 μm emission band of coronene did not fit the observed band at 11.3 μm. However, Leger and D'Hendecourt (1987) proposed that a mixture of larger PAHs could account for this discrepancy.

In the meantime, in 1983, with the launch of the Infrared Astronomical Satellite (IRAS), for the first time we had the possibility to make an all-sky map of the IR emission (see Fig. 2.5). This satellite was built to observe at four wavelengths: 12 μm, 25 μm, 60 μm and 100 μm.

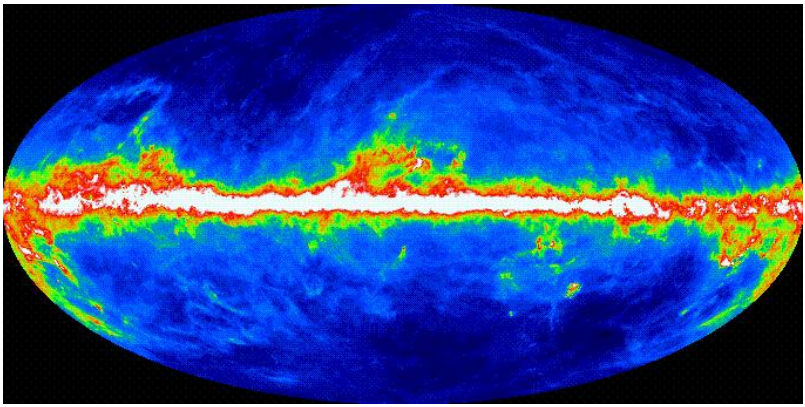

Figure 2.5: All-sky view of the IRAS 100 μm imaging data, representing a MONTAGE-generated combination of the individual images created by Schlegel et al. (1998). The Galactic Aitoff projection is shown in false color (blue is low intensity, red/white is high intensity).

Many more satellites have been launched since then. The improved sensitivity and spatial resolution of detectors and optical systems has allowed us to have a very good estimate of the dust emission across the whole IR-mm spectrum. In Table 2.1 we list the main satellites and detectors used for IR-mm observations until the present, their launch date, the wavelengths of operation and their angular resolution.

In Fig. 2.6 we show the IR observations of the diffuse interstellar medium as detected by several satellites. We notice that the MIR emission is characterized, as detected by Gillett et al. (1973), by strong features: the emission between 1 μm and 12 μm represents more than 20% of the total IR emission. Furthermore, the FIR spectrum is

Table 2.1: Telescopes/balloons and detectors used for IR observations.

Satellite	/ Detector	Launch	Wavelengths (μm)	Resolution
IRAS		1983	12, 25, 60, 100	$30'' - 2'$
AROME		1987	3.3	$30'$
COBE	/ DIRBE	1989	1.25, 2.2, 3.5, 4.9, 12, 25, 60, 100, 140, 240	$42'$
COBE	/ FIRAS	–	100 - 10^4	$420'$
ISO	/ ISOCAM	1995	2.2 - 5.5, 4 - 17	$6''$
ISO	/ ISOPHOT	–	3 - 120, 50 - 240, 2.5 - 5, 6 - 12	$1.3'$
Spitzer	/ IRAC	2003	3.6, 4.5, 5.8, 8	$2''$
Spitzer	/ MIPS	–	24, 70, 160	$6'' - 38''$
WISE		2009	3.4, 4.6, 12, 22	$6'' - 12''$
Herschel	/ PACS	2009	70, 100, 160	$5'' - 12''$
Herschel	/ SPIRE	–	250, 350, 500	$18'' - 37''$
Planck	/ HFI	2009	350, 550, 850, 1380, 2100, 3000	$4' - 10'$
Planck	/ LFI	–	4280, 6800, 10^5	$13' - 32'$

seemingly similar to a blackbody spectrum, which implies that interstellar grains are in thermal equilibrium and are almost perfect emitters. Finally we observe a flat region in the spectrum between 20 μm and 50 μm. The infrared spectrum, together with the dust extinction, provides very strong constraints for dust models.

2.3 Cosmic abundance of elements

The line of sight towards the bright O9.5V star ζ Ophiuchi is well studied and commonly used for absorption-line spectroscopy in order to estimate the gas phase abundances of different elements. Since there is observational evidence that the abundances in the ISM are close to the solar abundance, comparing the gas phase abundances towards ζOph with the solar ones, it is possible to calculate the fraction of the elements that are actually locked in dust grains. In Table 2.2 we report the element abundances and the calculated mass of elements locked in grains. In particular, it should be noted that the gas phase carbon abundance is mostly determined by the column density of CII, which strongly relies on the oscillator strength, f, of the weak intersystem line CII]2325 Å. Using *Copernicus* data, Morton (2003) estimated the oscillator strength at this wavelength to be $f(\text{CII}]2325\,\text{Å}) = 4.78\times10^{-8}$. However, Sofia et al. (2011) managed to use saturated strong lines (e.g. $\lambda = 1334$) to have a more accurate estimate of the CII column densities. With this method they estimated a higher oscillator strength

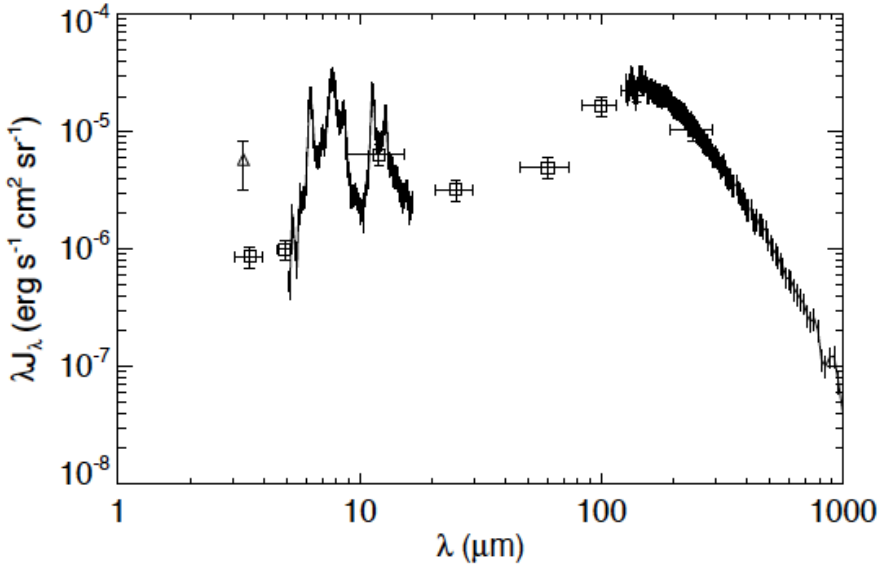

Figure 2.6: The dust SED as observed by various instruments: $\sim 5-15\,\mu$m ISOCAM/CVF ISO spectrum, $\sim 100-1000\,\mu$m FIRAS/COBE spectrum, $3.3\,\mu$m AROME narrow band measurement (triangle) and DIRBE/COBE photometry (squares).

$f(\text{CII}]2325\,\text{Å}) = 1.0\times10^{-7}$ therefore implying that less carbon than previously thought, resides in the gas phase. We note that the major constituents of dust grains must be carbon, silicon, oxygen, iron and magnesium. The cosmic abundance of these elements therefore represents a stringent constraint for the chemical composition and mass of dust.

2.4 Dust models

Over the last seventy years many dust models have been proposed in order to explain these observations leading to a progressivly better understanding of the dust chemical composition and size distribution. The first dust model ever proposed was in the 1940s by Oort and van de Hulst (1946). They were able to explain the available optical extinction observations assuming the presence of ice grains in the interstellar space that follow a power law distribution. This work paved the way for the first model that succeeded in explaining the UV bump extinction: the Mathis, Rumpl, and Nordsieck (1977, hereafter MRN) dust model. They proposed that dust is composed of two separate dust components: graphite and silicate grains and that the assumed dust size

Table 2.2: Elemental abundances towards ζOph, Draine (2011).

X	$(N_X/N_H)^a_\odot$ (ppm)	$N_{X,gas}/N_H^b$ (ppm)	$N_{X,dust}/N_H$ (ppm)	$10^3 M_{X,dust}/M_H$
C	295 ± 36	$135 \pm 33^{d,e}$	160 ± 49	1.92 ± 0.59^e
		$85 \pm 20^{d,f}$	210 ± 41	2.52 ± 0.49^f
N	74.1 ± 9.0	78 ± 13^g	-14 ± 16	0
O	537 ± 62	295 ± 36^d	242 ± 72	3.87 ± 1.15
		$[383]^c$	154 ± 8	2.46 ± 0.13
Mg	43.7 ± 4.2	4.9 ± 0.5^g	39 ± 4	0.94 ± 0.10
Si	35.5 ± 3.0	1.7 ± 0.5^h	34 ± 3	0.95 ± 0.08
Fe	34.7 ± 3.3	0.13 ± 0.01^g	35 ± 3	1.96 ± 0.17

[a] Asplund et al. (2009).
[b] Assuming $N(H) + 2N(H_2) = 10^{21.13 \pm 0.03} cm^{-2}$.
[c] Assuming $N_{O,dust}/N_H = 154$ ppm.
[d] Cardelli et al. (1993).
[e] If $f(CII]2325Å) = 4.78 \times 10^{-8}$ (Morton 2003).
[f] If $f(CII]2325Å) = 1.00 \times 10^{-7}$ (see text).
[g] Savage et al. (1992).
[h] Cardelli et al. (1994).

distribution follows a power law with an index of -3.5, *i.e.*

$$n(a) \propto a^{-3.5}. \tag{2.4.1}$$

A simple power law distribution and only two grain populations were able to explain the wavelength dependence of the extinction observations. This dust model therefore had a great deal of success, and in the following decades many MRN-like models were proposed in order to better fit the best available observational data (see following). Furthermore, fragmentation (Hellyer 1970, see also Section 3.5) and coagulation (Norman and Silk 1980) processes naturally lead to power law distributed dust grains, giving a physical interpretation of the assumed size distribution.

A few years later, Draine and Lee (1984) greatly extended the MRN model, introducing more physics. In particular, using the Kramers - Kronig relations, they calculated the dielectric functions for graphitic grains and synthesized ad hoc dielectric functions for silicate grains (called "astronomical silicates").

However, while the expected dust emission suggested by this model was consistent with the FIR emission data by IRAS, MIR observed features were still not explained. The identification of the MIR emission features by Leger and Puget (1984) together with the IRAS observations at 12 μm and 25 μm, made necessary a significant revision of the previous dust models. A couple of teams (Draine and Anderson 1985; Desert

et al. 1990), estimated the temperature fluctuations of the PAHs as they are irradiated by the interstellar radiation field. They updated a MRN-like dust model by lowering the minimum grain size. The inclusion of the PAH properties into such models led to a good fit to both the extinction and emission data at the same time.

More recently, Kogut et al. (1996), de Oliveira-Costa et al. (1997) and Leitch et al. (1997) reported the detection of an emission excess in the mm range that is correlated to the 100 μm dust emission. This discovery imposed another puzzle to solve by the subsequent dust models. Draine and Lazarian (1998) proposed that this excess could be explained by the electric dipole radiation from small spinning dust grains and explored the possible mechanisms leading grains to rotate.

All these dust models were developed starting from MRN-like dust models and by improving on the match to the available observables. However, it is worth mentioning that Zubko et al. (1996, 1998, 2004) developed a dust model that differs from MRN-like models and is derived using the method of regularization, a common method used to solve inverse problems. They showed that this method is a suitable tool in the analysis of interstellar extinction. Furthermore, another alternative dust model was provided by Kim et al. (1994). They used the Maximum-Entropy Method to determine the best size distribution able to explain the extinction as well as the polarization data.

A few years later, Li and Draine (2001), basing their study on laboratory measurements and using observational constraints, proposed an updated dust model consisting of a mixture of amorphous silicate grains and graphitic grains. The distribution of the two populations range from molecular sizes up to grains larger than 1 μm in diameter. This model was then able to reproduce both the extinction data and the NIR to sub-mm emission spectrum of the diffuse interstellar medium.

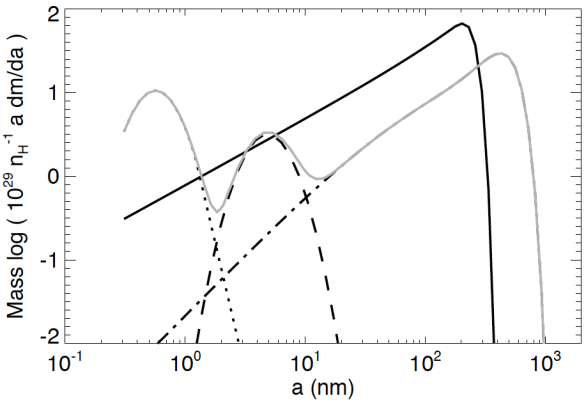

Figure 2.7: Size distribution for the Draine and Li (2007) dust model. PAHs (dotted), graphitic-type (dashed and dash-dotted lines) and silicate grains (solid line) are shown. The gray line indicates the total carbonaceous grain distribution.

Later, Li and Greenberg (2002) proposed a silicate core - aliphatic carbonaceous mantle dust model. Within this model, the bulk of the optical-IR extinction and polarization data can be explained by the single core-mantle dust population. The 3.4 μm and 9.7 μm absorption features are attributed to the stretching of C-H and Si-O respectively and are therefore expected to be associated with the aliphatic mantle and silicate core respectively. The observation of these absorption bands in polarization are therefore critical for the rejection or acceptance of such a core-mantle model. However, at that time it was known that the aliphatic 3.4 μm emission feature was mostly unpolarised towards the Galactic centre (Adamson et al. 1999) but no information was available on the polarization of the silicate 9.7 μm feature along the same line of sight. More recently, Chiar et al. (2006) found that, along the line of sight towards the Galactic centre, the 3.4 μm feature is unpolarized while the 9.7 μm is. This observation would then rule out this chemical composition for large silicate grains.

With the launch of *Spitzer*, more precise MIR data became available leading to more stringent constraints on the PAH properties. In the post-*Spitzer* era, Draine and Li (2007) updated the Li and Draine (2001) model revising the wavelength-dependent absorption of photons by PAHs. In this way they were able to produce the distribution of PAH temperatures as a function of the radiation field and finally compute the time-averaged emission for PAHs of different size. The assumed dust size distribution for this model is shown in Fig. 2.7.

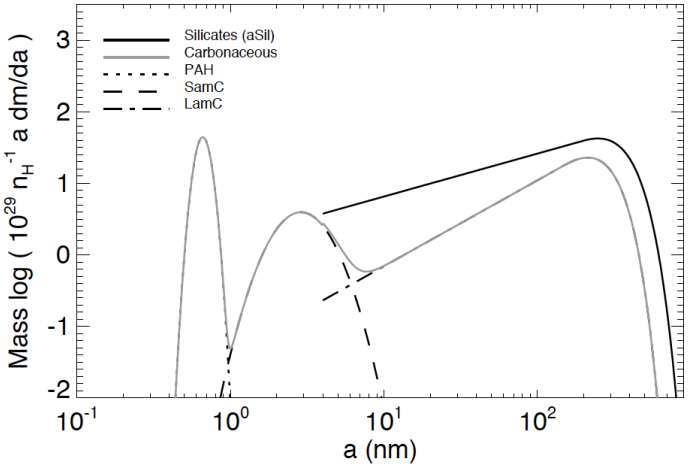

Figure 2.8: Size distribution for the Compiègne et al. (2011) dust model. Line style and colour coding as per Fig. 2.7.

Another dust model was proposed by Compiègne et al. (2011). The dust components in their model are PAHs, amorphous carbon and amorphous silicates (2.8). They

also developed a versatile numerical tool, DustEM[2], that predicts the emission and extinction of dust grains given their size distribution and their optical and thermal properties.

Last year, Chiar et al. (2013) basing their study on the MIR spectrum observation towards the Galactic centre (see Fig. 2.9) proposed a core-mantle dust model. The spectrum between 3.2 and 3.6 μm was fit with different Gaussian functions to represent the aromatic (red curve) and aliphatic (green curves) spectrum. On the other hand,

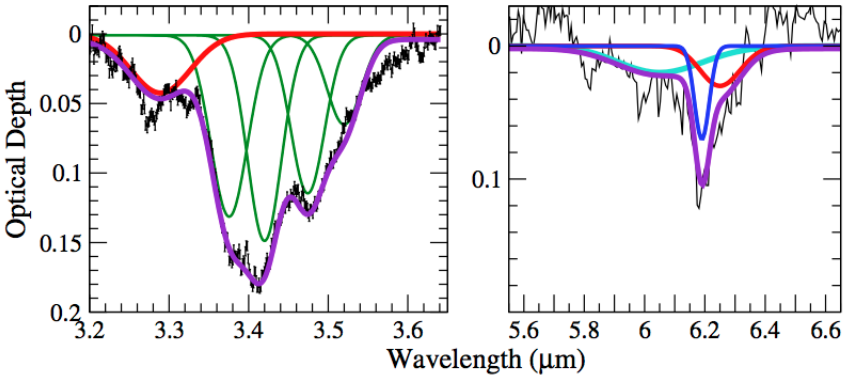

Figure 2.9: Optical depth spectra towards the Galactic centre. Left panel: spectrum between 3.2 and 3.6 μm indicating both aliphatic and aromatic features. Right panel: spectrum between 5.6 and 6.6 μm spectrum showing aromatic and olefinic features. Chiar et al. (2013).

the spectrum between 5.6 and 6.6 μm shows aromatic (red curve) and olefinic (blue curve) features. The light blue curve represent an unidentified feature, may be due to the carbonyl groups which absorb in this region. They were therefore able to determine the column density of the different carriers of the aromatic, aliphatic and olefinic modes and estimate the ratio of sp^2 / sp^3 bonds and H content. They found that interstellar carbonaceous grains towards the galactic centre are mostly aromatic (see Fig.2.10) and therefore proposed that the large carbon grains are core-mantle in structure: an aromatic-rich core with an aliphatic-rich mantle.

In the same year, yet another core-mantle dust model was proposed (Jones et al. 2013). The composition of the carbon grains is opposite with respect to the one proposed by Chiar et al. (2013): the core is aliphatic-rich while the mantle aromatic-rich. We give the details of this model in the next section.

Finally, at the beginning of this year, a new dust model was proposed by Siebenmorgen et al. (2014). This model is able to reproduce the observed extinction, emission as well as the linear and circular polarization of light in the diffuse interstellar medium

[2]http://www.ias.u-psud.fr/DUSTEM.

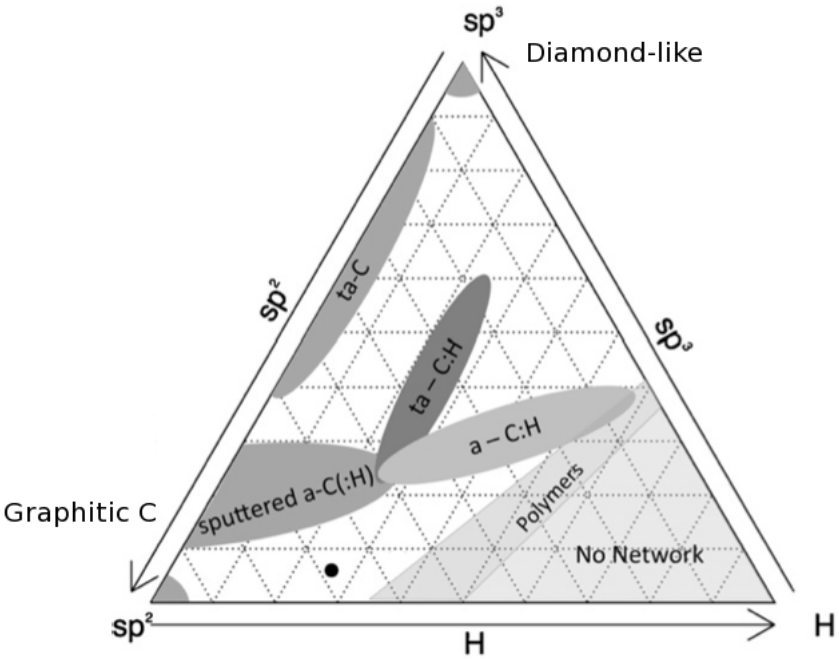

Figure 2.10: Ternary diagram by Chiar et al. (2013). The black circle indicate the galactic centre composition as found in that study.

of our Galaxy. It does use a small number of parameters and a mixture of amorphous carbon and silicate grains ranging from molecules up to 500 nm.

2.5 The Jones et al. (2013) dust model

This recently proposed dust model was developed at the IAS and uses only two materials: (hydrogenated) amorphous carbon, a-C(:H), and amorphous forsterite-type silicate material with the inclusion of iron nano-particles (a-$\mathrm{Sil_{Fe}}$). The model is built upon the derived optical properties of a-C(:H) materials (Jones 2012a,b,c), which are a key new element in dust modelling. The small carbonaceous grains are mostly aromatic rich, while large carbonaceous grains are core-mantle in structure: the inner core is aliphatic rich while the external, $\sim 20\,\mathrm{nm}$ thick, layer is aromatic rich due to photo processing. Silicate grains are also core-mantle in structure. They consist of an amorphous silicate core and a $\sim 5\,\mathrm{nm}$ thick aromatic-rich carbonaceous mantle. Fig. 2.11 shows the chemical composition and sizes of the assumed grains in the model. We notice that grains as large as 10 - 30 nm are completely aromatic rich while still larger grains are

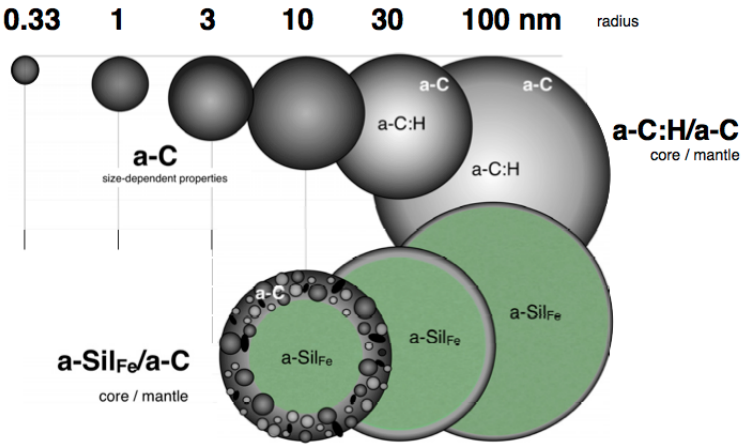

Figure 2.11: Dust chemical composition and sizes as seen in cross-section. Jones et al. (2013).

core-mantle in structure.

The dust size distribution consists of:

- a power law distribution of small ($a \simeq 0.4 - 100\,\mathrm{nm}$) aromatic-rich a-C grains,
- a log-normal distribution, centred at $a \sim 130\,\mathrm{nm}$, of large aliphatic-rich core/aromatic-rich mantle, a-C:H/a-C grains,
- a log-normal distribution, centred at $a \sim 160\,\mathrm{nm}$, of large amorphous silicate grains with 5 nm thick a-C mantle, a-$\mathrm{Sil_{Fe}}$/a-C.

In Fig. 2.12 we show the dust mass distribution as a function of grain size. Black and gray lines indicate the adopted size distribution in this model, while the blue line shows the MRN dust model. In Table 2.3 we summarize the main physical parameters of the dust model used as input for the DustEM code.

It should be noted that in this dust model, most of the carbonaceous dust mass is aromatic rich, which is in accordance to the MIR spectra observed towards the Galactic centre by Chiar et al. (2013). Furthermore, the carbonaceous mantle on the surface of the silicate grains is assumed to be aromatic rich. In fact, as stated by Chiar et al. (2006) the 9.7 μm absorption feature is observable in polarization towards the Galactic centre while the aliphatic 3.4 μm is not. This rules out the possibility of aliphatic rich mantles on the surface of silicate grains.

This dust model uses laboratory-based optical and physical properties for carbonaceous and silicate grains. In particular, small carbonaceous grains follow a power law and they are not divided into sub-populations as in previous dust models (e.g. Draine

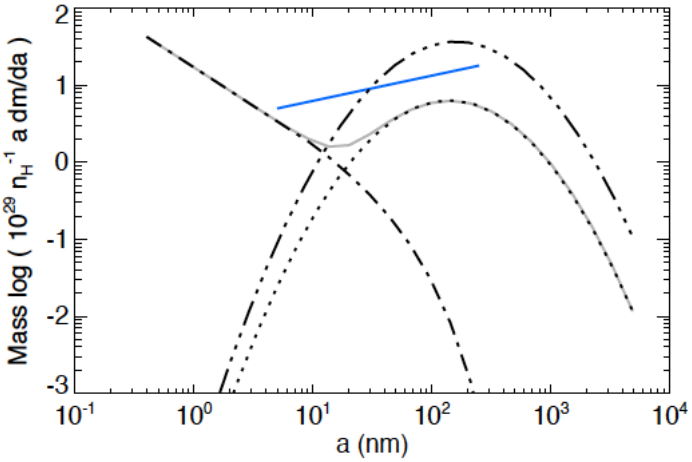

Figure 2.12: Size distribution of the three dust populations in the Jones et al. (2013) dust model. The dot-dashed line and the dotted lines represents the small and large carbonaceous grain distributions, respectively, the sum of the two is shown by the grey solid line. The triple-dot-dashed line shows the silicate grain distribution and the blue solid line represents the MRN graphitic and silicate grains size distribution.

and Li 2007; Compiègne et al. 2011) and their optical properties represent a continuum from ~ 200 nm down to 0.4 nm therefore making the characterization of the grains much more physical.

With the calculated optical properties, the dust model gives a good fit to all the available dust observables in the diffuse ISM (emission, extinction and albedo). Finally, with small variations in the physical and optical properties of carbonaceous grains, this model is able to describe the evolution of dust in a wide range of different environments in the ISM and possibly also in extragalactic environments.

Table 2.3: Parameters for the Jones et al. (2013) dust model as input for the DustEM code. The power-law distribution is defined as $dn/da \propto a^{\alpha}$ and an exponential decay is applied multiplying it by $\exp(-[(a - a_{\rm t})/a_{\rm c}]^{\gamma})$ for $a > a_{\rm t}$, while the log-normal distribution is defined as $dn/dloga \propto \exp(-\frac{(log(a/a_0))^2}{2\sigma^2})$.

composition core/mantle	size distribution	ρ (g cm^{-3}) core/mantle	α	$a_{\rm min}/a_{\rm max}$ (nm)
a-C:H/a-C	p-law	1.3/1.6	5.0	0.4/4900
a-C:H/a-C	log-n	1.3/1.6	–	0.5/4900
a-SilFe/a-C	log-n	2.5/1.6	–	1.0/4900
–/a-C	mantle	–/0.1	–	d = 5 nm

composition core/mantle	$a_{\rm c}$, $a_{\rm t}/a_0$ (nm)	γ/σ	Y (M/M$_{\rm H}$)
a-C:H/a-C	50, 10/–	1.0/–	1.6×10^{-3}
a-C:H/a-C	–, –/7.0	–/1.0	0.6×10^{-3}
a-SilFe/a-C	–, –/8.0	–/1.0	5.8×10^{-3}
–/a-C	–, –/–	–/–	0.6×10^{-3}
		TOTAL	8.6×10^{-3}

Chapter 3

Dust processing in the Universe

An understanding of the natural world and what is in it is a source of not only a great curiosity but great fulfillment.

David Attenborough

Contents

THIS chapter describes the different processes that dust undergoes in various environments in the Universe. We mainly focus on 1) the interaction between photons and grains, 2) atoms/ions, electrons and grains and on 3) grain-grain collisions.

3.1 Photon - grain interaction

As seen in the previous chapter, dust is responsible for the dimming of starlight and dominates the emission spectrum in the IR to sub-mm wavelength range. In order to understand these two processes we first of all need a good knowledge of the optical properties of the dust grains and of the local radiation field. Furthermore, this interaction plays a major role in the process of grain charging: the absorption of a sufficiently energetic photon leads to the ejection of an electron from the surface of the grain (photoelectric effect, see Section 3.4.1).

3.1.1 The interstellar radiation field

The interstellar radiation field (ISRF) is the stellar radiation that a test particle would detect at each point in and around a galaxy. Of course, since the stellar distribution is not uniform inside a galaxy, the ISRF will depend on the distance from the galactic centre and from the galactic plane. The spectrum of the ISRF in the solar vicinity of the Milky Way was estimated by Mathis et al. (1983) based on observational data. They assumed that the stellar emission is due to four components corresponding to the spectrum of stars at different temperatures and with different dilution factors. The mean radiation field flux, $F_\lambda^\odot = 4\pi J_\lambda^\odot$ (with $J_\lambda^\odot$ the radiation field intensity), in the solar vicinity is expressed as (Mathis et al. 1983):

$$\begin{aligned}
0 \rightarrow 91.2\,\mathrm{nm} \quad & 4\pi J_\lambda^\odot = 0 \\
91.2\,\mathrm{nm} \rightarrow 110\,\mathrm{nm} \quad & 4\pi J_\lambda^\odot = 38.57\lambda_{\mu\mathrm{m}}^{3.4172} \\
110\,\mathrm{nm} \rightarrow 134\,\mathrm{nm} \quad & 4\pi J_\lambda^\odot = 2.04510^{-2} \\
134\,\mathrm{nm} \rightarrow 246\,\mathrm{nm} \quad & 4\pi J_\lambda^\odot = 7.115 \times 10^{-4}\lambda_{\mu\mathrm{m}}^{-1.6678} \\
246\,\mathrm{nm} \rightarrow \infty \quad & 4\pi J_\lambda^\odot = 4\pi[W_2 B_\lambda(T_2) + W_3 B_\lambda(T_3) + W_4 B_\lambda(T_4)].
\end{aligned} \tag{3.1.1}$$

The radiation field at shorter wavelengths than 246 nm (0.246 μm) represents the radiation by an old stellar population (Mezger et al., 1982), while at longer wavelengths the

Table 3.1: Stellar components as per Mathis et al. (1983).

l	$T_{\rm star}$	W_l
1	-	-
2	7500	10^{-14}
3	4000	10^{-13}
4	3000	4×10^{-13}

radiation is expressed as the sum of three stellar components. The stellar temperatures and dilution factors deduced by Mathis et al. (1983) are shown in Table 3.1. In Fig. 3.1 we show the total interstellar radiation field as estimated by Mathis et al. (1983) in the solar vicinity. The interstellar radiation field intensity is usually expressed by the scal-

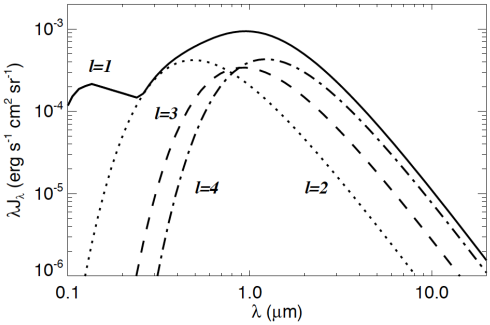

Figure 3.1: Standard interstellar radiation field in the solar vicinity as determined by Mathis et al. (1983).

ing factor, G_0, that is the ratio between the observed radiation field and that measured by Mathis et al. (1983) in the solar vicinity:

$$G_0 = \frac{\int_{91.2\,\rm nm}^{207\,\rm nm} J_\lambda d\lambda}{\int_{91.2\,\rm nm}^{207\,\rm nm} J_{\rm Mathis,\,\lambda} d\lambda}. \tag{3.1.2}$$

The interaction between the interstellar radiation field in the UV and a dust grain is mathematically well described by the set of the Maxwell's equations in matter, which

in the differential form are:

$$\nabla \cdot \boldsymbol{D} = \rho_{\rm f}, \tag{3.1.3}$$

$$\nabla \times \boldsymbol{E} = -\frac{\partial \boldsymbol{B}}{\partial t}, \tag{3.1.4}$$

$$\nabla \cdot \boldsymbol{B} = 0, \tag{3.1.5}$$

$$\nabla \times \boldsymbol{H} = \boldsymbol{J}_{\rm f} + \frac{\partial \boldsymbol{D}}{\partial t}, \tag{3.1.6}$$

where t is time, $\boldsymbol{E}$ the electric field, $\boldsymbol{H}$ the magnetic field, $\boldsymbol{B}$ the magnetic induction, $\boldsymbol{D}$ the electric displacement and $\rho_{\rm f}$ and $\boldsymbol{J}_{\rm f}$ the free charge and current density, respectively. The vector fields entering Eqs. 3.1.3 - 3.1.6, for linear materials, are related by the so-called constitutive relations:

$$\boldsymbol{D} = \epsilon \boldsymbol{E}, \tag{3.1.7}$$

$$\boldsymbol{B} = \mu \boldsymbol{H}, \tag{3.1.8}$$

where ϵ and μ are the dielectric permittivity and magnetic permeability of the medium, respectively.

3.1.2 Scattering and absorption from grains

When photons interact with particles the light is both absorbed and scattered by the grain according to its optical properties: the absorption and scattering efficiencies, $Q_{\rm abs}$ and $Q_{\rm sca}$. In the general case $Q_{\rm abs}$ and $Q_{\rm sca}$ are wavelength-dependent and the grain absorption and scattering cross sections, $C_{\rm abs}$ and $C_{\rm sca}$, for the interaction with photons are determined as

$$C_{\rm abs} = Q_{\rm abs} \pi a^2, \tag{3.1.9}$$

$$C_{\rm sca} = Q_{\rm sca} \pi a^2, \tag{3.1.10}$$

where a is the grain radius. Extinction is the result of both absorption and scattering and its efficiency and cross section are defined as:

$$Q_{\rm ext} = Q_{\rm abs} + Q_{\rm sca}, \tag{3.1.11}$$

$$C_{\rm ext} = C_{\rm abs} + C_{\rm sca}. \tag{3.1.12}$$

In order to calculate the optical properties of a dielectric, in this case a dust grain, a good knowledge of the permittivity, or dielectric function, and therefore a solution to the Maxwell's equations is required. A commonly used solution to the Maxwell's equations for the case of spherical or spheroidal objects is the Mie solution (named after the German physicist Gustav Mie, 1869 - 1957). The dielectric function, ϵ, can be written as:

$$\epsilon(\lambda) = \epsilon_1(\lambda) + i\epsilon_2(\lambda), \tag{3.1.13}$$

where λ is the wavelength of the incident radiation, i is the imaginary number $\sqrt{-1}$ and ϵ_1 and ϵ_2 are the real and imaginary part of ϵ. The dielectric function of a material is related to the refractive index , $m = n + ik$, by the Maxwell relation

$$m^2 = \epsilon. \tag{3.1.14}$$

The absorption and scattering efficiencies are, in the general case, related to both the real and imaginary part of m, and are wavelength dependent.

The imaginary part, k, of the refractive index for a material can be deduced from measurements of the absorption coefficient, $\alpha = \frac{2\pi k}{\lambda}$, of a thin film, accounting for both the reflected and scattered light. Evaluating the quantity n from laboratory measurements is much more complicated and is therefore usually calculated using the Kramers-Kronig relations:

$$n = \frac{1}{\pi}\mathcal{P}\int_{-\infty}^{\infty}\frac{k(\omega')}{\omega' - \omega}d\omega', \tag{3.1.15}$$

where $\mathcal{P}$ is the principal value of the integral and $\omega = 2\pi\nu$ is the angular frequency.

Knowing the refractive index of a material for different incident angles, is then possible, solving the Maxwell's equations, to calculate the absorption and scattering efficiencies. Nowadays there are several available codes (e.g. BHMIE, Bohren and Huffman 1998) able to solve the general case using modified versions of the Mie theory. These calculations, depending on the shape and size of the particles can be very time consuming. In the case of a spherical object, whose dimensions are small compared to the wavelength of the incident light *i.e.* $x = 2\pi a/\lambda \ll 1$ and $|m|x \ll 1$, its optical properties can be calculated analytically (Rayleigh approximation):

$$Q_{\rm abs} = 4x\,{\rm Im}\left(\frac{m^2-1}{m^2+2}\right), \tag{3.1.16}$$

$$Q_{\rm sca} = \frac{8}{3}x^4\left|\frac{m^2-1}{m^2+2}\right|^2. \tag{3.1.17}$$

If $(m^2-1)/(m^2+2)$ is a weak function of wavelength over some interval, then for sufficiently small particles

$$Q_{\rm abs} \propto \frac{1}{\lambda}, \qquad Q_{\rm sca} \propto \frac{1}{\lambda^4}. \tag{3.1.18}$$

However, interstellar dust grains, interacting with the ISRF, are rarely in the Rayleigh limit and the optical properties must be computationally calculated. Recently, the optical properties for hydrogenated amorphous carbon, a-C(:H), grains as a function of the band gap, $E_{\rm g}$, were derived by Jones (2012a,b,c,d,e). These optical properties are calibrated on laboratory data (e.g., Lewis et al. 1989; Mennella et al. 1995; Rouleau and Martin 1991; Zubko et al. 1996; Henning et al. 1999) and rely on theoretical calculations based on the structure and composition of carbonaceous material similar to those by Kassavetis et al. (2007).

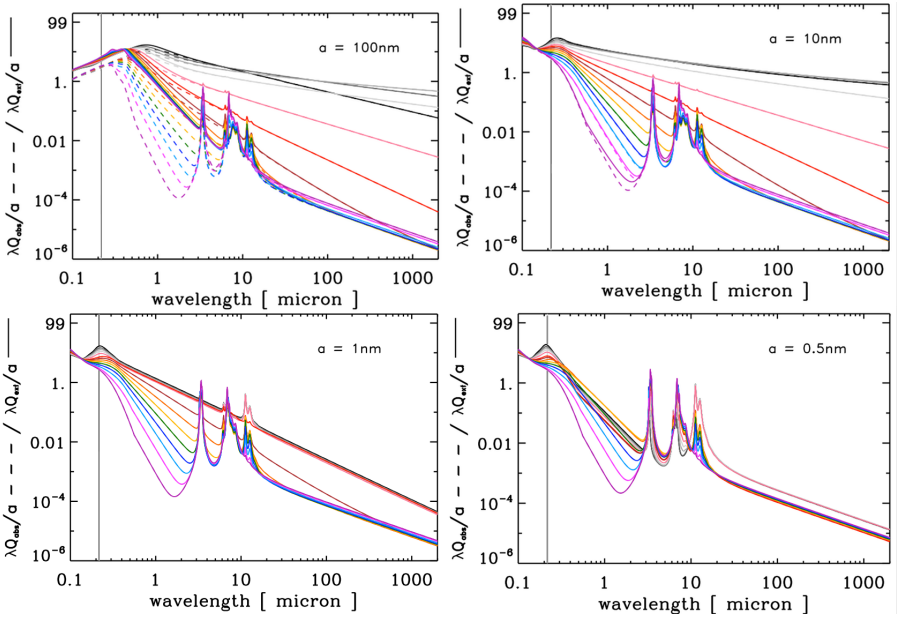

Figure 3.2: $\lambda Q_{\rm ext}/{\rm a}$ (solid) and $\lambda Q_{\rm abs}/a$ (dashed) for a-C(:H) grains for different radii a and $E_{\rm g}$. At $\lambda = 2\,\mu$m, $E_{\rm g}$ decreases from 2.67 eV (lower purple line) to -0.1 to 0.25 eV (the four upper grey and black lines). The vertical grey line marks the position of the UV extinction bump at 217 nm. Taken from Jones (2012c,e).

The hydrogen atom content in a carbonaceous grain determines the number of sp^2 and sp^3 bonds in the structure and therefore its degree of aromatization Jones (2012a). Furthermore, the number of aromatic rings in the aromatic clusters in the lattice is inversely related to the width of the band gap. Wide band gaps corresponds to aliphatic-rich grains while narrow band gaps to aromatic-rich grains. Figs. 3.2 and 3.3 show the optical properties for a-C(:H) grains as a function of size and band gap. We note that the optical properties strongly depend on the band gap of the material. For large grains ($a \gg 10\,$nm) at short wavelengths the extinction is dominated by both absorption and scattering. However, for small grains ($a \leqslant 10\,$nm) the extinction is dominated by absorption at all wavelengths because the particles are in the Rayleigh regime, regardless of the band gap. Finally, the stretching and bending modes of the C-H and C-C bonds are responsible for the characteristic IR bands (3 - 16 μm, see Fig. 3.2).

The UV-visible extinction efficiency for aromatic-rich carbonaceous nano-particles ($a \sim 1\,$nm) shows a bump at $\sim 217.5\ \mu$m (see Fig. 3.3). The intensity of the peak and the slope of the FUV rise strongly depend on the band gap, more aromatic-rich particles produce a stronger bump signature but a weaker slope at FUV wavelengths.

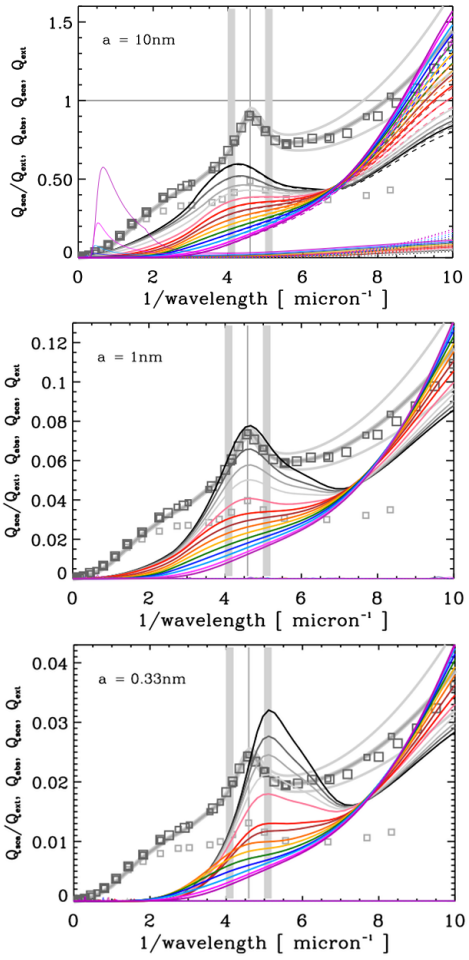

Figure 3.3: $Q_{\rm ext}$ (thick solid lines), $Q_{\rm abs}$ (dashed lines), $Q_{\rm sca}$ (dotted lines) and $Q_{\rm sca}/Q_{\rm ext}$ (thin solid lines) for 0.33, 1 and 10 nm a-C(:H) grains for different band gaps. Color coding as per Fig. 3.2. Jones (2012c).

Furthermore, the position of the peak depends on the particle size, smaller particles produce a bump at shorter wavelengths and larger particles at longer wavelengths (Jones 2012e).

The optical properties for a-C coated silicate grains were recently calculated by Jones et al. (2013). In Fig. 3.4 we show the silicate absorption and extinction efficiency for different grain sizes. The 9.7 μm feature due to the stretching of SiO bonds is

clearly seen in absorption for all the grain sizes shown here. In the case of large grains, at short wavelengths, scattering gives a major contribution to the extinction, while in general the extinction is dominated by the absorption.

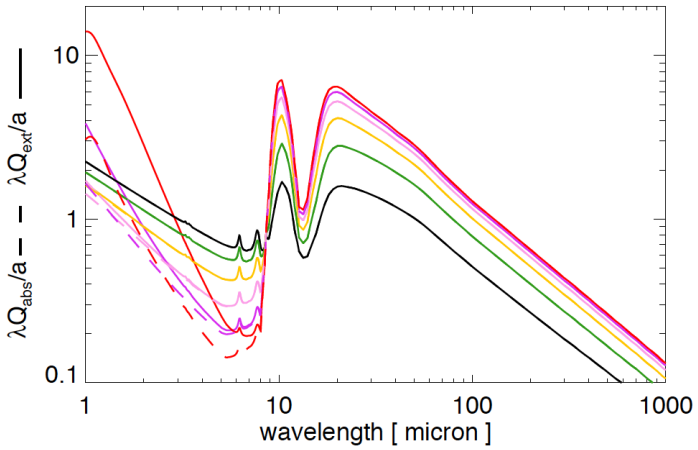

Figure 3.4: $Q_{\rm abs}$ and $Q_{\rm ext}$ for a-C coated amorphous silicate grains with radii ranging from 8 nm to 250 nm (from bottom to top). The optical properties are from the Jones et al. (2013) dust model.

In order to compare the observed extinction coefficient, A_λ, to the extinction produced by a given dust distribution, we need to integrate the calculated extinction efficiency over the entire dust population. The optical depth is then given by

$$\tau_\lambda = \int da\, \pi a^2\, Q_{\rm ext}(a,\lambda)\, N_{\rm H}\, dn/da \tag{3.1.19}$$

and then A_λ results from

$$A_\lambda = 1.086\, \tau_\lambda. \tag{3.1.20}$$

The observed extinction is therefore directly proportional to the extinction coefficients weighted by the dust size distribution, which allows us to explain the different features in the UV, visible and IR extinction. The characteristic UV bump at 217.5 nm and the FUV rise in the range $8-10\,\mu{\rm m}^{-1}$ (see Fig. 2.2a) result from of the extinction produced by small carbonaceous grains with a range of different sizes. Furthermore, the presence of silicate grains lead to the so-called very-broad structure at $< 3\,\mu{\rm m}^{-1}$. Finally, the observed extinction features at 9.7 μm and 18 μm (see Fig. 2.2b) directly arise from the extinction coefficient of the silicate grains. However, while the UV bump position is sensitive to the size distribution of the small carbonaceous grains, the position of the silicate features does not strongly depend on the grain size and therefore does not lead to a stringent constraint on silicate dust.

3.1.3 Grain temperature distribution and emission

As seen in the previous chapter the dust SED can be naively divided into IR-MIR features and blackbody emission in the FIR-mm. The key to understanding the dust SED is the temperature evolution of the different grains.

Grains in the interstellar medium are predominantly heated by the absorption of UV-visible stellar photons and emit in the IR-mm range. The energy absorption rate for a grain, H_γ, is function of the grain size, the optical properties of the grain (and therefore its composition) and the radiation field (e.g. Draine 2011):

$$H_\gamma(a) = \pi a^2 \int_{\lambda_{\min}}^{\lambda_{\max}} Q_{abs}(a,\lambda) J_\lambda d\lambda \,, \tag{3.1.21}$$

where $\lambda_{\min}$ and $\lambda_{\max}$ are the minimum and maximum wavelengths of the radiation field, $\pi a^2 Q_{abs}$ is the absorption cross section and J_λ the intensity of the radiation field at wavelength λ.

As a consequence of the absorption of a photon, the internal energy of a grain, $E_{\rm int}$, increases with the energy of the absorbed photon. In this way the temperature of the grain, initially at $T_{\min}$, will increase up to a temperature $T_{\max}$ according to its internal energy and heat capacity, $C(a, T_{\rm d})$ (e.g. Draine 2011):

$$E_{\rm int}(a) = \int_{T_{\min}}^{T_{\max}} C(a, T_{\rm d}) dT_{\rm d}. \tag{3.1.22}$$

Fig. 3.5 shows the temperature evolution during a day ($\sim 10^5$ s) as a function of time for a-C(:H) grains of different sizes as heated by the ISRF. We note that during a day the smallest grains typically do not absorb any photons because of their small cross section and their temperature can therefore drop below 5 K between photon absorptions. On the other hand, larger grains have a larger cross sections and show temperature spikes corresponding to the absorption of photons. The maximum temperature of the spikes is related to the grain heat capacity. Large grains ($a \gtrsim 20$ nm) undergo small temperature fluctuations. The rate of photon absorption for such grains is high and they do not have time to cool radiatively before being heated by another photon. However, the increase in temperature due to the absorption of a photon is not high because of their large heat capacity. This leads to an equilibrium between radiative cooling and photon heating corresponding to an almost constant grain temperature.

A grain will then emit the absorbed energy in the IR-mm according to its optical properties and its temperature at a given time with a spectrum, I_λ, which can be expressed as (e.g. Draine 2011)

$$I_\lambda(a) = \pi a^2 Q_{\rm em}(a,\lambda) \times \int_0^\infty B_\lambda(T) \frac{dP}{dT} dT \tag{3.1.23}$$

where $Q_{\rm em}(a,\lambda)$ is the grain emission efficiency, $\frac{dP}{dT}$ is the probability for the grain to be in a temperature interval between T and $T + dT$ and $B_\lambda(T)$ is the blackbody

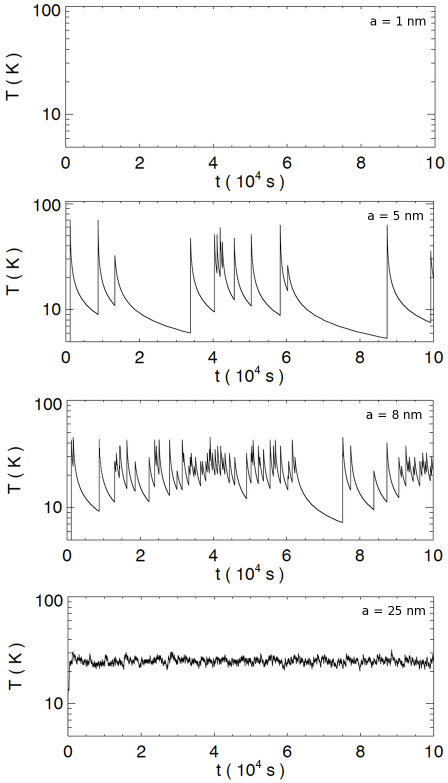

Figure 3.5: Temperature fluctuations as a function of time for a-C(:H) grains of different sizes as irradiated by the standard radiation field in the solar vicinity.

radiation for a temperature T. It should be noted that $Q_{\rm em}(a,\lambda) = Q_{\rm abs}(a,\lambda)$ for each wavelength, according to the Kirchoff's law. The temperature distribution for large grains, which are in thermal equilibrium, is almost a Dirac delta distribution peaked at the equilibrium temperature, $T_{\rm eq}$ (see Fig. 3.6). In this case, I_λ is well represented by a greybody radiation

$$I_\lambda(a) \propto B_\lambda(T_{\rm eq})\lambda^{-\beta}, \tag{3.1.24}$$

where β is the emissivity spectral index at the wavelength λ (determined by the grain optical properties, i.e. $Q_{\rm em}$). This leads to the observed greybody emission in the FIR range as seen in the Milky Way and other galaxies.

On the other hand, if the grains undergo significant fluctuations (e.g. in the case of a small grain in the standard ISRF), then the temperature distribution is no longer a Dirac delta distribution but a broader distribution (see Fig. 3.6). In this case the emission is dominated by the blackbody radiation at high temperatures (i.e. the grain

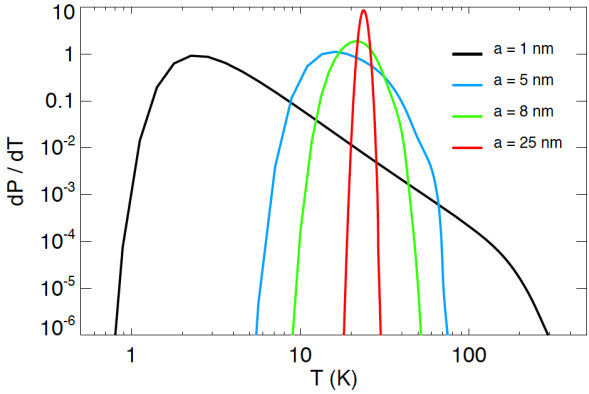

Figure 3.6: Temperature distribution dP/dT for different grain sizes. Grains in the range 0.4 - 1.1 nm have very similar temperature probability distribution.

emission peaks in the MIR range). However, we do not observe a high-temperature blackbody emission at short wavelengths. This is because, the emission efficiency for small grains is not constant at short wavelengths but presents strong features (see Fig. 3.2). Multiplying $Q_{\rm em}$ by the blackbody radiation will then produce the characteristic observed MIR spectrum.

In particular, the emission produced by a dust population following a given size distribution, dn/da, can be calculated as

$$I_\lambda = N_{\rm H} \int_{a_{\rm min}}^{a_{\rm max}} da\, \pi a^2\, \frac{dn}{da}\, Q_{\rm em}(a,\lambda) \int_0^\infty dT\, B_\lambda(T)\, \frac{dP}{dT}, \qquad (3.1.25)$$

where $N_{\rm H}$ is the hydrogen column density. We now focus on the emission from small grains with radii from 0.4 to 1.1 nm. These grains have a very similar temperature probability distribution, dP/dT, and therefore the quantity $\int_0^\infty dT\, B_\lambda(T)\, \frac{dP}{dT}$ will be identical for these considered sizes. This integral corresponds to the emission spectrum of these grains with $Q_{\rm em} = 1$ (black line Fig. 3.7). We note that the spectrum presents a broad bump peaking at $\sim 100\,\mu$m due to the emission from grains at a range of temperatures ($T \sim 15 - 60\,$K) and a shoulder at 2-3 μm due to the emission at very high temperatures ($T \sim 1000\,$K).

Furthermore, we calculate the $Q_{\rm em}$ for three sizes (0.4, 0.8 and 1.1 nm) of aromatic-rich carbonaceous grains and multiply these quantities by their relative abundances given by dn/da, as assumed by Jones et al. (2013). In Fig. 3.7 we show the $dn/da \times Q_{\rm em}$ (red, green and blue curves for 0.4, 0.8 and 1.1 nm grains, respectively). We clearly see that the multiplication of the optical properties by the dust emission continuum (calculated assuming $Q_{\rm em} = 1$) gives rise to the observed characteristic aromatic features.

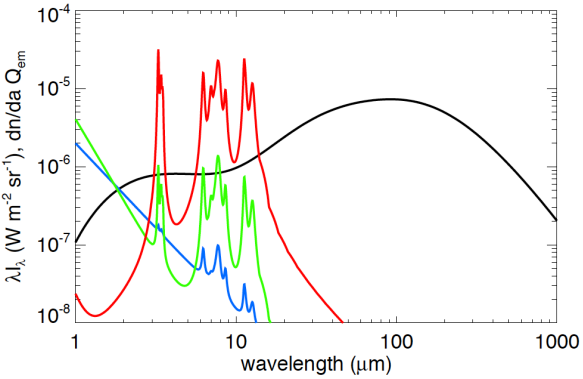

Figure 3.7: Small aromatic-rich carbonaceous grain emission continuum (black curve, see text) and $Q_{\rm em}$ for a grain of radius 0.4, 0.8 and 1.1 nm (red, green and blue curves).

3.1.4 Aromatization of carbonaceous grains

Experimental studies on a-C:H solids show that UV irradiation can lead to the so-called photo-darkening of the material (Smith 1984; Iida et al. 1985) a process that must also occur in the ISM (Jones 2012a,b,c; Jones et al. 2013, 2014). The absorption of energetic photons lead to the breaking of C-H bonds inside these grains and to the release of H atoms from the grain structure. This phenomenon, for EUV photons ($h\nu \geqslant 10\,$eV) affects grains to a depth of $\sim 20\,$nm and the rearrangement of the chemical network then transforms sp^3 aliphatic bonds into sp^2 aromatic bonds.

We can estimate the timescale for this process as a function of the radiation field, the grain radius and its optical properties. The photo-darkening rate can be expressed as (Jones et al. 2014):

$$\Lambda_{\rm UV,pd}(a) = F_{\rm EUV}\,\sigma_{\rm CH}\,Q_{\rm abs}(a,E)\,\epsilon \qquad {\rm s}^{-1}, \tag{3.1.26}$$

where $F_{\rm EUV} \simeq 3\times10^7$ photons cm^{-2} s^{-1} is the EUV photon flux in the solar vicinity (Henry 2002) that is able to break the C-H bonds, $\sigma_{\rm CH}$ is the photodissociation cross section (Welch and Judge 1972; Gruzdkov et al. 1994; Mennella et al. 2001; Muñoz Caro et al. 2001) and ϵ is the photo-dissociation efficiency (Jones 2012b,d; Jones et al. 2014):

$$\epsilon(a) = \begin{cases} \left(\frac{2}{a[{\rm nm}]}\right) & {\rm for}\ a > 2\,{\rm nm} \\ 1 & {\rm for}\ a \leqslant 2\,{\rm nm} \end{cases} \tag{3.1.27}$$

Then the timescale for the dissociation can be expressed as

$$\tau_{\rm UV,pd}(a,G_0) = \frac{1}{\Lambda_{\rm UV,pd}(a)\,G_0}, \tag{3.1.28}$$

where G_0 is a radiation field scaling factor (Eq. 3.1.2). An analytical approximation to the size-dependent photo-processing timescale is given by

$$\tau_{\rm UV,pd}(a, G_0) = \frac{10^4}{G_0}\left\{2.7 + \frac{6.5}{(a[\rm nm])^{1.4} + 0.04(a[\rm nm])^{1.3}}\right\} \rm yr \quad (3.1.29)$$

Of course as the grain enters a cloud, the starlight is dimmed and the photo-processing timescale becomes longer. Furthermore, as the density inside the cloud increases, another phenomenon, the re-hydrogenation (see Section 3.1.5) starts to be important and will compete with the photo-processing. In Fig. 3.8 we compare the photo-darkening timescale, $t_{\rm pd}$, and the re-hydrogenation timescale , $t_{\rm Hin}$ (assuming an incorporation efficiency of 1%, i.e. only 1% of the H atoms sticking to the grain are incorporated), as a function of the extinction coefficient $A_{\rm V}$ inside a cloud. The re-hydrogenation will increase the H-atom fraction in the structure of the grain therefore leading to the aliphatization of the grain while the hard radiation field leads to its aromatization. Alternatively, and equally viable, could be the direct accretion of H-rich aliphatic mantles onto grains in the outer regions of molecular clouds. In Fig. 3.8 it is clear that in diffuse clouds (such as in the diffuse medium of the Milky Way) the aromatization process is faster than aliphatization and the outer layers of carbonaceous grains are expected to be aromatic-rich. On the contrary for media slightly denser, the

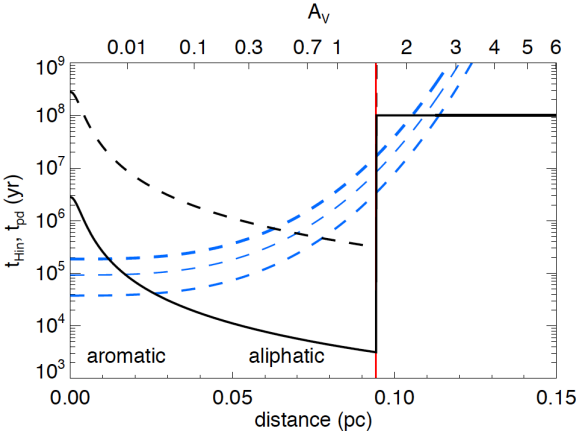

Figure 3.8: The dust processing time-scales as a function of the depth into the cloud and the corresponding $A_{\rm V}$: H atom collision timescale, $t_{\rm H}$ (black), H atom incorporation timescale, $t_{\rm Hin}$ (black dashed, with an efficiency of 1%), and the EUV photo- processing time-scale, $t_{\rm pd}$, for 1, 10 and 100 nm radius a-C(:H) grains (thin, medium and thick dashed blue lines respectively). The red vertical dashed line corresponds to the division between the atomic and molecular phases of the cloud (assumed to be at $A_{\rm V} = 1.5$).

radiation field is dimmed because of the extinction of the medium and aliphatization,

or aliphatic mantle accretion, wins against aromatization making the grains mostly aliphatic rich.

3.1.5 Re-hydrogenation or aliphatization of carbonaceous grains

Experimental studies (Mennella et al. 2002; Mennella 2006, 2008, 2010) have shown that at low temperatures ($T_{\rm kin} \sim 80\,{\rm K}$), the sticking of H atoms onto the surface of carbonaceous grains can lead to the H atom incorporation and therefore to their re-hydrogenation. The H atom sticking timescale onto all grains is

$$t_{\rm H} = [\Sigma_{\rm tot} n_{\rm H} v_{\rm H} S_{\rm H}]^{-1}, \tag{3.1.30}$$

where $v_{\rm H} = [8 k_{\rm B} T_{\rm kin}/(\pi m_{\rm H})]^{0.5}$ is the H atom thermal velocity and $S_{\rm H}$ is the H atom sticking coefficient, here we assume the canonical value $S_{\rm H} = 0.3$. We define the low temperature a-C(:H) grain (re-)hydrogenation rate as

$$t_{\rm Hin} = [\xi \Sigma_{\rm tot} n_{\rm H} v_{\rm H} S_{\rm H}]^{-1}, \tag{3.1.31}$$

where ξ is the efficiency for H atom incorporation into the a-C(:H) structure.

Since most of the incident H atoms will combine with other incident H atoms to form H_2 molecules, ξ should be significantly less than unity, we suppose $\xi \sim 10^{-2}$. For the size distribution in the Jones et al. (2013) standard diffuse ISM dust model Jones et al. (2014) derive $\Sigma_{\rm tot} = 7.3 \times 10^{-21}\,{\rm cm}^2$ / H atom. This process is in competition with the aromatization of grains due to EUV photon absorption and have a shorter timescale than the latter in clouds where the density is sufficiently high and the starlight dimmed.

3.2 Atom / ion - grain interactions

A grain embedded in a hot gas or traveling at high velocities in a gas undergoes energetic collisions with gas ions and electrons. These events are crucial in understanding dust destruction and heating in different environments. In this section we describe how we can model these processes and predict their consequences.

3.2.1 Ion collisions

As an energetic ion hits the surface of a bulk material, it generates a collisional cascade inside the solid (Sigmund 1981). A collisional cascade is a series of binary collisions between the target nuclei: the impinging ion displaces a first nucleus from its equilibrium position, which will then become the projectile for another binary collision, leading to an increasing number of collisions (see Fig. 3.9, Section 4.B for details). This process can cause the ejection of one or more atoms from the grain surface and is generally called "sputtering". The sputtering yield, Y, is defined as the number of ejected atoms for each ion hitting the surface. The sputtering yield will then be larger

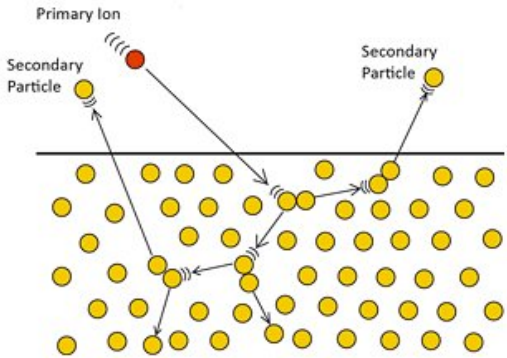

Figure 3.9: Schematics of a collisional cascade inside a solid.

than or equal unity in the case of the ejection of one or more atoms while $Y < 1$ if the impinging ion is not energetic enough to trigger a significant cascade in the solid and is itself implanted in the lattice (Gray and Edmunds 2004). A theoretical model for sputtering was developed by Sigmund (1981) and then extended by Tielens et al. (1994) for different astrophysically significant materials. The sputtering yield, Y, can be expressed as a function of the energy E of the impinging ion as:

$$Y(E) = 4.2 \times 10^{14} \frac{\alpha S_{\rm n}(E)}{U_0}, \tag{3.2.1}$$

where α is a function of the mass ratio between the projectile and the target, $S_{\rm n}(E)$ is the nuclear stopping cross section (in erg cm^2) and U_0 is the binding energy (in eV) of the target surface atoms. For a collision between a projectile and a target of masses M_1 and M_2 and atomic number Z_1 and Z_2, respectively, the nuclear stopping power is expressed as (Sigmund 1981):

$$S_{\rm n}(E) = 4.2\pi a Z_1 Z_2 e^2 \frac{M_1}{M_1 + M_2} s_{\rm n}(\epsilon_{12}), \tag{3.2.2}$$

where e is the electron charge and a the screening length, which can be approximated as (Ziegler and Biersack 1985)

$$a \simeq 0.885 a_0 (Z_1^{0.23} + Z_2^{0.23})^{-1}, \tag{3.2.3}$$

with $a_0 = 0.529$ Å the Bohr radius. The reduced nuclear stopping power, $s_{\rm n}$, depends on the adopted form of the screened Coulomb interaction and an approximated expression was found by Matsunami (1980):

$$s_{\rm n}(\epsilon_{12}) = \frac{3.441\sqrt{\epsilon_{12}}\, ln(\epsilon_{12} + 2.718)}{1 + 6.35\sqrt{\epsilon_{12}} + \epsilon_{12}(-1.708 + 6.882\sqrt{\epsilon_{12}})}, \tag{3.2.4}$$

Table 3.2: Sputtering parameters for silicate and graphitic-type grains.

Material	U_0 (eV)	M_2 (amu)	Z_2	K
Silicate	5.7	23	11	0.1
Graphite	4	12	6	0.65

where ϵ_{12} is given by

$$\epsilon_{12} = \frac{M_2}{M_1 + M_2} \frac{a}{Z_1 Z_2 e^2} E. \tag{3.2.5}$$

Furthermore, the function α can be approximated as (Tielens et al. 1994):

$$\alpha \simeq \begin{cases} 0.2 & M_2/M_1 < 0.5 \\ 0.3 \left(\frac{M_2}{M_1}\right) & 0.5 < M_2/M_1 < 10 \end{cases} \tag{3.2.6}$$

For our purposes, M_2/M_1 is typically larger than 0.5 and this expression for α, in the case of light projectiles, gives unreasonably high values (Andersen and Bay 1981). This is mainly because this expression was estimated neglecting the electronic stopping, which is important for light projectiles, therefore leading to a large number of multiple collisions. This can be corrected multiplying by the ratio between the mean projected range and the mean penetration depth (Bohdansky 1984; Tielens et al. 1994):

$$\frac{R_\mathrm{p}}{R} = \left(K \frac{M_2}{M_1} + 1\right)^{-1}, \tag{3.2.7}$$

where K is a free parameter in the model by Tielens et al. (1994). We can define the threshold energy as the minimum energy necessary to trigger a collisional cascade inside a solid. This quantity is a function of the surface binding energy, U_0, which corresponds to the energy necessary to displace a surface atom, and the maximum fractional energy transfer possible in a head-on elastic collision, g (Bohdansky 1980; Andersen and Bay 1981):

$$E_\mathrm{th} = \begin{cases} \frac{U_0}{g(1-g)} & M_1/M_2 \leqslant 0.3 \\ 8U_0 \left(\frac{M_1}{M_2}\right)^{1/3} & M_1/M_2 > 0.3 \end{cases} \tag{3.2.8}$$

where $g = \frac{4M_1M_2}{(M_1+M_2)^2}$. Near threshold, projectiles do not trigger a collisional cascade and their momentum is not an isotropic distribution. In order to correct for these effects we need to introduce the following correction factors (Bohdansky et al. 1980; Yamamura et al. 1983; Bohdansky 1984):

$$S_{\mathrm{n},1} = S_\mathrm{n} \left[1 - \left(\frac{E_\mathrm{th}}{E}\right)^{2/3}\right] \tag{3.2.9}$$

$$S_{\mathrm{n},2} = S_{\mathrm{n},1} \left(1 - \frac{E_\mathrm{th}}{E}\right)^2. \tag{3.2.10}$$

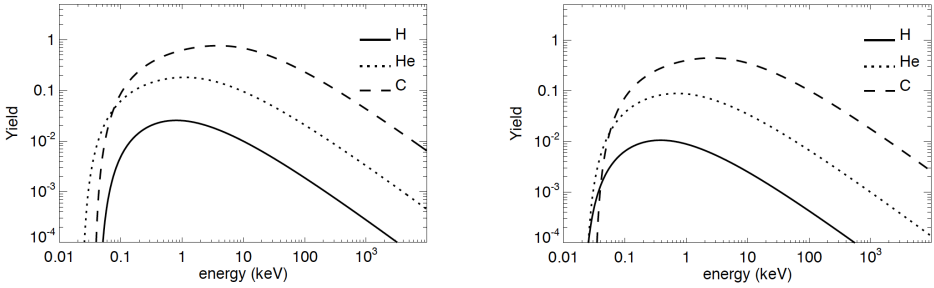

(a) (b)

Figure 3.10: Sputtering yield for silicate (a) and graphitic-type (b) grains with different incident projectile atoms/ions.

The final expression for the sputtering yield at normal incidence is then given by (Tielens et al. 1994):

$$Y(E) = \frac{3.56}{U_0(\mathrm{eV})} \frac{M_1}{M_1 + M_2} \frac{Z_1 Z_2}{\sqrt{Z_1^{2/3} + z_2^{2/3}}} \alpha \frac{R_\mathrm{p}}{R} s_\mathrm{n}(\epsilon) \times \left[1 - \left(\frac{E_\mathrm{th}}{E}\right)^{2/3}\right] \left(1 - \frac{E_\mathrm{th}}{E}\right)^2 \text{ atoms per ion.} \quad (3.2.11)$$

With the available experimental data, Tielens et al. (1994) calibrated this expression for the sputtering yield for different astronomically relevant materials and derived the parameters for silicate and graphitic-type grains (see Table 3.2).

Fig. 3.10 shows the sputtering yield for silicate and graphitic-type grains for different projectiles: H, He and C ions in the 1-10 keV region. We note that at low energies ($E \lesssim 20\,\mathrm{eV}$), the energy of the impinging ion is not high enough to trigger a collisional cascade inside the solid and the sputtering is negligible. Increasing the energy of the projectile, the sputtering yield increases and reaches almost unity for C ions. Then, for high energies ($E \gtrsim 10\,\mathrm{keV}$), the projectile is implanted too deeply in the target and the sputtering yield drops.

It should be noted that, near threshold, the sputtering yield was poorly constrained by experimental data at that time. This represents the main source of uncertainty in the model by Tielens et al. (1994).

3.2.2 Sputtering of amorphous carbon grains and finite size correction

Since the pioneering works by Sigmund (1981) and Tielens et al. (1994), many efforts have been made to improve the modelling of the sputtering of carbonaceous grains.

Table 3.3: SRIM input parameters for graphite and a-C:H as determined by Jurac et al. (1998) and Serra Díaz-Cano and Jones (2008). ρ is the density in g cm^{-3} and E_S, E_D and E_B are the surface binding energy, displacement energy and lattice binding energy, respectively, (see text) in eV.

Material	ρ	E_S	E_D	E_B
graphite	2.3	3	11	2
a-C:H	1.5	4	10	3

A first work to take into account the angular dependence of the sputtering yield and the size of the target was carried out by Jurac et al. (1998) using graphitic targets and then extended by Serra Díaz-Cano and Jones (2008) to hydrogenated amorphous carbon (a-C:H) materials.

A Monte Carlo (MC) binary collision code called SRIM (Stopping and Range of Ions in Matter, www.srim.org, Ziegler et al. 1985) allows us to simulate the collisional cascade inside solid materials with different incident ions, therefore making this code very useful to estimate the sputtering yield.

The sputtering process is determined by four main input parameters:

- the density of the material, ρ,
- the surface binding energy, E_S, i.e. the energy that holds a surface atom to the lattice,
- the lattice binding energy, E_B, i.e. the energy needed to displace an atom within the lattice,
- the displacement energy, E_D, i.e. the energy that binds an atom to the lattice.

Jurac et al. (1998) and later Serra Díaz-Cano and Jones (2008) determined these parameters for graphite and a-C:H materials, respectively (see Table 3.3).

The sputtering yield is typically assumed to depend on the incident angle, θ, as

$$Y \propto (\cos\theta)^{-1} \tag{3.2.12}$$

However, experimental studies by Haasz et al. (1989) showed that the sputtering of real carbonaceous materials has a different angular dependence. Jurac et al. (1998), using the TRIM code (old version of the SRIM code), and assuming the input parameters listed in Table 3.3, found an angular dependence similar to laboratory data. Fig. 3.11a shows the sputtering yield due to collisions of He^+ on a graphitic target as a function of the incident angle for different projectile energies: 100 eV, 300 eV and 1 keV (dot-dashed, dash and dotted lines respectively). Depending on the projectile energy, the angular dependence of the SRIM-calculated sputtering yield is slightly different and in any case does not follow the $(\cos\theta)^{-1}$ dependence but it is rather close to the

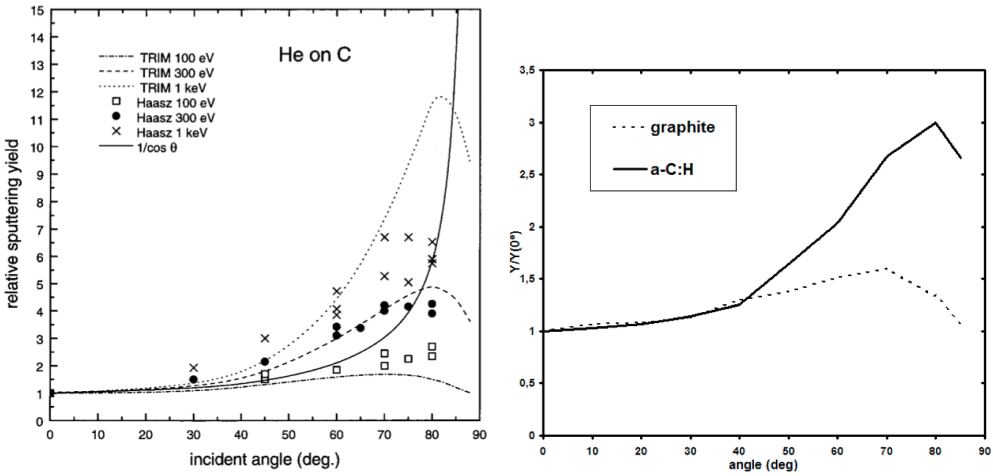

(a) (b)

Figure 3.11: Sputtering yield as a function of the angle of incidence. (a) TRIM results (dot-dashed, dashed and dotted lines) are compared to experimental studies (squares, circles and crosses) by Haasz et al. (1989) and to the $(\cos\theta)^{-1}$ dependence. (b) SRIM results for graphite (dotted) and a-C:H (solid) for $E = 100\,\mathrm{eV}$.

experimental studies by Haasz et al. (1989), indicated by squares, circles and crosses in Fig. 3.11a for 100 eV, 300 eV and 1 keV, respectively.

Later, Serra Díaz-Cano and Jones (2008), using the parameters listed in Table 3.3 calculated the sputtering yield as a function of the angle of incidence for both graphite and a-C:H material. They found that both materials follow the same trend from normal incidence until $\sim 40°$ but for grazing angles, a-C:H materials are much more easily sputtered than graphite leading to a sputtering yield of ~ 3 (a factor two more than for graphite) at $\sim 80°$. This is mainly due to the lower density of a-C:H (i.e., $\rho \sim 1.5\,\mathrm{g\,cm^{-3}}$, Smith 1984) with respect to the graphite. It has to be noted that, with the typically assumed $(\cos\theta)^{-1}$ angular dependence, the sputtering yield averaged over angles, $< Y >_\theta$, gives a factor two enhancement with respect to the sputtering yield at normal incidence. On the other hand, the angular dependence obtained for a-C:H grains gives

$$< Y_{\mathrm{a-C:H}} >_\theta = 4 Y_{a-C:H}(\theta = 0). \tag{3.2.13}$$

In order to account for the finiteness of grains, Jurac et al. (1998) completely reformulated the available version of TRIM at that time and introduced a spherical boundary instead of using a semi-infinite slab. We define the ratio Y_a/Y_∞ as the ratio between the sputtering yield accounting for the finiteness of the grain and the sputtering yield in the case of a semi-infinite target. Fig. 3.12a shows Y_a/Y_∞ as a

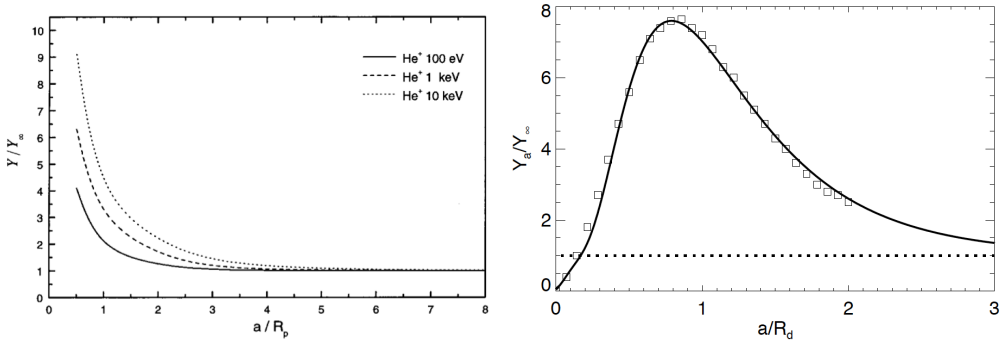

(a) (b)

Figure 3.12: Ratio $Y_{\rm a}/Y_{\infty}$ as a function of $a/R_{\rm p}$ for graphite (a) and as a function of $a/R_{\rm D}$ for a-C:H material (b) as derived by Jurac et al. (1998) and Serra Díaz-Cano and Jones (2008), respectively.

function of $a/R_{\rm p}$, where $R_{\rm p}$ is the penetration depth, which is a quantity tabulated in TRIM/SRIM for different projectiles as a function of the their energy. We note that the sputtering yield increases in the case $a \lesssim R_{\rm p}$ and that Y/Y_{∞} is larger for higher energies.

Serra Díaz-Cano and Jones (2008) adopted a different approach which did not require a revision of the original SRIM code. The SRIM code does provide the final position of the implanted incident ions but unfortunately does not provide the position of the displaced target atoms. However, Serra Díaz-Cano and Jones (2008), using a simple scaling argument were able to estimate the position of the displaced target atoms. They assumed that the majority of the target atoms are displaced to the position, $R_{\rm D}$, where the impinging ions lose most of their energy and found the following relation:

$$R_{\rm D} = 0.7 R_{\rm p}. \tag{3.2.14}$$

In this way they were then able to derive the distribution of the displaced target atoms and integrating over a sphere of radius a they calculated the ratio $Y_{\rm a}/Y_{\infty}$ of the sputtering yield for a grain of radius a with respect to the sputtering yield of a semi-infinite slab (open squares in Fig. 3.12b).

The sputtering yield for a grain of radius a for a-C:H as deduced by Serra Díaz-Cano and Jones (2008) can be approximated by the following analytical expression:

$$Y/Y_{\infty} = 1 + 6.6 \exp\left[\frac{-\log^2\left(\frac{a/R_d}{a_0}\right)}{2\sigma^2}\right] - \exp\left(-\left(7a/R_d + 0.25\right)^2\right) \tag{3.2.15}$$

where $\sigma = 0.552$ and $a_0 = 0.79$ (solid line in Fig. 3.12b).

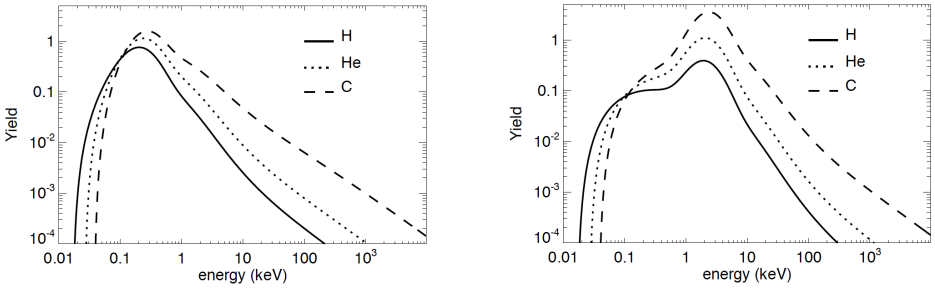

(a) (b)

Figure 3.13: Sputtering yield for a-C:H grains of radius 13 nm (a) and 130 nm (b) as hit by different projectiles.

We note that the sputtering yield ratio Y_a/Y_∞ is smaller than 1 for low a/R_D, which means that the ions pass through the grain without affecting it. On the other hand, when $a \sim R_D$ the sputtering yield is maximum and can reach almost eight times the value for a semi-infinite slab. Then, for $a/R_D \gtrsim 2$ the approximation of a semi-infinite slab starts to be valid and the ratio $Y_a/Y_\infty \to 1$.

Furthermore, assuming a H atom fraction of $X_H = 0.4$ (e.g. Smith 1984), Serra Díaz-Cano and Jones (2008) calculated the mean atomic mass, $< M_2 >$, and atomic number, $< Z_2 >$ as:

$$< M_2 > = [X_H M_H + (1 - X_H) M_C], \quad (3.2.16)$$

$$< Z_2 > = [X_H Z_H + (1 - X_H) Z_C], \quad (3.2.17)$$

where M_i and Z_i are the atomic mass and atomic number of hydrogen and carbon atoms. Therefore, fitting the SRIM results with the Tielens et al. (1994) formalism, they foud $K = -0.04$ for a-C:H in the case of normal incidence and assuming a semi-infinite slab.

Then, using the approach by Tielens et al. (1994) but with the parameters deduced by Serra Díaz-Cano and Jones (2008), we calculate the sputtering yield of a 13 (130) nm a-C:H grain as hit by H, He and C projectiles (see Fig. 3.13). We note that for a 13 (130) nm grain the sputtering yield presents a bump at 0.2 - 0.3 ($\sim$ 2) keV. This energy corresponds to the energy necessary for the different projectiles to displace most of the target atoms to the surface of the grains. More energetic projectiles will, on the contrary, pass through the grain leading to a lower destruction.

3.2.3 Erosion of nm size carbonaceous grains

As mentioned in the previous chapter many dust models include the presence of nano-particles that are responsible for the observed aromatic features, the PAHs, or such

as in the new model proposed by Jones et al. (2013), open structures composed by aromatic and aliphatic domaines.

A study by Micelotta et al. (2010b) developed a model to estimate the PAH dissociation as a consequence of collisions with H^+, He^+ and CNO group ions. The effect of the collision between ions and PAHs can be seen as the contribution by two different interactions: the nuclear and electronic interaction.

The nuclear interaction represents the direct collision between the projectile ion and a nucleus inside the target molecule leading to the ejection of single atoms (the yield for this process is always smaller or equal unity). On the other hand, an ion, passing through the molecule, interacts with its electronic cloud and leads to the excitation of the entire molecule. If the enhancement of the internal energy is high enough, then some of the bonds in the molecule can be broken therefore making possible the ejection of C_2 groups.

Despite the different approach between the molecular model developed by Micelotta et al. (2010b) and the classical approach by Tielens et al. (1994), we expect to find similar 'sputtering' yield with the two models for an intermediate size between PAHs and large grains. Bocchio et al. (2012) found that, in a hot gas, the number of carbon atoms ejected per unit time for nm size carbonaceous grains / molecules is, within a factor two, the same for the two approaches (see Section 4.1).

3.3 Electron - grain interactions

As an example we consider the case of a hot gas at a temperature $T \sim 10^7 - 10^8\,\mathrm{K}$, where electrons in thermal equilibrium have a kinetic energy $E_\mathrm{k} \sim 1 - 10\,\mathrm{keV}$, which is much lower than the relativistic case, i.e. $E_\mathrm{k} \sim 500\,\mathrm{keV}$. At these low energies, elastic collisions of electrons with target nuclei are not efficient (Micelotta et al. 2010b) and only the inelastic interaction between the impinging electron and the electronic cloud is relevant (as in the case of impacting ions). This process represents the main mechanism of energy transfer to the target molecule via electron collisions. This section represents part of the work presented in Bocchio et al. (2013b).

3.3.1 Injected energy

Following Dwek (1986), the power absorbed per grain due to electron collisions is given by:

$$H = \pi a^2\, n_\mathrm{e} \int_0^\infty f_\mathrm{M}(E)\, \mathrm{v}(E)\, \tilde{\sigma}(E)\, E\, \zeta(E)\, dE \tag{3.3.1}$$

where a is the grain radius, n_e is the electron density (equal to the proton density, n_H, since the gas is fully ionised), $f_\mathrm{M}(E)$ is the Maxwell-Boltzmann energy distribution, $\mathrm{v}(E)$ the velocity of the impinging electron, E its energy, $\tilde{\sigma}(E)$ represents the Coulomb focusing and $\zeta(E)$ the fraction of energy transferred to the target grain.

Table 3.4: Analytical fit (to within few %) of the electron stopping power in solid carbon (Micelotta et al. 2010b). The fit parameters are given to 3 significant digits and E is in keV.

$S(E) = (h\,ln(1+aE))/(fE^g + bE^d + cE^e)$			
a	b	c	d
-4.23×10^{-4}	-3.57×10^{-11}	-3.38×10^{-7}	-3.19
e	f	g	h
-0.588	-2.33×10^{-4}	1.54	1.41

Dwek (1986) gives an estimate of the transferred energy, $E\zeta(E)$, as a function of the energy of the impinging electron:

$$\zeta(E) = \begin{cases} 1 & \text{for } E < E_{\rm th} \\ 1 - \left[1 - (E_{\rm th}/E)^{3/2}\right]^{2/3} & \text{for } E > E_{\rm th} \end{cases} \tag{3.3.2}$$

with the threshold energy $E_{\rm th}({\rm erg}) = 3.7 \times 10^{-8}\,{\rm a(^-m)}^{2/3}$.

In Dwek (1987) he updated his previous estimate of the transferred energy function for electron collisions. His study is based on the experimental ranges of electrons in all media within the energy range of 20 eV to 1 MeV (Iskef et al. 1983; Berger and Seltzer 1964). The more recent estimate of the energy transferred is functionally very similar to the previous estimate but it has a lower threshold. Dwek (1987) does not give a simple expression for the threshold energy. For a 0.1 μm carbonaceous grain of density $\rho = 1.8\,{\rm g\ cm^{-3}}$, following this method, we can deduce from Fig. 1 by Dwek (1987), that the threshold energy $E_{\rm th} \sim 1.4\,{\rm keV}$ (see Fig. 3.14).

A more recent approach is given by Micelotta et al. (2010b). They derive the electron energy loss (for $E = 10\,{\rm eV} - 2\,{\rm keV}$) in carbon from measurements of dE/dx for solid carbon (Joy 1995). The data points are well fit by the following function:

$$S(E) = \frac{h\,ln(1+aE)}{fE^g + bE^d + cE^e} \tag{3.3.3}$$

where $S(E)$ is the stopping power and E the energy of the impinging electron. The fit parameters are listed in Table 3.4. In order to find the energy transferred to a spherical grain due to electron collisions Micelotta et al. (2010b) used the following procedure. Since $S(E) = -dE/dx$, integrating over the electron path through the grain gives:

$$l_{\rm max} = \int_{x_0}^{x_1} dx = -\int_{E_0}^{E_1} \frac{dE}{S(E)} = F(E_0) - F(E_1)\,, \tag{3.3.4}$$

where $F(E)$ is the path length travelled by an electron with an energy E, E_0 the energy of the impinging electron, E_1 the energy of the electron after having travelled through the grain and $l_{\rm max}$ is the maximum path length. The value of $l_{\rm max}$ is of course limited

to the maximum path length through the grain if the electrons are not stopped within the grain. In that case, the average path length traversed through a spherical grain is 4a/3, i.e. the angle-averaged path length through a sphere of radius a. Therefore, for a given E_0 we can derive E_1 and we define the transferred energy as:

$$E_{\rm tr} = E_0 - E_1 \,. \tag{3.3.5}$$

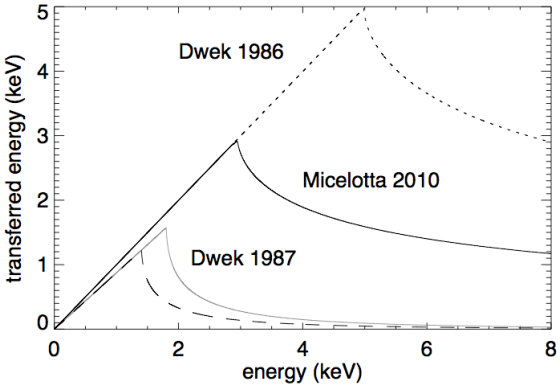

Figure 3.14: The transferred energy as a function of the kinetic energy of the incident electrons for carbonaceous and silicate grains with a radius of 100 nm. Carbonaceous grain (black lines): solid line Micelotta et al. (2010b), dotted line Dwek (1986), dashed line Dwek (1987). Silicate grain, grey solid line Dwek (1987).

In Fig. 3.14 we show the transferred energy as a function of the energy of the impinging electron kinetic energy. Black lines refer to the transferred energy for carbonaceous grains whilst the grey line refers to silicate grains. For these calculations we assume a carbon grain of density $1.8\,{\rm g\,cm^{-3}}$ and radius of 100 nm and a silicate grain of density $3\,{\rm g\,cm^{-3}}$ of the same radius. We compare the three approaches described for the transferred energy into carbonaceous grains. The dotted line shows the approach of Dwek (1986), the dashed line the approach of Dwek (1987) and the black solid line the approach of Micelotta et al. (2010b). We notice that, even if the methods used to calculate the transferred energy are quite different from one another, the functional behavior is very similar. The difference between the transferred energy function for carbonaceous and silicate grains adopted by Dwek (1987) is simply due to the different grain densities used. In our modeling we use the transferred energy function obtained by Micelotta et al. (2010b) for carbonaceous grains (black solid line) and, since there are no more recent estimates, we use that obtained by Dwek (1987) for silicate grains (grey solid line).

The energy transferred to the grain will then lead to an increase of the internal energy of the grain that can be dissipated following two channels:

- radiative relaxation: the transferred energy is distributed over the vibrational modes of the grain and its only effect is to increase the temperature of the grain. The grain will then cool down to the initial temperature by emitting IR photons.
- dissociation: the energy is not thermalized and leads to the breaking of one or more bonds.

We will describe these two processes in detail in Chapter 4, applying our modelling work to the case of grains embedded in a hot gas and then in Chapter 6 to the case of dust processing in interstellar shocks.

3.4 Grain charging

The grain charge in different environments is the result of the interactions of the grain itself with photons, ions and electrons. The variation in the grain charge per unit time, dQ/dt, can be express as

$$\frac{dQ}{dt} = \pi a^2 e \sum_i J_i, \tag{3.4.1}$$

where πa^2 is the geometrical cross section of a grain of radius a, e is the electron charge and J_i is the current per unit area due to the i-th process. Here we consider the release of photoelectrons, $J_{\rm pe}$, the sticking of ions, $J_{\rm ion}$, and the interaction with electrons, $J_{\rm e}$. As a convention we use negative and positive currents for electrons entering and leaving the grain, respectively.

It should be noted that very few experimental data on small a-C:H grains / molecules are available and in the following we mainly refer to the charging of large grains. It is clear that experimental and theoretical efforts should be undertaken in order to improve our understanding of the charging of particles at the nm and sub-nm scale.

3.4.1 Photoelectric effect on grain surfaces

The absorption of an energetic photon from a grain can lead to the release of an electron from its surface according to the photoelectric effect (Einstein 1905). This phenomenon will then lead to a net positive current per unit area, $J_{\rm pe}$, given by

$$J_{\rm pe} = Q_{\rm abs} Y_{\rm pe}, \tag{3.4.2}$$

where $Q_{\rm abs}$ is the absorption efficiency (see Section 3.1) and $Y_{\rm pe}$ the photoelectric yield. The photoelectric yield has been experimentally determined for different materials (thin lines in Fig. 3.15) and many efforts have been made in order to evaluate it theoretically (Draine 1978; Weingartner and Draine 2001; Weingartner et al. 2006). Draine (1978) approximates the photoelectric yield as

$$Y(h\nu) = Y_\infty \left(1 - \frac{B}{h\nu}\right), \tag{3.4.3}$$

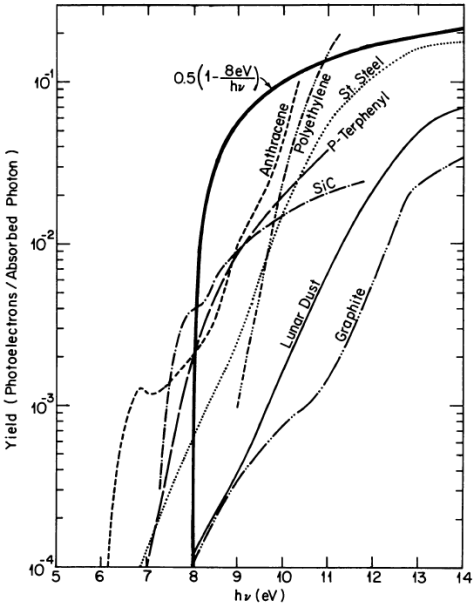

Figure 3.15: Photoelectric yield for any material as estimated by Draine (1978, thick line) compared the experimental data for different materials (thin lines, Draine 1978 and reference therein). The equation indicates the adopted photoelectric yield for any material (see text, Draine 1978).

where Y_∞ is the photoelectric yield for a semi-infinite plane, B is a parameter in the model and $h\nu$ is the energy of the impinging photon. Draine (1978) did not equate B and Y_∞ to the experimental values for the different materials as there were large uncertainties on the measurements but chose as standard values $B = 8\,\mathrm{eV}$ and Y_∞, which are appropriate for metallic, organic or silicate grains. In Fig. 3.15 we note that, for all the interstellar dust analogs (including graphitic-type, SiC and lunar dust), the photoelectric yield is larger than the experimental value for energies $E \sim 8 - 14\,\mathrm{eV}$. Weingartner and Draine (2001) developed a more physical model of photon absorption. They estimated the photoelectric yield for different materials.

This new estimate is still 3.4 times larger than experimental data at 10 eV for graphitic grains. However, this represents the model that best matches the experimental values at low energies ($E \lesssim 15\,\mathrm{eV}$). Very few experimental data are available for photons at higher energies and the only available and appropriate model for ISM studies is that of Weingartner et al. (2006) (see Fig. 3.16).

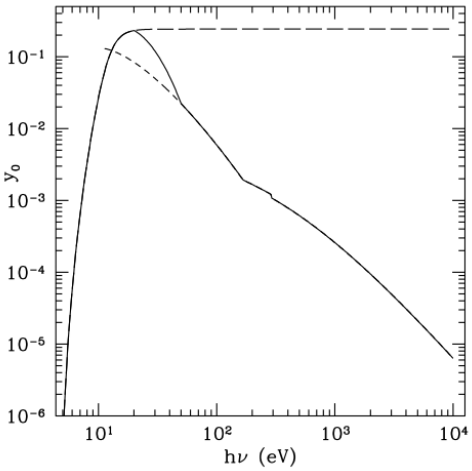

Figure 3.16: Photoelectric yield for carbonaceous dust as estimated by Weingartner and Draine 2001 (long-dashed line), Weingartner et al. 2006 (short-dashed line). The adopted yield by Weingartner et al. (2006) is indicated in solid line.

3.4.2 Ion and electron collisions

The collision of a particle of energy E and charge q with a grain of radius a and charge Ze will lead to a net current, J_c, according to the following:

$$J_c = \phi(< s > + < \delta >)\tilde{\sigma}(\epsilon, \nu), \tag{3.4.4}$$

where ϕ is the incident particle flux, $< s >$ is the sticking coefficient, $< \delta >$ is the secondary electron emission probability and $\tilde{\sigma}(\epsilon, \nu)$ is the reduced cross section as a function of

$$\epsilon \equiv \frac{Ea}{q^2}, \tag{3.4.5}$$

$$\nu \equiv \frac{Ze}{q}. \tag{3.4.6}$$

In order to estimate the reduced cross section, Draine and Sutin (1987) defined θ_ν, a parameter related to the maximum value assumed by the interaction potential between a charged particle and a grain. θ_ν can be assumed zero for $\nu \leqslant 0$ and to a good approximation

$$\theta_\nu \approx \frac{\nu}{1 + \nu^{-1/2}}, \tag{3.4.7}$$

which is accurate to within 0.7% for $1 \leqslant \nu \leqslant \infty$. Then the reduced cross section can be expressed as

$$\tilde{\sigma}(\epsilon,\nu) = \begin{cases} x^2 + \frac{1}{\epsilon}\left[\frac{1}{2(x^2-1)} - \nu x\right] & \text{for } \epsilon > \theta_\nu \\ 0 & \text{for } \epsilon \leqslant \theta_\nu \end{cases} \tag{3.4.8}$$

where $x > 1$ is a root of the equation

$$(2\epsilon x - \nu)(x^2-1)^2 - x = 0. \tag{3.4.9}$$

The sticking coefficient was estimated in the case of impinging electrons and ions by Weingartner and Draine (2001). An electron hitting the surface of a bulk material has a certain probability, $p_{\rm es}$, to undergo an elastic scattering on the surface of the grain. This probability was assumed to be 0.5 and therefore the sticking coefficient for bulk material will be $(1 - p_{\rm es}) \approx 0.5$. Furthermore, Weingartner and Draine (2001), comparing experimental studies on grains of different sizes (numerous references in Weingartner and Draine 2001), found analytical functions for the size dependence of the sputtering yield in the case of positively and negatively charged and neutral grains. The electron sticking coefficient for neutral grains is expressed as

$$s_{\rm e}(Z=0) = (1-p_{\rm e})(1-e^{-a/l_{\rm e}})\frac{1}{1+e^{(20-N_{\rm C})}} \tag{3.4.10}$$

where $l_{\rm e} = 10^{-7}\,{\rm cm}$, while for negatively charged grains

$$s_{\rm e}(Z<0) = \begin{cases} s_{\rm e}(Z=0), & Z > Z_{\rm min} \\ 0 & Z \leqslant Z_{\rm min} \end{cases} \tag{3.4.11}$$

and for positively charged grains results

$$s_{\rm e}(Z>0) \approx (1-p_{\rm e})(1-e^{-a/l_{\rm e}}). \tag{3.4.12}$$

On the other hand, positive ions of interest in ISM studies (i.e. H^+, He^+ and C^+) have a large ionisation potential and so have a high probability of recombination with an electron on the surface of a grain. Weingartner and Draine (2001) therefore assumed $s_i = 1$. This assumption is valid for negatively or neutral grains, while it will not be the case for highly positively charged grains. However, the rate of arrival of positive ions at the surface of such a grain is negligible and the sticking coefficient is always considered equal unity ($s_i = 1$).

3.4.3 Equilibrium charge

All the processes described above will then contribute to modify the charge of a dust grain. However, depending on the environment, a dust grain will, after a certain time, reach an equilibrium charge, which represents the most probable charge state. If we define the probability, $f(Z)$, of finding a grain with a net charge Ze, a grain

in charge equilibrium must satisfy the following condition (neglecting multiply ionised ions, Draine and Sutin 1987):

$$f_{\rm Z}(Z)[J_{\rm pe}(Z)+J_{\rm ion}(Z)]=f_{\rm Z}(Z+1)J_{\rm e}(Z+1). \tag{3.4.13}$$

Following Draine and Sutin (1987) it is possible to define the probability that a grain is found at a given charge Ze with

$$f(Z>0)=f(0)\prod_{Z'=1}^{Z}\left[\frac{J_{\rm pe}(Z'-1)+J_{\rm ion}(Z'-1)}{J_{\rm e}(Z')}\right], \tag{3.4.14}$$

$$f(Z<0)=f(0)\prod_{Z'=Z}^{-1}\left[\frac{J_{\rm e}(Z')}{J_{\rm pe}(Z'-1)+J_{\rm ion}(Z'-1)}\right], \tag{3.4.15}$$

where $f(0)$ can be determined imposing the condition

$$\sum_{-\infty}^{+\infty}f(Z)=1. \tag{3.4.16}$$

3.4.4 Ion and electron field emission

When a grain is charged to highly negative potentials, electrons in the grain can be ejected through quantum mechanical tunneling in order to reduce the negative charge of the grain. Quantum mechanical calculations as well as experimental studies (Gomer 1961) seem to indicate that for negative electric fields $|\vec{E}|\gtrsim 10^7\,{\rm V\ cm^{-1}}$ the quantum mechanical tunneling rate starts to be appreciable. This process is known as electron field emission.

In a similar way, grains with a too high positive charge ($\sim 3\times10^8\,{\rm V\ cm^{-1}}$) will eject atoms from their surface as positive ions (Muller and Tsong 1969). This process limits the maximum positive charge and is known as ion field emission. However, charging a grain to a highly positive potential will increase its tensile strength. The maximum tensile strength[1] for ideal spherical grains is estimated to be $S_{\rm max}\approx 10^{11}\,{\rm dyn\ cm^{-2}}$ (Weingartner et al. 2006). If a grain tensile strength exceeds this maximum value then fragmentation would occur, a mechanism called Coulomb explosion. The maximum grain potential that can be reached before the grain would experience Coulomb explosion is (Weingartner et al. 2006):

$$\Phi_{\rm max}=10\left(\frac{S_{\rm max}}{10^{10}\,{\rm dyncm^{-2}}}\right)^{1/2}\left(\frac{a}{\rm nm}\right)\ {\rm V}. \tag{3.4.17}$$

The maximum tensile strength for real objects is highly uncertain and if we assume $S_{\rm max}\sim 10^{10}\,{\rm dyn\ cm^{-2}}$ then $\Phi_{\rm max}\sim 10^8\ {\rm V\ cm^{-1}}$ and the Coulomb explosion rather than ion field emission may limit the grain charging.

[1]The maximum tensile strength is define as the maxim stress that a material can tolerate while being stretched or pulled before undergoing plastic deformation or breaking

3.5 Grain - grain interactions

Dust destruction in interstellar shocks, even if dominated by the sputtering process, is also partly due to grain-grain collisions. As a grain couples to the shocked gas, its relative velocity with respect to the gas varies according to its size, density and charge. Grains of different sizes couple more or less quickly to the gas, leading to a differential velocity between grains. The collision between two grains can be considered as the collision between a finite spherical projectile and a semi-infinite target and two main phases can be identified (Dienes and Walsh 1970). The first phase starts at the time of the collision, shocks simultaneously propagate inside the target and the projectile in opposite directions. As the shock in the projectile reaches the back surface, it will be reflected back towards the target as a rarefaction wave. The second phase begins when the rarefaction wave reaches the wave propagating in the target leading to its attenuation and modification of its structure making it more spherical. The theory of shocks in solids is well summarized in a review by Zeldovich and Raizer (1966) and retaken by Tielens et al. (1994) to put it in a suitable form to allow the study of the relevant astrophysical case of grain-grain collisions. We summarise here the main points that lead to the current theory.

Despite some general similar characteristics, shocks in a gas or in a solid do not behave in the same way. The strong interaction between the constituent atoms of the solid leads to a finite speed of sound even at zero pressure, while in a gas sound cannot propagate in absence of an initial pressure. In a solid the specific energy and pressure are characterized by an elastic (ϵ_c and P_c for specific energy and pressure, respectively) and a thermal component. At zero temperature the thermal components vanish and at equilibrium, the attractive and repulsive forces between the atoms compensate and the elastic components vanish as well. If the density is raised above the equilibrium density ρ_0 then the solid is compressed, the forces between atoms increase and ϵ_c and P_c rise rapidly. On the other hand, if the density is lowered below ρ_0 then ϵ_0 rises and P_c becomes negative. Therefore, fluctuations of the pressure in the solid around zero generate sound waves.

In the case of a collision between grains, we are mainly interested in shocks where the initial pressure is zero and the difference between the upstream and downstream pressures is large. In this case the shock is said to be strong even if its velocity is only mildly supersonic. Because of this relatively low velocity, the post-shock compression is not as large as for a strong shock in a gas (i.e. a factor four) but the jump conditions (or Rankine-Hugoniot conditions) are very similar (McKee and Hollenbach 1980):

$$\rho_1(v_s - v_1) = \rho_0 v_s, \tag{3.5.1}$$

$$P_1 + \rho_1(v_s - v_1)^2 = \rho_0 v_s^2, \tag{3.5.2}$$

$$\epsilon_1 + \frac{P_1}{\rho_1} + \frac{1}{2}(v_s - v_1)^2 = \frac{1}{2}v_s^2, \tag{3.5.3}$$

where the quantities denoted by the subscript "1" are behind the shock and velocities are evaluated in the unshocked matter reference frame; v_s is the shock velocity and

Table 3.5: Density, ρ_0, speed of sound, c_0 and parameter s for graphitic-type and silicate grains.

Material	ρ_0 (g cm^{-3})	c_0 (km s^{-1})	s
Graphite	2.2	1.8	1.9
Silicate	3.3	5.0	1.23

v_1 the velocity of the shocked matter. Combining Eq. 3.5.1 and 3.5.2 the post-shock pressure, P_1, then results:

$$P_1 = \rho_0 v_1 v_\mathrm{s}, \tag{3.5.4}$$

and similarly the energy of the shocked matter, ϵ_1, can be written as:

$$\epsilon_1 = \frac{1}{2} v_1^2. \tag{3.5.5}$$

For an ideal gas, these two quantities are related by an equation of state. In the case of a solid, this can be rather complicated. However, we can define an effective shock γ by:

$$P_1 = (\gamma - 1)\rho_1 \epsilon_1. \tag{3.5.6}$$

The value of γ is constant for ideal gases but in general it is not constant for shocks in a solid. However, it has been found experimentally (McQueen et al. 1970), that for a large range of shock velocities, γ is constant and the shock velocity is related to the velocity of the shocked solid matter by:

$$v_\mathrm{s} = c_0 + s v_1, \tag{3.5.7}$$

where c_0 is the speed of sound in the solid and s is a parameter. Finally, the Mach number of the shocked matter is defined as:

$$\mathcal{M}_1 \equiv v_1 / c_0. \tag{3.5.8}$$

Values for density, speed of sound and parameter s were deduced for graphitic-type and silicate grains by Tielens et al. (1994) and are shown in Table 3.5.

3.5.1 Energy transferred to the target during the first stage

In the first stage of the collision between two grains, we can define the velocities in the rest frame of the unshocked matter in the target. The scheme of the velocities involved in the collision is shown in Fig. 3.17. v_r indicates the velocity of the impinging projectile, v_s the shock velocity, $v'_{1\mathrm{P}}$ and v_1 the velocities of the shocked material in the projectile and in the target, respectively, as measured in the target rest frame. For continuity between the shocked matter in the projectile and in the target, the velocities

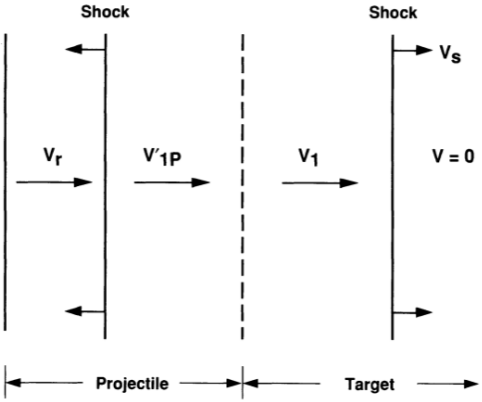

Figure 3.17: Schematic view of the propagation of shocks into solids due to the collision between two bodies (Tielens et al. 1994). The shock velocity (v_s) and the velocities of shocked (v'_{1P}, v_1) and unshocked matter (v_r) are measured in the target rest frame.

and pressures in these two media are identical. The conservation of the velocity implies that $v'_{1P} = v_1$. Then, if we define the velocity of the shocked projectile material in the projectile rest frame as $v_{1P} = v_r - v'_{1P} \equiv v_r - v_1$, we obtain:

$$v_r = v_1 + v_{1P}. \tag{3.5.9}$$

We now consider the conservation of the pressure across the interface between the projectile and the target. For the most destructive shocks, the shock velocity is high with respect to the speed of sound and therefore Eq. 3.5.7 reduces to $v_s = sv_1$. Using Eq. 3.5.4 we can then express the equivalence of the two pressures in this way:

$$\rho_0 s v_1^2 = \rho_{0P} s_P v_{1P}^2, \tag{3.5.10}$$

where ρ_0 and ρ_{0P} are the pre-shock densities of the target and the projectile, respectively. Combining Eq. 3.5.9 and 3.5.10 and defining

$$\Re = \left(\frac{s\rho_0}{s_P \rho_{0P}} \right)^{1/2}, \tag{3.5.11}$$

we obtain

$$v_1 = v_r/(1 + \Re), \tag{3.5.12}$$

$$v_{1P} = \Re v_r/(1 + \Re). \tag{3.5.13}$$

These two equations are particularly important since they relate v_1 and v_{1P} to the velocity of the impinging projectile and the physical properties of projectile and target.

We can therefore calculate the energy transferred during the collision, E_i, as the difference between the energy of the impinging projectile, $E_0 = \frac{1}{2} M_\mathrm{P} v_\mathrm{r}^2$, and the energy of the shocked projectile, $\frac{1}{2} M_\mathrm{P} v_{1P}^2$:

$$E_\mathrm{i} = \frac{1}{2} M_\mathrm{P} v_\mathrm{r}^2 \frac{(1+2\mathfrak{R})}{(1+\mathfrak{R})^2}. \tag{3.5.14}$$

In the case of similar materials, then $\mathfrak{R} \sim 1$ and $E_\mathrm{i} = \frac{3}{4} E_0$. For a rather dense projectile, $\mathfrak{R} \ll 1$ and all the energy of the projectile is transmitted to the target, while for a low-density projectile, $\mathfrak{R} \gg 1$ and only a small fraction of the energy is transmitted, $E_\mathrm{i} \sim \frac{2E_0}{\mathfrak{R}}$.

3.5.2 Fraction of mass shocked in the target by the blast wave

When the shock driven into the target has swept up more mass than in the projectile, the shock becomes a blast wave and if the shock velocity is large compared to the speed of sound then the flow becomes self-similar (i.e. its expansion is time-independent). In this case the radius increases following a power law (Zeldovich and Raizer 1966; Rae 1970):

$$R \propto t^\eta \tag{3.5.15}$$

and the energy scales as a power of the radius

$$E \propto R^{-k_\mathrm{E}}, \tag{3.5.16}$$

where η and k_E are related by (Ostriker and McKee 1988)

$$\eta = \frac{2}{5 + k_\mathrm{E}}. \tag{3.5.17}$$

The decrease in energy and increase in momentum, p, implies the conservation of the quantity $M v_\mathrm{s}^{3\alpha}$. The adopted values for the parameters k_E, η and α by Tielens et al. (1994) are

$$k_\mathrm{E} = 3/8,\ \eta = 0.372,\ \alpha = 0.593. \tag{3.5.18}$$

Under the assumption of a self-similar flow, the energy of the blast wave can be expressed as (Ostriker and McKee 1988):

$$E = \sigma_1 M v_1^2 = \sigma_1 M c_0^2 \mathcal{M}_1^2, \tag{3.5.19}$$

where σ_1 is a function of γ and k_E and typically of the order of unity. Following Eq. 3.5.16, we can express the energy at a given time as a function of the transferred energy, E_i and shocked mass, M_i, at the time when $E = E_\mathrm{i}$:

$$E = E_\mathrm{i} \left(\frac{M}{M_\mathrm{i}} \right)^{-k_\mathrm{E}/3}. \tag{3.5.20}$$

Then combining Eqs. 3.5.14, 3.5.19 and 3.5.20 we obtain that the ratio between the shocked mass in the target by the blast wave and the projectile mass

$$\frac{M}{M_{\rm P}} = \frac{(1+2\Re)}{2(1+\Re)^{6/(3+k_{\rm E})}} \frac{1}{\sigma_{1\rm i}^{k_{\rm E}/(3+k_{\rm E})}} \left(\frac{\mathcal{M}_{\rm r^2}}{\sigma_1 \mathcal{M}_1^2}\right)^{3/(3+k_{\rm E})} \tag{3.5.21}$$

Finally, using the pressure-gradient approximation (PGA) developed by Ostriker and McKee (1988), Tielens et al. (1994) found that σ_1 is nearly constant and relates to $\mathcal{M}_1$ and s as:

$$\sigma_1(\mathcal{M}_1) \simeq \frac{0.30(s+\mathcal{M}_1^{-1}-0.11)^{1.3}}{s+\mathcal{M}^{-1}-1} \tag{3.5.22}$$

In this way we have fully determined the mass in the target swept up by the blast wave triggered by a collision between two grains as a function of the velocity of the impinging projectile and the physical parameters of the colliding grains. As a consequence of such an impact, the shocked mass is then partly vaporized and shattered creating a crater in the target. Following the theory developed by Tielens et al. (1994) and Jones et al. (1996) we are able to determine the fraction of this mass that is vaporized and how this mass is fragmented.

3.5.3 Vaporization

As a shock passes through a solid, matter is compressed and its internal energy increases irreversibly. Part of this energy is in thermal form (vibrational and electronic excitation) while the rest is in elastic form (repulsion against pressure). After a certain time, pressure drops and the internal energy becomes entirely thermal. If the internal energy is large enough, then the solid will be partly vaporized. With the use of the Hugoniot conditions (Eq. 3.5.1 - 3.5.3) we are able to determine the critical point[2] of a material. All the isentrope curves[3] that pass above or are on the critical point will lead to the vaporization of solid matter. Typically we assume that the minimum internal energy, ϵ_1, necessary to vaporize the material is twice the average binding energy, $\epsilon_{\rm b}$. However, it has been shown experimentally (e.g. Hornung and Michel 1972) that under this condition, only $\sim 25\%$ is vaporized and complete vaporization is observed only for $\epsilon_1 \geqslant 5\epsilon_{\rm b}$. In Table 3.6 we report the threshold pressure for different astrophysically relevant materials as estimated by Tielens et al. (1994). These values are calculated using the limiting case $\epsilon_1 = 2\epsilon$b.

We consider now the limiting case where the pressure is at threshold. In this case part of the target will be vaporized during the first stage, but the late stage will not play a role since the pressure will decrease below threshold after the rarefaction wave reaches the shock propagating in the target. Combining Eq. 3.5.5 and 3.5.12 we obtain that the threshold velocity for the impinging projectile

$$v_{\rm t} = (1+\Re)(2\epsilon_{\rm v})^{1/2} \tag{3.5.23}$$

[2]Pressure and temperature conditions under which there is no boundaries between the different phases.

[3]Locus of points in the P, V diagram of constant entropy.

Table 3.6: Vaporization threshold parameters for graphitic-type and silicate grains

Material	$\epsilon_{\rm v}$ (10^{11} erg g^{-1})	$P_{\rm th,v}$ (10^{12} dyn cm^{-2})	$v_{\rm th,v}$ (km s^{-1})
Graphite	6.4	5.8	23
Silicate	4.8	5.4	19

where $\epsilon_{\rm v}$ is the specific vaporization energy. Then, considering a correction factor, $h_{\rm over}$, due to the relative sizes of target and projectile, the ratio between the vaporized mass in the target and the mass of the projectile is:

$$f_{\rm v1} = \frac{M_{\rm v1}}{M_{\rm P}} = \frac{1}{2}(1+2\Re)\frac{h_{\rm over}}{\sigma {\rm i}1} \tag{3.5.24}$$

where

$$h_{\rm over} = \left(1+\frac{a_{\rm P}}{a_{\rm T}}\right)^{-1} \tag{3.5.25}$$

On the contrary, if we consider the case of high impact velocities, the late stage will play an important role and the shock will form a self-similar flow. Averaging over all the possible impact angles, following the result by Tielens et al. (1994), the fraction of vaporized mass is

$$f_{\rm v2} = 0.78\frac{(1+2\Re)}{(1+\Re)^{16/9}}\frac{1}{\sigma_{\rm i1}^{1/9}}\left(\frac{\mathcal{M}_{\rm r}^2}{\sigma_1\mathcal{M}_1^2}\right)^{8/9}\Re^{0.18} \tag{3.5.26}$$

More realistically, the mass vaporized in the target will be in between these two limits. The ratio, $F_{\rm v}$, between the vaporized mass, $M_{\rm v}$, and the total target mass, $M_{\rm T}$, can be expressed as the combination of the two limiting cases:

$$F_{\rm v} = \frac{f}{1+f} \tag{3.5.27}$$

where f is defined as

$$f = \left[f_{\rm v1} + f_{\rm v2}\left(1-\frac{v_{\rm t}}{v}\right)^{1/2}\right]\frac{M_{\rm T}}{M_{\rm P}} \tag{3.5.28}$$

Following this method we calculate the fraction of the target mass that is vaporized as a consequence of the collision between two silicate grains. In Fig. 3.18 we show this fraction as a function of the relative velocity between the grains and for different ratios between the radii of the grains. We note that in the case large projectiles with respect to targets ($a_{\rm P}/a_{\rm T} \gtrsim 1$), even for low relative velocity ($v \gtrsim 10\,$km s-1), the target is entirely vaporized. On the other hand for $a_{\rm P}/a_{\rm T} \ll 1$ a large fraction of the target is vaporized only for very high relative velocities $v \sim 1000\,$km s^{-1}. It has to be noted that a very similar plot is found in the case of the collision between graphitic-type and silicate grains.

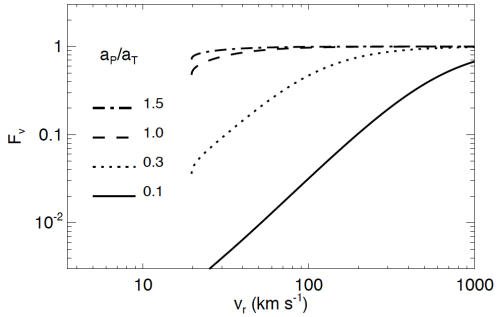

Figure 3.18: Fraction of the target mass that is vaporized for the collision between silicate grains as a function of the collision velocity for different projectile / target size ratios (adapted version from Tielens et al. 1994).

3.5.4 Shattering

In the previous sections, following the approach by Tielens et al. (1994), we showed how the fraction of mass in the target that is swept up by a collision between grains and the fraction that is vaporized can be determined. Following the approach of Jones et al. (1996) we are also able to determine the fraction of the target that is fragmented and the size distribution of the fragments created in this way. As the matter released after the passage of the shock, the density drops to a value larger than the initial one which will remain constant in time. The excavation flow can then be described as an incompressible flow and its velocity field can be described by a radial, $U_{\rm R}$, and a tangential, U_θ, component, which can be expressed to a good approximation by

$$U_{\rm R} = \frac{A_{\rm R}}{R^z}, \tag{3.5.29}$$

where $A_{\rm R}$ and z are constant and

$$U_\theta = U_{\rm R}(z-2)\frac{sin\theta}{1+cos\theta}. \tag{3.5.30}$$

We can then define the streamlines as the loci of the points where the velocity field is tangential.

Under the assumption of an elastic - perfectly plastic material[4], the boundaries of the crater formed because of the collisions are defined as the points where the pressure in the excavation flow has dropped to the critical pressure, $P_{\rm cr}$, where the material

[4]An elastic - perfectly plastic material is a material that responds linearly to a given strain until a critical pressure and beyond that becomes perfectly plastic, i.e. its stress remain constant whilst strain increases.

starts to be plastic. If we define with R_c the position of each point on the boundary of the crater, the velocity $U(R_c)$ follows

$$U(R_c) = \frac{P_{cr}}{\rho_0 c_0}, \tag{3.5.31}$$

where ρ_0 is the material density. We then find that the crater volume is

$$V_c = \frac{2\pi}{3}\left[R_c\left(\frac{\pi}{2}\right)\right]^3 I(z), \tag{3.5.32}$$

where $I(z)$ is given by $I(z) = -8.53 + 13.04z - 6.42z^2 + 1.35z^3 - 0.1z^4$. The streamline that passes on the edge of the crater on the surface of the grain will define the ejected matter. All matter above this line will be ejected while the rest will be only displaced to form a lip (Croft 1980). The ejected volume, V_e, is then given by

$$V_e = \frac{2\pi}{3}\frac{(z-2)}{(z+1)}\left[R_c\left(\frac{\pi}{2}\right)\right]^3. \tag{3.5.33}$$

For $3 < z < 4$, between the 30% and 60% of the crater volume is ejected from the target.

However, the material ejected in this way will not conserve its shape but it will be torn to pieces by the velocity field created in the crater. In order to determine the size of the ejected fragments, we assume that at the boundaries of each fragment the stress due to the differential velocity will be larger than the critical shear stress. The ejection velocity, $U_e(R)$, of a fragment at a distance R is given by

$$U_e(R) = U_R(R)[1 + (z-2)^2]^{1/2}. \tag{3.5.34}$$

Using Eq. 3.5.29, the differential velocity, ΔU, between the two points at distance $2a_f$ yields

$$\Delta U = 2z a_f \frac{U_e(R)}{R}. \tag{3.5.35}$$

We then obtain that the radius of the fragments, a_f, at distance R from the collision centre is

$$a_f = a_{f+}\left[\frac{R}{R_c(\pi/2)}\right]^{z+1}, \tag{3.5.36}$$

where the maximum grain radius a_{f+} is given by

$$a_{f+} = \frac{R_c(\pi/2)}{2z}. \tag{3.5.37}$$

For each fragment size a_f we can define a streamline and, integrating along it, we obtain the volume of matter that eject fragments of that size. Following the approach by Jones et al. (1996), defining $\tilde{a} = a_f/a_{f+}$, the number of grains $n(\tilde{a})$ in a size interval $[\tilde{a}, \tilde{a} + d\tilde{a}]$ is given by

$$n(\tilde{a})d\tilde{a} = \frac{12z^3(z-2)}{(z+1)^2}\tilde{a}^{-\alpha_f}d\tilde{a}, \tag{3.5.38}$$

where $\alpha_{\rm f} = (4z+1)/(z+1)$.

In Fig. 3.19, following Jones et al. (1996), we reproduce the size distribution of the fragments as a consequence of the collision between a 5 nm and a 100 nm graphitic-type grains. We consider different relative velocities between the two grains: 1.2 (solid), 25 (dotted), 75 (dashed) and 100 km s^{-1} (dot-dashed).

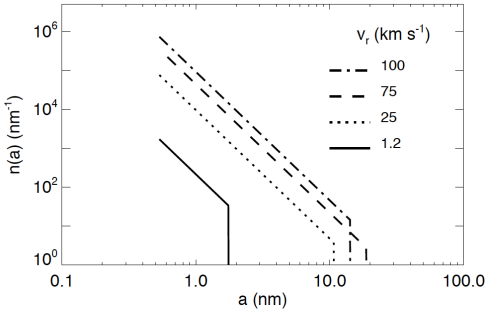

Figure 3.19: Size distribution of the fragments generated due to the collision of a 5 nm and a 100 nm graphitic-type grains. (adapted version from Jones et al. 1996).

3.5.5 Shattering and vaporization parameters for a-C(:H) grains

As shown by Tielens et al. (1994) and Jones et al. (1996), the shattering and vaporization of colliding grains can be modeled in the framework of shocks in solids. The first step is to estimate the relevant parameters involved in the model for the average binding energy of the target material. Graphitic-type materials consists of purely sp^2 hybridized bonds, C=C, while diamond is of pure sp^3 C-C bonds. An a-C(:H) material is somewhat in between the two materials and presents a mix of sp^3 and sp^2 hybridized bonds with a significant H atom concentration. The binding energy, $E_{\rm b}$, for this material can be expressed as:

$$E_{\rm b} = E_{\rm C-C} + {}^1\!/_2 E_{\rm C=C}\,, \tag{3.5.39}$$

where $E_{\rm C-C}$ (= 3.6 eV) and $E_{\rm C=C}$ (= 6.3 eV) are the energy of the sp^3 and sp^2 bonds, respectively. The a-C(:H) binding energy then yields $E_{\rm b} = 6.7\,$eV.

As discussed by Tielens et al. (1994), the threshold vaporization energy density, $\epsilon_{\rm v}$, is related to the binding energy and can be estimated as:

$$\epsilon_{\rm v} = \frac{E_{\rm b}}{m_{\rm p} M}\,, \tag{3.5.40}$$

where $m_{\rm p}$ is the proton mass and M the carbon atomic mass. Then the minimum relative velocity between the colliding grains for vaporization (i.e. the threshold vapor-

ization velocity, $v_{\rm th}$) is

$$v_{\rm th} = 2(2\epsilon_{\rm v})^{1/2}. \tag{3.5.41}$$

For a-C(:H) grains we then obtain a threshold vaporization energy and velocity of $\epsilon_{\rm v} = 5.2 \times 10^{11}\,{\rm erg\ g^{-1}}$ and $v_{\rm th} = 20.3 \times 10^5\,{\rm cm\ s^{-1}}$.

At threshold, the pressure of the shock in the solid, $P_{\rm th,v}$, can be expressed as:

$$P_{\rm th,v} = \frac{\rho v_{\rm th}(v_{\rm th} - c_0)}{s} \times 10^{10}\,{\rm dyne\,cm^{-2}}, \tag{3.5.42}$$

where c_0 is the speed of sound in the target, ρ its density and s a parameter introduced by McQueen et al. (1970) and estimated to be $s \approx 1.9$ for graphite/a-C materials. We assume that $c_0 \ll v_{\rm th}$ and confirm the validity of this assumption below.

In order to estimate the corresponding parameters for the shattering process, we assume that the threshold vaporization and shattering pressure scale for a-C(:H) materials as for graphite. Jones et al. (1996) made a detailed estimation of these parameters for graphite obtaining $P_{\rm th,v} = 5.8 \times 10^{12}\,{\rm dyne\ cm^{-2}}$ and $P_{\rm th,sha} = 4.0 \times 10^{10}\,{\rm dyne\ cm^{-2}}$. Scaling these parameters, for a-C(:H) grains as per Serra Díaz-Cano and Jones (2008) we then have $P_{\rm th,sha} = 2.0 \times 10^{10}\,{\rm dyne\ cm^{-2}}$. Furthermore, the threshold shattering pressure is a good estimate of Young's modulus for the material, $E_{\rm Y}$, and we can therefore calculate the speed of sound in the medium as

$$c_0 \sim \sqrt{\frac{E_{\rm Y}}{\rho}}, \tag{3.5.43}$$

obtaining $c_0 \approx 1$. We finally conclude that the assumption $c_0 \ll v_{\rm th}$ is valid in this case and we show the fragmentation and vaporization parameters for both graphitic-type and a-C(:H) grains in Table 3.7. However, it should be noted that updating the fragmentation and vaporization parameters for carbonaceous grains to those for a-C(:H) materials, in the framework of the model developed by Tielens et al. (1994) and Jones et al. (1996), the fraction of the target vaporized and the distribution of the fragments formed upon grain-grain collisions shown in Fig. 3.18 and 3.19 are little affected by this change.

3.5.6 Collisions between large and nm size grains

In the previous chapter we showed that the recent dust model by Jones et al. (2013) has an abundant population of small carbonaceous grains and large silicate grains. In this case grain-grain collisions will mainly occur between these two populations. In the classical theory of grain-grain collisions described in this chapter, grains are treated as 'hard spheres'. However, small a-C(:H) grains are low density, open structures and will therefore act as 'soft', low-density impactors, rather than hard spheres. For example, a molecular dynamics study of collisions between fullerenes C_{60} (which have a rather resistant and stable configuration) and graphite surfaces show that up to energies of 6 keV both the projectile and the target are little affected by the collision (Smith and

Table 3.7: Fragmentation and vaporization parameters for graphitic-type and a-C(:H) grains

	Fragmentation		Vaporization	
Parameter	Graphite	a-C:H	Graphite	a-C:H
$\rho_0\,[\mathrm{g\,cm^{-3}}]$	2.2	1.4	2.2	1.4
$c_0\,[\mathrm{km\,s^{-1}}]$	1.8	1.0	1.8	1.0
s	1.9	1.9	1.9	1.9
$P_{\mathrm{th}}\,[\mathrm{dyn\,cm^{-2}}]$	0.4×10^{11}	0.2×10^{11}	5.8×10^{12}	2.8×10^{12}
$\epsilon_{\mathrm{v}}\,[\mathrm{erg\,g^{-1}}]$	1.8×10^{9}	0.75×10^{9}	6.4×10^{11}	5.2×10^{11}
$v_{\mathrm{th}}\,[\mathrm{km\,s^{-1}}]$	1.2	0.8	23	20

Webb 1993). This range of energies is typical for collisions between small and large grains in 50 km s^{-1} shocks. In order to study 'soft' molecule impacts on 'hard' surfaces dedicated molecular dynamics modelling will be required, which is clearly beyond the scope of this thesis.

Chapter 4

Dust destruction and heating in a hot gas

> If you can't understand it simply, you don't understand it well enough.
>
> Albert Einstein

Contents

Dust grains embedded in a hot gas experience energetic collisions with ions and electrons in thermal motion. As seen in the previous chapter, depending on the energy of such a collision and on the size of the target grain, this process will lead to two different events: the erosion and the heating of the grain.

In particular, as a consequence of a collision between a gas particle and a grain, a fraction of the initial energy of the impinging particle is transferred to the grain. Ions in a hot gas with a sufficient energy will generate a collisional cascade inside the bulk of the grain therefore eroding it, a process known as "thermal sputtering". The thermal sputtering of dust in the ISM is only important for gas kinetic temperatures, $T_{\rm k}$, greater than 10^6 K (*e.g.*, Draine and Salpeter 1979a; Jones 2004) and is therefore unimportant in "cold" interstellar media such as photodissociation regions ($T_{\rm k} \lesssim 10^3$ K), HII regions and in the warm inter-cloud medium with $T_{\rm k} \simeq 10^4$ K. Thus, it is only in a low-density ($n_{\rm H} \simeq 10^0 - 10^{-4}\,{\rm cm}^{-3}$) hot coronal-type gas ($T_{\rm k} \simeq 10^6 - 10^8$ K), such as in the hot ionised medium (HIM) of galaxies, in hot post-shock gas, in galactic fountains or in the intracluster medium (ICM, $n_{\rm H} \simeq 10^{-2} - 10^{-4}\,{\rm cm}^{-3}$), that thermal sputtering is an important process.

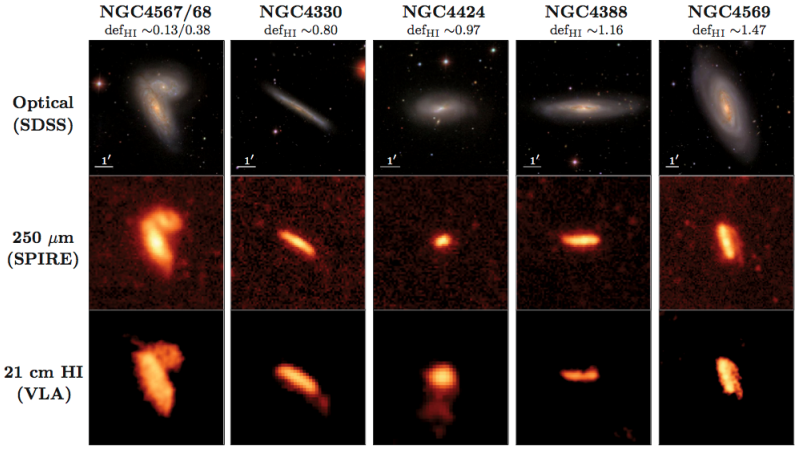

Figure 4.1: Optical, 250 μm and 21 cm images of different Virgo Cluster galaxies of the HeViCS sample. Cortese et al. 2010b.

On the contrary, energetic electrons in a hot gas are inefficient in eroding large dust grains. However, crossing the grain, electrons deposit a fraction of their energy leading to an increase of the grain internal energy. As a consequence of several collisions, this process can therefore lead to a significant enhancement of the grain temperature. This process is known as "collisional heating" and, in a low-density hot coronal-type gas ($T_{\rm k} \simeq 10^6 - 10^8$ K, $n_{\rm H} \simeq 10^0 - 10^{-4}\,{\rm cm}^{-3}$), competes with photon absorption in grain heating. Furthermore, in such an energetic medium, thermal sputtering and collisional

heating are coupled together and cannot be considered separately. These two processes, depending on gas conditions, therefore lead to variations in the dust abundance and temperature. However, while the collisional heating has an almost immediate effect on the dust temperature, dust destruction will act on different timescales depending on the environment.

Galaxies in clusters can provide good test cases for destruction and heating of dust in the hot ICM. As an example, observations of ram-pressure stripped galaxies in the Virgo Cluster have shown perturbed dust distributions (e.g. Cortese et al. 2010b, Fig. 4.1). As a consequence of the infall of a galaxy in a cluster, the pressure exerted by the ICM wind pushes the dust outside the galactic plane where it then encounters the more tenuous and much warmer ICM. As a grain enters the ICM, it will be heated to high temperatures but also destroyed on short timescales.

In this chapter we re-visit the problem of small hydrocarbon particle erosion and, in particular, consider the effects of electron collisions, electronic interactions and charging effects. Furthermore, we will compare the electron collisional heating effect with that due to photon absorption in the ICM in order to investigate if dust, embedded in a hot gas, would be able to emit enough energy to be detected by modern IR-FIR telescopes.

4.1 Thermal sputtering

As seen in the previous chapter, the erosion of bulk carbonaceous grains under the effect of bombardment of energetic ions is well described by the approach followed by Tielens et al. (1994). Later, this model was greatly extended to a-C(:H) grains by Serra Díaz-Cano and Jones (2008). A few years later, Micelotta et al. (2010a,b) developed a molecular approach for the dissociation of PAH-like particles. The aim of this section is to calculate the sputtering rate of carbonaceous grains and molecules in a hot gas and compare them. Most of this section is taken from the published paper Bocchio et al. (2012).

4.1.1 Grain/molecule characterization

In this study we are mostly interested in grains/molecules ranging from sub-nm up to a few nm in size. For a bulk carbonaceous spherical grain the number of carbon atoms, $N_{\rm C}$, contained in it , following Serra Díaz-Cano and Jones (2008), can be expressed as:

$$N_{\rm C} = \frac{4\pi\rho N_{\rm A} a^3}{3 \times [(1-X_{\rm H})M_{\rm C} + X_{\rm H} M_{\rm H}]} (1 - X_{\rm H}) \tag{4.1.1}$$

where a is the grain radius, $N_{\rm A}$ the Avogadro's number, ρ the grain density, $X_{\rm H}$ the atomic fraction of hydrogen in the particle, i.e. $X_{\rm H} = N_{\rm H}/(N_{\rm C} + N_{\rm H})$ (ρ and $X_{\rm H}$ are given in Table 6.1), and $M_{\rm C}$ and $M_{\rm H}$ the atomic masses of carbon and hydrogen atoms respectively ($M_{\rm C} = 12$ and $M_{\rm H} = 1$).

Table 4.1: Parameters for target and projectile materials. M_1 is the mean atomic mass of the projectile (amu), χ the abundance, U_0 the cohesion surface energy (eV), K a free parameter, ρ the density (g cm^{-3}) and $X_{\rm H}$ the atomic fraction of hydrogen in the particle.

Projectile parameters		
Material	M_1	χ
H	1.0	1.0
He	4.0	0.1
C	12.0	10^{-4}

Target parameters				
Material	U_0	K	ρ	$X_{\rm H}$
a-C	4	0.65	2.2	0
a-C:H	4	-0.04	1.4	0.4

On the other hand PAH-like molecules can be modeled like thick disks and their radius, a, is expressed as (Omont 1986):

$$a(\mathrm{nm}) = 0.09\sqrt{N_{\rm C}}. \tag{4.1.2}$$

Considering the thickness of a PAH as $d \simeq 0.3354\,$nm then its geometrical cross-section will be

$$\sigma_{\rm PAH}(\theta) = \pi a^2 \cos(\theta) + 2ad\sin(\theta) \tag{4.1.3}$$

where θ is the inclination from the normal axis of the planar molecule (Micelotta et al. 2010a). Then, following Micelotta et al. (2010a), averaging over the solid angle it results

$$\begin{aligned}\overline{\sigma_{\rm PAH}} &= \frac{\int_0^{\pi}\sin(\theta)d\theta\int_0^{2\pi}d\phi\,\sigma_{\rm PAH}(\theta)}{4\pi} \\ &= \frac{2\pi}{4\pi}\left(\pi a^2\int_{-1}^{1}\cos(\theta)d\cos(\theta) + 2ad\int_0^{\pi}\sin^2(\theta)d\theta\right) &(4.1.4)\\ &= \frac{\pi a^2}{2} + \frac{\pi ad}{2} &(4.1.5)\end{aligned}$$

Carbon grain erosion

We can calculate the sputtering yield of a bulk carbonaceous grain using the parameters in Table 6.1 for projectile and target materials as per the approach of Tielens et al. (1994) but as updated by Serra Díaz-Cano and Jones (2008). In the original work by Tielens et al. (1994) a graphitic-type material was used and it is indicated in Table 6.1 by a-C, while Serra Díaz-Cano and Jones (2008) updated the material to an

hydrogenated amorphous carbon, indicated as a-C:H. Furthermore, in the latter work, the finiteness of the grains has been taken into account (see Section 3.2.3). It should be noted that the adopted carbon abundance in the ISM is an intermediate value between what has been estimated by Sofia and Parvathi (2009) and Cardelli et al. (1996)[1] and that the inclusion of nitrogen and oxygen into the sputtering calculation does not change our results significantly.

Using the classical approach by Tielens et al. (Eq. 3.2.3 in Chapter 3), we can calculate the carbon ejection rate,

$$\frac{dN_{\rm sp}}{dt} = 2\pi a^2 \sum_i n_i < Y_i v F_{\rm C} >, \tag{4.1.6}$$

where $N_{\rm sp}$ is the number of sputtered atoms, the factor 2 takes into account the average of the yield over all angles of incidence, $n_i = n_{\rm H}\chi_i$ is the density of a given projectile with abundance χ_i, $n_{\rm H}$ is the proton density and

$$< Y_i v F_{\rm C} >= \int_0^\infty Y_i v F_{\rm C}(v) f(v,T) dv \tag{4.1.7}$$

with Y_i the sputtering yield for a given projectile, v the projectile velocity, $F_{\rm C}(v)$ the Coulomb focusing and $f(v,T)$ the Maxwell-Boltzmann velocity distribution for a given gas temperature, T. As we will see in Section 6.3.2 the Coulomb focusing for high gas temperatures is unimportant and can therefore be neglected. The target carbon atom ejection rate constant is then given by $1/n_{\rm H} \times dN_{\rm sp}/dt$.

PAH erosion

As mentioned in the previous chapter (Section 3.2.3 and 3.3) ions and electrons, colliding with PAHs lead to a net loss of carbon atoms and this process is well described with a molecular approach by Micelotta et al. (2010a,b). Following this approach, the collision between ions and a PAH can be modeled as the combination of two processes: the binary collision between the impinging ion and a nucleus in the target molecule (nuclear interaction) and the interaction of the impinging ion with the electronic cloud of the molecule as the ion passes through (electronic interaction). In the case of nuclear interaction, following Micelotta et al. (2010a) the PAH erosion rate, $\frac{dN_{\rm sp}}{dt}$, can be expressed as

$$\frac{dN_{\rm sp}}{dt} = 0.5 N_{\rm C} \sum_i n_i < \sigma(v) v F_{\rm C}(v) > \tag{4.1.8}$$

where the factor 0.5 takes into account the averaging over all the orientation angles,

$$< \sigma(v) v F_{\rm C} >= \int_0^\infty \sigma(v) v F_{\rm C}(v) f(v,T) dv \tag{4.1.9}$$

[1] A more recent work by Parvathi et al. (2012) measured the gas-phase carbon abundance along 15 Galactic sight lines and found $\chi_{\rm C} \sim 1 - 4 \times 10^{-4}$. However, since the grain erosion is dominated by H and He collisions, the variability in the gas-phase carbon abundance little affects our results.

and $\sigma(v)$ is the cross section averaged over all the collisions that deposit an energy larger than $T_0 = 7.5\,\mathrm{eV}$ per C-atom (a value close to the energy of the double C-bond, Micelotta et al. 2010a,b).

On the other hand, in the case of electronic interaction, the key parameter to calculate the destruction rate is the dissociation probability, $P(v,\theta)$, as a function of the velocity of the impinging projectile and its orientation angle, θ. The carbon ejection rate due to electronic interaction as a consequence of ion collision is given by

$$\frac{dN_{\rm sp}}{dt}(v) = \sum_i n_i F_{\rm C}(v) \int_{\theta=0}^{\pi/2} \sigma_{\rm g}(\theta) P(v,\theta) \sin(\theta) d\theta, \tag{4.1.10}$$

where v is the velocity of the impinging ion and $\sigma_{\rm g}$ is the PAH cross section. In the case of a hot gas, we can then express the thermal carbon ejection rate averaging over the Maxwell-Boltzmann distribution:

$$\frac{dN_{\rm sp}}{dt} = \sum_i n_i \int_0^{\infty} F_{\rm C}(v) \int_{\theta=0}^{\pi/2} f(v,T) \sigma_{\rm g}(\theta) P(v,\theta) \sin(\theta) dv d\theta. \tag{4.1.11}$$

Furthermore, the collision between electrons and a PAH is a process similar to the ion electronic interaction: the impinging electron, crossing the PAH electronic cloud transfers some energy to the PAH and slows down. Micelotta et al. (2010b) adopted Eq. 4.1.11 for both ion electronic interaction and electron collisions.

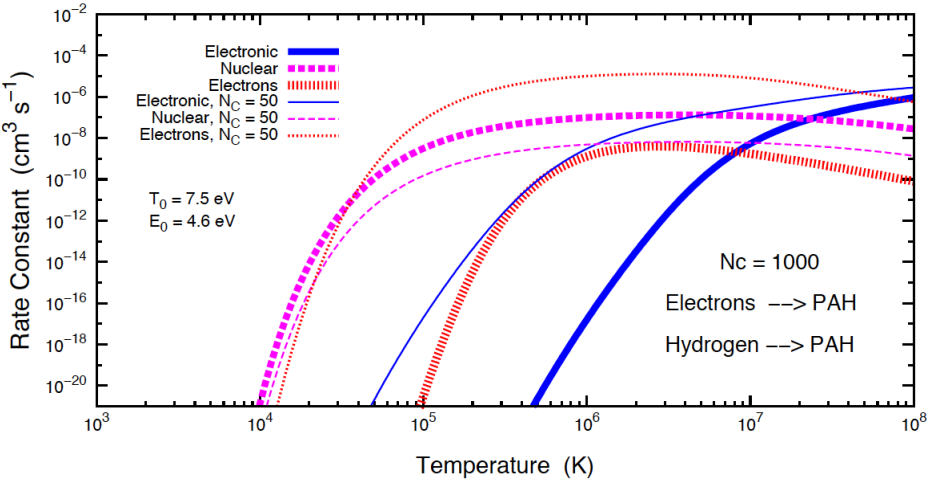

Figure 4.2: Rate constant due to electronic and nuclear ion interaction and electron collisions for $N_{\rm C} = 1000$ (thick lines) and $N_{\rm C} = 50$ (thin lines). Micelotta et al. (2010b).

Fig. 4.2 shows the destruction rate constant, $\frac{1}{N_{\rm C}} \frac{dN_{\rm sp}}{dt}$ as a function of the gas temperature, for ion and electron collisions and for PAHs of two different sizes ($N_{\rm C} = 50$

and $N_C = 1000$).

4.1.2 Grain charging

As seen in Section 3.4, the grain equilibrium charge is the result of the competition of different processes: ion and electron collisions and photoelectric effect due to the absorption of photons. Using the yields estimated by Weingartner and Draine (2001) for each process we can calculate the grain charge as a function of the gas parameters, the UV radiation field intensity, G_0, and the grain size. Then assuming spherical grains, the electric potential, U, (in SI units) results:

$$U = \frac{q_g}{4\pi\epsilon_0 \mid a \mid}, \tag{4.1.12}$$

with q_g the grain charge and ϵ_0 the vacuum permittivity. Fig. 4.3 illustrates the grain electric potential as a function of the gas temperature, T_{gas}, for a gas density $n_H = 10^{-3}$, and for different grain sizes. Two cases are shown: ambient starlight ($G_0 = 1$, black lines) and $G_0 = 0.1$ (red lines). The ratio, $\phi = \frac{eU}{k_B T_{gas}}$, between the grain electrostatic

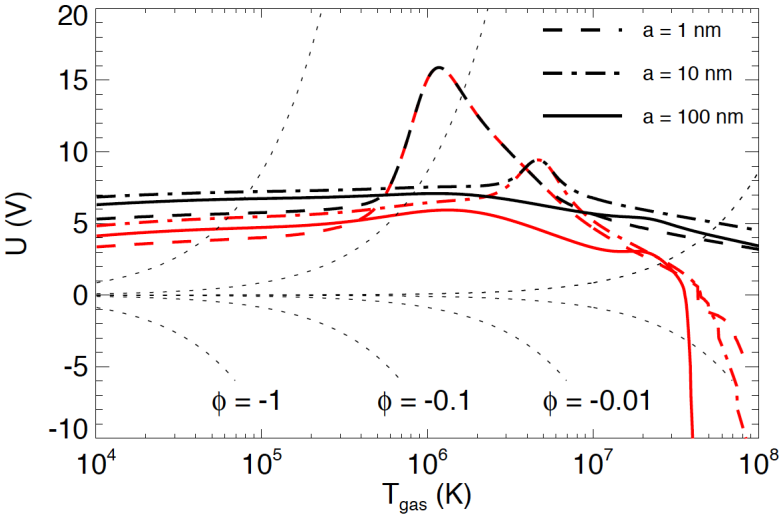

Figure 4.3: Grain electric potential, U, as a function of the gas temperature for different grain sizes. The assumed gas density is $n_H = 10^{-3}\,\mathrm{cm}^{-3}$. Red and black lines represents $G_0 = 0.1$ and 1 respectively. Loci of constant ϕ are indicated by thin dashed lines (see text for details).

energy and gas thermal energy is shown as well. We notice that the ϕ parameter, for high temperatures, $T_{gas} \sim 10^6 - 10^7\,\mathrm{K}$, is small enough ($\mid \phi \mid \lesssim 0.2$) and therefore the Coulomb focusing can be neglected.

On the other hand, sufficiently high electric potentials may lead to ion field emission or even to the shattering of the grain because of the Coulomb explosion effect (Draine and Salpeter 1979a; Waxman and Draine 2000; Weingartner et al. 2006, Section 3.4.2). The maximum positive electric field before the grain would experience ion field emission is $\sim 3 \times 10^8\,\mathrm{V\ cm^{-1}}$, which lead to a maximum electric potential of $U_{\max} = 30, 300, 3 \times 10^3\,\mathrm{V}$ for 1, 10 and 100 nm grains, respectively, which are higher than the maximum potentials reached in a hot gas. However, because of the high charge, the grain undergoes an increase of its tensile strength and Coulomb explosion is expected if the grain potential is higher than $U_{\max}$ (Weingartner et al. 2006):

$$U_{\max} = 10 \left(\frac{S_{\max}}{10^{10}\,\mathrm{dyncm^{-2}}} \right)^{1/2} \left(\frac{a}{\mathrm{nm}} \right)\ \mathrm{V}, \tag{4.1.13}$$

where $S_{\max}$ is the maximum tensile strength for a material. The maximum tensile strength for an ideal spherical grain is estimated to be $S_{\max} = 10^{11}\,\mathrm{dyn\ cm^{-2}}$ while for real grains, this quantity is highly uncertain. We will then assume that grains in a hot gas do not undergo ion field emission nor Coulomb explosion.

On the contrary, a sufficiently negative electric potential would lead to electron field emission (Draine and Salpeter 1979a). The minimum negative potential for which we would not observe any electron field emission is:

$$U_{\min} = -\frac{a}{100\,\mathrm{nm}} V \tag{4.1.14}$$

For our study, only in the case of a very hot gas ($T_{\mathrm{gas}} > 5 \times 10^7\,\mathrm{K}$) and a low UV radiation field ($G_0 = 0.1$), grains would experience electron loss, therefore limiting the negative grain charge.

4.1.3 Results

In Fig. 4.4 we compare the sputtering rate constants of Tielens et al. (1994) and Serra Díaz-Cano and Jones (2008) for different gas temperatures and for different grain sizes expressed as N_{C}. We notice that the use of different parameters for a-C:H together with the size effect (more important for high temperatures) taken into account to calculate the sputtering yield do change the sputtering rate quite significantly (see Section 3.2.2).

In Fig. 4.5 we compare the thermal sputtering for PAHs and a-C:H grains. For the PAHs we use the molecular approach (Micelotta et al. 2010a), while for a-C:H grains we use the classical approach (Serra Díaz-Cano and Jones 2008) with the size effect included. We see that for the a-C:H model the sputtering rate constant increases with the increasing number of carbon atoms (N_{C}), while for the PAH model the behavior changes at $N_{\mathrm{C}} \approx 1000$. For $N_{\mathrm{C}} \gtrsim 1000$ the sputtering rate constant increases as N_{C} increases, as per a-C:H, but for $N_{\mathrm{C}} \lesssim 1000$ it increases as N_{C} decreases. For $N_{\mathrm{C}} \gtrsim 1000$ the two models agree for temperatures $T = 10^5 - 10^6\,\mathrm{K}$ and within a factor of about 2 for $T = 10^7\,\mathrm{K}$. On the other hand they lead to different results for small grains, which is clearer in the following plot (Fig. 4.6) where we show the carbon ejection rate constant

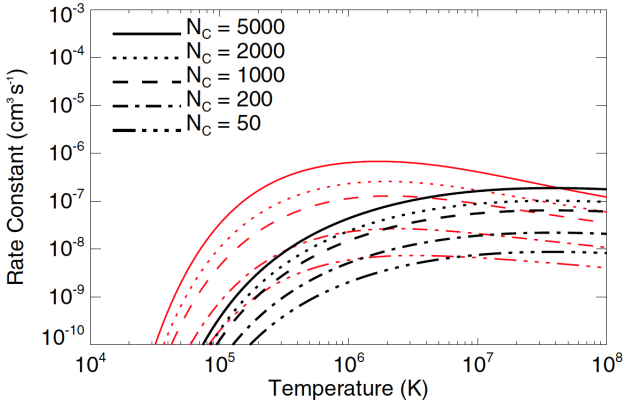

Figure 4.4: $1/n_{\rm H} \times dN_{\rm sp}/dt$. Comparison between a-C (black) and a-C:H (red) sputtering due to H^+, He^+ and C^+ projectiles.

for a-C:H grains (red lines) and PAHs (black line) for gas temperatures $T = 10^5$ K and $T = 10^7$ K as a function of the number of carbon atoms in the grain/molecule.

The dotted black line (in Fig. 4.6) shows the sputtering due to nuclear interaction (binary collisions between impinging ions and target atoms) only, the dashed line represents the sputtering due to both nuclear and electronic interactions, whilst the black solid line includes electron collisions as well. The effect of collisions between electrons and the particles is remarkable for grains with a small number of carbon atoms, where the transferred energy is sufficient to excite the whole molecule and trigger dissociation and the ejection of carbon atoms. In the absence of electron collisions and electronic interactions the two models would be very close, regardless of the gas temperature in this range. We can see that, for $N_{\rm C} \gtrsim 1000$ (for $T = 10^7$ K), the electron collisions and the electronic interactions are negligible in the approach used to treat the PAHs. In the classical model described by Tielens et al. and Serra Díaz-Cano and Jones electron collisions are not taken into account but they clearly will be important for particles with a sufficiently small number of carbon atoms.

The other important fact here is the extremely good agreement between the classical model and the nuclear interaction of the PAH model. This can be seen as the combination of two different effects. In the classical approach, since we consider 3D grains, a collisional cascade contributes to the sputtering yield allowing the possibility of ejecting more than one target atom. On the other hand, in the PAH approach there is no such effect, because only binary collisions are considered, but the cross-section increases with the number of carbon atoms more rapidly than in the 3D case.

In the molecular approach, if we consider only the nuclear interaction, which is represented by the dotted lines in Fig. 4.6, we only have binary collisions. If the transferred energy in the collision is higher than a certain threshold energy, $T_0 = 7.5$ eV

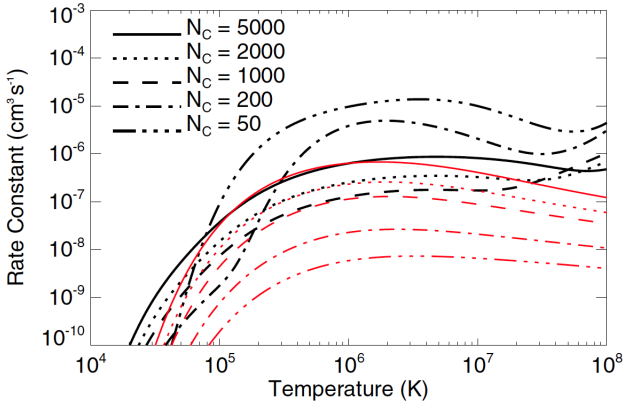

Figure 4.5: $1/n_{\rm H} \times dN_{\rm sp}/dt$. Comparison between PAH (black) and a-C:H (red) sputtering due to H^+, He^+, C^+ and electrons (only for PAHs) projectiles. The finiteness of the target is taken into account in calculating the sputtering of a-C:H grains.

(the standard value adopted by Micelotta et al. 2010a), then this leads to a loss of a single carbon atom. We would expect that, in the classical approach, the enhancement of the sputtering yield due to the collisional cascade compensates for the enhancement of the sputtering yield in the molecular approach due to the difference in cross-section. It should be noted that, if a threshold energy $T_0 = 4.5\,\mathrm{eV}$ (close to the energy of a single C-bond) is considered the erosion rate would be higher by a factor 1.5 and the agreement between the ion nuclear interaction and the classical approach would not be as good as it is in the case of $T_0 = 7.5\,\mathrm{eV}$.

In order to investigate this "compensation" effect we built a simple model of collisional cascade (Section 4.B). We simulate the collision between an impinging proton and a cubic lattice of C atoms and we treat the target nuclei as hard spheres. The output from this simple model is the number of C atoms ejected, $\epsilon_{\rm C}$, as a consequence of the collisional cascade triggered inside the solid because of the collision with the proton. To calculate $\epsilon_{\rm C}$ we consider only the case where the initial collision is above threshold and we averaged over the possible impact angles and over the Maxwell-Boltzmann energy distribution. This quantity can be seen as an efficiency of C atom ejection and therefore the C atom ejection rate can be expressed as

$$\frac{dN_{\rm sp}}{dt} \propto \sigma \epsilon_{\rm C}, \tag{4.1.15}$$

where σ is the collision cross section (see Eq. 4.1.4 for $\sigma_{\rm 2D}$). If the larger PAH cross section is compensated by the larger ejection efficiency in 3D grains due to the collisional

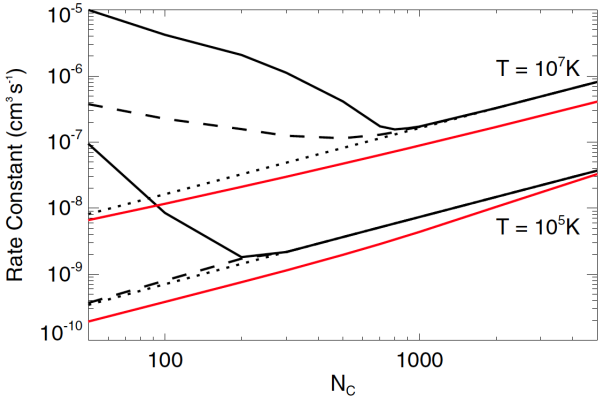

Figure 4.6: $1/n_{\rm H} \times dN/dt$ at $T = 10^5$ K and at $T = 10^7$ K. Red line: rate constant for a-C:H grains. Black lines: rate constant for PAHs; the dotted line shows nuclear interaction only, the dashed line the summed effects of nuclear and electronic interactions, whilst the solid line includes electron collisions as well. The results for $T = 10^6$ K are not shown here but are very similar to those for $T = 10^7$ K.

cascade, then we would expect that

$$\frac{\sigma_{\rm 2D}}{\sigma_{\rm 3D}} \simeq \frac{\epsilon_{\rm C,3D}}{\epsilon_{\rm C,2D}}. \tag{4.1.16}$$

In Fig. 4.7 we show (red solid line) the ratio between the number of sputtered atoms due to collisional cascade in a 3D a-C:H grain and that for a PAH molecule (i.e. single sputtered atoms for the molecular case for a transferred energy larger than 7.5 eV) as a function of the number of carbon atoms in the particle. We see that in larger grains the collisional cascade is more important and, consequently, a larger number of atoms are sputtered. On the other hand, the geometrical cross-section of a 2D PAH for a given number of carbon atoms is larger than that of a 3D grain. Following Eq. 4.1.4 the ratio between the cross-sections of PAHs and a-C:H grains is given by:

$$\begin{aligned}\frac{\sigma_{\rm PAH}}{\sigma_{\rm aCH}} &= \frac{1/2\,\pi(a_{\rm PAH}^2 + a_{\rm PAH}d_{\rm PAH})}{\pi a_{\rm aCH}^2} \\ &= \frac{9\times10^{-9}(9\times10^{-9}N_{\rm C}^{1/2} + 3.4\times10^{-8})\,[4\pi\rho N_{\rm A}(1-X_{\rm H})]^{2/3}}{2\times3^{2/3}N_{\rm C}^{1/6}[(1-X_{\rm H})M_{\rm C} + X_{\rm H}M_{\rm H}]^{2/3}}\end{aligned} \tag{4.1.17}$$

where $a_{\rm PAH}$ and $a_{\rm aCH}$ are the radii for a PAH and aCH grain, ρ is expressed in g cm^{-3}, $M_{\rm C}$ and $M_{\rm H}$ in amu. In Fig. 4.7, the black dashed line gives the ratio between the PAH cross-section and the 3D grain cross-section as a function of the number of carbon atoms in the particle. We can see that, even with a simple model like this, the behaviours of

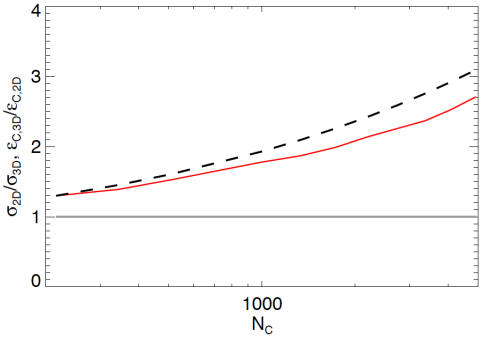

Figure 4.7: Red solid line: ratio between the number of sputtered atoms in the 3D case (obtained by our simple model of collisional cascade for $T = 10^7$ K) and the single atoms ejected in the PAH case (considering only the nuclear interaction above threshold). Black dashed line: ratio between the geometrical cross-section of a planar PAH and that of a 3D a-C:H grain. The x axis shows the number of carbon atoms in the particle.

the two ratios are similar. This means that the effect of the cross-section compensates the effect of the collisional cascade in 3D grains. This would explain the agreement between the sputtering rate constants for the two models.

Thus, the molecular approach of Micelotta et al. (2010a,b) can and should be used when considering the erosion of any small hydrocarbon particles, be they PAHs or a-C:H grains, in a hot gas because the classical sputtering approach, extended to particles with less than ~ 1000 carbon atoms, does not take into account electronic excitation effects and thus underestimates the degree of destruction.

4.1.4 Astrophysical implications

Considering a hydrocarbon particle (PAH or 3D a-C:H grain) of a given size we can follow its time-dependent evolution using the equation below:

$$t - t_0 = \int_{N_{\rm C}(t_0)}^{N_{\rm C}(t)} \frac{dN_{\rm C}}{dN_{\rm C}/dt} \tag{4.1.18}$$

where $dN_{\rm C}/dt$ is the ejection rate calculated in the previous sections. The time $t_{\rm dest}$ when the grain/molecule is totally dissociated corresponds to its life-time. At $t = t_{\rm dest}$, we have $N_{\rm C}(t_{\rm dest}) = 0$. In Fig. 4.8 we show the PAH life-time as a function of the number of carbon atoms, $N_{\rm C}$, in the molecule for unit proton density and gas temperatures of 10^5, 10^6, 10^7 K and 10^8 K. It should be noted that hydrocarbon particles with $N_{\rm C} \leqslant 5000$ have radii $\lesssim 7$ nm.

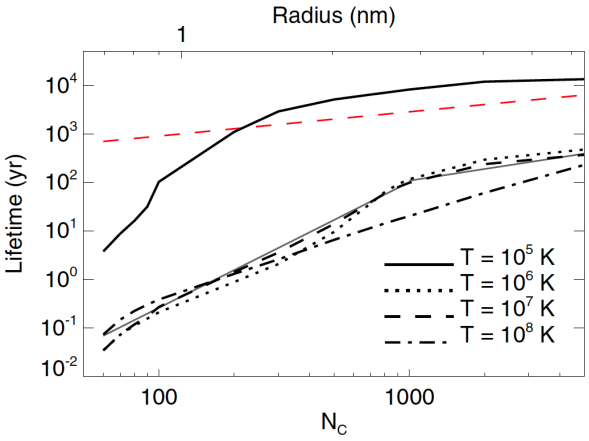

Figure 4.8: PAH lifetime (in years) as a function of the number of carbon atoms, $N_{\rm C}$, in the particle for a gas phase proton density $n_{\rm H} = 1\,{\rm cm}^{-3}$ and for temperatures of 10^5 (solid line), 10^6 (dotted line), 10^7 (dashed line) and $10^8\,{\rm K}$ (dash-dot line). The fit (see text for details) for the case $T = 10^7\,{\rm K}$ is shown in gray solid line. We compare our fit to previous estimates (Draine and Salpeter 1979a; Jones 2004), which are shown by red dashed line (see text for details).

In the hot post-shock gas behind a fast shock ($T_{\rm k} \sim 5 \times 10^5\,{\rm K}$ and $n_{\rm H} \sim 1\,{\rm cm}^{-3}$) the hydrocarbon nano-particle life-time will be $< 10^3\,{\rm yr}$, which is consistent with the results of Jones et al. (1996) for $200\,{\rm km\,s}^{-1}$ shocks. Nevertheless, our results indicate that, in such shocks, the thermal sputtering of hydrocarbon nano-particles should be even more pronounced than in this earlier work. However, and given that in the Jones et al. (1996) study, thermal sputtering was already the dominant destruction process for small carbon grains, our new erosion rates do not qualitatively change their results.

In the HIM or IGM, with $n_{\rm H} \simeq 10^{-2}\!-\!10^{-4}\,{\rm cm}^{-3}$ and $T_{\rm k} = 10^6\!-\!10^7\,{\rm K}$, Fig. 4.8 indicates hydrocarbon nano-particle lifetimes of $< 10^7$, $< 10^6$ and $< 10^5\,{\rm yr}$, for $n_{\rm H} \simeq 10^{-4}$, 10^{-3} and $10^{-2}\,{\rm cm}^{-3}$, respectively. For typical IGM conditions, *i.e.*, $n_{\rm H} \simeq 10^{-3}\,{\rm cm}^{-3}$ and $T_{\rm k} = 10^7\,{\rm K}$, the hydrocarbon nano-particle life-time, $t_{\rm dest}$, is less than a thousand years and the exact size-dependent life-times can be approximated by (gray solid lines in Fig. 4.8):

$$t_{\rm dest} \approx \begin{cases} 2 \times 10^{-6}\,\frac{N_C^{2.6}}{n_{\rm H}/{\rm cm}^{-3}}\,{\rm yr} & \text{for } N_{\rm C} \leqslant 1000\,(\equiv a \lesssim 3\,{\rm nm}) \\ 0.43\,\frac{N_C^{0.8}}{n_{\rm H}/{\rm cm}^{-3}}\,{\rm yr} & \text{for } N_{\rm C} > 1000. \end{cases} \tag{4.1.19}$$

For PAHs with $N_{\rm C} \geqslant 1000$ the above expression is equivalent to

$$t_{\rm dest} \approx \frac{20\,a({\rm nm})^{1.6}}{n_{\rm H}/cm^{-3}}\,{\rm yr} \qquad \text{for } a \gtrsim 3\,{\rm nm}, \tag{4.1.20}$$

where a is the PAH radius in nm. These life-times show a stronger size-dependency than previous estimates, *i.e.*, $t_{\rm dest} \approx 10^3\, a({\rm nm})/(n_{\rm H}/cm^{-3})\,{\rm yr}$ (Draine and Salpeter 1979a; Jones 2004), see red dashed line in Fig. 4.8. It has to be noted that a large a-C:H grain ($\sim 100\,{\rm nm}$), following these new estimates, under typical ICM conditions, will survive for only 10^7 yr, almost an order of magnitude less than in previous studies by Draine and Salpeter (1979a) and Jones (2004).

In the calculation of the particle life-times, the sputtering rate plays a central role. As is clearly shown in Fig. 4.6, the addition of electron collisional sputtering and electron interaction in our calculations dramatically increases the sputtering rate for small particles. As a consequence, we have that the particle life-times are shorter than the previous estimates, which were based on the presumed dominance of proton sputtering in the hot gas where only the nuclear interaction was taken into account. Evidently, for small particles (*i.e.*, $N_{\rm C} < 1000 \equiv a \lesssim 3\,{\rm nm}$), the destruction time-scale is significantly shorter than the previous estimates and, additionally, shows a stronger size-dependence.

From Eq. 4.1.18, we can also calculate the time-dependent evolution for a grain of a given size. In Fig. 4.9, we show the time-dependent evolution of a hydrocarbon grain initially of 5000 carbon atoms ($\equiv a \sim 7\,{\rm nm}$) in a gas with unit proton density and temperature of 10^5 (solid line), 10^6 (dotted line), 10^7 (dashed line) and $10^8\,{\rm K}$ (dash-dot line). The time-dependent evolution of grains with $N_{\rm C} < 5000$ can be seen

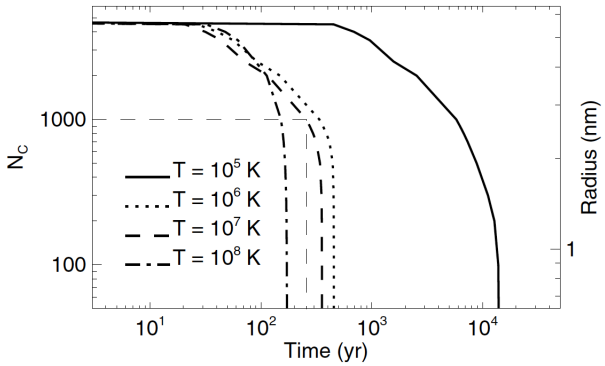

Figure 4.9: The time-dependent evolution of PAHs, with $N_{\rm C} = 5000$, for a gas phase proton density $n_{\rm H} = 1\,{\rm cm}^{-3}$ and for temperatures of 10^5 (solid line), 10^6 (dotted line), 10^7 (dashed line) and $10^8\,{\rm K}$ (dash-dot line).

as a shift in time of the plot in Fig. 4.9. For example a 5000 carbon atoms PAH in a gas at $T = 10^7\,{\rm K}$ evolve with time as indicated in Fig. 4.9 (dashed line) and at a time $t_0 \approx 2.5 \times 10^2$ yr it contains only 1000 carbon atoms. The time-dependent evolution of a 1000 carbon atoms PAH is given by the same line in Fig. 4.9 but starting from t_0.

Finally, it has to be noted that, for this study we neglect the Coulomb focusing

effect (see Section 6.3.2) and the grain Coulomb explosion was not considered.

4.2 Dust heating in a hot gas

In a hot gas, dust undergoes not only destruction but also part of the energy of the impinging projectiles represent an extra source of heating that will possibly lead to a more important dust emission. This source of heating will be added to the heating due to photon absorption.

In this study, taken from Bocchio et al. (2013b), we introduce electron collisional heating into the DustEM code and compare its effect with that due to photon absorption in the ICM in order to investigate if dust would be able to emit enough energy to be detected by modern IR-FIR telescopes.

This work was performed before the Jones et al. (2013) dust model was developed and published, using the Compiègne et al. (2011) dust model (see Section 2.4). It is clear from the previous section (Bocchio et al. 2012) that, for small carbonaceous particles ($a \leqslant 5\,\mathrm{nm}$), the 2D and 3D effective cross sections are equivalent. This allows us to use a 3D approach to describe PAH destruction.

4.2.1 Electron collisional heating

In a fully ionised hot coronal-type gas, be it galactic HIM or nearby ICM, dust is heated by inelastic collisions with the ambient ions and electrons (in addition to photons from any ambient radiation field). At a given gas temperature ions and electrons will have the same energy but, because electrons have a much smaller mass, they will reach higher velocities with respect to the ions. This implies that the electron flux is larger than that of the ions and therefore the major contribution to the collisional heating is given by electrons. The effect of electron collisional heating has already been studied in the case of dust in a low density, X-ray emitting plasma by Dwek (1986, 1987) who calculated the equilibrium temperature of very small grains heated only by collisions with the ambient electrons of a hot gas ($T \approx 10^7\,\mathrm{K}$). He also calculated the dust-temperature distribution which is a key factor in determining the dust spectral energy distribution (SED).

Following Dwek (1986), the power absorbed per grain (be it a carbon or a silicate grain) due to electron collisions is given by:

$$H = \pi a^2 n_\mathrm{e} \int_0^\infty f_\mathrm{M}(E,T)\mathrm{v}(E)\tilde{\sigma}(E)E\zeta(E)dE \tag{4.2.1}$$

where a is the grain radius, n_e is the electron density (which equals the proton density, n_H, since the gas is fully ionised), $f_\mathrm{M}(E,T)$ is the Maxwell-Boltzmann energy distribution for a gas temperature T, $\mathrm{v}(E)$ the velocity of the impinging electron, E its energy, $\tilde{\sigma}(E)$ represents the Coulomb focusing and $\zeta(E)$ the fraction of energy transferred to the target grain (see Section 3.3.1). As discussed in Section 6.3.2, Coulomb focusing has little effect on the grain charge under these conditions and is ignored here.

Table 4.2: Parameters for NGC 891 derived by Xilouris et al. (1999). The values of z_d and h_d represent the average values of those found by Xilouris et al. (1999) for the different bands.

Parameter	B	V	I	J	K
$L_{\rm s}\left[\frac{\rm erg}{\rm s\,pc^3\,sr\,nm}\times 10^{28}\right]$	2.66	3.53	3.44	6.2	1.41
$z_{\rm s}$ [kpc]	0.43	0.42	0.38	0.43	0.34
$h_{\rm s}$ [kpc]	5.67	5.48	4.93	3.86	3.87
$L_{\rm b}\left[\frac{\rm erg}{\rm s\,pc^3\,sr\,nm}\times 10^{31}\right]$	12.0	7.4	2.23	4.99	1.71
$R_{\rm e}$ [kpc]	1.12	1.51	1.97	0.87	0.86
b/a -	0.6	0.54	0.54	0.71	0.76
τ^f -	0.87	0.79	0.58	0.23	0.10
$z_{\rm d}$ [kpc]	0.27	0.27	0.27	0.27	0.27
$h_{\rm d}$ [kpc]	7.97	7.97	7.97	7.97	7.97

In our model we use the transferred energy function obtained by Micelotta et al. (2010b) for carbonaceous grains and, since there are no more recent estimates, we use that obtained by Dwek (1987) for silicate grains.

4.2.2 Photon heating

In regions where a radiation field is present, grains can be heated by photon absorption. In this case the power absorbed per grain (H_γ) is given by:

$$H_\gamma = \pi a^2 \int_{\nu_{\rm min}}^{\nu_{\rm max}} Q_{abs} J_\nu d\nu \,, \tag{4.2.2}$$

where $\nu_{\rm min}$ and $\nu_{\rm max}$ are the minimum and maximum frequencies of the radiation field, $\pi a^2 Q_{abs}$ is the absorption cross section and J_ν the intensity of the radiation field at the given frequency ν. To quantify the power absorbed in this way we need to estimate the radiation field in the region we want to consider, in this case in the ICM, a few kpc away from the galactic plane in a halo or in a region affected by galaxy collisions or ram pressure stripping.

We focus here on the study of the radiation field in the proximity of spiral galaxies. Edge-on galaxies play an important role in this study since we have experimental data on the radiation field in the optical-NIR bands around the galactic plane. A good example of an edge-on galaxy is NGC 891 and its radiation field has been widely studied in the literature (e.g. Xilouris et al. 1999; Popescu et al. 2000). We use this galaxy only as an example to have an estimate of the radiation field around a typical spiral galaxy. Xilouris et al. (1999) modeled the distribution of stars and dust in the optical and NIR bands. The stellar distribution that they use is composed of an exponential

(both in the radial, R, and vertical, z, directions) disk and a bulge (which in projection is given by the well-known $R^{1/4}$ law, Christensen 1990) described by:

$$\eta_0(R,z) = L_{\rm s} exp\left(-\frac{R}{h_{\rm s}} - \frac{|z|}{z_{\rm s}}\right) + L_{\rm b} exp\left(-7.67B^{1/4}\right) B^{-7/8}\,, \tag{4.2.3}$$

where η_0 is the total stellar emissivity (in erg s^{-1} pc^{-3} sr^{-1} nm^{-1}) at (R,z), L_s and L_b are the normalization constants for the stellar emissivity of the disk and the bulge, $h_{\rm s}$ and $z_{\rm s}$ are the stellar scalelength and scaleheight and

$$B = \frac{\sqrt{R^2 + z^2(a/b)^2}}{R_{\rm e}} \tag{4.2.4}$$

with $R_{\rm e}$ the effective radius of the bulge and a and b the semi-major and semi-minor axes respectively. To model the presence of a dust disk in the galaxy they used an exponential law for the extinction coefficient:

$$\kappa_\lambda(R,z) = \kappa_\lambda(0,0)\exp\left(-\frac{R}{h_d} - \frac{|z|}{z_d}\right)\,, \tag{4.2.5}$$

where $\kappa_\lambda(R,z)$ is the extinction coefficient (in kpc^{-1}) at wavelength λ at (R,z), $h_{\rm d}$ and $z_{\rm d}$ are the dust scalelength and scaleheight respectively. $\kappa_\lambda(0,0)$, the extinction coefficient at the centre of the disk, is related to the optical depth of the galaxy as seen face-on, τ_λ^f and the scaleheight:

$$\tau_\lambda^f = 2\kappa_\lambda(0,0)\, z_d\,. \tag{4.2.6}$$

In this work we use the parameters listed in Table 4.2 (Xilouris et al. 1999).

The same model has been used by Popescu et al. (2000). Starting from the optical-NIR SED, they calculated the FIR SED emitted by the dust distribution and compared this with the observational data from Alton et al. (1998). The observed differences between the results of the model and the data were assumed to be due to the absence of the UV radiation field. They assumed a distribution of young stars with a scaleheight smaller than the dust scaleheight. In fact, in edge-on galaxies, it is very difficult to observe any radiation in the UV because it is absorbed by the dust lane.

To compute the radiation in the UV it is possible to use the relation between SFR and the luminosity at different UV wavelengths, based on population synthesis models (e.g. Fioc and Rocca-Volmerange 1997). Misiriotis et al. (2004) calculated this relation with the PEGASE population synthesis model of Fioc and Rocca-Volmerange (1997) and obtained:

$$SFR = 8.12\times10^{-28} L_\lambda\,[\mathrm{erg\,s^{-1}Hz^{-1}}]\,\mathrm{at}\,\lambda = 91.2\,\mathrm{nm}$$

and

$$SFR = 1.4\times10^{-28} L_\lambda\,[\mathrm{erg\,s^{-1}Hz^{-1}}]\,\mathrm{at}\,\lambda = 150\,\mathrm{nm\,and}\,\lambda = 280\,\mathrm{nm}\,.$$

Furthermore, Popescu et al. (2000) assumed that a fraction $y_{\rm UV}$ of the non-ionising UV is absorbed in star-forming complexes (e.g. HII regions). They fit the FIR SED to the observational data and find a value SFR = 3.5 $M_\odot$/yr and $y_{\rm UV} = 0.28$ for NGC 891. As per Popescu et al. (2000) we assume that the young stellar population has a scaleheight of $z_{\rm UV} = 90$ pc and a scalelength similar to that of the disk in the blue-band (i.e. $h_{\rm UV} = 5.67$ kpc). From the SFR - luminosity relations, using Eq. 4.2.3 and assuming $y_{\rm UV} = 0.28$ we calculate the stellar emissivity at wavelengths $\lambda = 91.2, 150$ and 280 nm:

$$L_s \left[\frac{\rm erg}{\rm s\,pc^3\,sr\,nm} \times 10^{29} \right] = \begin{cases} 2.45 & \text{for } \lambda = 91.2\,\text{nm}, \\ 5.25 & \text{for } \lambda = 150\,\text{nm}, \\ 1.51 & \text{for } \lambda = 280\,\text{nm}. \end{cases} \quad (4.2.7)$$

We now need to calculate the radiation field that dust would experience at each point in the galaxy NGC 891. To do this, we use the method described by Dasyra et al. (2005) (see also Misiriotis et al. 2006). Given the parameters of the stellar and dust distributions, we calculate the radiation field at a given point inside the galaxy taking into account both the effects of absorption and multiple scattering by dust and the subsequent re-emission at FIR/submm wavelengths.

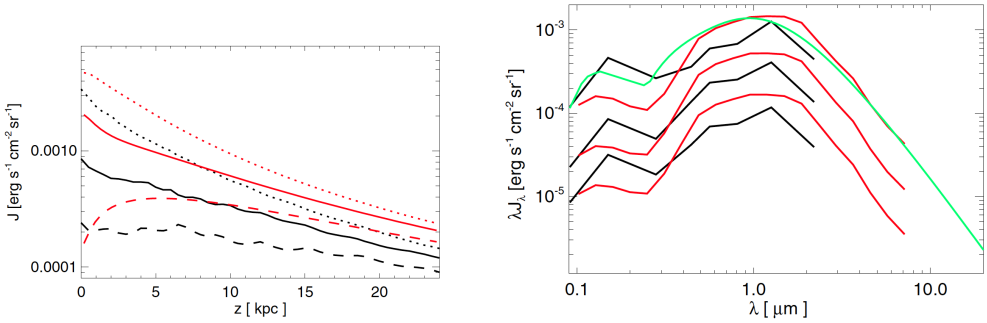

(a) (b)

Figure 4.10: (a) Integrated radiation field J [erg s^{-1} cm^{-2} sr^{-1}] as a function of the distance from the galactic plane for $R = 1, 2, 3\,h_{\rm s}$ (dotted, solid and dashed lines respectively) where $h_{\rm s} = 5.6$ kpc. (b) Spectral energy distribution of the radiation field λJ_λ for $R = 11$ kpc and for $z = 0, 8, 22$ kpc (from top to bottom). Red lines represent the radiation field obtained with the TRADING model, black lines represent the model described in this section and the green line represents the galactic radiation field in the solar vicinity obtained by Mathis et al. (1983) rescaled to have the same G_0 that we obtain in our model at (R [kpc], z [kpc]) = (11,0).

We compare our model with the more sophisticated TRADING model (Bianchi 2008; Bianchi and Xilouris 2011) based on Monte Carlo (MC) simulations. The TRADING model of NGC891 has been derived from the geometric properties and dust opac-

ities obtained by Xilouris et al. (1999). For the intrinsic stellar spectrum a template for an Sb galaxy was used, scaled to match available NIR/optical/UV fluxes. As per Popescu et al. (2000), an additional dust component was included to fit the observed FIR/submm SED. In the TRADING model, this component is in the form of an exponential disk distribution of spherical (molecular) clouds, heated internally by a UV-dominated radiation field from young stars. In Bianchi and Xilouris (2011) the model was fine-tuned to match both the global SED and the spatial distribution of the dust emission observed by the Herschel Space Observatory.

Fig. 4.10a presents the radiation field integrated over the wavelengths J [erg s^{-1} cm^{-2} sr^{-1}] as a function of the distance from the galactic plane, z, for a radial distance $R = 1, 2, 3\,h_{\rm s}$ (dotted, solid and dashed lines respectively) where $h_s = 5.6$ kpc. Red lines show the TRADING model results, black lines show the model described in this paper. We notice a different behaviour between the two models for the radiation field at $R = 3\,h_s$. This is due to the fact that in the TRADING model there is a cutoff in the stellar distribution at about $R = 13$ kpc which is necessary to fit the dust SED with the observations while in the model described in this paper we set a cutoff at $3\,h_{\rm d} \sim 24\,$kpc.

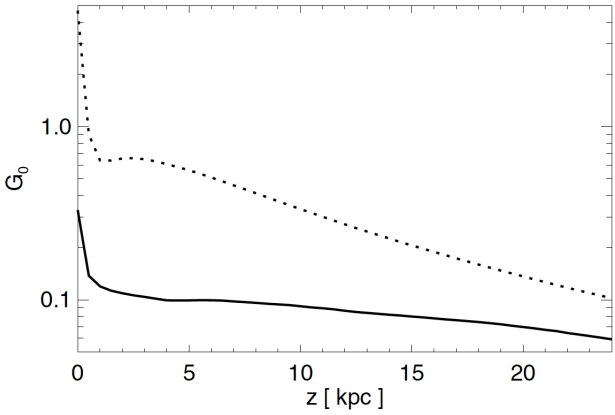

Figure 4.11: G_0 as a function of the distance from the galactic plane for a radial distance $R = 0$ kpc (dotted line) and $R = 22$ kpc (solid line) as calculated by our model.

Fig. 4.10b shows the spectral distribution of the radiation field λJ_λ (red lines: TRADING model, black lines: our model and green line: Mathis et al. 1983) for a radial distance $R = 2\,h_{\rm s} \approx 11$ kpc and for vertical distances $z = 0, 8, 22$ kpc (from top to bottom). In order to compare the radiation field that we calculate in this paper with the radiation field in the solar vicinity we use the parameter G_0:

$$G_0 = \frac{\int_{w_1}^{w_2} J_\lambda d\lambda}{\int_{w_1}^{w_2} J_{\rm Mathis,\,\lambda} d\lambda}, \tag{4.2.8}$$

where w_1 and w_2 are 91.2 and 207 nm, respectively, corresponding to photon energies of 13.6 and 6 eV. The value of G_0 at (R [kpc], z [kpc]) = (11,0) for our model is $G_0 = 1.47$. The green line in Fig. 4.10b refers to the radiation field in the solar vicinity but rescaled imposing the same G_0 calculated above. We notice that the shape of the radiation field in the solar vicinity is similar to the radiation field we calculate for NGC 891. In our model we compute the radiation field only up to the K band, while in the solar vicinity the radiation field is known up to $10^5 \mu$m. This does not affect the resulting SED since most of the emitted power is in the range 0.091 - 0.25μm.

In Fig. 4.11 we show the value of G_0 as a function of the distance from the galactic plane at a radial distance $R = 0$ kpc (dotted line) and $R = 22$ kpc (solid line) as calculated by our model.

4.2.3 PAH dissociation probability

As a consequence of the absorption of a photon or a collision with an electron, the internal energy of a PAH increases and this leads to the excitation of the entire molecule. The energy transferred to the molecule is spread over the vibrational modes and can lead to the dissociation of the molecule or to radiative relaxation.

In this study we are interested in the emission, for a given dust distribution, in different environments and for now we neglect time dependent effects. To do this, we estimate the probability that a PAH will dissociate before it can emit a sufficient amount of the absorbed energy as IR photons (dissociation probability). If this probability in a given environment is high then destruction dominates over radiative relaxation and we are unlikely to detect the emission from a PAH of this size in this environment. The dissociation probability varies with the size of the PAH. For large molecules the transferred energy can be spread over a larger number of vibrational modes and therefore the dissociation probability for a big molecule is lower than that for a smaller molecule. We set the probability threshold at 0.01. A molecule with a dissociation probability equal to the probability threshold will be the smallest molecule considered in the size distribution, molecules smaller than this are assumed to be quickly destroyed and unable to emit enough to be detected.

We use the approach developed by Micelotta et al. (2010b). What is important in this approach is that, for the grain that we consider, the time between two collisions is longer than the time needed to cool down. We verify this assumption in Section 4.2.5. We treat the problem in the microcanonical ensemble, the transferred energy, $E_{\rm tr}$, is related to the effective internal energy of the system, $E_{\rm eff}$, by:

$$E_{\rm eff} \simeq 0.17 \left(\frac{E_{\rm tr}({\rm eV})}{N_{\rm C}}\right)^{0.4} \left(1 - 0.2\frac{E_0({\rm eV})}{E_{\rm tr}({\rm eV})}\right) {\rm eV}\,, \tag{4.2.9}$$

where E_0 is the binding energy of the fragment, which we set equal to 4.6 eV as a standard value (Micelotta et al. 2010b)[2]. Then the unimolecular dissociation rate,

[2]The value E_0 is highly uncertain and is assumed $E_0 = 4.6$ eV by Micelotta et al. 2010b so that the lifetime for a 50 carbon atom PAH would survive for $\sim 10^6$ yr in the diffuse ISM.

$k_{\rm diss}$, written in Arrhenius form is given by:

$$k_{\rm diss} = k_0(E_{\rm eff}) \exp\left[-E_0/E_{\rm eff}\right] , \tag{4.2.10}$$

where k_0 has a weak dependency on the internal energy and in this calculation is considered constant and equal to $1.4 \times 10^{16}\,{\rm s}^{-1}$. As per Micelotta et al. (2010b), we consider that each emitted photon has an energy $\Delta\epsilon = 0.16\,{\rm eV}$ and that the maximum number of photons emitted scales with the number of carbon atoms, $N_{\rm C}$, in the PAH as $n_{\rm max} = N_{\rm C}/5$. Following Micelotta et al. (2010b), the drop in internal energy due to the emission radiative relaxation is given by

$$\frac{E_i}{E_{i-1}} = 1 - 0.4\Delta\epsilon/T_E, \tag{4.2.11}$$

where T_E is the maximum internal energy reached as a consequence of a collision and therefore the dissociation probability ratio is approximatively

$$\frac{p_i}{p_{i-1}} = \exp\left[\left(\frac{E_0}{E_{i-1}} 0.4 \frac{\Delta\epsilon}{\epsilon}\right)\right] . \tag{4.2.12}$$

In the case the PAH does not undergo another collision during the radiative relaxation, this leads to a total un-normalized dissociation probability (Micelotta et al. 2010b):

$$P(n_{\rm max}) = (n_{\rm max}+1)\frac{k_0 \exp(-E_0/E_{\rm av})}{k_{\rm IR}} , \tag{4.2.13}$$

where $P(n_{\rm max})$ is the total un-normalized dissociation probability after the ejection of $n_{\rm max}$ photons, the average temperature, $E_{\rm av}$, is chosen as the geometric mean ($E_{\rm av} = \sqrt{E_{\rm tr} \times E_{n_{\rm max}}}$), $E_{n_{\rm max}} = (E_{\rm tr} - n_{\rm max} \times \Delta\epsilon)$ and $k_{\rm IR}$ is assumed to be 100 photons ${\rm s}^{-1}$ (Jochims et al. 1994). We apply this method to put a lower limit on the dust population sizes for both photon and electron collisional heating.

Considering only photon heating in the solar vicinity, the transferred energy, $E_{\rm tr}$ is the energy of the single absorbed photon. For a given $E_{\rm tr}$ we can calculate the corresponding $P(n_{\rm max})$. We then need to average $P(n_{\rm max})$ over the Interstellar Radiation Field (ISRF) distribution as follows:

$$\overline{P(n_{\rm max})} = \frac{\int_0^{13.6\,{\rm eV}} P(n_{\rm max})_{E_{\rm tr}} J_{\rm ISRF}(E) dE}{\int_0^{13.6\,{\rm eV}} J_{\rm ISRF}(E) dE} . \tag{4.2.14}$$

This leads to a probability lower than 0.01 only for PAHs with $N_{\rm C} \gtrsim 30$, i.e. PAHs with $N_{\rm C} \lesssim 30$ do not survive, which is in agreement with previous estimates (Jochims et al. 1994). The calculation of smallest PAH that is not dissociated by a standard ISRF is not affected by the uncertainty on the E_0 parameter, i.e. $E_0 = 3.65, 4.6$ and 5.6 eV lead to approximately the same minimum PAH size.

We now consider electron collisional heating. In this case $E_{\rm tr} = \zeta(E)E$ and we need to average $P(n_{max})$ over the Maxwell-Boltzmann distribution, $f_{\rm M}(E)$:

$$\overline{P(n_{max})} = \int_0^\infty P(n_{\rm max})_{E_{\rm tr}} f_{\rm M}(E) dE \,. \tag{4.2.15}$$

For example, if we take a gas temperature $T_{gas} = 10^6 - 10^7$ K, the transferred energy is much higher than in the case of photon absorption and this method leads to a size limit of $N_{\rm C} \approx 200$. If we vary E_0 in the range 3.65 eV to 5.6 eV the minimum PAH size will be between 100 and 350 carbon atoms. We assume here the standard $E_0 = 4.6$ eV and therefore a minimum PAH size of 200 carbon atoms. This size limitation can be applied to both PAHs and hydrogenated amorphous carbon, a-C(:H), grains since the structure of the small a-C(:H) grains is very close to that of the PAHs, i.e. they are both highly aromatic (Jones 2012c). This number of carbon atoms corresponds to a PAH of radius $a \approx 0.77$ nm and an a-C:H grain of radius $a \approx 0.82$ nm with the density and the geometry (both PAHs and a-C:H grains considered as spherical) used in the Compiègne et al. (2011) dust model. As shown by Bocchio et al. (2012) the 2D and 3D grain approaches are equivalent up to radii as large as ≈ 5 nm.

4.2.4 Photon vs. electron collisional heating

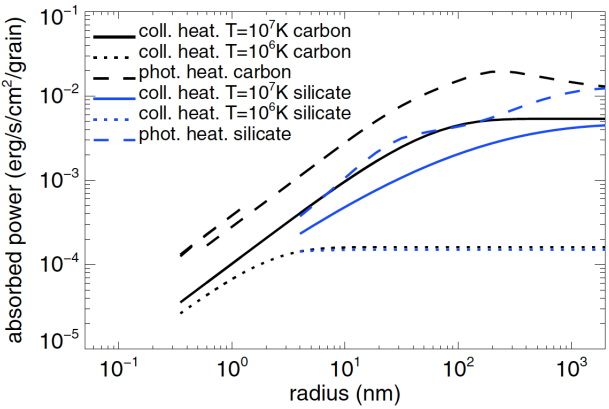

Figure 4.12: Power absorbed per unit area per grain due to photon and collisional heating at $z = 0$ and $R = 14$ kpc in NGC 891, where, according to our model, $G_0 = 1$. The collisional heating has been computed as if the plane of the galaxy was consisted of a hot gas with $T = 10^6$ and 10^7 K and for $n_{\rm H} = 10^{-3}$ cm^{-3}. In the three black lines there is a discontinuity around 1 nm because of the transition between PAHs and a-C:H grains.

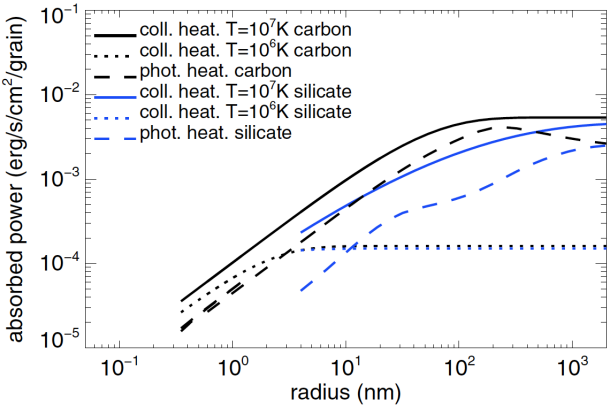

Figure 4.13: Power absorbed per unit area per grain due to photon and collisional heating at $z = 3.5$ kpc and $R = 22$ kpc in NGC 891, where, according to our model, $G_0 = 0.1$. The collisional heating has been computed for IGM gas with a temperature $T_{\rm gas} = 10^6$ and 10^7 K and a proton density $n_{\rm H} = 10^{-3}$ cm^{-3}. In the three black lines there is a discontinuity around 1 nm because of the transition between PAHs and a-C:H grains.

In this work we use the Compiègne et al. (2011) dust model where all of the molecules and grains are considered to be spherical. We compare the two dust heating processes: collisions with electrons and the absorption of photons. In Fig. 4.12 we show the absorbed energy per unit area per grain due to photon and collisional heating as a function of the grain/molecule radius. This plot refers to the point (R [kpc], z [kpc]) = (14,0) in the galaxy NGC 891 where, according to our model, $G_0 = 1$. The electron collisional heating has been calculated as if the plane of the galaxy contains only a hot gas with $T = 10^6 - 10^7$ K and $n_{\rm H} = 10^{-3}$ cm^{-3}. The discontinuity in the black lines around $a \sim 1$ nm is due to the transition between PAHs and a-C:H grains.

We notice that in the case of a gas temperature of 10^6 K the electron collisional heating for carbonaceous and silicate grains are very close to one other. This is because the peak of the Maxwell-Boltzmann distribution, corresponding to $T_{\rm gas} = 10^6$ K, is in the linear portion of the transferred energy function for both silicates and carbonaceous grains. This is not the case for $T_{\rm gas} = 10^7$ K, where the electron energy can be higher than the threshold of the transferred energy function. Furthermore, in the latter case, the electron collisional heating is less than an order of magnitude lower than the photon heating for each of the sizes.

From Fig. 4.11 we have that G_0 is about 0.1 at (R [kpc], z [kpc]) = (22,3.5). Therefore photon heating should be an order of magnitude lower than in the previous case and should be comparable with the collisional heating. Fig. 4.13 represents the power absorbed per unit area per grain due to both photon absorption and collisional

heating in the galaxy NGC 891 at (R [kpc], z [kpc]) = (22,3.5) where $G_0 \approx 0.1$. We notice that, in this region, the collisional heating is larger than the photon heating and therefore must be taken into account. Thus, at relatively large vertical distances above the plane of a galaxy, electron collisional heating could be as important, or more important than, photon heating. However, far from a galaxy, in the IGM, it is likely that dust may not survive long (e.g. Bocchio et al. 2012) and because of this we need to evaluate the gas and dust dynamics during the ram pressure stripping (see Chapter 7).

4.2.5 Updates to the DustEM code

The DustEM code is a numerical tool presented by Compiègne et al. (2011), which calculates the dust SED for a given dust model and given ISRF[3]. We have now included in DustEM the heating of dust due to collisions with electrons (see Appendix 4.A for details). The corresponding absorbed power (Eq. 4.2.1) is added to the photon heating power and the grain temperature distribution is derived using the method described by Désert et al. (1986).

Even if DustEM calculates the grain temperature distribution for each grain size, it is important to know if a grain of a given size in a certain environment is stochastically heated or is in thermal equilibrium. For example, to estimate the PAH dissociation probability in Section 4.2.3, we implicitly assumed that PAHs are not in thermal equilibrium but that they experience significant temperature fluctuations. First of all, we need to calculate the average time between the absorption of two photons, $\tau_{\rm abs}$, and the average time between two collisions with electrons, $\tau_{\rm coll}$. Then we need to compare these average times with the cooling time, $\tau_{\rm cool}$. If the cooling time is larger than the time between collisions or photon absorptions, then the grain will tend to thermal equilibrium, otherwise it will be stochastically heated.

The average time between the grain absorption of two photons is given by:

$$\tau_{\rm abs}^{-1} = \pi a^2 \int_0^\infty \frac{4\pi J_\lambda Q_\lambda \lambda}{hc} d\lambda \tag{4.2.16}$$

where $\pi a^2 Q_\lambda$ is the absorption cross section for a given wavelength λ. The average time between collisions with electrons is given by:

$$\tau_{\rm coll}^{-1} = \pi a^2 \sqrt{\frac{3 k_B T_{\rm gas}}{m_e}} n_{\rm H} \tag{4.2.17}$$

where m_e is the electron mass.

As a consequence of the absorption of the most energetic photons or the most energetic collisions with the electrons[4], the internal energy of a grain will increase and its temperature will reach the highest value $T_{\rm max}$. We define the cooling time as the

[3]http://www.ias.u-psud.fr/DUSTEM.

[4]The most energetic collisions with the electrons correspond, for a given size, to the maximum deposited energy i.e. the maximum of the transferred energy function $E\zeta(E)$.

time needed to cool down from the temperature $T_{\rm max}$ to a temperature where the radiative emission is negligible with respect to that at the highest temperature (see below). We calculate the highest temperature reached by a grain as a consequence of the injection (due to photon absorption or collisional heating) of an energy $E_{\rm in}$ by:

$$E_{\rm in} = \int_0^{T_{\rm max}} C(T_{\rm d}) dT_{\rm d}. \tag{4.2.18}$$

As given by Dwek (1986) we can write that, between two heating events, a grain cools at a rate:

$$\begin{aligned} dT_{\rm d}/dt &= L_{\rm d}/C(T_{\rm d}) \\ &= 4\pi a^2 < Q_{\rm abs} >_{T_{\rm d}} \sigma T_{\rm d}^4 / C(T_{\rm d}) \end{aligned} \tag{4.2.19}$$

where $L_{\rm d}$ is the the rate at which a dust particle radiates:

$$\begin{aligned} L_{\rm d} &= 4\pi a^2 \int_0^{\infty} \pi B_\lambda(T_{\rm d}) Q_\lambda(a) d\lambda \\ &= 4\pi a^2 \sigma T_{\rm d}^4 < Q_{\rm abs} >_{T_{\rm d}} \end{aligned} \tag{4.2.20}$$

with B_λ the Planck function, σ the Stefan-Boltzmann constant and $< Q_{\rm abs} >_{T_{\rm d}}$ the Planck-averaged value of $Q_\lambda(a)$. Following this approach, the cooling time can be written as:

$$\begin{aligned} \tau_0 &= \int_{T_{\rm i}}^{T_{\rm max}} dT_{\rm d} / |(dT_{\rm d}/dt)| \\ &= \int_{T_{\rm i}}^{T_{\rm max}} \frac{C(T_{\rm d}) dT}{L_{\rm d}} \end{aligned} \tag{4.2.21}$$

where $T_{\rm i}$ is the initial temperature of the grain ($T_{\rm i} = 0.1\,{\rm K}$ in the DustEM code). We note that this definition of the cooling time depends on the value of the minimum temperature of the grain and is dominated by the time spent close to the lowest temperatures. We therefore define the cooling time in this way:

$$\begin{aligned} \tau_{\rm cool} &= \int_{lnT_{\rm i}}^{lnT_{\rm max}} \frac{C(T_{\rm d}) T_{\rm d} L_{\rm d} \frac{dP}{dlnT_{\rm d}} dlnT_{\rm d}}{L_{\rm d} \int_{lnT_{\rm i}}^{lnT_{\rm max}} L_{\rm d} \frac{dP}{dlnT_{\rm d}} dlnT_{\rm d}} \\ &= \frac{\int_{lnT_{\rm i}}^{lnT_{\rm max}} C(T_{\rm d}) T_{\rm d} \frac{dP}{dlnT_{\rm d}} dlnT_{\rm d}}{\int_{lnT_{\rm i}}^{lnT_{\rm max}} L_{\rm d} \frac{dP}{dlnT_{\rm d}} dlnT_{\rm d}}, \end{aligned} \tag{4.2.22}$$

where $\frac{dP}{dlnT_{\rm d}}$ is the probability for a grain to be at a certain temperature. In this way, $\tau_{\rm cool}$ is weighted on the luminosity emitted by the grain, is not sensitive to the minimum temperature that we consider and represents the time needed for a grain to cool to a temperature where the radiative emission is negligible with respect to the radiative

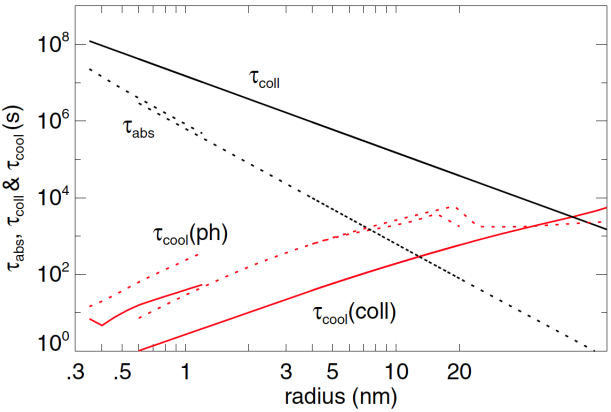

Figure 4.14: Photon absorption time ($\tau_{\rm abs}$), electron collision time ($\tau_{\rm coll}$) and cooling times ($\tau_{\rm cool}$(coll) and $\tau_{\rm cool}$(ph)) for carbonaceous grains as a function of radius for an assumed Compiègne et al. dust model and size distribution. In the case of photon absorption, we assume a radiation field with $G_0 = 1$, while in the case of electron collisions, $T_{\rm gas} = 10^7\,{\rm K}$ and $n_{\rm H} = 10^{-3}\,{\rm cm}^{-3}$ have been assumed. $\tau_{\rm cool}$(coll) represents the cooling time in the case of collisional heating only whilst $\tau_{\rm cool}$(ph) represents the cooling time in the case of photon absorption only. The discontinuity between 0.6 nm and 1.2 nm in the red lines is because of the transition between PAHs and a-C:H grains.

emission at the maximum temperature. If we consider the electron collisional heating only we call the cooling time $\tau_{\rm cool}(coll)$, while if only the photon heating is present we call the cooling time $\tau_{\rm cool}(ph)$.

In Fig. 4.14 we show $\tau_{\rm coll}$, $\tau_{\rm abs}$, $\tau_{\rm cool}(coll)$ and $\tau_{\rm cool}(ph)$. There is a discontinuity in the cooling time at a size of about $a \approx 1\,{\rm nm}$ because of the transition between the assumed PAHs and a-C(:H) grains in the Compiègne et al. (2011) dust model (see Section 2.4). The other two small discontinuities at $a \approx 4\,{\rm nm}$ and $a \approx 20\,{\rm nm}$ are due to small differences in the adopted size distributions (power law and log normal) of a-C(:H) grains. We notice that for a grain of about $a_1 \approx 7\,{\rm nm}$, the cooling time, in the case of photon heating only, equals the absorption time. This means that, if we assume no collisional heating, grains with radii smaller than a_1 are stochastically heated, while larger grains tend to be in thermal equilibrium. If we consider the electron collisional heating only, the intersection between the two curves corresponds on a grain radius $a_2 \approx 27\,{\rm nm}$. When both processes occur, the average cooling time is very similar to the cooling time in the case of photon heating only, because the collision with an electron, for each of the grain sizes, is much rarer than the absorption of a photon. The average time between two events (be they electron collisions or photon absorption) can

be calculated as follow (if they are independent, which is the case here):

$$\tau_{\rm event} = \left(\frac{1}{\tau_{\rm abs}} + \frac{1}{\tau_{\rm coll}} \right)^{-1} . \tag{4.2.23}$$

Since electron collisions are much rarer than photon absorptions $\tau_{\rm event} \approx \tau_{\rm abs}$ and therefore the intersection between the two lines corresponding to the cooling time, and average time between two events, would be at around $a_{\rm both} \approx 7\,{\rm nm}$. In Section 4.2.3 we made the assumption that a-C:H grains smaller than $N_{\rm C} \approx 200$ (corresponding to $a_{\rm a-C:H} = 0.77\,{\rm nm}$) were stochastically heated. We therefore confirm that this assumption is valid.

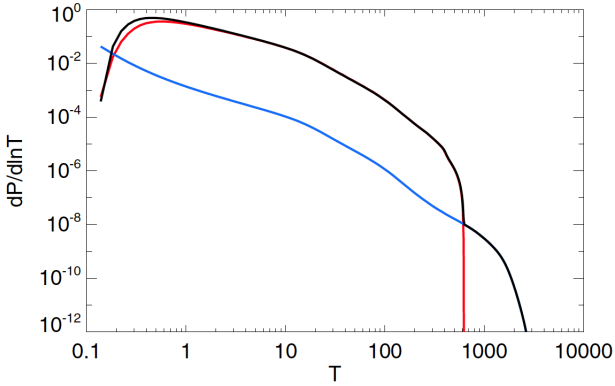

Figure 4.15: $dP/dlnT$ (probability for a grain to be at a certain temperature) in the case of a stochastically-heated PAH molecule (radius $a = 0.77\,{\rm nm}$) assuming a gas temperature $T_{\rm gas} = 10^7\,{\rm K}$, a gas proton density $n_{\rm H} = 10^{-3}\,{\rm cm}^{-3}$ and $G_0 = 1$. We notice that the probability distribution in the case of dust heating due to both collisions and photon absorption (black line) is, for most of the temperatures, the sum of the probability distribution due to only photon heating (red line) and the probability distribution due to collisional heating (blue line).

Using DustEM we obtain the dust temperature distribution for each grain size. We consider a small PAH ($a = 0.77\,{\rm nm}$) and compare the temperature distribution in the case of photon heating, collisional heating or both processes. As we can see in Fig. 4.14 such a grain is stochastically heated in all cases. This is confirmed by the shape of the temperature distributions in Fig. 4.15, which shows the probability for a grain to be at a certain temperature (dP/dlnT) with respect to the range of temperatures that the grains can assume. We assume a gas temperature $T_{\rm gas} = 10^7\,{\rm K}$, a gas proton density $n_{\rm H} = 10^{-3}\,{\rm cm}^{-3}$ and $G_0 = 1$. We notice that, for most temperatures, we have: dP/dlnT (collision + photon) = dP/dlnT (collision) + dP/dlnT (photon).

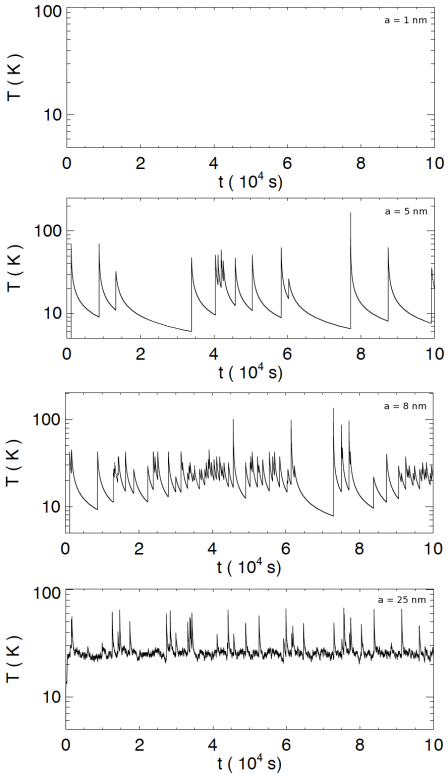

Figure 4.16: Temperature fluctuations as a function of the time for carbonaceous grains of different sizes as irradiated by the standard radiation field ($G_0 = 1$) and embedded in a hot gas with temperature $T_{\rm gas} = 10^7\,{\rm K}$ and density $n_{\rm e} = 10^{-3}\,{\rm cm}^{-3}$.

Fig. 4.16 shows the corresponding temperature evolution during a day ($\sim 10^5\,{\rm s}$) as a function of time for a-C(:H) grains of different sizes as heated by the standard ISRF ($G_0 = 1$) and by the collisions with energetic electrons ($T_{\rm gas} = 10^7\,{\rm K}$, $n_{\rm H} = 10^{-3}\,{\rm cm}^{-3}$). During a day the smallest grains do not undergo any temperature fluctuations and their temperature is lower than 5 K, while larger grains, as a consequence of a collision with an electron or the absorption of a photon undergo an increase in temperature followed by radiative cooling. For the given gas conditions, the energy transferred during a collision with an electron is larger than that due to photon absorption therefore leading to a higher grain temperature. Furthermore, the typical timescale between two collisions with electrons is longer than that between the absorption of two photons. This is clear in the case of a 25 nm grain: photon absorption leads to small temperature fluctuations, while electron collisions are responsible for the high spikes visible in Fig. 4.16.

Even a 25 nm grain is therefore not in thermal equilibrium in a hot gas, and only large grains have a sufficient large cross-section to have more frequent electron collisions and be in thermal equilibrium.

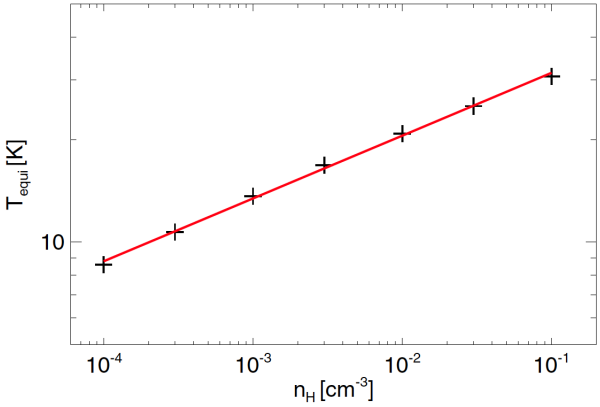

Figure 4.17: Equilibrium temperature, $T_{\rm equi}$, with respect to the proton density, $n_{\rm H}$, for a gas temperature $T_{\rm gas} = 10^7$ K and for a grain of radius a =320 nm, heated only by electron collisions. The black plus signs have been obtained with DustEM and the red line is the straight line fit to these values ($T_{\rm equi} \propto n_{\rm H}^{0.184}$).

If we now consider a grain that is large enough to be in thermal equilibrium with collisional heating only, then in this case we can analytically calculate the equilibrium temperature, equating the rate of absorbed energy H (see Eq. 4.2.1), to the rate at which a dust particle radiates, $L_{\rm d}$ (see Eq. 4.2.20). If we assume $Q_\lambda \sim \lambda^{-\beta}$, where β is the opacity power law index (in our case $\beta \approx 1.55$, see Compiègne et al. 2011), the predicted equilibrium temperature is:

$$T_{\rm d} \sim \left(\frac{n_{\rm H} < v(E)\zeta(E)E >}{4\sigma} \right)^{\left(\frac{1}{4+\beta}\right)} \tag{4.2.24}$$

where the averaging is over the Maxwell-Boltzmann distribution. We consider for example a grain of radius $a = 0.32\,\mu$m and look at the equilibrium temperature for $n_{\rm H} = 10^{-4} - 10^{-1}\,{\rm cm}^{-3}$. We can fit the obtained values with a power law and obtain:

$$T_{\rm equi} \propto n_{\rm H}^{0.184} \tag{4.2.25}$$

In Fig. 4.17 we show the equilibrium temperature with respect to the proton density of the gas. The black plus signs represent the values obtained with DustEM (with the method described by Désert et al. 1986) while the red line is the fit to these values given by Eq. 4.2.25. The value of the exponent, $\gamma_{\rm DustEM} = 0.184$, is close to what we would expect analytically, $\gamma_{th} = (4 + 1.55)^{-1} = 0.180$, they differ by only 2%. This

small difference can be explained by the fact that DustEM considers a temperature distribution rather than single equilibrium temperature and the parameter β is not exactly 1.55 as assumed in the analytical approximation.

4.2.6 Results

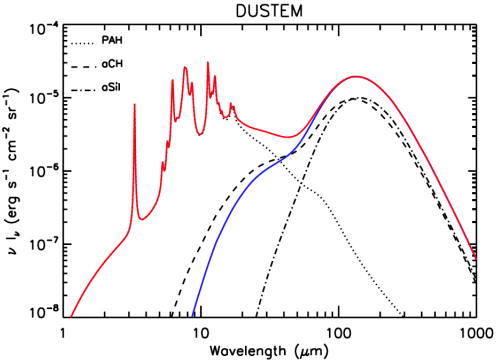

Figure 4.18: Dust SED for $G_0 = 1$ in the region (R [kpc], z [kpc]) = (14,0) in the galaxy NGC 891 for an assumed column density $N_{\rm H} = 10^{20}\,{\rm cm}^{-2}$. The red and blue lines represent the SED due to photon heating only, with (blue line) and without (red line) the size limitation at $a_{\rm min} = 2\,{\rm nm}$ caused by the presence of a gas at $T_{\rm gas} = 10^7\,{\rm K}$ and $n_{\rm H} = 10^{-3}\,{\rm cm}^{-3}$. Black lines represent the various contribution to the SED shown by the red line.

We apply the present model to the region (R [kpc], z [kpc]) = (14,0) in NGC 891 where, following the method described above, $G_0 = 1$. We consider here two cases: (A) a standard dust distribution heated by photon absorption only and (B) dust affected by the presence of a hot gas $(T_{\rm gas}, n_{\rm H}) = (10^7\,{\rm K}, 10^{-3}\,{\rm cm}^{-3})$. In the second case we assume a minimum grain size of 2 nm (under these conditions a 2 nm carbonaceous grain is destroyed in a timescale of $\sim 10^4\,{\rm yr}$) and later discuss the variability of the dust SED due to the minimum grain size. In Fig. 4.18 illustrates the dust SED calculated with DustEM due to only photon heating without (red line) and with (blue line) the size limitation (in the PAH and a-C:H size distributions) at $a_{\rm min} = 2\,{\rm nm}$ (added to show the destructive effect in the case of the presence of a hot gas). The silicate grains considered in the Compiègne et al. (2011) model are big enough ($a_{\rm (min,\,sil.)} = 4\,{\rm nm}$) to be unaffected by destruction during heating so no change in the lower limit of the size distribution has been imposed on this population.

The black lines show the different contributions to the SED calculated without any size limitation. The black dash-dotted line represents the contribution to the SED coming from silicate grains, the dotted line represents the contribution due to PAH

emission, the dashed line represents the contribution from the a-C:H grains while the red line represents the total dust SED. Including electron collisional heating in this case would not affect the result, as it is negligible with respect to the photon heating (see Fig. 4.12). We note that the size limitation that we impose on the PAHs and a-C:H grains has a major effect on the emission features, in particular the intensity of the peak at 3.3μm is decreased dramatically (blue line).

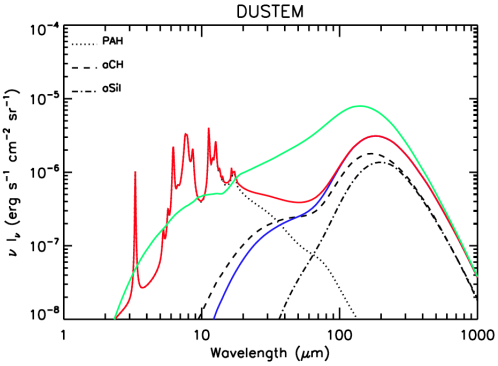

Figure 4.19: Dust SED for $G_0 = 0.1$, in the region (R [kpc], z [kpc]) = (22,3.5) in the galaxy NGC 891. The red and blue lines represent the SED due to photon heating only, with (blue line) and without (red line) the size limitation at $a_{\rm min} = 2\,$nm. The green line represents the SED due to both photon and collisional heating with the size limitation at $a_{\rm min} = 2\,$nm (we assume the totality of the dust as embedded in the hot gas). Black lines represent the various contribution to the SED shown by the red line. We assume the same column density and gas properties as in Fig. 4.18.

Fig. 4.19 shows the SED in the region (R [kpc], z [kpc]) = (22, 3.5) in the galaxy NGC 891. Following our method, in this region we have a radiation field with $G_0 = 0.1$. The red line shows the SED in the case of photon heating only and with no evolution of the smallest particles. The blue line shows the SED due to only photon heating as in the case of the red line but we here impose a cut in the size distribution at $a_{\rm min} = 2\,$nm given by the destructive effect of a hot gas. The green line shows the SED as in the case of the blue line but with the addition of electron collisional heating, as in the case of an IGM gas ($T_{\rm gas}$, $n_{\rm H}$) = ($10^7\,$K, $10^{-3}\,$cm^{-3}). The black lines represent the contributions to the red line.

Comparing the green and blue lines in Fig. 4.19 it is clear that the short wavelength emission ($\lambda < 10\mu$m) from a hot tenuous gas with low G_0 can come only from the electron collisional heating of larger grains ($a > 2\,$nm), or equivalently we can say that the ISRF does not have sufficiently high energy photons to heat small grains to high enough temperatures to produce this short wavelength emission. Also, the mid- and far-IR emission are significantly enhanced by the inclusion of electron collisional

heating.

Since the value of $a_{\rm min}$ depends not only on the properties of the gas where dust is embedded, but also on the dynamics of dust in this medium, we plot in Fig. 4.20 the resulting dust SED (for $G_0 = 0.1$, $T_{\rm gas} = 10^7$ K and $n_{\rm H} = 10^{-3}\,{\rm cm}^{-3}$) for different values of $a_{\rm min}$, ranging from 0.77 to 5 nm. We note that the dust SED presents PAH features only for $a_{\rm min} = 0.77$ nm because the other values of $a_{\rm min}$ are larger than that of the PAHs in our model.

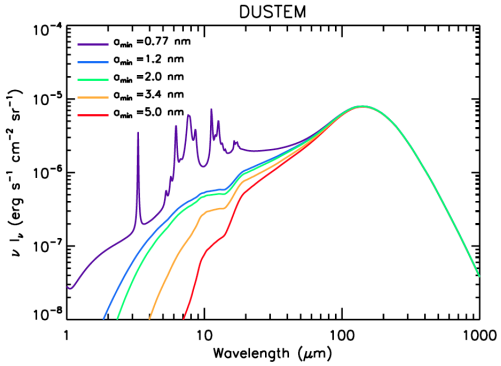

Figure 4.20: Dust SED due to both photon ($G_0 = 0.1$) and electron collisional heating ($n_{\rm H} = 10^{-3}\,{\rm cm}^{-3}$, $T_{\rm gas} = 10^7$ K) for different values of $a_{\rm min}$.

4.2.7 Astrophysical implications

From this work it is clear that the inclusion of electron collisional heating and the destruction of the smallest grains/molecules (Section 4.1, Micelotta et al. 2010a,b; Bocchio et al. 2012, 2013b) lead to significant changes in the shape of the IR-mm SED (green and red lines in Fig. 4.19). The most obvious effect is the complete loss of the aromatic emission bands, in the 3-20 μm wavelength region, due to the destruction of the PAHs. Here this effect is modeled by increasing the minimum grain radius to 2 nm, which is larger than that of PAHs in the Compiègne et al. model.

The next most obvious effect of including electron collisional heating, in a low density and weak radiation field environment, is a shift in the peak wavelength of the big grain emission, from $\sim 200\,\mu$m (T $\sim$ 15 K) to $\sim 130\,\mu$m (T $\sim$ 23 K), and the appearance of the emission bands at 10 and 18 μm due to small, hot silicate grains.

We also note that there is an important change in the slope of the dust SED between 70 μm and 100 μm, which is not strongly affected by small grain size cut-off in our model. We have calculated the PACS 70 μm to 100 μm band ratio, $I_{70/100}$, as a function of G_0 both with and without electron collisional heating. In Fig. 4.21 we plot $I_{70/100}$ for the Compiègne et al. (2011) dust model (red lines) and the Draine and Li (2007)

dust model (blue lines) as a function of G_0. The gas proton density is kept constant at $n_H = 10^{-3}\,\mathrm{cm}^{-3}$, the solid lines represent the case where collisional heating and destruction are ignored (no gas), while the dotted lines and the dashed lines correspond to a gas temperature of $T_{\mathrm{gas}} = 10^7\,\mathrm{K}$ and $T_{\mathrm{gas}} = 10^8\,\mathrm{K}$, respectively. We note that the ratio $I_{70/100}$ is significantly affected by the presence of a hot gas for $G_0 = 0.1$. The introduction of dust heating and destruction arising from electron collisions in a hot gas leads to changes in $I_{70/100}$ that could be a good SED diagnostic signature of the presence of a hot gas and a weak radiation field ($G_0 \sim 0.1$). Furthermore we note that the two dust models predict very similar SEDs for wavelengths longer than $10\,\mu$m, i.e. they show the same behaviour (the red and blue lines in Fig. 4.21), with respect to G_0, therefore indicating the robustness of our results.

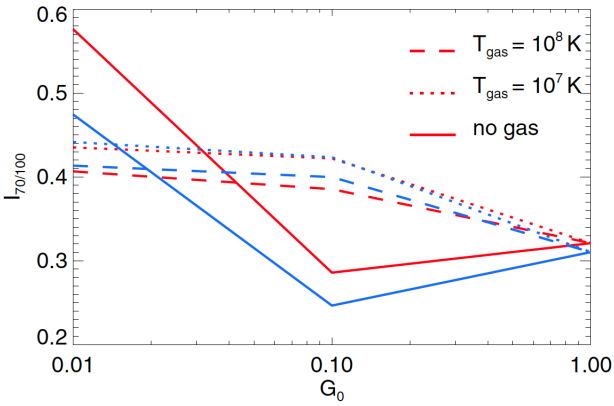

Figure 4.21: Ratio $I_{70/100}$ computed for the Compiègne et al. (2011) dust model (red lines) and for the Draine and Li (2007) dust model (blue lines). The gas proton density is kept constant at $n_{\mathrm{H}} = 10^{-3}\,\mathrm{cm}^{-3}$, the solid lines represent the case of the absence of collisional heating and destruction, while the dotted lines and the dashed lines correspond to a gas temperature of $T_{\mathrm{gas}} = 10^7\,\mathrm{K}$ and $T_{\mathrm{gas}} = 10^8\,\mathrm{K}$ respectively.

From Fig. 4.19 and 4.20 we notice that, regardless the value of a_{min} we choose in our model, there is a change in the slope between $24\,\mu$m and $70\,\mu$m. We have therefore calculated the MIPS $24\,\mu$m to PACS $70\,\mu$m band ratio ($I_{24/70}$) for different G_0 and we plot this in Fig. 4.22 for the Compiègne et al. (2011) dust model and the Draine and Li (2007) dust model. We use the same style-color code as in Fig. 4.21. Since in the case of a hot gas electron collisions also destroy the small grains, we therefore calculated the ratio $I_{24/70}$ for the different values of a_{min} shown in Fig. 4.20. This range of possible values of a_{min} gives rise to a variability of the ratio $I_{24/70}$ of $\pm\,50\%$, which is shown in Fig. 4.22 by the two shaded regions (light blue for $T_{\mathrm{gas}} = 10^7\,\mathrm{K}$ and orange for $T_{\mathrm{gas}} = 10^8\,\mathrm{K}$). Despite the variability of $I_{24/70}$ for low G_0, this band ratio could be, together with $I_{70/100}$, a good SED diagnostic signature of the presence

of a hot gas acting on dust grains through both electron collisional heating and dust destruction.

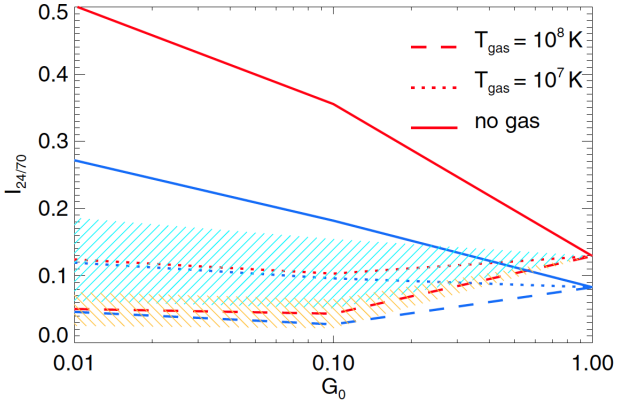

Figure 4.22: Same as Fig. 4.21 but for the ratio $I_{24/70}$. The two shaded regions represent the variability in the ratio $I_{24/70}$ due to the uncertainty on $a_{\rm min}$ (see Fig. 4.20) for our model.

It is clear that PAH-sized particles ought to be destroyed in a hot gas through collisions with energetic ions and electrons on timescales of the order of 10^4 yr (see Section 4.1). Given that this time-scale is so short the aromatic band emission from the outer regions of the entrained clumps will be of extremely limited spatial extent and therefore hard to detect (Micelotta et al. 2010b). Therefore any observation of the aromatic emission bands in the SEDs of dust in the IGM local to galaxies would imply very large quantities of dust and gas embedded within entrained dense clumps immersed in the hot gas. These clumps will probably be in pressure equilibrium with the coronal-type IGM gas ($n_{\rm H}T \sim 10^4\,{\rm K\ cm^{-3}}$) if they have densities and temperatures of either the warm inter-cloud medium or the cold neutral medium of the galaxy. However, dynamical processes such as conduction or ablation in the outflowing gas will lead to their eventual evaporation. Any aromatic band emission should therefore come from the shells or halos around embedded clumps, the thickness of which will depend upon the local dynamical conditions and so it is difficult to generalize on the observability of aromatic emission bands in the IGM. Nevertheless, if we consider a dense clump in pressure equilibrium with the hot coronal-type IGM gas ($n_{\rm H}T \sim 10^4\,{\rm K\ cm^{-3}}$) we can estimate the lifetime of small grains for different shell conditions around dense clumps with $T_{\rm clump} = 10^2\,{\rm K}$ and $n_{\rm H} = 10^2\,{\rm cm^{-3}}$. In Fig. 4.8 we plot the lifetime of grains as a function of size for different gas temperatures. Note that since the shells are assumed to be in pressure equilibrium with the IGM gas, fixing the temperature in a given shell, fixes the proton density as well.

We find that emission from grains smaller than $2-3\,{\rm nm}$ will be difficult to detect

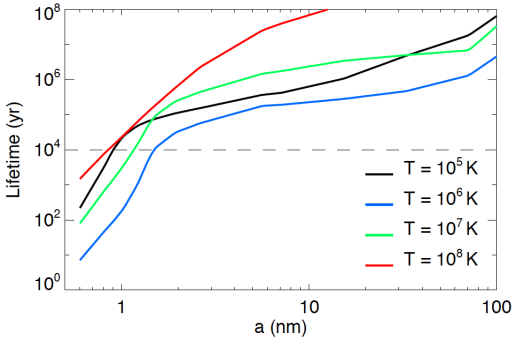

Figure 4.23: Lifetime of carbonaceous grains as a function of the grain size for different gas temperatures. The dashed horizontal line at 10^4 yr represents the threshold for observability.

in the IGM near and far from galaxies because the small particle destruction time is rather short. On the other hand, if we assume that in order to be observable a grain must have a lifetime $> 10^4$ yr, then, in the lower density evaporating regions around entrained clumps, emission from grains larger than $2-3$ nm ought to be observable in a gas with $n_{\rm H}T \sim 10^4$ K cm^{-3}. We note that shells with $T_{\rm gas} < 10^5$ K the dust lifetime is $\gg 10^8$ yr. Furthermore, if the evaporation dynamics of these dense clumps is fast, as we clearly see from Fig. 4.23, then we could observe dust emission from larger grains ($a \gtrsim 3$ nm) even in a hot and diffuse gas at $T_{\rm gas} = 10^8$ K and $n_{\rm H} = 10^{-4}$ cm^{-3}.

4.3 Conclusions

We find that the PAH, or molecular, approach to hydrocarbon nano-particle erosion provides an excellent means of determining the processing of 3D particles with the same number of carbon atoms. This approach indicates that electronic interactions and electron collisions are important for particles with fewer than about 1000 carbon atoms and must be taken into account in determining hydrocarbon nano-particle life-times in a hot gas.

From our study it appears that hydrocarbon nano-particles (with $N_{\rm C} < 1000$ or $a < 3$ nm) cannot be abundant in a hot coronal-type gas, be it galactic HIM or nearby IGM (e.g. $t_{\rm dest} \leqslant 10^6$ yr for $T = 10^6 - 10^7$ K and $n_{\rm H} = 10^{-3}$ cm^{-3}). Thus, it is to expected that any dust emission coming from the HIM of a galaxy or from the IGM in the close proximity of a galaxy must be dominated by emission from large hydrocarbon grains with life-times $> 10^8$ yr (see Eq. 4.1.20), with radii $\gtrsim 100$ nm, or perhaps more likely from amorphous silicate grains that appear to be more resistant to thermal sputtering than carbonaceous dust (*e.g.*, Jones et al. 1996). We have not re-evaluated

the effects of amorphous silicate thermal sputtering here but, in the light of important small particle sputtering effects apparent in hydrocarbon dust (Serra Díaz-Cano and Jones 2008), the size-dependent sputtering effect will need to be carefully evaluated for amorphous silicate dust as well.

Furthermore, in such a hot medium, the processes of thermal sputtering and collisional heating are coupled and dramatically affect the dust SED.

In the case of a hot and tenuous gas with $(n_{\rm H},\, T_{\rm gas}) = (10^{-3}\,{\rm cm}^{-3},\, 10^{7}\,{\rm K})$, the power absorbed per grain is comparable to that due to photon heating in a region where $G_0 \approx 0.1$. In this environment, due to energetic collisions with ions and electrons, small grains are destroyed on short timescales. Conservatively, we set the size distribution lower limit to $a = 2\,{\rm nm}$ but we do explore the changes in the SED due to the uncertainty of this parameter. This change in the size distribution, together with the extra energy input due to electron collisions, leads to important differences in the mid- and far-IR part of the SED. In particular, including electron collisional heating leads to an enhancement in the ratio $I_{70/100}$ with respect to the case of photon heating only in weak radiation fields (with $G_0 = 0.1$).

In our model we treated the problem in a stationary way: in the case of the presence of a hot gas, we derive a lower limit to the size distribution, which is determined by the radius where the grains are too small to survive long enough to be detected. However, a full analysis really needs to take into account the time dependency of the dust population evolution, which can be calculated at each instant using the destruction rates given in Section 4.1, and the relevant dust dynamics.

In the case of ram pressure stripped galaxies, our results for the electron collisional heating and collisional destruction represent an upper limit because we assumed that dust was embedded in the IGM gas. In reality the dust could be embedded in a gas which is a mix of IGM gas and HI gas ejected from the stripped galaxy. Therefore a detailed analysis of the dynamics of dust and gas coupling resulting from extragalactic halo formation during ram pressure stripping needs to be undertaken on a case by case basis.

4.A Upgrades to DustEM

In the DustEM model version 4.0, the only source of heating is the absorption of photons. As we have seen, in the IGM, electron collisional heating can play an important role and can be also more important than the photon heating.

In addition to the already present photon heating we implemented an electron collisional heating routine (*DM_get_collheat*) in the model. In this routine we evaluate the power absorbed per grain due to collisions between grains and electrons as described in Section 4.2.1.

The routine *DM_get_collheat* is then called in the routine *DM_get_tdist*, responsible for the calculation of the temperature distribution. This latter routine has been changed in order to take into account the electron collisional heating and the fact that

the total power absorbed per grain is the sum of photon and collisional heating.

In the routine *DM_get_collheat*, the variable called *nbrpho* represents the rate of the absorbed photons multiplied by their energy. We created an equivalent variable called *nbrcoll* which is expressed by:

$$nbrcoll(E) = n_{\rm e} v(E) f_{\rm M}(E) \zeta(E) E \tag{4.A.1}$$

where $n_{\rm H}$ is the gas number density, $v(E)$ the velocity of the impinging electrons, $f_{\rm M}(E)$ the Maxwell-Boltzmann distribution and $\zeta(E)E$ the fraction of energy deposited in the grain.

In the routine *DM_get_tdist* the variable *hnumax* represents the maximum energy that can be absorbed by a grain. If we consider only the photon absorption, the energy of the hardest photons in a HI region is 13.6 eV. In the case of electron collisional heating, this value can be much larger. We modified the variable *numax* in order to be the maximum between 13.6 eV and the energy of the most energetic electrons.

In the routine *DM_get_tdist*, to make the program faster, we distinguish between stochastic heating and thermal equilibrium of dust grains. In Section 4.2.5 we compared the average time between two events (be they the absorption of photons or collisions with electrons) and the cooling time. When the cooling time starts to be longer than the average time between two events the grain is in a transition between stochastic heating and thermal equilibrium but it is still considered as stochastically heated by the routine *DM_get_tdist*. Then, when the cooling time is much longer than the average time between two events, it is considered to be in thermal equilibrium. This condition is modelled in the following way: if $(U_{\rm equi} - h\nu_{\rm max}) > U_{\rm min}$ is satisfied then the grain is in thermal equilibrium. $U_{\rm equi}$ is defined as the internal energy when the grain is in thermal equilibrium and $U_{\rm min}$ is the internal energy corresponding to the grain at a temperature equals to the CMB temperature. This is valid since the only source of heating is the photon absorption. After the addition of the collisional heating we changed this condition in this way: $(U_{\rm eq} - E^*) > U_{\rm min}$, with $E^* = n\_pho\_int * 13.6\,{\rm eV} + n\_el\_int * max(transf)$. We define:

$$n\_pho\_int = \frac{1}{h} \int_0^{\infty} n_{\rm e} v(E) f_{\rm M}(E) \zeta(E) E dE \tag{4.A.2}$$

$$n\_el\_int = \frac{1}{h} \int_{\nu_{\rm min}}^{\nu_{\rm max}} Q_{\rm abs} J_\nu d\nu \tag{4.A.3}$$

and $max(transf)$ as the maximum transferred energy due to collisional heating.

Finally, the number of points used for the characterization of the temperature distribution has been changed to 400, instead of 200, when we take into account collisional heating. This slows the program a little but allows us to derive the correct temperature distribution for the largest absorbed energies.

4.B Collisional cascade model

Grains are modeled as cubes where the carbon atoms occupy fixed positions. We consider an a-C(:H) grain with $N_{\rm C} = 1000$, density $\rho = 1.4\,{\rm g\ cm^{-3}}$ and mean atomic mass $M = 7.6$ (Serra Díaz-Cano and Jones 2008). Its molar volume, $V_{\rm m}$, is given by

$$V_{\rm m} = \frac{M}{\rho}. \tag{4.B.1}$$

Then, the volume, V, of the cube containing $N_{\rm C}$ carbon atoms can be expressed as

$$\begin{aligned} V &= \frac{N_{\rm C} V_{\rm m}}{N_{\rm A}} \\ &\sim 9 \times 10^{-21}\,{\rm cm^{-3}} \end{aligned} \tag{4.B.2}$$

with $N_{\rm A}$ the Avogadro's number. We then obtain that each side of the cube is $\sim 20\,$Å wide and that the mean interatomic distance is $\sim 2\,$Å. We dispose the carbon atoms as shown in Fig. 4.24a and treat them as hard spheres.

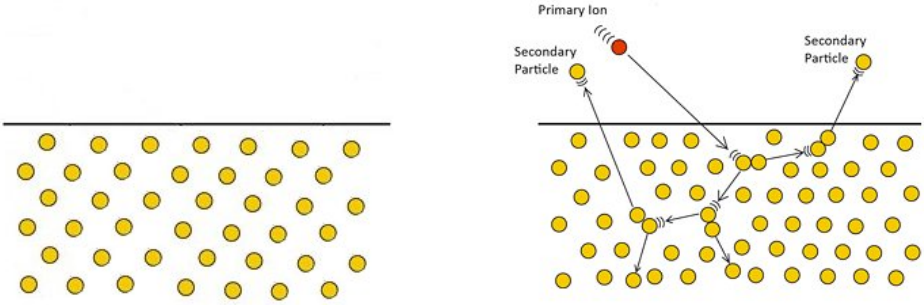

(a) (b)

Figure 4.24: Vertical cut of the assumed grain lattice. (a) Unperturbed and (b) after the collision with an impinging proton.

As initial projectile we take a proton with an energy distribution given by the Maxwell-Boltzmann energy distribution for a gas temperature $T_{\rm gas} = 10^7\,$K. The proton (H^+ particle) hits a carbon atom on the top of the grain with a given angle with respect to the normal incidence and, if its energy is sufficiently high, then it will trigger a collisional cascade (a series of binary collisions) in the cube. For each collision we calculate the energy transfer cross section, $\sigma(E)$. Following Micelotta et al. (2010b), we first calculate the energy-dependent nuclear cross-section. This quantity can be expressed as a function of the Lindhard's reduced energy ϵ and the reduced nuclear

stopping cross section $s_{\rm n}(\epsilon)$ (**?**). The Lindhard's reduced energy can be written as:

$$\epsilon = \frac{M_2}{M_1+M_2}\frac{a}{Z_1 Z_2 e^2}E \tag{4.B.3}$$

where M_1 and Z_1 are the mass and atomic number of the incident particle, M_2 and Z_2 the mass and atomic number of the target particle, e the electron charge, E the kinetic energy of the incident particle and a the screening length. We adopt here the Universal Ziegler-Biersack-Littmark (ZBL) screening length $a_{\rm U}$ (Ziegler and Biersack 1985):

$$a_{\rm U} \simeq 0.885 a_0 \left(Z_1^{0.23}+Z_2^{0.23}\right)^{-1} \tag{4.B.4}$$

where $a_0 = 0.529\,\text{Å}$ is the Bohr radius. We then adopt the ZBL reduced nuclear stopping cross section $s_{\rm n}^{\rm U}$ (Ziegler and Biersack 1985), which is an analytical approximation to the numerical solution that well reproduces the experimental data:

$$s_{\rm n}^{\rm U}(\epsilon) = \begin{cases} \frac{0.5\ln(1+1.383\epsilon)}{\epsilon+0.01321\epsilon^{0.21226}+0.19593\epsilon^{0.5}} & \epsilon \leq 30, \\ \frac{\ln\epsilon}{2\epsilon} & \epsilon > 30. \end{cases} \tag{4.B.5}$$

and the nuclear stopping cross section can be expressed as

$$S_{\rm n}(E) = 4\pi a_{\rm U} Z_1 Z_2 e^2 \frac{M_1}{M_1+M_2} s_{\rm n}^{\rm U}(\epsilon) \tag{4.B.6}$$

After some algebra (Micelotta et al. 2010a, Appendix A) the total energy transfer cross section results to be:

$$\sigma(E) = 4\pi a Z_1 Z_2 e^2 \frac{M_1}{M_1+M_2} s_{\rm n}^{\rm U}(\epsilon)\frac{1-m}{E}\frac{1}{\gamma E}\left[\left(\frac{E_{\rm m}}{m}\right)^{-m}-1\right] \tag{4.B.7}$$

where $\gamma = \frac{4M_1M_2}{(M_1+M_2)^2}$ and m is a quantity introduced by Ziegler and Biersack (1985):

$$m(E) = 1-\exp\left[-\exp\left[\sum_{i=0}^{5} a_i \left(0.1\ln\left(\frac{\epsilon(E)}{\epsilon_1}\right)\right)^i\right]\right] \tag{4.B.8}$$

with $\epsilon_1 = 10^{-9}$ and $a_i = -2.432, -0.1509, 2.648, -2.742, 1.215, -0.1665$. Since the collisional cross section between two spheres of radius r_1 and r_2 is given by

$$\sigma_{\rm coll} = \pi(r_1+r_2)^2 \tag{4.B.9}$$

we then assume that the 'radius' of the colliding atoms (assumed as hard spheres), $a_{\rm hard}$, is expressed as

$$a_{\rm hard} = \sqrt{\frac{\sigma(E)}{4\pi}}. \tag{4.B.10}$$

Then, using a Fortran routine[5] to solve the kinematics of a single collision between hard spheres in 3D we can predict the momentum and energy of the C target atom. If the transferred energy is larger than the threshold energy ($T_0 = 7.5\,\mathrm{eV}$)[6] then the target atom is displaced from its initial position in the lattice. We implemented this routine in our collisional cascade code and computed the number of ejected atoms from the grain for 1000 randomly chosen impact angles and projectile energies. We then calculate the average number of ejected atoms over the impact angles and over the Maxwell-Boltzmann energy distribution.

[5] http://www.plasmaphysics.org.uk/programs/coll3d_for.htm, T. Smid

[6] The value of the threshold energy in carbonaceous grains is unfortunately not well constrained experimentally nor theoretically. We choose a threshold energy $T_0 = 7.5\,\mathrm{eV}$ which is the standard value used by Micelotta et al. (2010a,b).

Chapter 5

Evidence for collisional heated dust?

Appreciation is born
through struggle.

Unknown

Contents

As seen in the previous chapter, a hot coronal-type gas represents an e xtreme environment for dust and the collision of fast ions and electrons in the gas with a grain leads to both destruction and heating (Tielens et al. 1994; Micelotta et al. 2010b,a; Bocchio et al. 2012, 2013b). With the tools developed in these papers we are

now able to directly compare the observed dust emission with that predicted by our models.

In normal, undisturbed galaxies dust is mostly embedded in the diffuse atomic and molecular gas where photon absorption is the main source of dust heating. On the other hand, in the case of galaxy-galaxy collisions, the mixing between the ISM and the hot IGM / ICM occurs and, at the interface between these two media, dust is mainly heated by collisions with the fast electrons in the gas. However, as predicted by dust destruction models (Tielens et al. 1994; Micelotta et al. 2010b,a; Bocchio et al. 2012) the lifetime of dust in such a harsh environment is rather short. This process then confines the dust to a thin interface region and therefore very good resolution is needed in order to observe dust destruction and heating in a hot gas. This chapter focuses on *Herschel* observations of a couple of astronomical sources and on the comparison between the modeled and observed IR-submm spectrum.

5.1 The Eyes Galaxies

The Eyes Galaxies (NGC 4438 and NGC 4435) are two galaxies in the Virgo Cluster, only about 1° ($\sim 300\,\mathrm{kpc}$) from the cluster centre. Fig. 5.1 shows the Very Large Telescope (VLT) V-band image of the two galaxies (north is up and west is right; we use this convention for all the images in this section): NGC 4438 to the south-east and NGC 4435 to the north. On the western side of NGC 4438 we note a diffuse light from stars displaced from the inner regions as well as a dark obscuration due to the presence of dust. The Eyes Galaxies are only $4'$ apart and because of this short distance, they are assumed to be in mutual interaction (Combes et al. 1988; Kenney et al. 1995; Vollmer et al. 2005). However, only NGC 4438 shows a perturbed stellar distribution (see Fig. 5.1), while NGC 4435 seems unperturbed. Moreover, the radial velocity of NGC 4435 is 700 km s^{-1} higher than that of NGC 4438 and it is probably not related to the disturbance of the latter (Kenney et al. 2008).

Kenney et al. (2008) presented the Hα+[NII] image of the region around M86 (Fig. 5.2). This image shows a filamentary structure connecting NGC 4438 and M86 suggesting a collision between the two galaxies $\sim 100\,\mathrm{Myr}$ ago. Furthermore, Kenney et al. (2008), measuring the radial velocity of the ISM, detected a velocity gradient between the two galaxies, supporting the idea of a collision. Other evidence for a collision between these two galaxies was shown by Gomez et al. (2010). Using *Herschel* SPIRE data in the region around M86 they found a large amount of dust ($M_\mathrm{d} \sim 10^6\,M_\odot$) outside the stellar distribution and spatially coincident with atomic and ionized hydrogen, indicating that it was probably stripped during the tidal interaction between these two galaxies. Furthermore, as a consequence of this violent event, the diffuse gas around NGC 4438, being less gravitationally bound to the bulk of the galaxy, is likely undergoing the effects of ram pressure (Vollmer et al. 2009).

The HI observations show an elongated feature on the western side of the galaxy with an extent of $\sim 9.8\,\mathrm{kpc}$ and a mass of $1.8 \times 10^8\,\mathrm{M}_\odot$ (Hota et al. 2007, Fig. 5.10a).

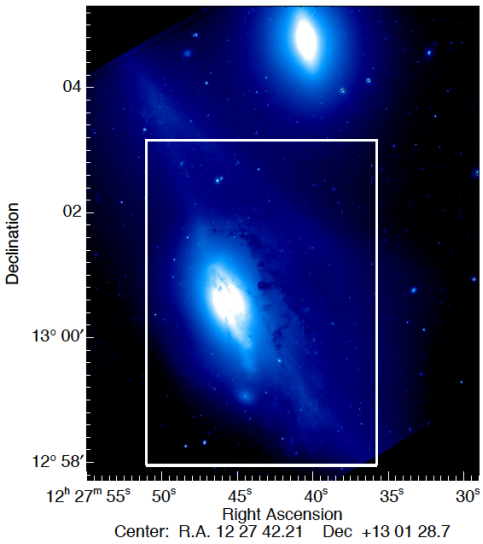

Figure 5.1: Credit: ESO. V-band image of NGC 4438 (centre) and NGC 4435 (top) taken by the FORS2 instrument on the Very Large Telescope. M86 lies outside the field, 20′ west from NGC 4438. The white rectangle shows the region that we use for our *Herschel* and multi-wavelength analysis. North is up, west is right.

The Chandra observations (Chandra ObsID 2883) show X-ray emission from a ~ 700 pc nuclear region, a ~ 2.3 kpc spherical bulge and a network of filaments extending 4-10 kpc to the west and southwest of the galaxy (Machacek et al. 2004, Fig. 5.10b). The *Herschel* SPIRE observations reveal the presence of extra-planar dust up to 4-5 kpc away from the galactic disk (Cortese et al. 2010a, Fig. 5.3). We use these images for a multi-wavelength study of this galaxy (Sect. 5.1.4).

The presence of an extended distribution of galactic interstellar medium outside the boundaries of NGC 4438, suggests that the mixing and interaction between the ISM and the ICM is ongoing. NGC 4438 is therefore an ideal test-case to study dust heating and destruction in the ICM close to interacting galaxies.

Furthermore, from a Chandra survey of nearby highly-inclined galaxies (Li and Wang 2013a,b) it has been shown that NGC 4438 is an unusually X-ray bright galaxy among their sample of 53 galaxies. They propose that this high X-ray radiation intensity may be the result of the cool ISM interacting with the hot ICM. We have analyzed the dust emission in regions outside of the galactic plane to test this interaction hypothesis.

However, dust in a hot gas is expected to be destroyed on short timescales and be confined in interphase regions. Using *Herschel* PACS/SPIRE data we have the unique possibility to achieve the sensitivity and the spatial resolution to measure the

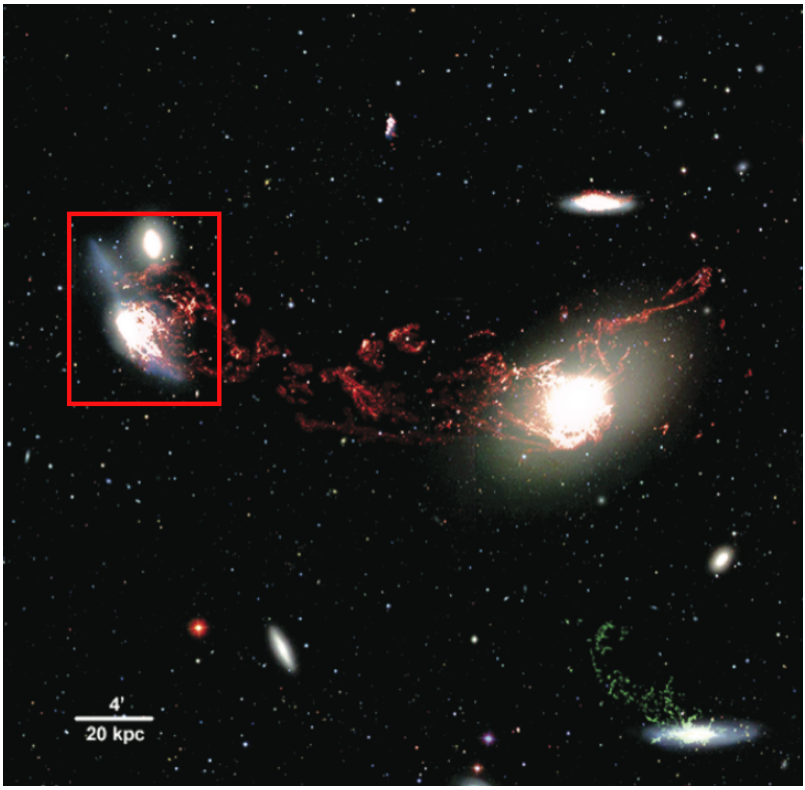

Figure 5.2: Hα+[NII] image of the M86 region superimposed on a color SDSS image (g, r and i filters). The ÒlowvelocityÓ ($< 500\,\mathrm{km\ s^{-1}}$) H$\alpha$+[NII] emission is colored red, and the ÒhighvelocityÓ ($> 2000\,\mathrm{km\ s^{-1}}$) H$\alpha$+[NII] emission is colored green. Kenney et al. (2008). The red rectangle indicates the region observed by the VLT and shown in Fig. 5.1.

temperature of dust embedded in a hot gas. Furthermore, combining *Herschel* data and *Spitzer* data, we are able to derive the full dust spectral energy distribution (SED), which allows us for the first time to quantify the effects of dust heating and erosion in a hot gas.

5.1.1 *Herschel* observation and data reduction

The region around NGC 4438 was observed by *Herschel* in parallel mode (i.e. using both PACS and SPIRE instruments) as part of the *Herschel* Virgo Cluster Survey (HeViCS, Davies et al. 2010). HeViCS is a blind survey, meaning that observations are

not targeted, such that four large fields, about $4.5° \times 4.5°$, partially overlapping, were imaged in fast-scan mode ($60''$/sec) with four cross-scans each.

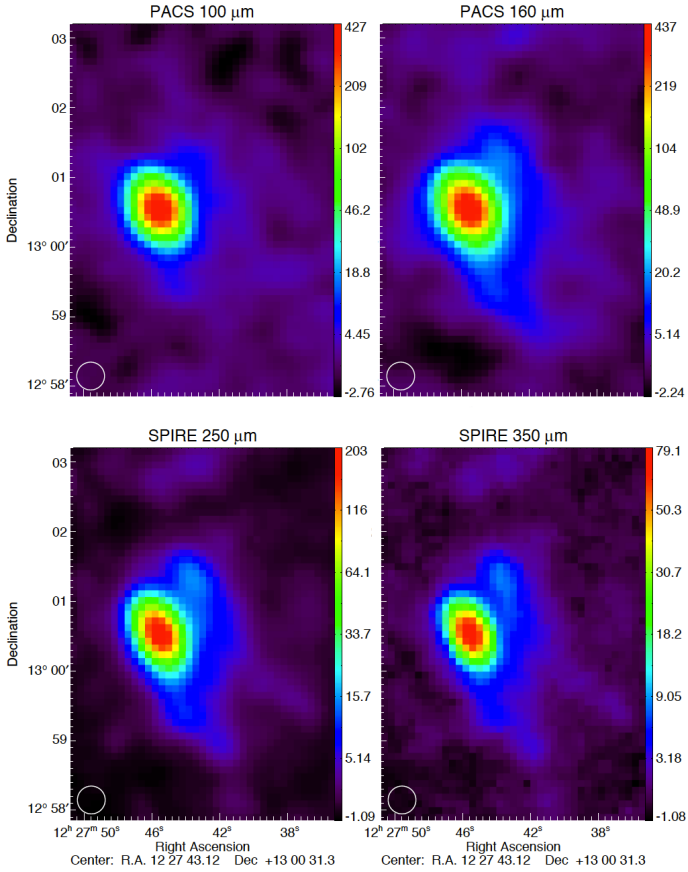

Figure 5.3: *Herschel* data (in MJy/sr): PACS 100 μm and and 160 μm in the upper row and SPIRE 250 μm and 350 μm in the lower row.

The PACS data reduction was performed in two separate steps. Firstly, the raw data were processed from Level-0 to Level-1 within HIPE (v10.0.0) using the calibration file v48. This pre-processing includes pixel flagging, flux density conversion and coordinates assignment. To remove the $1/f$ noise, which still affects the pixel timelines, a second step was performed: the Level-1 data were fed into `Scanamorphos`, (version 21, Roussel 2013) a software which subtract the low-frequency noise exploiting the redundancy in the observations of each sky pixel. No noise modeling is hence needed. With the `cutout` option in `Scanamorphos` we extracted a field which includes our target galaxy.

The SPIRE data used in this study were reduced as part of the *Herschel* Reference Survey (HRS, Ciesla et al. 2012).

The astrometric uncertainty is $\sim 2''$ and the full widths at half maximum (FWHM) of the PACS-SPIRE beams are 9.4″,13.5″,17.6″, 23.9″ and 35.2″ at 100,160, 250, 350 and 500 μm, respectively[1]. The absolute flux accuracy is estimated to be $\pm 20\%$ (a conservative value in the case of extended emission) for PACS data (Paladini et al. 2012) and $\pm 7\%$ for SPIRE data[2] and these are taken as the standard deviations throughout this section. The real shape of the "effective" PSFs is discussed in Section 5.2.

5.1.2 *Herschel* data analysis

In order to evaluate the large grain equilibrium temperature and therefore understand the dust heating processes in the different regions around NGC 4438 we use *Herschel* PACS and SPIRE data to generate a dust temperature map.

Convolution and regridding

Since we are mainly interested in the extended dust emission around NGC 4438 we decided not to use the *Herschel* SPIRE 500 μm map because its beam size is large with respect to the apparent size of the extra-planar dusty region.

First of all, we convolve all the maps to a common resolution (the beam size of the 350 μm SPIRE data, 24.9″ / beam) assuming Gaussian beams (see Section 5.2) and regrid the images to a common pixel size (the pixel size of the 250 μm SPIRE data, 36 arcsec^2 / pixel). Then, for each band we remove a tilted background plane. The total error, $\sigma_{\rm TOT}$, on the flux in each pixel has been estimated from the calibration errors ($\sigma_{\rm CAL}$) and statistical errors ($\sigma_{\rm STAT}$):

$$\sigma_{\rm TOT} = \sqrt{\sigma^2_{\rm CAL} + \sigma^2_{\rm STAT}}\,. \tag{5.1.1}$$

The statistical error is calculated as the standard deviation of the background flux (computed from all the pixels with flux lower than 5×10^{-3} of the flux of the brightest pixel in the field), while the calibration error is taken as indicated in Section 5.1.1.

In Fig. 5.3 we show the four *Herschel* maps (in MJy/sr) of NGC 4438: PACS 100 μm and 160 μm in the upper row and SPIRE 250 μm and 350 μm in the lower row. All the maps are convolved and regridded as explained above. The beam size of the 350 μm SPIRE data is shown by the small white circle in the bottom left corner of the images.

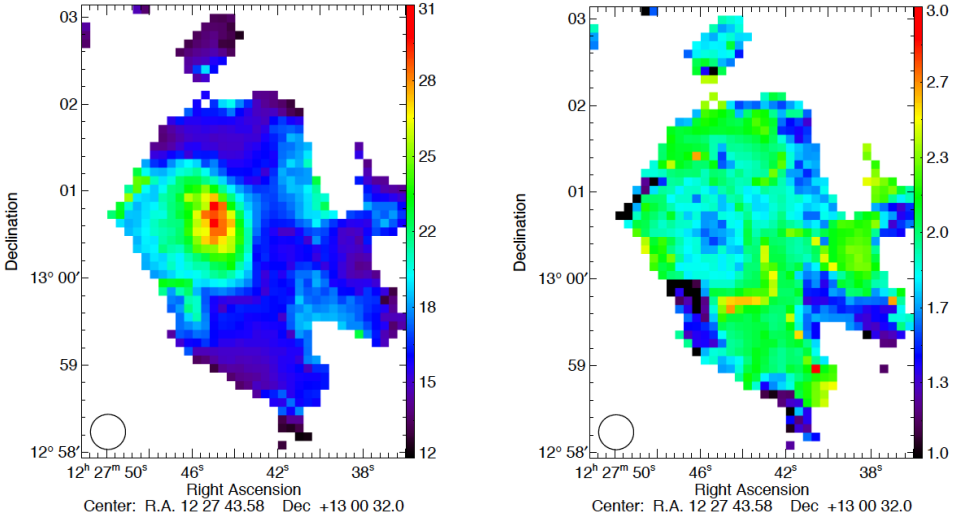

(a) (b)

Figure 5.4: The dust temperature (a) and β (b) maps for all the pixels with $I_{250} > 3\sigma_{250}$ and $\Delta T < 3\,\mathrm{K}$, obtained with β as a free parameter.

5.1.3 Data fitting

Using a χ^2 minimization technique, we fit the SED on a pixel-by-pixel basis with a modified blackbody:

$$I_\nu = \tau_{\nu_0} B_\nu(T)(\nu/\nu_0)^\beta\,, \tag{5.1.2}$$

where τ_{ν_0} is the optical depth at the reference frequency $\nu_0 = 3000\,\mathrm{GHz}$ ($100\,\mu\mathrm{m}$, τ_{100} hereafter), $B_\nu(T)$ is the Planck blackbody emission for a given temperature T and β is the spectral index at the frequency ν_0. For a proper calculation of the errors on the fit parameters see the discussion in Section 5.A. Initially, we leave the three parameters (τ_{100}, β and T) to vary. Fig. 5.4a and 5.4b show the temperature and β maps, respectively, for all the pixels in and around NGC 4438 with $I_{250} > 3\sigma_{250}$ and $\Delta T < 3\,\mathrm{K}$. We notice that there seems to be a weak anticorrelation between T and β. The pixels in the central part of the galaxy correspond to the highest dust temperatures but also to the lowest values of β. In Fig. 5.5 we plot the $T - \beta$ relation; the error bars represent the errors that we obtain with the fitting procedure. We notice a cluster of points for temperatures between 10 K and 20 K (corresponding to the west-side region) with an average $< \beta >= 1.9 \pm 0.3$, while for temperatures between 20 K and 32 K (corresponding to the central and eastern regions) we clearly see a trend with

[1]The PACS (SPIRE) PSFs were characterized from observations of Vesta (Neptune) by the Instrument Control Centre.

[2]From the SPIRE observersÕ manual, available on the webpage: http://Herschel.esac.esa.int/

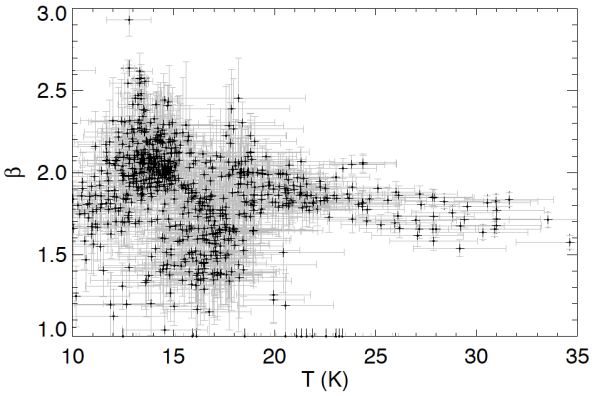

Figure 5.5: $T - \beta$ relation for all the pixels with $I_{250} > 3\sigma_{250}$ and $\Delta T < 3\,\mathrm{K}$.

$< \beta >= 1.8 \pm 0.15$. We want to focus here on the warmer dust in the eastern regions. In order to obtain a better estimate of the dust temperature and of the optical depth we decide to fix $\beta = 1.8$ for the rest of our analysis.

However, fixing the value of β, we might introduce a bias in the measurement of the dust temperature. In order to check that when fixing β the dust temperature is not highly affected but that we get a lower error, in Fig. 5.6 we plot the temperature obtained with a fixed β, $T_{\mathrm{fixed}\beta}$, as a function of the temperature in the case of a free β, $T_{\mathrm{free}\beta}$. We note that the points follow the 1:1 correspondence line between the

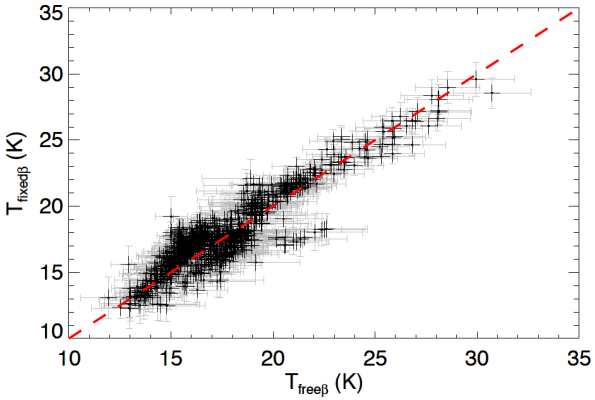

Figure 5.6: Dust temperature obtained with fixed $\beta = 1.8$ as a function of the dust temperature for a free β. The red dashed line shows $T_{\mathrm{fixed}\beta} = T_{\mathrm{free}\beta}$.

temperatures and that the errors on $T_{\mathrm{fixed}\beta}$ are always lower than $T_{\mathrm{free}\beta}$. Therefore our method does not introduce any significant bias into the temperature map.

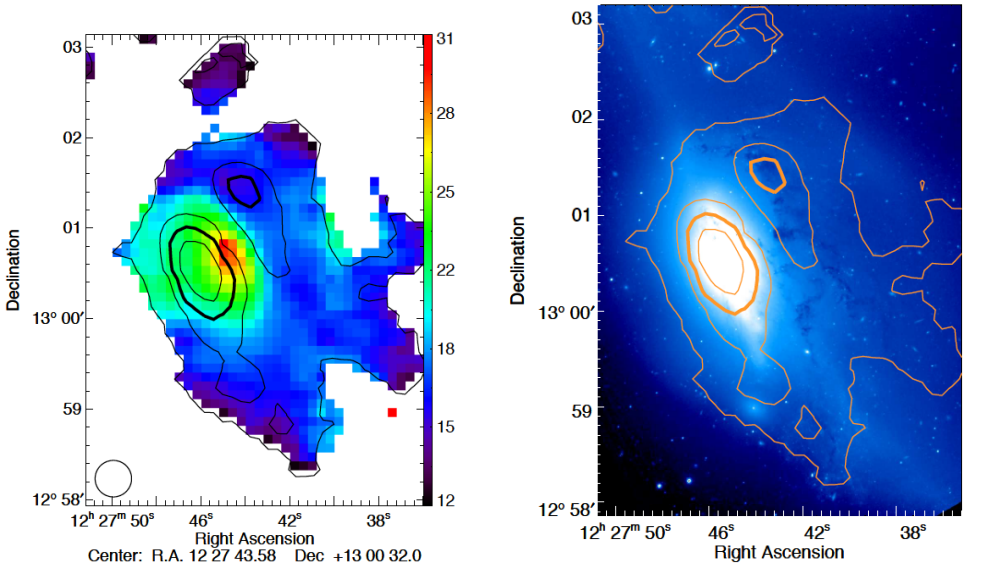

Figure 5.7: (a) Temperature map (obtained using a fixed $\beta = 1.8$) for pixels with $\Delta T < 3\,\mathrm{K}$ with A_V (contours). Contour levels: $A_\mathrm{V} = (0.3, 0.6, 1.0, 2.0)$ mag. The thick contour indicates $A_\mathrm{V} = 1.0\,\mathrm{mag}$. (b) V-band image with A_V (contours, same levels). This image has been saturated in order to highlight the dust extinction on the west-side of the galaxy.

Fig. 5.7a shows the temperature map for all the pixels with $\Delta T < 3\,\mathrm{K}$. We note that dust in the nuclear and east-side regions of the galaxy has a temperature between $\sim 22\,\mathrm{K}$ and $30\,\mathrm{K}$, while dust on the west-side region can be as cool as $\sim 15\,\mathrm{K}$.

Furthermore, from the fitting procedure we obtain the optical depth, τ_{100}, for each pixel. The optical depth is related to the total extinction in the V filter band, A_V, as:

$$\frac{\tau_{100}}{A_\mathrm{V}} = \frac{\tau_{100}}{N_\mathrm{H}} \frac{N_\mathrm{H}}{A_\mathrm{V}}\,, \tag{5.1.3}$$

where N_H is the total hydrogen column density, be it in the form of atomic or molecular gas. We adopt the standard values for the ratio $\frac{\tau_{100}}{N_\mathrm{H}}$ ($\simeq 6.25 \times 10^{-25}\,\mathrm{cm}^2$, Boulanger et al. 1996) and for the ratio $\frac{N_\mathrm{H}}{A_\mathrm{V}}$ ($\simeq 1.8 \times 10^{21}\,\mathrm{cm}^{-2}\mathrm{mag}^{-1}$, Predehl and Schmitt 1995). The optical depth to visual extinction ratio is then:

$$\frac{\tau_{100}}{A_\mathrm{V}} \simeq 1.1 \times 10^{-3}\,\mathrm{mag}^{-1}\,. \tag{5.1.4}$$

In Fig. 5.7a we superimpose the A_V contours on the dust temperature map. We consider that regions where $A_V \leq 1$ mag are optically thin and most of the UV-visible-NIR light can pass through, while if $A_V > 1$ mag the medium is optically thick. We note that, with the exception of the central part of the galaxy and a small region at north-west with respect to the centre, most of the regions in and around NGC 4438 are optically thin.

For a qualitative comparison between the optical image and the *Herschel* image Fig. 5.7b shows the V-band image taken at the VLT (saturated in order to highlight the dust extinction on the west-side region) with the A_V contours (calculated from the IR emission as described above) superimposed. The dark clouds in the west-side of the galaxy indicate a high extinction due to the presence of dust in that region (see Fig. 5.7b). From the A_V contours we notice a peak in the A_V map corresponding to the darkest clouds seen in the V-band image. This correspondence tells us that dust is seen not only in extinction in the optical image but also in emission by *Herschel*.

5.1.4 Multi-wavelength analysis

The high dust temperatures (Fig. 5.7a) we find on the east-side and the nuclear region could be explained by either a sufficiently intense radiation field or by the presence of a hot gas in that region. In the case of the nuclear region the dust heating is probably dominated by the intense radiation field coming from the central AGN (Nesvadba 2014). In order to estimate the surface brightness of the galaxy we convolved the

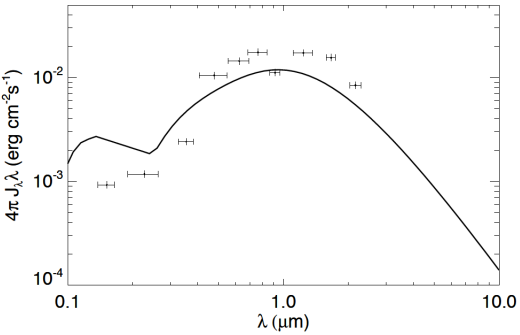

Figure 5.8: Radiation field for a pixel where $U = 1$ (data points, the x-axis error bar represents the band width) compared to the Mathis et al. (1983) radiation field in the solar vicinity (solid line).

GALEX (FUV and NUV), SDSS (u, g, r, i and z bands) and 2MASS (J, H, K_s) maps to a common resolution (the beam size of the 350 μm SPIRE data) and regrided to a common pixel size (the pixel size of the 250 μm SPIRE data). In optically thin regions ($A_V \leq 1$), and to a good approximation assuming an isotropic radiation field,

we can say that the surface brightness (in MJy/sr) obtained from the UV-optical-NIR data gives the local radiation field. For the optically thick regions, a radiative transfer model would be needed in order to estimate the local radiation field, which is beyond the scope of this study. Since NGC 4438 is a perturbed galaxy it is not easy to model the radiation field in and around the galaxy, we therefore show a map of the surface brightness and consider this to be a tracer of the local radiation field in the optically thin regions. In optically thick regions the surface brightness will represent only a lower limit to the radiation field.

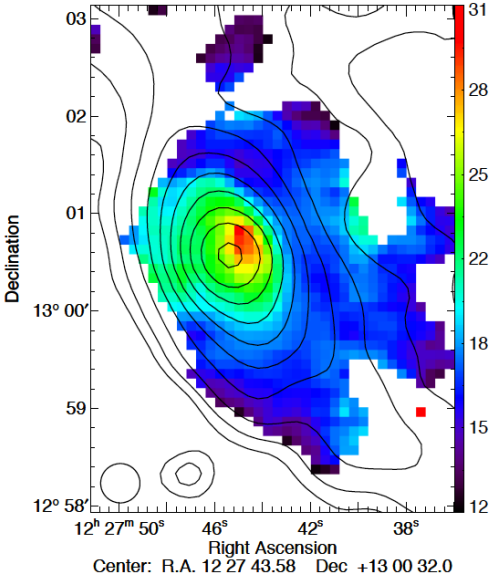

Figure 5.9: U factor (contours) overlaid on the dust temperature map. Contour levels: U = (0.10, 0.18, 0.34, ...) in logarithmic steps until a maximum of 24. We notice that for a given U factor, the dust temperature for a few independent point spread functions (PSFs) on the east-side is higher than on the west-side. The black circle on the bottom left corner indicates the Gaussian beam assumed for SPIRE 350 μm.

We define a factor U (using a similar nomenclature as Draine and Li 2007) as the ratio between the integrated radiation field and the radiation field in the solar neighborhood estimated by Mathis et al. (1983):

$$U = \frac{\int_{0.1\mu m}^{2.3\mu m} 4\pi J_\lambda d\lambda}{\int_{0.1\mu m}^{2.3\mu m} 4\pi J_\lambda (\mathrm{Mathis}) d\lambda}\,, \tag{5.1.5}$$

where the limits of integration (i.e. 0.1 μm and 2.3 μm) are the wavelengths of the *GALEX* FUV and 2MASS K_s band, respectively. Fig. 5.8 illustrates the spectrum of

the radiation field for a pixel in the west-side of the galaxy where $U = 1$ and $A_V \sim 0.3$ mag (the x-axis error bar represents the band width) and we compare this to the standard Mathis et al. (1983) radiation field in the solar vicinity. As noted by Boselli et al. (2005), because of the collision between NGC 4438 and M86, the west-side region of the galaxy shows little contribution from a recent starburst, leading to a reduced UV component with respect to the radiation field in the solar vicinity.

We plot the contours of U on the dust temperature map (Fig. 5.9). We notice, qualitatively, that the drop in the dust temperature going from the nuclear region towards the west-side of the galaxy follows the drop in the radiation field. This is not the case in going from the nuclear region to the east-side. Here, for a few independent PSFs, the dust temperature is higher than on the west-side for a given value of integrated radiation field. To explain this unusually high dust temperature the presence of an extra source of heating is suspected. However, this effect may be due to artifacts produced by an erroneous characterization of the PACS/SPIRE PSFs and this hypothesis has still to be ruled out (Section 5.2).

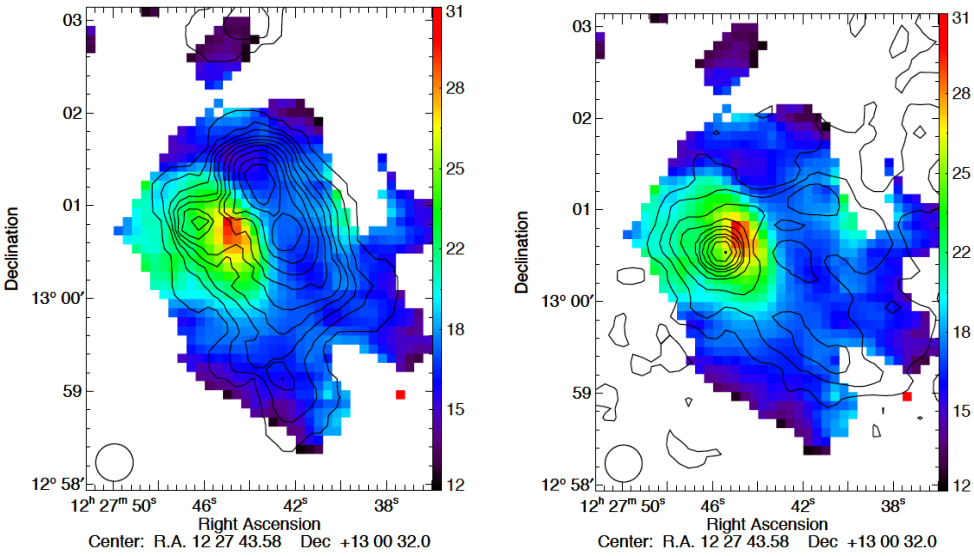

Figure 5.10: (a) HI (contours) overlaid on the dust temperature map. Contour levels: (0.20, 4.81, 9.42, ...) $\times 10^{19}$ cm^{-2} in linear steps until a maximum column density of $\sim 4 \times 10^{20}$ cm^{-2}. (b) X-ray (contours) overlaid on the dust temperature map. Contour levels: (5.50, 8.78, 14.0, ...) $\times 10^{-9}$ photons/s/cm^2/arcsec^2 in logarithmic steps until a maximum of 3.7×10^{-7} photons/s/cm^2/arcsec^2.

In order to study the distribution of the neutral gas we use the VLA D observations of NGC 4438 (Hota et al., 2007) to build the HI column density map. Since the galaxy

is optically thin except in a few regions close to the galactic centre, we convert the HI integrated flux to the HI column density in the usual manner (valid for $N_{\rm H} \leq 10^{21}\,{\rm cm}^{-2}$, Ryan-Weber et al. 2003):

$$N_{\rm H} = \frac{1}{a \times b} 1.823 \times 10^{18} \times 1.36 \lambda^2 \int S\,dv\,, \tag{5.1.6}$$

where $N_{\rm H}$ is the HI column density in ${\rm cm}^{-2}$, a and b are the major and minor beam axis ($a = 58$ arcsec and $b = 48$ arcsec in this case) respectively, $\lambda = 21.1$ cm (the HI line), S is the flux density in mJy and v is the radial velocity in km/s. In Fig. 5.10a we show the HI column density superimposed on the dust temperature map. We observe that dust in the west-side of the galaxy has a low temperature ($T_{\rm d} \sim 15 - 18\,{\rm K}$) and is embedded in a cold atomic hydrogen cloud while on the east-side we note a displacement between the dust and the atomic gas. There appears to be an anti correlation between the hot dust and the HI gas column density.

We use the Chandra X-ray data (Machacek et al. 2004) to look at the hot gas distribution. Fig. 5.10b shows the X-ray data overlaid on the dust temperature map and we clearly see that the warmer dust ($T_{\rm d} \sim 20 - 28\,{\rm K}$) on the extended east-side region is embedded in a hot X-ray emitting gas. Machacek et al. (2004) estimated that the X-ray emitting gas in the bulge around the nuclear region has a temperature $T \simeq 4.8{\times}10^6$ K, a density $n_{\rm e} \simeq 2.3{\times}10^{-2}\,{\rm cm}^{-3}$ and a column density $N_{\rm H} \simeq 2.64{\times}10^{20}\,{\rm cm}^{-2}$. In such a hot gas, because of bombardment by fast ions and electrons, the dust will undergo erosion (Bocchio et al. 2012; Micelotta et al. 2010b,a) as well as receive an extra source of heating from the hot electrons (Bocchio et al. 2013b). In the following section we explore this scenario in detail.

5.1.5 Modelling

From our multi-wavelength study it seems that in the east-side region an extra source of heating might be required in order to explain the dust temperature. This source of heating could come from the collisions with the ions and electrons in the hot gas. On the other hand, in the west-side region, photon heating alone might be sufficient to match the dust SED with observations. We have built a simple model to quantitatively explain what we see in the east- and west-side regions with our multi-wavelength analysis.

East-side region: dust erosion and heating

Dust grains embedded in a hot gas, undergoing collisions with fast ions and electrons, are eroded. In particular, small grains ($a \lesssim 1\,{\rm nm}$) are greatly affected by this process and destroyed on rather short timescales ($t \lesssim 10^6\,{\rm yr}$). In order to estimate the dust SED that we would observe in the east-side region we study both the spatial and temporal evolution of the dust. We assume for simplicity that at the time t_0 when the hot gas (with density and temperature estimated by Machacek et al. 2004) starts to enfold dust grains, the dust size distribution follows the Compiègne et al. (2011)

dust model. We then let the size distribution evolve under the effects of erosion due to the collisions with hot electrons and ions for a given time ($t_{\rm hot}$ hereafter). We use a modified version of the Jones et al. (1996) shock code. This dust evolution code includes dust destruction and heating studies by Bocchio et al. (2012, 2013b, 2014) and Micelotta et al. (2010b,a). The code is presented in detail in Chapter 6 (Bocchio et al. 2014). Fig. 5.11a illustrates the change in the size distribution for different $t_{\rm hot}$. Solid lines refer to carbonaceous grains while long dashed lines to silicate grains. Red lines represent the size distribution at $t_{\rm hot} = 0\,$yr, green lines at $t_{\rm hot} = 10^5\,$yr and blues lines at $t_{\rm hot} = 10^6\,$yr. We notice that PAHs are quickly destroyed, while 2-3 nm size a-C:H grains are still present for $t_{\rm hot} = 10^5\,$yr but totally destroyed for $t_{\rm hot} = 10^6\,$yr. The smaller silicate grains are significantly affected by the presence of the hot gas as well.

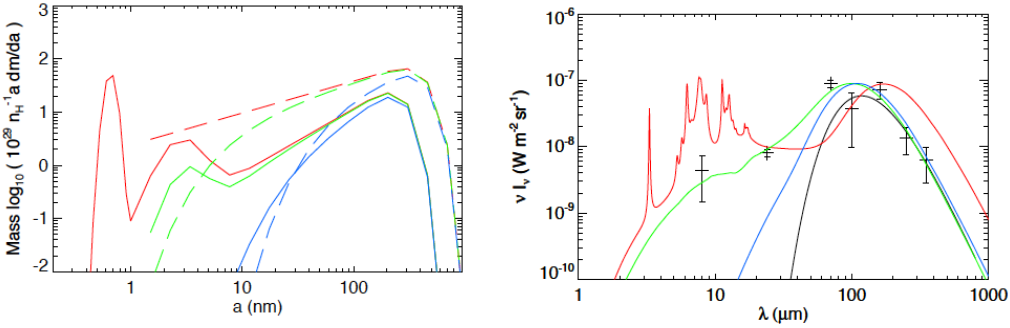

(a) (b)

Figure 5.11: (a) Dust size distribution. Solid lines: carbonaceous grains, long dashed lines: silicate grains. Red lines: standard case (no erosion), green lines: $t_{\rm hot} = 10^5\,$yr, blue lines: $t_{\rm hot} = 10^6\,$yr. (b) Dust SED in the east-side of NGC 4438. The data points are IRAC 8 μm, MIPS 24 μm and 70 μm, PACS 100 μm and 160 μm and SPIRE 250 μm and 350 μm. Black line: modified blackbody fit to the PACS and SPIRE data ($A_{\rm V} \sim 3.5 \times 10^{-2}\,$mag, $\beta = 1.8$ and $T_{\rm e} \sim 21.2$). Red line: SED model due to only photon heating as estimated from UV-visible-NIR data ($U = 0.2$, $N_{\rm H} = 2 \times 10^{21}\,{\rm cm}^{-2}$). Green and blue lines: SED model due to photon and collisional heating with erosion included for $t_{\rm hot} = 10^5\,$yr and $t_{\rm hot} = 10^6\,$yr respectively ($N_{\rm H} = 10^{20}\,{\rm cm}^{-2}$ and $N_{\rm H} = 2.2 \times 10^{20}\,{\rm cm}^{-2}$ respectively).

Using the DustEM code[3], with the inclusion of collisional heating due to the presence of a hot gas (Section 4.2 and Bocchio et al. 2013b), we can calculate the dust SED that would be observed after a time $t_{\rm hot}$ for a given pixel.

In Fig. 5.11b we show the dust SED for a representative pixel in the east-side region. The data points are from *Spitzer* IRAC 8 μm, *Spitzer* MIPS 24 μm - 70 μm

[3]http://www.ias.u-psud.fr/DUSTEM.

(Bendo et al. 2012b), *Herschel* PACS 100 μm, 160 μm and *Herschel* SPIRE 250 μm and 350 μm. The black line is the fit to the PACS and SPIRE data with a modified blackbody. The red line shows the dust SED we would expect if there were no hot gas (i.e., photon absorption is the only source of heating, $U = 0.2$), the green line shows the case for $t_{\rm hot} = 10^5$ yr and the blue line is the case for $t_{\rm hot} = 10^6$ yr. We notice that the position of the peak of the dust SED, and therefore the large grain equilibrium temperature, in the case of only photon heating (red line) is far from the best fit to the PACS and SPIRE data. We note that we would need a radiation field ~ 20 times larger than the observed one for a good match of the large grain equilibrium temperature. In this region the optical depth is $A_{\rm V} \sim 3.5 \times 10^{-2}$ mag and therefore the error we made estimating the local radiation field directly from the surface brightness cannot explain this discrepancy.

The green line fits to the entire dataset for this pixel better than the blue line, which underestimates the emission at short wavelengths, and seems to indicate significant dust erosion and heating by hot electrons. We take a column density of $N_{\rm H} = 2 \times 10^{21}$ cm^{-2}, $N_{\rm H} = 10^{20}$ cm^{-2} and $N_{\rm H} = 2.2 \times 10^{20}$ cm^{-2} for the red, green and blue lines respectively.

West-side region

In Fig. 5.12 we plot the dust SED in a representative pixel on the west-side region of NGC 4438. We use the same color-coding as per Fig. 5.11b. In this region $A_{\rm V} \sim 0.3$ mag, and to a good approximation we can estimate the radiation field directly from the observed surface brightness. We expect dust to be embedded in a cold diffuse gas and therefore we do not include any effect of heating or destruction due to collisions in the calculations of the dust emission, the only source of heating is then photon absorption ($U \sim 1$). We notice that the modeled dust emission gives a good match to the data points throughout the entire SED for an assumed column density of $N_{\rm H} \sim 5 \times 10^{20}$ cm^{-2}.

5.1.6 Discussion

From the comparison between the *Spitzer*/*Herschel* data points and the modeled SED in the east-side region, it seems that dust spent $\sim 10^5$ yr in a hot gas. A shorter timescale would lead to a higher emission at short wavelengths and to a lower dust temperature, while if we assumed a longer timescale we would underestimate the short wavelengths emission. We can compare this timescale with the dynamical timescale. If we consider that the hot gas wind moves at the speed of sound in the IGM ($c_{\rm s} \sim 1000$ km/s), the time needed to travel from the nuclear region out to the border of the east-side region would be $\sim 10^6$ yr. The discrepancy between these two timescales could be covered by a better estimate (with a deeper X-ray observation) of the density and temperature in the east-side outskirt of NGC 4438. We currently assume a gas with $T \sim 5 \times 10^6$ K and $n_{\rm H} \sim 2 \times 10^{-2}$ cm^{-3}, if the actual gas density was an order of magnitude lower, then $t_{\rm hot}$ would be an order of magnitude lower and would then match with the dynamical timescale.

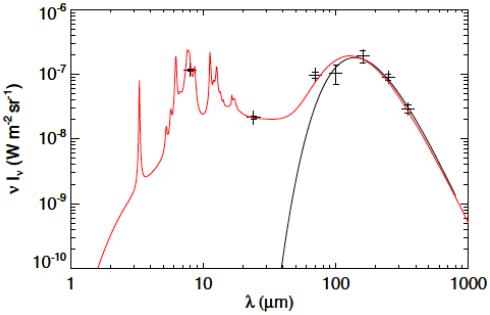

Figure 5.12: Dust SED in the west side of NGC 4438. Black line: modified blackbody fit to the PACS and SPIRE data ($A_V \sim 0.3$ mag, $\beta = 1.8$ and $T_e \sim 18$). Data points and red line as per Fig. 5.11b ($U \sim 1$).

Alternatively, if the dust was entrained in dense clumps it would be slowly released into the gas due to the clump evaporation and the dust would be destroyed on a timescale of $\sim 10^5$ yrs. In this way dust could survive in a hot gas region for a longer time thus matching the estimated dynamical timescale.

In the east-side region we computed the hot gas cooling rate pixel by pixel using the cooling function, Λ_d, calculated by Dwek (1987). From Fig. 5.11a we can assume that the average dust grain radius is ~ 80 nm and, since the gas temperature is $\simeq 4.8 \times 10^6$ K, from Fig. 4 by Dwek (1987) we can infer that dust is expected to be the main coolant in this case. In each of the pixels in the east-side region of NGC 4438 the cooling rate is to within a few percent equal to the IR dust emission. This leads us to conclude that there is a transfer of energy between the hot gas and dust grains, which is further supporting evidence for the collisional heating of dust.

Furthermore, we note that in the case of $t_{hot} \sim 10^5$ yr, our model for the east-side region requires a column density of $N_H \sim 10^{20}$ cm^{-2} in order to fit the observational data. This value is only a factor two lower than the X-ray column density estimated by Machacek et al. (2004) using the Chandra observations. On the west-side region, the column density we estimate is $N_H \sim 5 \times 10^{20}$ cm^{-2} which is within a factor of two of the column density obtained from the HI data in that region.

5.1.7 Conclusions

We have combined *Spitzer* and *Herschel* data (assuming Gaussian PSFs) for NGC 4438 and shown the full dust SED in two different regions around this galaxy. We performed a multi-wavelength analysis of the dust and gas around NGC 4438 and we can conclude that:

- in the west-side region the dust is embedded in a cold atomic hydrogen cloud

and therefore even the smallest grains are preserved. The large grain equilibrium temperature ($T \sim 15 - 18\,\mathrm{K}$) is lower than in the solar neighborhood, which can be explained by the lower radiation field and by the lack of a young stellar population in the region.

- In the east-side region the dust is embedded in a hot X-ray emitting gas, the smallest grains are destroyed and the dust is collisionally heated. The large grain equilibrium temperature ($T \sim 21 - 24\,\mathrm{K}$) is therefore higher than in the case of photon absorption only.

- In the east-side region there is clear interaction between the cool ISM and the hot IGM. This is consistent with the scenario formulated by Li and Wang (2013a), who proposed that the excess in the X-ray brightness of NGC 4438 might come from the mixing between cool and hot gas.

This preliminary analysis may be the first observational proof that large grains embedded within a hot coronal gas are heated by electron collisions and that the smallest grains are rather rapidly destroyed by collisions with electrons. However, the assumption made on the shape of the PSFs (Gaussian PSFs) may create artifacts in the convolved images, leading to an erroneous of the dust temperature. We therefore perform a detailed analysis of the PACS and SPIRE PSFs to rule out this possibility.

5.2 PACS to SPIRE convolution

In the study presented above we convolved the PACS and SPIRE data to the resolution of the SPIRE 350 μm data assuming Gaussian PSFs. However, the choice of a Gaussian function is only an approximation to the real PSFs of the two instruments. In this section we explore the real PSFs, their dependence on the source spectrum and the methods to convolve PACS maps to SPIRE maps.

5.2.1 PACS and SPIRE PSFs

The PSF represents the image seen by a given instrument when observing a point source. A PSF is usually characterized by a primary lobe and secondary lobes. Making the approximation of a Gaussian PSF, we assume a Gaussian shape for the primary lobe and neglect the secondary lobes.

The PACS and SPIRE Instrument Control Centre (ICC) provide a model for the PSF that the two instruments would observe in the different bands (i.e. modeled broadband PSF). In particular, for SPIRE, the modeled PSFs are obtained assuming a spectral slope for each band (see Table 5.1), in order to reproduce the observations of Neptune. For PACS, it was assumed that the spectral slope is the same in all the three bands, and is equal to the Rayleigh-Jeans regime slope of a blackbody radiation (i.e. similar to the radiation detected observing asteroids or planets). Fig. 5.13 shows the radialized modeled broadband PSFs for PACS (blue, green and red bands in solid

lines) and SPIRE (PSW, PMW and PLW bands, in blue, green and red dashed lines respectively) instruments.

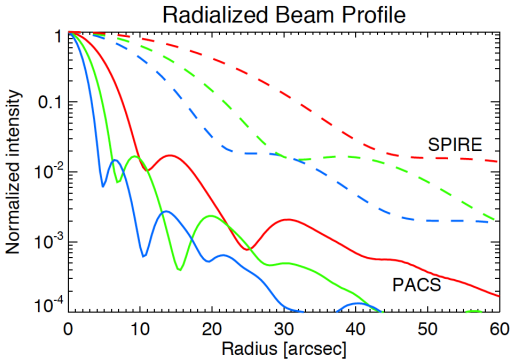

Figure 5.13: Radialized modeled broadband beam profiles for PACS and SPIRE. See text for details.

We note that the intensity of the secondary lobe of the SPIRE 350 μm PSF is about 10^{-2} the intensity of the peak at about 40″ from the centre. This can become critical when observing sources that are particularly structured and with a steep gradient between their bright and faint regions. The *Herschel* data of NGC4438 (see Fig. 5.3) shows that the flux of the galaxy centre is $\sim 10^2$ times the flux in the east-side region of the galaxy, which is $\sim 40''$ away from the centre. Therefore, in order to confirm the observed excess in temperature we need to carefully characterize the PACS and SPIRE PSFs and convolve the images correctly.

The PACS and SPIRE PSFs are estimated using the observations of planets (e.g. Neptune, Mars, Uranus) or asteroids (Vesta, Ceres). The core of the PSF is better characterized by observing fainter sources (asteroids) which do not lead to any saturation of the central pixels, while the secondary lobes are best characterized observing bright sources (planets) which leads to the complete saturation of the central pixels but allow for the access to fainter features. For SPIRE the measured PSF is very close to the broadband PSF model, while for PACS the modeled PSF is systematically narrower than the observed one. In Fig. 5.14 we show the PACS observations of Vesta used for the characterization of the PACS PSFs, while Fig. 5.15 shows the observations of Neptune, used for the characterization of the SPIRE PSFs.

However, the observations of Vesta or Neptune represent good estimates of the observed PSF only if the source we are observing has a similar spectrum to the one of these sources. According to thermal models for asteroids (Lebofsky et al. 1986) and planets (Moreno 1998, 2010) Vesta and Neptune have a rather high surface temperature (~ 170 K and ~ 70 K, respectively) and are almost perfect emitters ($\beta \sim 0$). When observing diffuse interstellar dust, the temperature is rarely so high and the value of

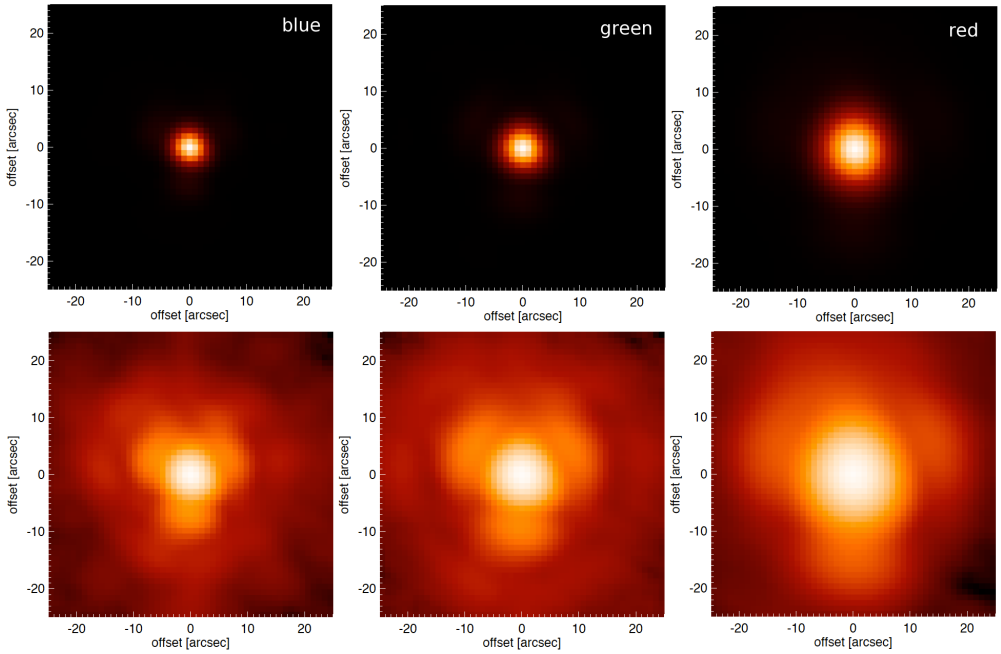

Figure 5.14: PACS PSF for the three bands in linear (top row) and logarithmic scale (bottom row) for a pixel scale of 1″. Observations of Vesta, standard data reduction by the ICC.

β ranges roughly from 1.5 to 2.5 and therefore the observed spectrum are different, affecting the observed PSF.

5.2.2 Source spectrum dependent PSF

SPIRE PSF width

The radius of the first minimum, $\theta_{\min}$, of the diffraction pattern by a circular aperture is given by

$$\theta_{\min} = 1.22\frac{\lambda}{D}, \tag{5.2.1}$$

where λ is the wavelength of the received light and D the diameter of the aperture. Therefore, if we consider only diffraction effects, the width of the PSF is directly proportional to the wavelength. Following the SPIRE Observer Manual (SOM)[4] we are able to calculate, starting from the observed SPIRE PSF, the PSF that we would

[4]http://herschel.esac.esa.int/Docs/SPIRE/pdf/spire_om.pdf

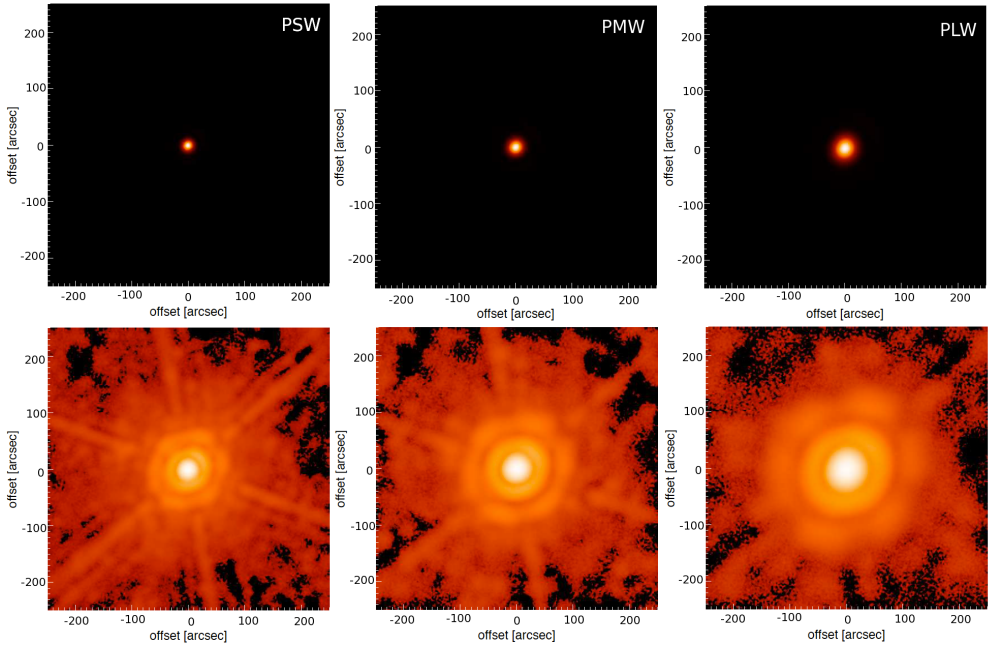

Figure 5.15: SPIRE PSF for the three bands in linear (top row) and logarithmic scale (bottom row) for a pixel scale of 1″. Observations of Neptune, standard data reduction by the ICC.

observe if the spectrum of the source were different from that of Neptune. We define the intensity of the PSF, $B(\theta, \nu)$, at a given angular distance θ from the centre and for a given frequency ν as

$$B(\theta, \nu) = B(\theta \times \left(\frac{\nu}{\nu_{\rm eff}}\right)^{\gamma}, \nu_{\rm eff}), \tag{5.2.2}$$

where $\nu_{\rm eff}$ is the effective frequency of the observed PSF and γ is a factor that depends on the optics of the instrument.

An ideal diffraction-limited optical system would have a factor $\gamma = -1$ (Eq. 5.2.1). However, real instruments may have their resolution limited by imperfections in the lenses or misalignment, therefore leading to a different frequency dependancy. From simulations of the SPIRE optics[5], the ICC estimated the factor $\gamma = -0.85$. Furthermore, in order to evaluate the effective frequency of the observed PSF, the ICC measured the isophotal frequency, which is assumed to be a good estimate of this quantity. The isophotal frequency is the frequency of the monochromatic beam profile whose

[5]The ICC took into account the change in diffraction from the focal plane array and the edge-taper at the edge of the primary mirror to perform simulations of the SPIRE optics.

solid angle is equal to the solid angle of the measured PSF. The isophotal frequencies for the different SPIRE bands are listed in Table 5.1. It is then possible to calculate the PSF for a given spectrum in this way:

$$B(\theta, T, \beta) = \frac{\int_0^\infty T(\nu)S(\nu)W(\nu)B(\theta,\nu)d\nu}{\int_0^\infty T(\nu)S(\nu)W(\nu)d\nu}, \tag{5.2.3}$$

where $T(\nu)$ is the transmission of the filter at a given frequency ν, $S(\nu)$ is the source spectrum and $W(\nu)$ is the response of the bolometers used by SPIRE and the integral at the denominator is a normalization factor.

Table 5.1: Measured beam solid angle, isophotal frequencies and Neptune spectral index for the three SPIRE bands.

Band	PSW	PMW	PLW
Measured beam solid angle (arcsec^2)	450	795	1665
Isophotal frequency (GHz)	1215.14	865.43	610.18
Index α	-3.29	-3.42	-3.47

In order to check that this method is valid to calculate the PSF for a given spectrum, we first perform a test. The measured PSF is obtained by the observations of Neptune, therefore, knowing the effective slope of the Neptune spectrum in the three bands it should be possible to reproduce the observed PSF. The effective slope index α represents the exponent of the intensity:

$$F_\lambda \propto \lambda^\alpha, \tag{5.2.4}$$

and for Neptune was measured by the ICC (see Table 5.1). We note that for a very high temperature source with $\beta = 0$, the SPIRE bands would be in the Rayleigh-Jeans regime and $\alpha \sim -4$. In the case of Neptune, the temperature is not sufficiently high and even for the PLW band the effective slope is lower.

Following the method described in the SOM, in order to compare the measured and the calculated PSFs we fit the two images to a 2D Gaussian function, including the secondary lobes, i.e. we fit the images until a distance of ~ 5 HWHM from the centre. Table 5.2 shows the major and minor FWHM of the measured and calculated PSFs. For each band, the FWHM of the two PSFs are very close one to the other (at the percent level) and therefore the method used is valid.

We therefore calculate the PSF in the case of sources with $T = 25, 20$ and 15 K and with $\beta = 2$ and give the major and minor FWHM in Table 5.3. The difference between the measured (Neptune image) and calculated FWHM for the assumed spectra are never higher than 3%.

Table 5.2: Major × minor FWHM (arcsec) of the measured and calculated SPIRE PSFs for the three SPIRE bands.

Band	Neptune	calculated
PSW	17.40×18.39	17.36×18.35
PMW	23.44×24.73	23.29×24.58
PLW	33.36×36.66	32.90×36.17

Table 5.3: Major × minor FWHM (arcsec) of the measured and calculated SPIRE PSFs for the three SPIRE bands for different source spectra.

Band	Neptune	$T = 25\,\mathrm{K}$	$T = 20\,\mathrm{K}$	$T = 15\,\mathrm{K}$
PSW	17.40×18.39	17.20×18.18	17.28×18.23	17.41×18.40
PMW	23.44×24.73	23.01×24.27	23.07×24.34	23.18×24.46
PLW	33.36×36.66	32.24×35.44	32.31×35.52	32.44×35.67

PACS PSF

Performing the same analysis as the PACS PSF is a more delicate matter. In the PACS Observer Manual (POM)[6] there are several observations of asteroids. These sources are unresolved by PACS and are bright enough to have access to the secondary features of the diffraction pattern, making them good estimates of the PACS PSFs.

Unfortunately, a reliable model for the monochromatic PACS PSF is not available yet. At present the monochromatic model provided in the POM is based on an ideal diffraction-limited system. We then choose $\gamma = -1$, which is the factor that we would expect for the scaling of the PSF for ideal diffraction (Eq. 5.2.1). Furthermore, as stated in the POM, the modeled monochromatic PSF is systematically narrower than the observed one and so, in this case, the isophotal frequency is not a good estimate of the effective frequency. Therefore we estimate ν_{eff} in another way. We calculate the averaged frequency over the transmission bands, bolometer responses and the source spectrum:

$$\bar{\nu} = \frac{\int_0^\infty \nu S_\nu T_\nu W_\nu d\nu}{\int_0^\infty S_\nu T_\nu W_\nu d\nu}. \tag{5.2.5}$$

For the asteroid Vesta (used as the standard observation for the characterization of the PACS PSFs) the spectrum is characterized by $T = 168\,\mathrm{K}$ and $\beta = 0$. We report the obtained effective frequencies in Table 5.4.

We then compare the FWHM of the measured and calculated PACS PSFs in order to check the method. For each band the two FWHM are compatible to within 2% (see Table 5.5).

[6] http://herschel.esac.esa.int/Docs/PACS/pdf/pacs_om.pdf

Table 5.4: $\nu_{\rm eff}$ for the three PACS bands.

Band	blue	green	red
$\nu_{\rm eff}$ (GHz)	4321.79	3051.17	1947.31

Table 5.5: Major × minor FWHM (arcsec) of the measured and calculated PACS PSFs for the three PACS bands.

Band	Vesta	calculated
blue	5.53×5.93	5.53×5.92
green	6.77×7.21	6.73×7.16
red	10.68×12.12	10.45×11.86

We then calculate, as for the SPIRE bands, the PACS PSFs for source spectra with $T = 25, 20$ and 15 K and $\beta = 2$ (see Table 5.6).

Table 5.6: Major × minor FWHM (arcsec) of the measured and calculated PACS PSFs for the three PACS bands for different source spectra.

Band	Vesta	$T = 25\,\mathrm{K}$	$T = 20\,\mathrm{K}$	$T = 15\,\mathrm{K}$
blue	5.53×5.93	5.79×6.19	5.91×6.32	6.10×6.53
green	6.77×7.21	6.90×7.34	7.02×7.46	7.20×7.66
red	10.68×12.12	10.54×11.95	10.68×12.12	10.99×12.47

Following the POM and SOM, we calculate the geometric mean[7] value of the major and minor FWHM for the calculated PSF for the different source spectra. These are shown in Fig. 5.16 normalised to the FWHM of the measured FWHM (from Vesta and Neptune observations for PACS and SPIRE, respectively). We note that the FWHM for SPIRE is at most $\sim 3\%$ narrower than the observed one, but for PACS the effect is more important and can be up to $\sim 10\%$ for the blue band for a source with $T = 15\,\mathrm{K}$.

5.2.3 Convolution kernels

A convolution kernel is a matrix used to smooth one image, observed by an instrument with a given PSF, to the resolution of a second instrument. For example, Aniano et al. (2011) calculated convolution kernels for the smoothing of images taken by a number of instruments. The main constraint of their method is that the PSFs must

[7]The geometric mean, $\bar{x}$, of a data set $\{x_1, x_2, ..., x_n\}$ is given by $\bar{x} = \left(\prod_{\rm i=1}^{\rm n} x_{\rm i}\right)^{1/\rm n}$.

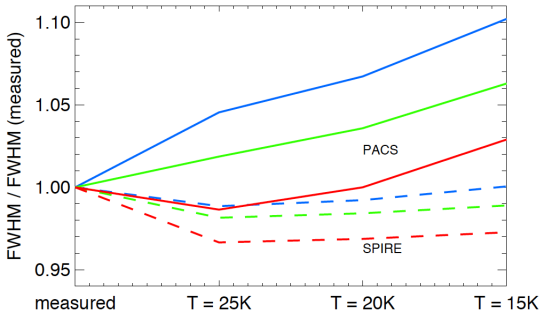

Figure 5.16: FWHM of the calculated PSF for different source spectra normalised to the FWHM of the measured PSF. Color and line style coding as per Fig. 5.13.

be approximated by rotationally symmetric functions. However, as seen in Fig. 5.14 and 5.15, the PACS and SPIRE PSFs present asymmetric features and in circularizing them, some information is lost and artifacts are generated in the convolved images. Furthermore, the assumed PSFs are those estimated from the observations of asteroids and planets without taking into account the variations in the width of the PSF due to the different source spectra.

We used the Aniano et al. (2011) convolution kernels to convolve our multi-wavelength data of the Eyes Galaxies to the SPIRE 350 μm resolution. We observe that, in the case of the convolution of the MIPS 70 μm to SPIRE 350 μm the convolution kernel produces ring-shaped features around the brightest sources (see Fig. 5.17a). We note that the intensity ratio between the source and the ring is $\sim$ 100 and that the gap between the source and the ring has a negative flux (with respect to the background flux, Fig. 5.17b). We then conclude that this feature is certainly an artifact induced by the convolution. In particular such an artifact might be created if the assumed PSFs (used to calculate the convolution kernel) are wider or narrower than the observed ones or because of the circularization of the PSFs. The kernels provided by Aniano et al. (2011) are therefore not optimal for the processing of the images of the Eyes Galaxies and we do not use them.

The choice of Gaussian PSFs is in principle not correct either. A convolution kernel assuming Gaussian PSFs will not produce any artifacts around sources and therefore is often considered as correct but on the contrary can produce distortions which are not easily detectable (Bendo 2013).

Source spectrum dependence of the convolution kernels

As seen in Section 5.2.2 the "effective" PSFs are affected by the spectrum of the source that we are observing and, depending on the temperature (and β) of the source, the FWHM of the PSFs can be up to $\sim$ 10% different from the observed one. This effect

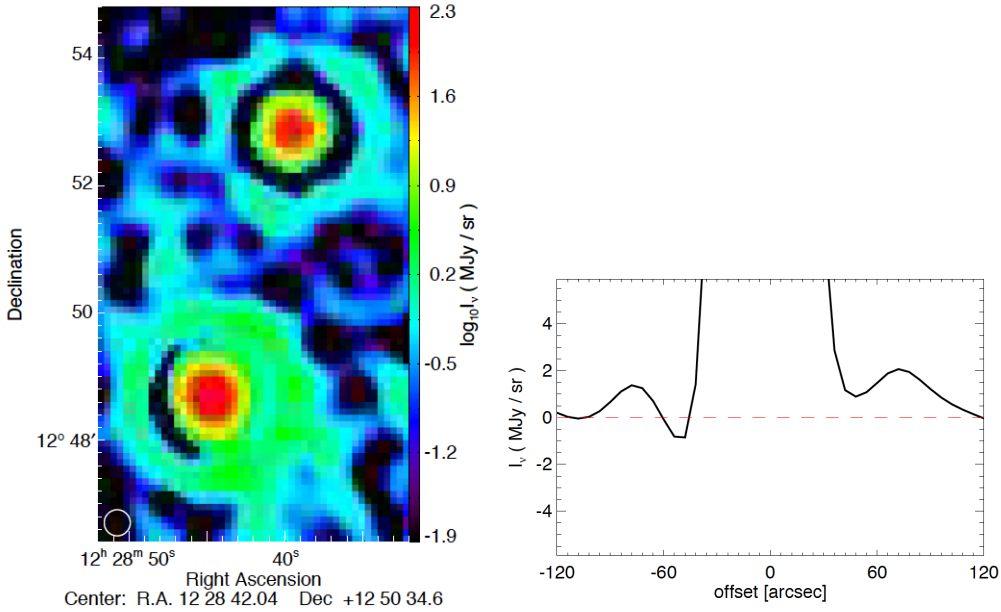

(a) (b)

Figure 5.17: (a) Saturated MIPS 70 μm image of the Eyes Galaxies. This image is smoothed to the resolution of SPIRE 350 μm using the convolution kernels by Aniano et al. (2011). (b) A horizontal cut of NGC 4438.

is of course reflected on the calculated kernels. Then, using the calculated PSFs for different spectra, we are now able to compute the associated convolution kernels.

In particular, using the same method as Aniano et al. (2011) we calculated the convolution kernels[8] to pass from the resolution of the PACS 70, 100, 160 μm and SPIRE 250 μm to that of SPIRE 350 μm, for the three temperatures considered ($T = 15, 20, 25$ K) and $\beta = 2$. The assumed PSFs to perform this calculation are characterized in Section 5.2.2. We also calculated the convolution kernels using the measured (Vesta for PACS and Neptune for SPIRE) PSFs[9] and we compare their FWHM in Table 5.7. We finally compute the ratio between the kernel FWHM assuming "modified" PSFs and the kernel FWHM for the measured PSFs (Fig. 5.18).

We note that, accounting for the source spectrum, the convolution kernels to pass from the resolution of the PACS bands to that of SPIRE 350 μm present a difference never larger than 3%. This is due to the fact that, even if the source spectrum plays

[8]The author of this manuscript would like to thank A. Boucaud (Postdoctoral fellow at the IAS) for having performed these calculations.

[9]Since the method to calculate the convolution kernels is the same as that of Aniano et al. (2011), the convolution kernels calculated using the measured PSFs are the same as those provided by them.

Table 5.7: FWHM (arcsec) of the convolution kernels to smooth to the resolution of the SPIRE 350 μm.

Band	measured	$T = 25\,\mathrm{K}$	$T = 20\,\mathrm{K}$	$T = 15\,\mathrm{K}$
blue	22.44	21.87	21.89	21.93
green	22.07	21.57	21.52	21.50
red	20.80	20.16	20.16	20.17
PSW	19.19	18.16	18.19	18.24

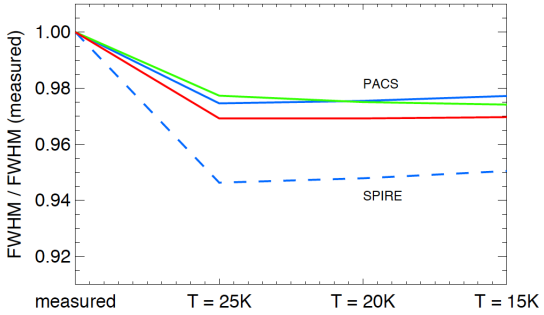

Figure 5.18: FWHM of the calculated kernels for different source spectra normalised to that of the kernel calculated using the measured PSFs. Color and line style coding as per Fig. 5.13.

an important role in calculating the "effective" PACS PSFs (difference up to 10%), the PSF FWHM are much narrower for PACS bands than for SPIRE 350 μm. On the contrary, little variations in the SPIRE 250 μm lead to a larger discrepancy in the computed kernels ($\sim$ 5%). Furthermore, this routine is known not to optimally deal with calculations of kernels that assume two similar starting PSFs (Aniano 2013), which is the case in passing from the resolution of SPIRE 250 μm to SPIRE 350 μm. Finally, it has to be noted that, as mentioned above, this routine has the stringent limitation that the starting PSFs must be circularized, which will produce circularized kernels, not taking into account the asymmetric features of the PACS and SPIRE PSFs.

A way to improve these calculations would be to implement a Bayesian approach. This method has already been used to calculate convolution kernels for PACS and SPIRE by Arab et al. (2012), assuming measured PSFs. We plan to extend this method, in collaboration with Hacheme Ayasso[10], to calculate convolution kernels accounting for the source spectrum. This method does not assume the circularization of the starting PSFs and will then allow us to consider their real shape.

[10]Hacheme Ayasso is currently working as Maître de conférences at the UJF in Grenoble, France.

5.3 Conclusions and perspective

Dust is commonly embedded in cold and diffuse clouds in galaxies and heated by stellar photon absorption. This same dust embedded in a hot gas is expected to receive an extra source of heating from collisions with fast electrons in the gas (Dwek 1986, 1987; Bocchio et al. 2013b). However, a hot gas represents a harsh environment for dust and the interaction with energetic ions, atoms and electrons lead to the sputtering of grains on rather short timescales (Tielens et al. 1994; Micelotta et al. 2010b; Bocchio et al. 2012, 2013b). Therefore the mixing and interaction between interstellar dust and a hot coronal-type gas is expected to be a localized phenomenon, difficult to observe.

As shown in Section 5.1, the interaction between cluster galaxies lead to the displacement of interstellar matter outside the galactic plane and its mixing with the ICM is expected. However, in order to observe dust emission from the interphase between the cold diffuse gas and the hot ICM a good spatial resolution is needed. The *Herschel* Space Telescope gives us the possibility to achieve this goal but requires a good knowledge of the instruments' PSFs to perform multi-wavelength studies on a pixel-by-pixel basis.

Convolving the images to a common resolution implies the use of convolution kernels. Using Gaussian PSFs for the calculation of these kernels we do not take into account the secondary lobes of PSFs, producing artifacts in the convolved images. However, a more sophisticated method for the computation of convolution kernels (Aniano et al. 2011), using measured and circularized PSFs, does not account for the spectrum of the observed source and ignores asymmetric features of the PSFs. We therefore plan to use a different approach (Bayesian method, Arab et al. 2012) to calculate convolution kernels accounting for both these effects.

The mixing between interstellar dust and hot gas is expected to occur each time there is a violent event, such as galaxy-galaxy collisions or ram pressure stripping. This phenomenon is often not taken into account but is an important source of destruction of small grains and may contribute significantly to the dust heating in galaxies.

We identified another couple of interacting galaxies, the galaxy system M51, that might be interesting to retrieve more information on this mechanism. The galaxy system M51 represents the collision between two galaxies: the spiral SAbc galaxy NGC 5194 (the larger central galaxy in Fig. 5.20) and the SB0p NGC 5195 (the small galaxy to the north in Fig. 5.20, north is up and west is right; we use this convention for all the images in this section). This galaxy system is closer than the Eyes Galaxies (23 Mly wrt 52 Mly of the eyes galaxies) and therefore might be less affected by resolution problems.

5.3.1 The galaxy system M51

The grand-design system M51 is the result of a complicated gravitational interaction between two galaxies, following their first encounter $\sim 300-500$ Myr ago (Salo and Laurikainen 2000; Dobbs et al. 2010). In agreement with this scenario, a color-magnitude

Figure 5.19: Galaxy system M51 as observed by Hubble Space Telescope. Composite image of B-band (435 nm), V-band (555 nm), H-α + NII (658 nm) and infrared (814 nm). North is up, west is right. Credit: NASA, ESA, S. Beckwith (STScI), and The Hubble Heritage Team STScI/AURA).

diagram measured using the *Hubble* Space Telescope (HST), suggests a burst of star formation both in NGC 5194 and in its companion galaxy NGC 5195 $\sim 380 - 450$ Myr ago (Tikhonov et al. 2009). However, while in NGC 5194 $\sim 19,600$ HII regions are detected proving the ongoing star formation (Lee et al. 2011), there is little evidence for recent star formation in NGC 5195 as indicated by a lack of Hα emission (Thronson et al. 1991) and lack of dense molecular clouds (Kohno et al. 2002).

The system M51 has been well studied in the last 30 years and observations at different wavelengths are available. In particular, for a preliminary analysis we used the the *Chandra* (ObsID 13813) X-ray data and the *Herschel* PACS and SPIRE data (Mentuch Cooper et al. 2012). We focus here on the *Herschel* data. The PACS data reduction was performed[11] using the recent version of `Scanamorphos` (version 23, Roussel 2013) and the SPIRE data reduction using HIPE (version 12). The assumed FWHM

[11]The author of this manuscript would like to thank Karin Dassas (research engineer at the IAS) for having performed the PACS and SPIRE data reduction of M51.

of the PACS-SPIRE beams and the flux accuracies are the same as those mentioned in Section 5.1.

In order to study the heating of dust in this system, in a similar way to the approach shown in Section 5.1 we build the dust temperature map using PACS 70 and 160 μm and SPIRE 250 and 350 μm. We convolved all the images to the resolution of the SPIRE 350 μm assuming Gaussian PSFs. The dust temperature map that we obtain (Fig. 5.20) is both qualitatively and quantitatively similar to that shown by Mentuch Cooper et al. (2012).

As noted in this previous study, the companion galaxy NGC 5195 presents the highest dust temperature ($T \sim 28 - 35\,\mathrm{K}$) in the whole system and so represents an interesting case to study. Mentuch Cooper et al. (2012) explored different heating mechanisms: (1) an ongoing star formation, (2) heating by an evolved stellar population and (3) heating by its active galactic nucleus. The first hypothesis is firmly ruled out, there is little evidence for star formation in this galaxy (Thronson et al. 1991; Kohno et al. 2002). Furthermore, evolved stellar populations are found to play an important role in dust heating in galaxies (Bendo et al. 2012a; Boselli et al. 2012), but the dust temperature measured in NGC 5195 is too elevated for this mechanism to be dominant. Finally, the nucleus of NGC 5195 harbors an AGN (Moustakas et al. 2010) and this object might play an important role in heating the dust in this galaxy. However, mid-infrared observations with ISOCAM show a lack of AGN emission lines (Boulade et al. 1996) and rule out LINER activity as the dominant source of mid-infrared emission.

We propose that this high dust temperature might be explained with the mechanism of electron collisional heating. Diffuse soft (0.5 - 1.2 keV) X-ray emission is observed from the central region of NGC 5195 (Fig. 5.20) suggesting the presence of a hot and diffuse gas (Ehle et al. 1995). This would be consistent with the global scenario. A star burst occurred in this galaxy $\sim 380 - 450\,\mathrm{Myr}$ ago, and there is no evidence of recent star formation. Stellar radiation is therefore not intense enough to explain the measured high dust temperature. However, starburst galaxies generally present associated soft X-ray emission indicating the presence of a hot fully-ionised gas (e.g., Cappi et al. 1999; Pietsch et al. 2000; Tschöke et al. 2001). We can imagine that also in this galaxy, at the time of the starburst a hot gas was present. A hot gas cools on very long timescales ($\sim 10^8\,\mathrm{yr}$, see Section 5.B) and it is therefore likely that this same gas is still observable today. This hot gas would then, through electron collisions, heat the dust grains explaining the hot dust temperature.

This represents a very preliminary study of the system M51 and a full and quantitative investigation will be necessary. Morover, we performed the convolution of different images assuming Gaussian PSFs as in the study described in Section 5.1 and we will need to test other convolution kernels in order to confirm the detected high dust temperature. However, in this case, the central region of NGC 5195 represents a bright source in all the PACS and SPIRE bands and is certainly less affected by the width and shape of the PSFs than the interesting "east-side region" of NGC 4438.

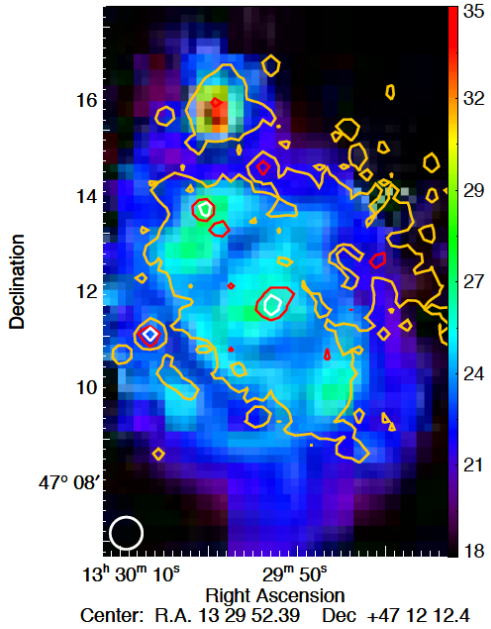

Figure 5.20: Dust temperature map of M51 calculated from *Herschel* data assuming fixed $\beta = 2$. X-ray data (orange and white contours indicate lowest and highest intensities, respectively) are superimposed.

5.A Rigorous error estimation

In order to estimate the errors on the different parameters in a more accurate way we perform a Monte Carlo iteration of a χ^2 fit. The error on the flux in each band is given by the quadratic sum of calibration and statistical errors (see Sect. 5.1.1). We assume that the statistical errors follow a Gaussian distribution while the calibration errors follow a uniform distribution with $\sigma = \sigma_{\rm CAL}$.

To test our method, we select one pixel in the west-side of the galaxy with $A_{\rm V} \sim 0.3$. We perform a fit to the four *Herschel* bands using a modified blackbody and, assuming a fixed $\beta = 1.8$, we obtain $T = (18.6 \pm 0.5)\,{\rm K}$ and $\tau_{100} = (3.3 \pm 0.4) \times 10^{-4}$. We randomly perturb the measured flux in each band in order to generate 300 SEDs and we fit them to a modified blackbody (with fixed $\beta = 1.8$). We obtain in this way two ensembles (T and τ_{100}) of 300 parameters. In the histograms in Fig. 5.21a and 5.21b we show the distribution of temperature and optical depth in the ensembles. The black solid line is the mean value of the ensemble, while the dashed black lines represent the 66.67 % confidence level between 0.1667 and 0.8333 of the repartition function. We obtain $T = (18.5^{+0.8}_{-0.7})\,{\rm K}$ and $\tau_{100} = (3.4^{+0.17}_{-0.6}) \times 10^{-4}$. We notice that the uncertainties

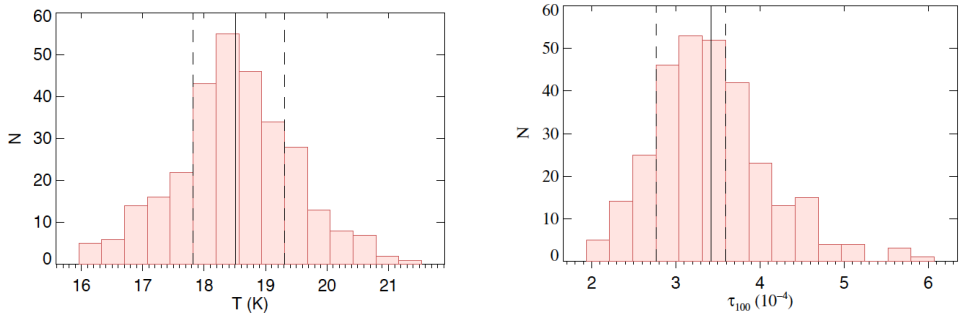

(a) (b)

Figure 5.21: (a) Parameter distribution of temperature after 300 MC sampling. The black solid line represents the mean value of the ensemble while the two dashed lines represent the inferior and superior 1σ limits. (b) Parameter distribution of τ_{100} after 300 MC sampling.

on both temperature and optical depth estimated with this MC method are very similar to the ones we obtain using the fitting routine. We therefore use the errors obtained with the fitting routine for our analysis.

5.B Hot gas cooling

A low-density and high-temperature plasma, radiating in soft X-ray bands, cools down. Its radiative cooling was calculated by Raymond et al. (1976). The power radiated per unit volume, Λ, is related to the cooling coefficient, L as

$$\Lambda = L\, n_{\rm e} n_{\rm H}, \tag{5.B.1}$$

where $n_{\rm e}$ and $n_{\rm H}$ are the electron and hydrogen number density in the gas, respectively. The cooling coefficient has been approximated by Draine (2011) as:

$$L \sim 1.1 \times 10^{-22}\, T_6^{-0.7}\, {\rm erg\,cm^3\,s^{-1}} \qquad \text{for } 10^5 < T(K) < 10^{7.3} \tag{5.B.2}$$

$$L \sim 2.3 \times 10^{-24}\, T_6^{0.5}\, {\rm erg\,cm^3\,s^{-1}} \qquad \text{for } T(K) \geqslant 10^{7.3} \tag{5.B.3}$$

In a dust-free plasma, soft X-ray emission represents the main source of cooling and knowing the initial gas temperature we can therefore estimate the cooling timescale. The time derivative of the internal energy of a hot plasma ($T \sim 10^4 - 10^7$ K), according to Raymond et al. (1976) and Draine (2011) is given by

$$\frac{dE}{dt} = -1.7 \times 10^{-18} T^{-0.7} n_{\rm e} n_{\rm H}. \tag{5.B.4}$$

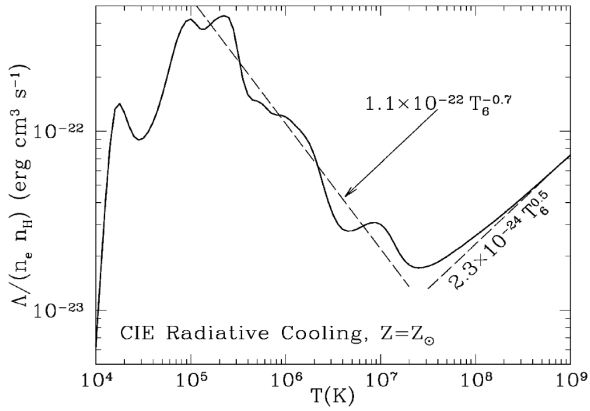

Figure 5.22: Cooling function L as a function of the gas temperature as approximated by Draine (2011).

The energy radiated by a gas at a temperature T is $E \sim k_{\rm B}T$ and therefore its derivative with respect to the gas temperature is

$$\frac{dE}{dT} = \frac{3}{2} n_{\rm e} k_{\rm B}, \tag{5.B.5}$$

with $k_{\rm B}$ the Boltzmann constant. Then, combining the two equations we find

$$\frac{dT}{dt} = -8.2 \times 10^{-3} T^{-0.7} n_{\rm H} \tag{5.B.6}$$

and finally, integrating over time and temperature, the cooling timescale results

$$t = \frac{71.6}{n_{\rm H}({\rm cm}^{-3})} T_0({\rm K})^{1.7}\, s, \tag{5.B.7}$$

where T_0 is the initial gas temperature. For example, a hot coronal-type gas with $T_0 = 5 \times 10^6$ K and $n_{\rm H} \sim 10^{-3}\,{\rm cm}^{-3}$ will radiatively cool in a timescale of $\sim 5 \times 10^8$ yrs.

On the contrary, if dust is present in the plasma, ions and electrons colliding with dust grains will transfer a significant amount of energy to the dust and this will mechanism will represent the main source of gas cooling. The cooling coefficient, $L_{\rm d}$, for a dusty plasma has been estimated by Dwek (1987) as:

$$L_{\rm d}(T) = \frac{1}{n_{\rm e} n_{\rm H}} \int_{a_1}^{a^2} H(a, T, n) \frac{dn_{\rm d}}{da} da. \tag{5.B.8}$$

where $H(a, T, n)$ is the dust heating rate due to collisions and $\frac{dn_{\rm d}}{da}$ is the dust size distribution between sizes a_1 and a_2. In Fig. 5.23 we show the cooling coefficient as a

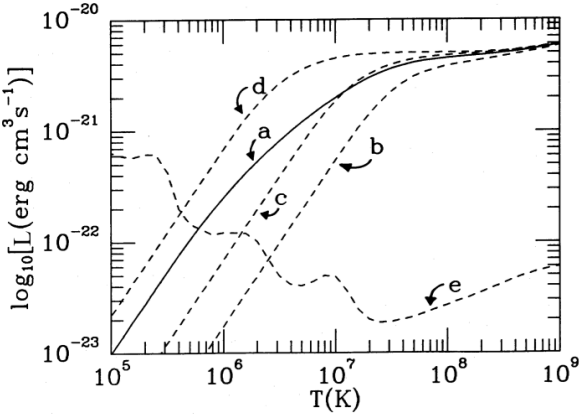

Figure 5.23: Cooling coefficient for a fusty plasma for an extended MRN distribution (a), a silicate-graphite mixture of 400 nm (b), 100 nm (c) and 10 nm (d). The curve labeled as (e) represents the radiative cooling. Dwek (1987).

function of the gas temperature for an extended MRN size distribution (1 - 500 nm) and for grains of different sizes.

We note that for high-temperature plasma ($T \gtrsim 10^6\,\mathrm{K}$) the cooling mechanism is dominated by energy transfer to the dust while for lower temperatures the radiative cooling is more efficient. Also, we note that, for a given grain abundance, the presence of smaller grains lead to a more efficient cooling of the plasma.

Chapter 6

A re-evaluation of dust processing in supernova shock waves

> If you want to go quickly, go alone. If you want to go far, go together.
>
> African proverb

Contents

Dust processing in interstellar shock waves dominates the destruction of dust in the ISM and is key to estimating the dust lifetime in a galaxy. In this chapter we apply our updated dust destruction modelling to the case of the coupling between dust and supernova-triggered shock waves and give an estimate for the dust destruction timescale in the Milky Way. Furthermore, we calculate the dust emission and extinction we would expect from a shocked region in the ISM and compare them to those observed in unshocked diffuse medium. Most of this chapter is taken from the published paper Bocchio et al. (2014).

6.1 A supernova explosion: the different stages

As mentioned in Chapter 1, a supernova represents the explosion of a massive star ($M \gtrsim 8M_\odot$). During this violent phenomenon a large amount of energy is released ($E \approx 10^{51}$ erg) and a blast wave is triggered. The initial shock velocity can be as high as 3×10^4 km s^{-1} and during the expansion it slows down and sweeps up the encountered interstellar material and in the meantime injects gas and dust in the ISM.

We assume that a supernova of energy E_0 accelerates a gas mass M_0 to an initial velocity v_0 and that at a given time t the supernova has swept up a sphere of radius R_t of interstellar matter of density ρ_0. Following Woltjer (1972) the dynamics of the expansion of a supernova is classically divided into four phases:

I the large energy and pressure released by a supernova in a small region triggers a blast wave. During the first phase, the gas mass accelerated to its initial velocity is larger than that of the swept up material, $M_0 \gg {}^4\!/_3\pi R_t^3 \rho_0$, and the dynamics of expansion will solely depend on the explosive process.

II During the second phase, the swept-up matter dominates the remnant, $M_0 \ll {}^4\!/_3\pi R_t^3 \rho_0$ but the radiative cooling is negligible and the energy is conserved. This is the so-called Sedov-Taylor phase (Taylor 1950; Sedov 1969). The radius of the shocked interstellar region, for a monatomic gas, is related to the initial energy injected by the supernova and to the density of the ISM as

$$R_\mathrm{t} = 1.17 \left(\frac{E_0}{\rho_0}\right)^{1/5} t^{2/5}. \tag{6.1.1}$$

The velocity, v_s, of the expanding shell is then given by

$$v_\mathrm{s} = \frac{dR}{dt} \tag{6.1.2}$$

$$= \frac{2}{5}\frac{R_\mathrm{t}}{t}. \tag{6.1.3}$$

We note that in this case the quantity R^3t^2 is constant. A supernova shock wave hitting the cold interstellar medium represents a strong shock and so the density, ρ^*, and pressure, p^*, of the post-shock gas are

$$\rho^* = 4\rho_0 \tag{6.1.4}$$

$$p^* = \frac{3}{4}\rho_0 v_\mathrm{s}^2 \tag{6.1.5}$$

and, according to the ideal gas law, the temperature, T^*, behind the shock front is given by

$$T^* = \frac{3}{16}\frac{v_\mathrm{s}^2 \bar{m}}{k_\mathrm{B}}, \tag{6.1.6}$$

where $\bar{m}$ is the average mass per particle in the post-shock gas. Therefore, as the gas shell slows down, its temperature drops quickly. The mass of gas, $M_\mathrm{s}(v_\mathrm{s})$, shocked to a velocity of at least v_s during this phase can be expressed as (McKee 1989):

$$M_\mathrm{s}(v_\mathrm{s}) = \frac{E_0}{\sigma v_\mathrm{s}^2} \tag{6.1.7}$$

$$= 6800\frac{E_{51}}{v_{\mathrm{s}7}^2}\, M_\odot, \tag{6.1.8}$$

where the constant $\sigma = 0.736$ (Ostriker and McKee 1988), E_{51} is the energy of the supernova expressed in 10^{51} erg and $v_{\mathrm{s}7}$ is the shock velocity in units of 100 km s^{-1}.

III For a sufficiently low shock velocity ($v_\mathrm{s} \lesssim 200\,\mathrm{km\ s^{-1}}$), radiative cooling starts to be an important process and the matter behind the shock cools quickly. Pressure forces are no longer important and the shell expands conserving its momentum:

$$\frac{4}{3}\pi R_\mathrm{t}^3 \rho_0 v_\mathrm{s} = \text{constant}. \tag{6.1.9}$$

Most of the interstellar dust destruction occurs during this phase.

IV Finally the velocity of the expanding shell becomes compatible to the velocity of the random motion of the surrounding gas ($v_\mathrm{r} \sim 10\,\mathrm{km\ s^{-1}}$) and the remnant merges with the ISM.

6.2 Dust destruction and formation

It is observationally well established that shock waves in the ISM are able to destroy dust grains (Routly and Spitzer 1952; Cowie 1978; Welty et al. 2002). The most recent theoretical studies (e.g. Jones et al. 1994, 1996; Serra Díaz-Cano and Jones 2008;

Jones and Nuth 2011) estimated the dust destruction in supernova (SN) shock waves, restricting their calculations to shocks in the warm ionised medium (WIM), where the dominant destruction occurs (Seab 1987; McKee 1989). They found a lifetime of $\sim 2 \times 10^8$ yr for carbonaceous grains and $\sim 4 \times 10^8$ yr for silicate grains. However, since the early studies of dust processing in shock waves (Barlow 1978b,a; Draine and Salpeter 1979b,a; Dwek and Scalo 1980; Seab and Shull 1983; McKee et al. 1987; Jones et al. 1994, 1996) our dust modelling has evolved considerably and so it is therefore timely to re-visit this issue.

Dust is formed in cirmustellar regions (around AGB stars) and also in supernovae (SNe). The dust injection timescale from AGB stars has been estimated to be $\sim 3 \times 10^9$ yr (Dwek and Scalo 1980; Gehrz 1989; Jones and Tielens 1994). On the other hand, the formation of dust in the ejecta of core collapse SNe is a debated topic. For example, observations of type II SNe such as Cas A or Supernova 1987A reveal the presence of newly formed dust ($\lesssim 0.1\,M_\odot$ for CasA, Arendt et al. 2014, $\sim 0.4 - 0.7\,M_\odot$ for Supernova 1987A, Matsuura et al. 2011). However, these SNe have not yet reached the phase where the reverse-shock would destroy part of the observed dust. Furthermore, analyses of presolar dust grains within primitive meteorites seem to indicate evidence for SiC and graphite grains formed in Type II SNe (*e.g.* Lodders 2006; Hoppe et al. 2009, 2010). If a significant amount of dust was formed in SN ejecta, this could considerably reduce the dust injection timescale but as yet the evidence is inconclusive.

Based on these results, the injection timescale is much longer that the theoretical lifetime of dust and we would therefore expect to see a large fraction of heavy elements (i.e. C, Si, Fe, Mg, O, etc.) in the gas phase and almost nothing in dust grains. On the contrary, the observational evidence shows that most of the heavy elements are locked into grains (i.e. $\geqslant 50\%$ for C and $\geqslant 90\%$ for Si, Fe and Mg) in the diffuse ISM (Snow and Witt 1996; Jenkins 2009 and references therein). This represents a long-standing conundrum and implies the re-formation of dust grains by accretion from the gas phase in denser regions of the ISM in order to match the observations. It has been shown that there are viable mechanisms for the re-formation of carbonaceous grains from the gas phase under low temperature and pressure conditions (e.g. Dartois et al. 2005). On the other hand, experimental and observational results seems to indicate that silicate grains are hard to form under ISM conditions and must therefore be formed in AGB stars and preserved in interstellar shocks (Jones and Nuth 2011).

In this study we re-evaluate the dust processing and lifetime using updated dust processing. We model the dust destruction in SN shock waves and the evolution of the size distribution of dust using a new version of the GRASH code used by Jones et al. (1994, 1996). We improve upon the erosion calculations by updating the carbonaceous material from graphite to hydrogenated amorphous carbon, use a molecular approach for the dissociation of small carbonaceous grains, update the grain charge treatment replacing the McKee et al. (1987) analytical charge scheme with the Weingartner and Draine (2001) grain charge calculations and introduce a new and more physical dust model (i.e. Jones et al. 2013). Finally we couple the GRASH code to the DustEM code

(Compiègne et al. 2011) in order to calculate the emission and extinction of shocked dust.

6.3 The GRASH code

The GRASH code is a FORTRAN code[1] that follows the processing of dust in supernova-generated interstellar shock waves. The methodology of the code was first presented by Jones et al. (1994). In the code they implemented the grain acceleration theory from McKee et al. (1987) and the treatment of destructive processes from Tielens et al. (1994). In order to guarantee the mass conservation throughout the shock they modelled the mass loss processes using an algorithm based on the grain coagulation model of Nakagawa et al. (1981) and Mizuno et al. (1988). The processes taken into account were thermal and inertial sputtering and vaporization. In 1996 shattering was added to the dust processing (Jones et al. 1996). They assumed graphitic-type carbon and silicate grains following a MRN-like (Mathis, Rumpl, and Nordsieck 1977) size distribution. They did not co-solve the shock dynamics and grain physics but followed the dust evolution self consistently with the steady-state shock structure profiles (Raymond 1992). This represents a good approximation for shock velocities $\lesssim 200\,\mathrm{km\,s^{-1}}$ since dust is the main coolant only for faster shock waves (Draine 1981) and the dust feedback into the shock structure is negligible.

In this study we have updated and extended the original GRASH code (now called GRASH_EX). In this section we describe the new physics and features. Based on a recent dust model (Jones et al. 2013, Section 2.5) we update the carbonaceous grains by replacing graphite/a-C with (hydrogenated) amorphous carbon, a-C(:H), and by considering a molecular approach to the small grain destruction. Furthermore, we model the destruction of silicates taking into account their core-mantle structure. We update the grain charge treatment replacing the McKee et al. (1987) analytical charge scheme to the Weingartner and Draine (2001) approach and treat thermal and inertial sputtering as a single process. Finally we couple the GRASH_EX code with the DustEM code[2] in order to predict the post-shock dust emission and extinction in the ISM.

6.3.1 Dust composition effects

Since the formulation of the MRN model, our understanding of the dust composition has made significant progress. Recent dust models have adopted amorphous carbonaceous grains instead of graphitic-type grains and include aromatic-rich nano-particles such as polycyclc aromatic hydrocarbons (PAHs) or arophatic clusters (Micelotta et al. 2012). Furthermore the Jones et al. 2013 model, in order to take into account dust

[1]The GRASH code was originally written and developed by A. P. Jones in the period 1990 to 1995.

[2]The DustEM code (Compiègne et al. 2011, http://www.ias.u-psud.fr/DUSTEM) is a FORTRAN code that calculates the dust emission and extinction for a given dust size distribution and interstellar radiation field.

evolution in the ISM, considered a-C coated silicate grains. It is therefore necessary to update the modelling of dust destruction in order to properly account for the proposed core/mantle dust composition.

(Hydrogenated) amorphous carbon sputtering

In interstellar shocks the gas temperature can be as high as $\sim 5 \times 10^5$ K and grains therefore undergo sputtering due to collisions with the hot ionised gas. The sputtering of graphitic-type grains can be estimated following Tielens et al. (1994). In this study they adopted an analytical function for the sputtering yield which depends on the grain physical parameters and fits the experimental data well with only one free parameter, K (Tielens et al. 1994, Eq. 4.13). This model was then updated by Serra Díaz-Cano and Jones (2008), based on the ideas of Jurac et al. (1998), in order to calculate the size-dependent sputtering yield of a-C(:H) grains. In Table 6.1 we summarize the main parameters for the two materials based on studies by Tielens et al. (1994) for graphitic-type grains and by Serra Díaz-Cano and Jones (2008) for a-C(:H) grains. ρ is the density of the material, X_H is the H atom fraction, U_0 the surface binding energy, K is a free parameter in this formalism and $< Z_2 >$ and $< M_2 >$ are the average atomic number and mass of the target atoms[3]. We note in particular that there is a big difference in the density between the two materials. Serra Díaz-Cano and Jones (2008) showed that, regardless the H atom fraction of the a-C(:H) grains, they are much more susceptible to sputtering than graphitic-type grains due to their lower density.

Table 6.1: Parameters for sputtering of graphitic-type and a-C:H grains.

Material	ρ (g cm^{-3})	X_H	U_0 (eV)	K	$< Z_2 >$	$< M_2 >$
graphite	2.2	0	4	0.65	6.0	12
a-C:H	1.4	0.4	4	-0.04	4.0	7.6

Furthermore, Serra Díaz-Cano and Jones (2008), took into account the finiteness of the a-C(:H) grains (see Section 3.2.3). Fig. 6.1 and 6.2 illustrate the thermal sputtering rate constant per carbon atom, $\frac{1}{N_C n_H}\frac{dN_{sp}}{dt}$, for grains of radius $a = 13$ nm and $a = 130$ nm, respectively, for different projectile atoms/ions (H, He, C, N and O) as a function of the gas temperature, T_{gas}. The blue solid lines refer to the estimate by Tielens et al. (1994) for a graphitic-type grain, the black lines refer to the erosion rate of a-C:H grains without any correction due to the size while red lines refer to a-C:H grains with the size effect included. We notice that, due to the lower density of a-C:H with respect to graphite, without including the correction due to the finiteness of the grain, the rate constant for a-C:H grains is about an order of magnitude larger than the rate constant for graphitic grains in the range of temperatures $T = 10^4 - 10^8$ K.

[3]The average atomic number and mass of the target atoms are related to the H atom fraction ($X_H = \frac{N_H}{N_H + N_C}$) by: $< Z_2 >= [X_H Z_H + (1 - X_H) Z_C]$, $< M_2 >= [X_H M_H + (1 - X_H) M_C]$.

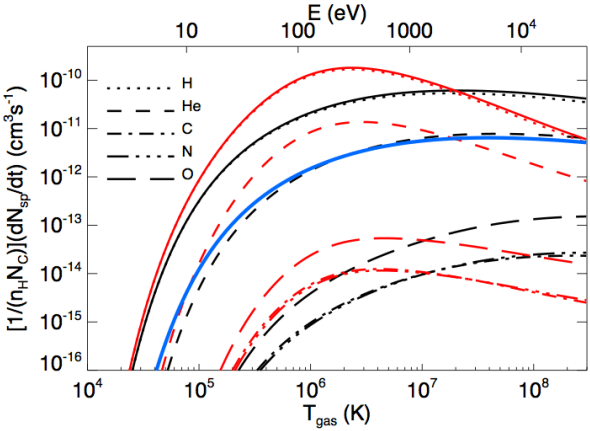

Figure 6.1: Thermal sputtering rate constant for an a-C:H grain of radius 13 nm with (red lines) and without (black lines) the size correction included for different projectiles (the total sputtering is indicated by solid lines). The blue solid line refers to the erosion rate for a graphitic-type grain of radius 13 nm.

Furthermore, comparing the thermal sputtering with and without the size effect included (red and black lines) for both $a = 13$ and 130 nm (see Fig. 6.1 and 6.2), we note that for low temperatures ($T_{\rm gas} \sim 10^4 - 10^5\,{\rm K}$), the inclusion of the size effect does not affect the rate constant. On the other hand, for intermediate temperatures ($T_{\rm gas} \sim 10^6 - 5 \times 10^7\,{\rm K}$), a significant enhancement of the rate constant is seen, which corresponds to the enhancement in the sputtering yield due to the finiteness of the grain. Then, for high temperatures ($T_{\rm gas} > 2 \times 10^7\,{\rm K}$ for 13 nm and $T_{\rm gas} > 3 \times 10^8\,{\rm K}$ for 130 nm), the penetration depth is larger than the grain size and the inclusion of the size effect in the calculation of the sputtering rate leads to a reduction in the rate constant.

Amorphous carbon fragmentation and vaporization

Following the collision between grains, depending on the energy of the impact, the grains can undergo fragmentation or even vaporization. Serra Díaz-Cano and Jones (2008) deduced the parameters for fragmentation and vaporization for a-C:H grains scaling the parameters used by Tielens et al. (1994) according to the physical properties of a-C:H and graphitic grains (see Section 3.5.5). Fragmentation and vaporization are affective at lower energies for a-C(:H) grains than for graphitic grains, which leads to stronger effect in shock waves.

The parameters for fragmentation and vaporization due to collisions between grains are based on the physics of collisions between hard spheres. However, the small car-

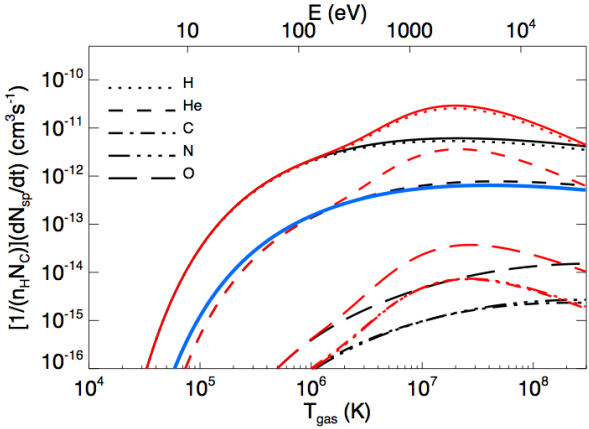

Figure 6.2: Same as per Fig. 6.1 but for a grain of radius 130 nm.

bonaceous grains we consider in the Jones et al. (2013) dust model are in the molecular regime and cannot be considered as hard spheres. Therefore this approach is probably not valid in the case of collisions between nano-particles and large grains (see discussion in Section 3.5.6 and 6.5.2).

Small carbonaceous grain destruction

The erosion of polycyclic aromatic hydrocarbons (PAHs), nm-size particles, in a hot gas has been studied in detail by Micelotta et al. (2010a). They considered dissociative sputtering resulting from the combination of nuclear interaction and electronic interactions, and electron collisions. They showed that the destruction of very small carbonaceous grains, for temperatures $T_{\rm gas} \leqslant 5 \times 10^7$ K, is dominated by electron collisions. On the other hand, the sputtering of larger grains ($a \gtrsim 3$ nm, corresponding to $N_{\rm C} \gtrsim 900$) is dominated by nuclear and electronic interactions (see also Section 4.1).

Bocchio et al. (2012) showed that, the sputtering rate constant for $T_{\rm gas} \lesssim 10^7$ K and $a \gtrsim 3$ nm, calculated using the molecular approach of Micelotta et al. (2010a) and the classical approach used by Tielens et al. (1994) and Serra Díaz-Cano and Jones (2008) are the same to within a factor two (Section 4.1). Therefore, in the GRASH_EX code, the large grain sputtering is treated using the classical approach while the sputtering of grains with $a \lesssim 3$ nm is treated using the molecular approach.

Treatment of the core-mantle structure of grains

As presented in Section 1.5, in the Jones et al. (2013) dust model both carbonaceous and silicate grains have core-mantle structure and we need to use two different approaches for the two materials.

The sputtering yield of amorphous carbon is little affected by its H atom content (Serra Díaz-Cano and Jones 2008) thus the aliphatic-rich core and the aromatic-rich mantle of the carbonaceous grains are treated in the same way. We therefore do not keep track of the thickness of the aromatic mantle on the carbonaceous grains.

The treatment of silicate grains must take account of the different mantle and core sputtering properties; silicate core with a carbonaceous mantle. However, to keep track of the mantle thickness on the surface of the silicate grain core throughout the whole shock, and for each bin in the mass distribution, is difficult to keep track of and is time consuming. We therefore make an approximation: during the time needed to destroy the a-C mantle, the grain core is little affected and none of its atoms is ejected. To check whether this assumption is valid, we use the *Stopping and Range of Ions in Matter* software[4] (SRIM, Ziegler et al. 1985) to simulate the sputtering of core-mantle silicate grains due to collisions with H^+ and He^+ ions (i.e. the ions that dominate the sputtering process). We consider a thick semi-infinite plane made of amorphous forsterite-type silicate covered by a thin layer of amorphous carbon. We vary the carbonaceous mantle thickness in order to mimic the destruction of the mantle. The relevant parameters involved in the sputtering processes are: the density of the material, ρ, the surface binding energy, E_S, the displacement energy, E_D, and the lattice binding energy, E_B (see Section 6.5.1 for details). Despite the uncertainties on these parameters (see Section 6.5.1) we are here interested in the relative sputtering yield for different mantle thicknesses and not in their absolute values. We use here the parameters adopted by Serra Díaz-Cano and Jones (2008) for amorphous carbon and the parameters presented in Table 6.6 for silicate grains. We consider a maximum shock velocity of 200 $\mathrm{km\,s^{-1}}$. In this case the energy of the impinging H^+ and He^+ ions reaches at most $\sim 100\,\mathrm{eV}$ and $\sim 470\,\mathrm{eV}$ respectively. We use these energies for all the simulations presented in this section.

We simulate 10^5 collisions and average the resulting sputtering yield depending on the atomic mass of the sputtered atom from the silicate core (see Section 6.5.1, Eq. 6.5.2). In Table 6.2 we report the obtained silicate sputtering yield. We notice

Table 6.2: SRIM calculations (based on 10^5 collisions) of the silicate core sputtering yield, Y_i, due to bombardment by H^+ and He^+ ions. The energy of the impinging H^+ and He^+ is 100 eV and 470 eV, respectively, and the a-C mantle thickness varies from 5 nm to 0 nm in order to mimic the destruction of the mantle.

	Y_i	
Mantle thickness	H^+	He^+
5 nm	$< 10^{-5}$	$< 10^{-5}$
1 nm	$< 10^{-5}$	$\sim 4.3\,10^{-4}$
0 nm	$< 10^{-5}$	$\sim 5.5\,10^{-2}$

[4]SRIM is a collection of software packages which calculates the transport of ions in matter, calibrating the results on the available experimental data.

that the sputtering yield for H^+ projectiles is negligible even for bare silicate grains, while the sputtering yield for He^+ is highly affected by the presence of the mantle; even in the case of 1 nm carbonaceous mantle, the sputtering yield is two orders of magnitude lower than in the case of bare silicates. This leads us to the conclusion that our approximation is valid.

We then define a time needed for the carbonaceous mantle to be completely destroyed, $t_{\rm man}$. We run the GRASH_EX code a first time for different shock velocities to estimate $t_{\rm man}$ for a silicate grain of radius $a = 160\,{\rm nm}$, *i.e.* the most abundant silicate grains in the Jones et al. (2013) dust model. We then consider that the silicate grains are not eroded until a time $t_{\rm man}$ has passed (in order to mimic the effect of carbonaceous mantles on silicate grains) and then remove the mantles and allow silicate grain sputtering. In Table 6.3 we summarize $t_{\rm man}$ for a grain of radius $a = 160\,{\rm nm}$ for different shock velocities. It is clear that $t_{\rm man}$ for all of the shock velocities is much

Table 6.3: $t_{\rm man}$ (yr) for different shock velocities ($\rm km\,s^{-1}$).

$V_{\rm shock}$	50	75	100	125
$t_{\rm man}$	2.0×10^4	1.8×10^3	1.0×10^3	7.1×10^2

$V_{\rm shock}$	150	175	200
$t_{\rm man}$	1.1×10^3	8.8×10^2	4.0×10^2

shorter than the typical shock timescale (i.e. $\sim 10^5\,{\rm yr}$). Therefore the presence of a carbonaceous mantle is not able to significantly protect silicate grains from erosion.

6.3.2 Grain charge

The acceleration, $dV_{\rm rel}/dt$, of a grain with respect to a shocked gas can be expressed as (McKee et al. 1987):

$$\frac{dV_{\rm rel}}{dt} = \frac{d\chi}{dt}\frac{V_{\rm rel}}{2\chi} - \frac{F_{\rm D}}{m} \tag{6.3.1}$$

The first term on the right (Cowie 1978; Shull 1978) is called betatron acceleration and is proportional to the time-derivative of the magnetic field strength (related to the shock compression χ). This acceleration is due to the gyration velocity around a magnetic field line. The second term is the drag deceleration, where $F_{\rm D}$ is the drag force and m the mass of the grain. The drag force was evaluated by Draine and Salpeter (1979b):

$$F_{\rm D} = F_{\rm D}({\rm direct}) + F_{\rm D}({\rm plasma}), \tag{6.3.2}$$

where $F_{\rm D}({\rm direct})$ is the direct collisional drag and $F_{\rm D}({\rm plasma})$ is the plasma drag. While the direct collisional drag only depends on the geometrical cross section and mass of projectiles and target, the plasma drag, which strongly depends on the grain

charge, can be expressed as:

$$F_{\rm D}({\rm plasma}) = 4\pi a^2 k_{\rm B} T_{\rm gas} \phi^2 \ln\Lambda \sum_i n_i z_i^2 H(s_i), \tag{6.3.3}$$

where a is the grain radius, $k_{\rm B}$ is the Boltzmann constant, $T_{\rm gas}$ the gas temperature, $\ln\Lambda$ the Coulomb logarithm, n_i and z_i the density and charge of the i-th ion. The electric potential parameter ϕ is expressed as:

$$\phi \equiv \frac{z_{\rm g} e^2}{a k_{\rm B} T_{\rm gas}}, \tag{6.3.4}$$

with $z_{\rm g}$ the grain charge and the function $H(s_i)$ given by:

$$H(s_i) = s_i \left(\frac{3}{2}\sqrt{\pi} + 2 s_i^3 \right)^{-1}, \tag{6.3.5}$$

where s_i is defined as:

$$s_i^2 = \frac{m_i V_{\rm rel}^2}{2 k_{\rm B} T_{\rm gas}}, \tag{6.3.6}$$

with m_i the mass of the i-th ion.

In the original work by Jones et al. (1994, 1996) the grain charge was calculated using the analytical charge scheme of McKee et al. (1987), which was based on calculations by Draine (1981) and Draine and Salpeter (1979a). A more recent study by (Weingartner and Draine, 2001, WD01) uses a better estimate of the electron sticking coefficient and the photoelectric yield and is based on experimental results.

We find (as noticed for the case of a hot gas in Section 4.1.2) that this update to the grain charge calculation leads to only small variations in the grain potential and therefore little affects the dust dynamics. Fig. 6.3 shows the potential parameter ϕ (see Eq. 6.3.4) as a function of the gas temperature, $T_{\rm gas}$ for a silicate grain of radius of 160 nm. The potential is calculated using both the analytical scheme of McKee et al. (1987) (black lines) and the more recent estimates by WD01 (red lines). The ζ parameter was introduced by McKee et al. (1987) and is defined as:

$$\zeta = \frac{G_0}{n_{\rm e}} \left(\frac{a}{10\,{\rm nm} + a} \right), \tag{6.3.7}$$

where G_0 is the incident UV intensity normalized to the average interstellar background flux ($2.4 \times 10^6\,{\rm cm^{-2} s^{-1}}$) adopted by Draine and Salpeter (1979a) and $n_{\rm e}$ is the electron density in the gas. In Fig. 6.3 we consider $\zeta = 0$, 1, 10 and 100 and assume that the gas is fully ionised ($n_{\rm e} = n_{\rm H}$). In the GRASH_EX code we have updated the grain charge calculation to the WD01 approach.

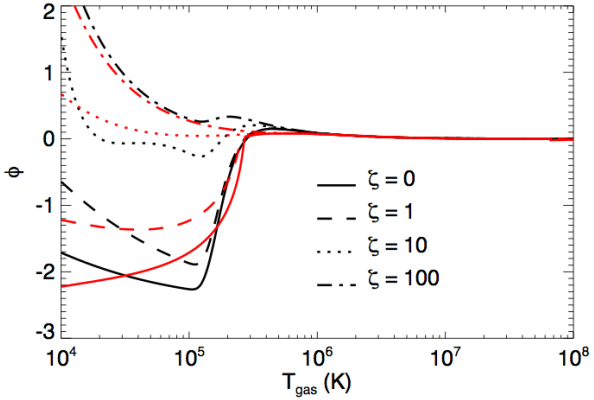

Figure 6.3: The potential parameter $\phi = \frac{z_g e^2}{a k_B T_{gas}}$ as a function the gas temperature for a 160 nm silicate grain. Different values of ζ (see text for details) are labeled with different line styles and the black and red curves refer to the McKee et al. (1987) analytical scheme and to the WD01 charge scheme, respectively.

6.3.3 The skewed Maxwellian distribution

In the formalism introduced by Tielens et al. (1994) a distinction is made between thermal sputtering (due to a hot gas) and the inertial sputtering of a grain as a function of its drift velocity in the gas. The thermal sputtering rate can be expressed as:

$$\frac{dN_{sp}}{dt} = 2\pi a^2 \sum_i n_i < Y_i v >, \tag{6.3.8}$$

where $\frac{dN_{sp}}{dt}$ is the number of sputtered atoms per unit time, a is the grain radius, n_i the density of the i-th ion in the gas and

$$< Y_i v >= \int Y_i v f_M(v) dv, \tag{6.3.9}$$

where Y_i is the sputtering yield of the i-th ion, v is the relative (thermal) velocity between the i-th ion and the target grain and $f_M(v)$ is the Maxwellian distribution for a velocity v.

The non-thermal or inertial sputtering rate can be expressed as:

$$\frac{dN_{sp}}{dt} = 2\pi a^2 v_g \sum n_i Y_i (E = 0.5 m_i v_g^2). \tag{6.3.10}$$

This corresponds to a thermal sputtering rate where the function used to average the sputtering yield is not the Maxwellian distribution but a Dirac delta function centered at the drift velocity of the grain in the gas, v_g.

However, inertial sputtering is only an approximation and in reality, the gas is at a given temperature and the relative velocity between a grain and the surrounding ions is not unimodal but it is a combination of the thermal motion of the ions and the drift of the grain in the gas. This motion is well described by the skewed Maxwellian distribution (Shull 1978; Guillet 2008, see Appendix 6.A for details).

$$f_{\rm skM} = \sqrt{\frac{m_{\rm i}}{2\pi k_{\rm B} T_{\rm gas}}} \frac{v}{V_{\rm drift}} \left[\exp\left(-\frac{m_{\rm i}}{2k_{\rm B}T_{\rm gas}} (v - V_{\rm drift})^2 \right) - \exp\left(-\frac{m_{\rm i}}{2k_{\rm B}T_{\rm gas}} (v + V_{\rm drift})^2 \right) \right], \tag{6.3.11}$$

where $f_{\rm skM}$ is the velocity probability function, $m_{\rm i}$ is the i-th ion mass, $k_{\rm B}$ is the Boltzmann constant, $T_{\rm gas}$ is the gas temperature, v is the relative velocity between the ions and the grain and $V_{\rm drift}$ is the drift velocity of the grain in the gas. Replacing $f_{\rm M}$ with $f_{\rm skM}$ in Eq. 6.3.9 and using this expression in Eq. 6.3.8 we obtain the erosion rate of a grain in the case of a grain drifting in a gas whose ions are in random thermal motion at a given temperature $T_{\rm gas}$.

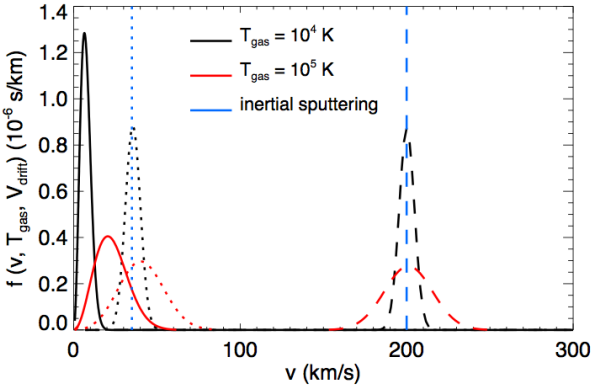

Figure 6.4: Skewed Maxwellian distribution as a function of the relative velocity between a grain and the gas for different drift velocities and gas temperatures. Solid lines show the case of $V_{\rm drift} = 0\,{\rm km\,s^{-1}}$, dotted lines the case of $V_{\rm drift} = 35\,{\rm km\,s^{-1}}$ and dashed lines the case of $V_{\rm drift} = 200\ {\rm km\,s^{-1}}$. Black lines are for a gas temperature $T_{\rm gas} = 10^4\,{\rm K}$, red lines are for $T_{\rm gas} = 10^5\,{\rm K}$ and the blue lines represent the inertial sputtering.

Fig. 6.4 shows the skewed Maxwellian distribution for $V_{\rm drift} = 0$, 35 and 200 km s^{-1} (solid, dotted and dashed lines respectively) for temperatures $T_{\rm gas} = 10^4\,{\rm K}$ (black lines) and $10^5\,{\rm K}$ (red lines) as a function of the relative velocity between a grain and an ion in the gas. We compare them to the corresponding Dirac delta functions at $V_{\rm drift}$

= 0, 35 and 200 km s^{-1} (blue lines). We notice that the Dirac delta function is a good approximation for $T_{\rm gas} = 10^4$ K but for $T_{\rm gas} = 10^5$ K the broadening of the distribution function and the shift of the peak position become important.

In the original code (Jones et al. 1994, 1996) thermal and inertial sputtering were assumed to be de-coupled. The thermal sputtering was neglected for a gas temperature $T_{\rm gas} < 10^4$ K, while the inertial sputtering was considered only in the case of a drift velocity $V_{\rm drift} > 0.1\,{\rm km\,s^{-1}}$. In the GRASH_EX code these two processes are coupled using the skewed Maxwellian distribution described above.

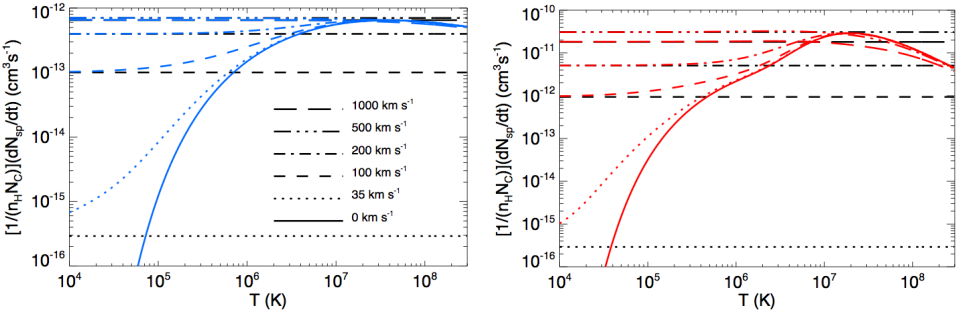

Figure 6.5: $\frac{1}{N_{\rm C} n_{\rm H}} \frac{dN_{\rm sp}}{dt}$ as a function of the gas temperature for a graphitic-type (a) and an a-C(:H) (b) grain of radius 130 nm for different relative velocities between the projectiles (H, He and C) and the target grain. Blue and red lines show the erosion rate computed using the skewed Maxwellian distribution while black lines show the inertial sputtering formulation.

To show the effect of the skewed Maxwellian distribution with respect to the Dirac delta function we consider the astrophysical relevant case of sputtering of a graphitic grain due to bombardment of H, He and C projectiles. As assumed by Bocchio et al. (2012), we consider the relative abundances 1, 0.1 and 10^{-4} for H, He and C, respectively. In Fig. 6.5a we plot the sputtering rate constant per carbon atom for a graphitic grain of radius $a = 130\,{\rm nm}$ as a function of the gas temperature for different $V_{\rm drift}$. We calculate the sputtering rate using the classical inertial sputtering (i.e. using a Dirac delta distributed velocity, black lines) and using the skewed Maxwellian distribution (blue lines). We clearly see in Fig. 6.5a that the inertial sputtering is not a good approximation at low drift velocities ($V_{\rm drift} \lesssim 100\,{\rm km\,s^{-1}}$) while it is a good approximation at higher velocities. In particular, for a drift velocity of 35 km s^{-1} and for $T \lesssim 10^5$ K, the sum of the thermal sputtering (blue solid line) and inertial sputtering (black dotted line) is lower, by a factor of 2 to 10, than the sputtering calculated using the skewed Maxwellian distribution (blue dotted line). This difference is due to the relevant high-energy tail in the case of the skewed Maxwellian approach (see Fig. 6.4).

Fig. 6.5 shows the sputtering rate constant per carbon atom for an a-C:H grain of radius $a = 130\,\mathrm{nm}$ as a function of the gas temperature with the inclusion of the size effect, which leads, as noticed in Section 6.3.1, to a lowering of the sputtering yield for high gas temperatures ($T_{\mathrm{gas}} \gtrsim 10^7\,\mathrm{K}$). In this case, the inertial sputtering, even for the largest velocities considered ($V_{\mathrm{rel}} = 1000\,\mathrm{km\,s^{-1}}$), is not a good approximation and the skewed Maxwellian distribution should be used instead.

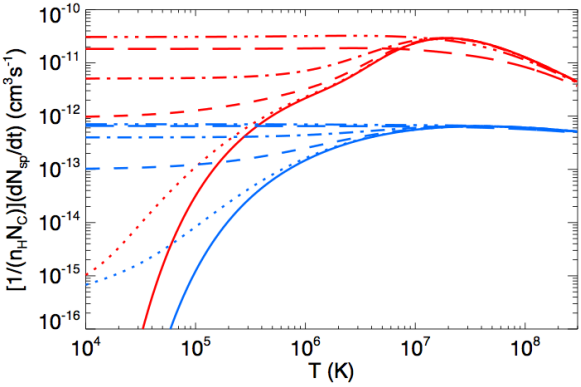

Figure 6.6: Erosion rate for an a-C:H (red lines) and a graphitic-type (blue lines) grain of radius 130 nm for different drift velocities between the projectiles and the target grain. The line style coding is the same as for Fig. 6.5a and 6.5.

Finally, to directly compare the erosion of a graphitic grain and an a-C:H grain in Fig. 6.6 we illustrate the sputtering rate constant for both grains and for different V_{drift} as a function of the gas temperature. We clearly see that the change in the physical properties of the grains (a-C:H with respect to graphitic-type) together with their finiteness leads to a substantial enhancement (by more than one order of magnitude for some temperatures) in the sputtering rate constant.

6.3.4 Interfacing GRASH_EX and DustEM

A coupling of the GRASH_EX and DustEM codes allows an exchange of the pre- and post-shock size distributions between the codes. This feature is introduced in the new version of the code and allows the user to 1) define any pre-shock size distribution, without being limited to power-law distributed grains and 2) to calculate the dust emission and extinction before and after a shock.

The dust size distribution

In the GRASH_EX code we exploit the coupling with the DustEM code to allow the user to define the grain size distribution in the same way as per the DustEM code,

i.e. with the use of the GRAIN.DAT file. To keep the structure of the GRASH_EX code relatively simple and optimise the computing time we decided here to limit the choice of the dust model to a two-material dust model. The Jones et al. (2013) dust model includes two different size distributions for the carbonaceous grains; the program automatically merges them together into one distribution in order to yield only two dust populations: carbonaceous and silicate grains.

The GRASH_EX code defines a dust population in terms of mass distribution in order to allow for mass conservation, while the DustEM code defines a dust population in terms of its size distribution. Then, in order to make the two programs interface with each other we wrote a routine to translate a mass distribution into size distribution and vice-versa.

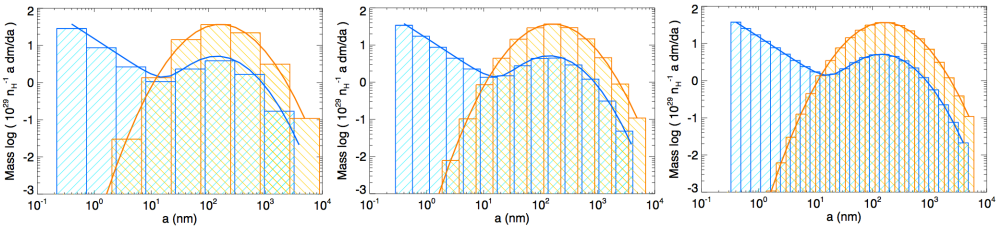

Figure 6.7: Jones et al. (2013) dust mass distribution. Blue and orange bins refer to carbonaceous and silicate grains respectively. The carbonaceous and silicate grains mass distributions are divided into 9, 15 and 25 bins. The solid lines indicate the case of an infinite number of bins.

To define a mass distribution from a user-supplied size distribution, firstly we define a logarithmic grid in mass with the desired number of bins and with the mass range corresponding to radius range in the size distribution. As in the DustEM code, for each bin, we define the quantity $\frac{a^4 dn}{da}$, where n is the number of grains in the bin and a the grain radius. The total mass, M_i, in the i-th bin can be expressed as:

$$M_i = \int \left(\frac{dn}{dm}\right)_i m\, dm, \tag{6.3.12}$$

where m is the grain mass. The fraction $\frac{dn}{dm}$ can be expressed as:

$$\frac{dn}{dm} = \frac{dn}{da}\frac{da}{dm}, \tag{6.3.13}$$

and since $m = \frac{4}{3}\pi a^3 \rho$ (where ρ is the grain density) we can write

$$\frac{dm}{da} = 4\pi a^2 \rho. \tag{6.3.14}$$

and after some algebra we obtain

$$\frac{dn}{dm} = \left(\frac{a^4 dn}{da}\right) \frac{4\pi\rho}{9m^2}, \tag{6.3.15}$$

and finally

$$M_i = \int \left(\frac{a^4 dn}{da}\right)_i \frac{4\pi\rho}{9m} dm. \tag{6.3.16}$$

Fig. 6.7 shows the mass distribution as a function of the grain mass divided into 9, 15 and 25 bins. As expected, increasing the number of bins, leads to a mass distribution that is defined with more and more precision, but the computing time to run the code through the whole shock wave increases at least as the square of the number of bins. For our standard run we choose to optimally divide the size distribution into 9 bins. We discuss the effect of the binning interval in Section 6.5.4

Dust emission and extinction in shocked regions

The processing of dust in a shock wave will determine its size distribution in shocked regions in galaxies. Coupling the GRASH_EX code with the DustEM code we have the possibility to predict the dust spectral energy distribution (SED) and extinction from regions that have been shocked, in order to allow comparison with observations. After the dust processing by a given shock wave, the post-shock mass distributions are translated into size distributions that can be read by the DustEM code, as explained in Section 6.3.4. In order to generate the dust SED and extinction we need to calculate the dust optical properties. In the Jones et al. (2013) dust model, these are defined by the mantle thickness and the band gap of the carbonaceous material.

6.4 Results

Here we assume shock processing in the WIM (as per McKee et al. 1987; Jones et al. 1994, 1996) and assume pre-shock density, n_0, and magnetic field, B_0, values typical of the WIM (i.e. $n_0 = 0.25\,\mathrm{cm}^{-3}$ and $B_0 = 3\,\mu\mathrm{G}$). We consider an initial ionisation fraction of 50% which corresponds, to a a good approximation, to the precursor ionisation caused by the shock. We choose a shock velocity of 100 km s^{-1} for our standard run since it is close to the optimum of the shock frequency and destructive potential in interstellar shocks (Draine and Salpeter 1979a,b; Jones et al. 1994, 1996).

Following Jones et al. (1994, 1996), we define the column density, N_H, through the shock as:

$$N_\mathrm{H} = v_\mathrm{shock}\, n_0\, t_\mathrm{shock}, \tag{6.4.1}$$

with t_shock the time after the beginning of the shock. Fig. 6.8 illustrates the shock profile for our standard shock. We show the gas temperature (T_4, in units of 10^4 K), density (n_H) and ionisation fraction (X_e) along the shock as a function of the column density.

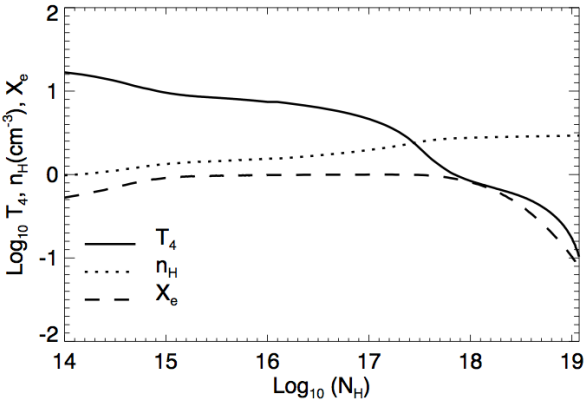

Figure 6.8: Shock profile for the standard 100 km/s shock. $T_4 \equiv \frac{T_{\rm gas}}{10^4\,{\rm K}}$, $n_{\rm H}$ and $X_{\rm e}$ are the temperature (in units of 10^4 K), density and ionisation fraction along the shock.

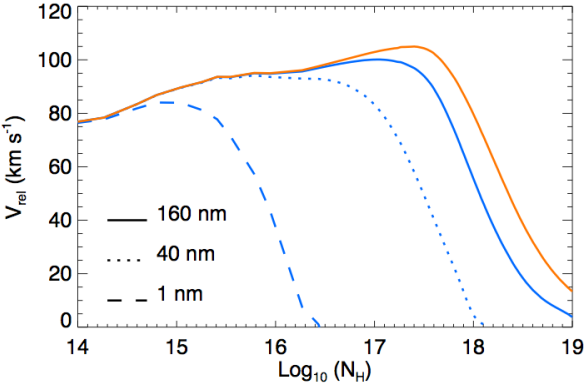

Figure 6.9: Relative velocity between a grain and the gas for $v_{\rm shock} = 100\,{\rm km\,s^{-1}}$ and for different grain sizes. We adopt the same color-coding as per Fig. 6.7.

The relative velocity, $V_{\rm rel}$, between a grain and the gas is a particularly important parameter as it determines the degree of grain destruction. Fig. 6.9 shows the grain drift velocity with respect to the gas as a function of the column density for our standard shock. We adopt different line styles for different carbonaceous grain sizes as labeled and the same color-coding as per Fig. 6.7, *i.e.* blue lines for carbonaceous grains and the orange line for a silicate grain. Focusing on the drift velocity of a 160 nm grain, we notice that the grain is first accelerated immediately after the shock front ($N_{\rm H} \sim 10^{14} - 10^{15}\,{\rm cm^{-2}}$) because of the sudden change in the gas density (due to ionisation)

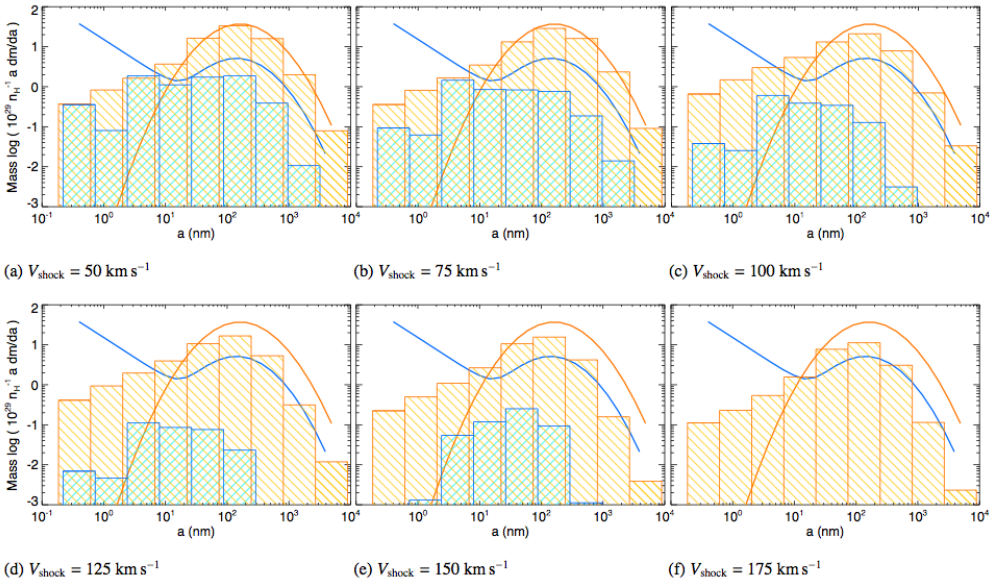

Figure 6.10: The post-shock size distribution for different shock velocities. The post-shock distribution is divided into 9 bins while the solid lines represent the pre-shock distribution; carbonaceous (blue) and silicate (orange). The 200 km s^{-1} post-shock size distribution is almost identical to the case of a 175 km s^{-1} shock, and is therefore not shown here.

and later at $N_{\rm H} \sim 10^{16} - 10^{17}\,{\rm cm}^{-2}$ because of the rapid cooling of the gas and the subsequent shock compression (betatron acceleration, Section 6.3.2). Furthermore, we notice that the higher density of silicate grains lead to a longer coupling time for a 160 nm silicate grain than for a carbonaceous grain of the same size.

We run the code for different shock velocities: 50, 75, 100, 125, 150, 175 and 200 km s^{-1} using the steady-state shock profiles generated by Raymond (1992). Fig. 6.10 illustrates the post-shock size distribution for $v_{\rm shock} \leqslant 175\,{\rm km\,s^{-1}}$. The post-shock size distribution in the case of a 200 km s^{-1} shock is almost identical to the 175 km s^{-1} case and is not shown in Figs. 6.10-6.13.

We notice that small carbonaceous grains are highly affected by the shock wave; even for a 50 km s^{-1} shock most of the mass of the smallest grains is transferred to the gas phase. For shock velocities $\geqslant 175\,{\rm km\,s^{-1}}$ all the carbonaceous grains are destroyed. On the other hand silicate grains are more resistant to sputtering and therefore undergo less destruction. However, for a 100 km s^{-1} shock, we clearly see a broadening of the silicate grain size distribution due to the fragmentation of the large grains.

6.4.1 Dust emission and extinction

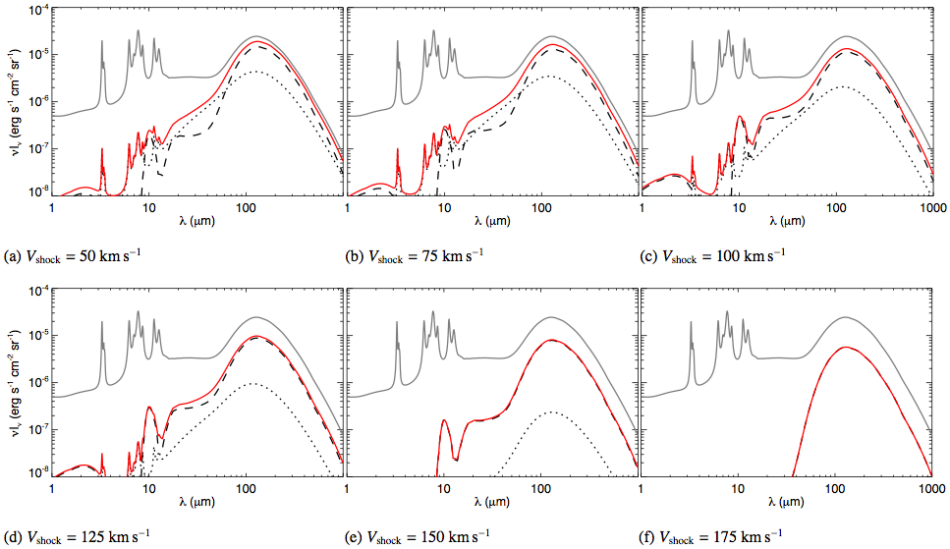

Figure 6.11: The post-shock SED as a function of shock velocity. Grey lines indicate the pre-shock SED and red lines the post-shock SED. Dotted and dashed lines indicate the contribution of carbonaceous and silicate grains respectively, to the post-shock SED. The assumed column density is $N_{\rm H} = 10^{20}\,{\rm cm}^{-2}$. The 200 km s^{-1} case is almost identical to the case of a 175 km s^{-1} shock and is therefore not shown here.

For all the considered shock velocities the carbonaceous mantle on the surface of silicate grains is destroyed (see Section 6.3.1). On the other hand, tracking the thickness of the aromatic mantle on the surface of carbonaceous grains is a more difficult task. However, energetic ion collisions and photon irradiation are able to re-aromatize the outer layer of the carbonaceous grains. Firstly, the available timescale is sufficiently long ($\sim 10^5$ yr) that the radiation field ($G_0 > 1$) would aromatize carbonaceous grain surfaces to a maximum depth of ~ 20 nm (Jones 2012d; Jones et al. 2014). Furthermore, sufficiently energetic ions can penetrate carbonaceous grains[5] up to ~ 5 nm contributing to the aromatization of the outer layer. We therefore consider that, for each of the shock velocities, the post-shock silicate grains are bare while carbonaceous grains have a 20 nm aromatic mantle with an aliphatic rich core for $a > 20$ nm and are aromatic-rich for $a < 20$ nm. We calculate the corresponding optical properties and then, using the post-shock size distribution as an input for the DustEM code, calculate the SED and extinction produced by the dust that has survived. Fig. 6.11 shows the dust SED for 50,

[5]The penetration depth, estimated with SRIM, for impinging H^+ (He^+) of energy 100 (470) eV (corresponding to the energy for a 200 km s^{-1} shock) in hydrogenated amorphous carbon is 4 (7) nm.

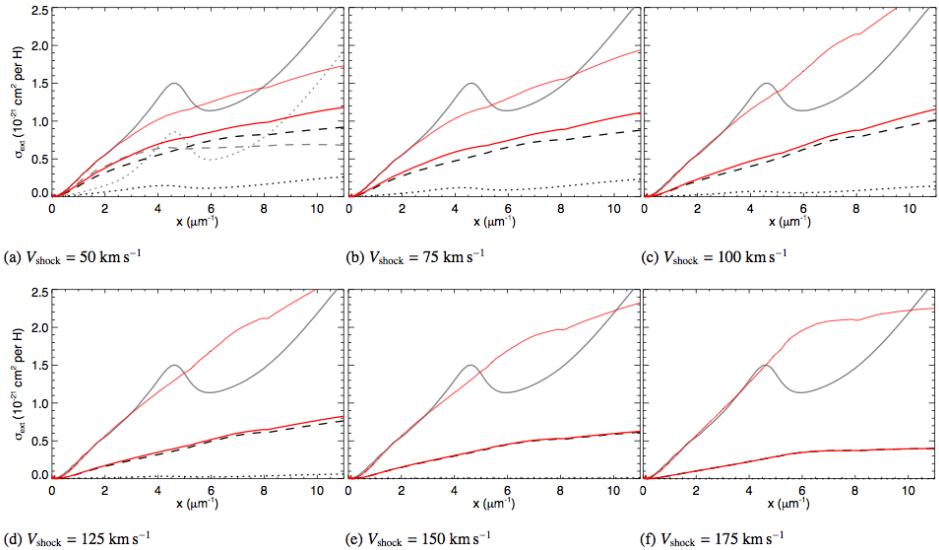

Figure 6.12: The post-shock NIR - UV dust extinction as a function of shock velocity. The color- and line style-coding are as per Fig. 6.11. The 200 km s^{-1} case is almost identical to that of the 175 km s^{-1} shock and is therefore not shown here. The thin red lines show the post-shock extinction normalised to the V-band pre-shock extinction. For $V_{\rm shock} = 50\,{\rm km\,s^{-1}}$ the pre-shock dust extinction due to carbonaceous (grey dotted line) and silicate (grey dashed line) grains is shown.

75, 100, 125, 150 and 175km s^{-1} shocks. The destruction of the smallest (carbonaceous) grains is reflected in the dust SED: even after a 50 km s^{-1} shock we clearly see a drop in the emission at short wavelengths. Furthermore, for shock velocities $\leqslant 150\,{\rm km\ s^{-1}}$, a small silicate grain signature is visible in the mid-infrared (9.7 and 18 μm bands). This is due to a significant production of small silicate grains as a consequence of large silicate grain fragmentation.

In Fig. 6.12 and 6.13 we show the dust extinction (in the NIR-UV and IR wavelength regions respectively) for $V_{\rm shock} \leqslant 175\,{\rm km\ s^{-1}}$. We notice that for all of the shock velocities, the characteristic UV bump at 217 nm disappears because of the destruction of the carriers, i.e. aromatic-rich hydrocarbon nanoparticles. Furthermore, we observe that, with increasing shock velocity, the UV extinction flattens primarily as a consequence of aromatic-rich nanoparticle destruction but also because of silicate grain destruction. On the other hand, the IR extinction shows small changes in shape. The large carbonaceous grain destruction is reflected by a drop in the 3 - 8 μm extinction, where carbonaceous grains give an important contribution to the total extinction.

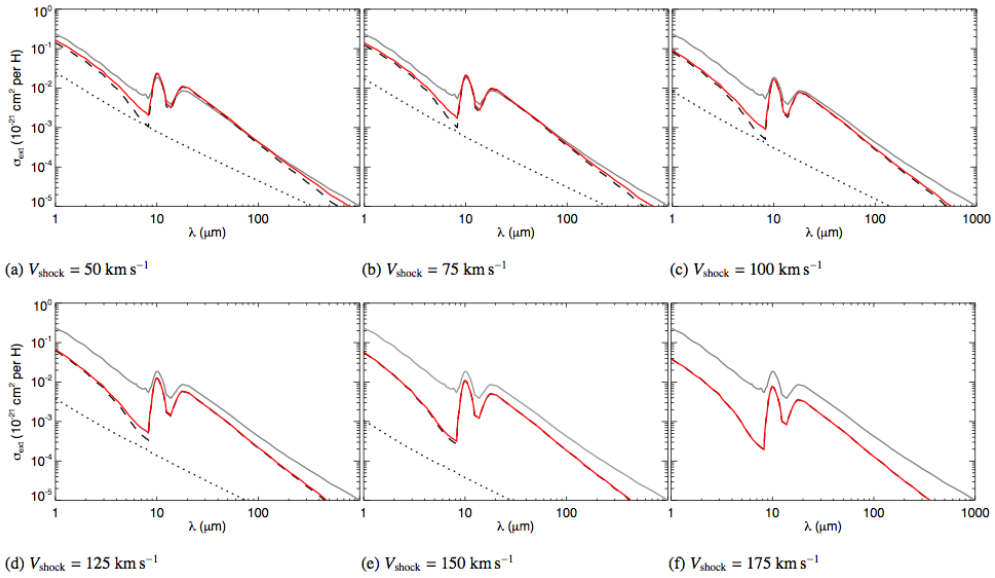

Figure 6.13: The post-shock IR dust extinction as a function of shock velocity. Color- and line style-coding are as per Fig. 6.11. The 200 km s^{-1} case is almost identical to the case of a 175 km s^{-1} shock and is not shown here.

6.4.2 Dust destruction potential

Comparing the pre-shock and post-shock size distributions we calculate the fraction of mass that has been destroyed during the shock for carbonaceous and silicate grains. Fig. 6.14 shows the carbonaceous (blue lines) and silicate (orange lines) grain destruction (as a percentage) as a function of the shock velocity. Dotted and dashed lines show the relative contribution of sputtering and vaporization to the total destruction (solid lines). We notice that for all of the shocks, the vaporization play little role and that the destruction is dominated by the sputtering process. The shattering is not directly responsible for any dust destruction but only affects the shape of size distribution transferring mass from the large grains to the smaller ones, which are more susceptible to destruction.

In Table 6.4 we compare our dust destruction results with those of Jones et al. (1996) and Serra Díaz-Cano and Jones (2008). In our study, both carbonaceous and silicate grains undergo more destruction than in the previous studies. This is mostly due to the adoption of the new dust model. In the Jones et al. (2013) dust model most of the carbonaceous mass is in small grains ($a < 20$ nm), which are rather fragile compared to larger grains (Micelotta et al. 2010b,a; Bocchio et al. 2012). Furthermore, the silicate grain distribution is almost mono modal and centered at a radius $a \sim 160$ nm, grains

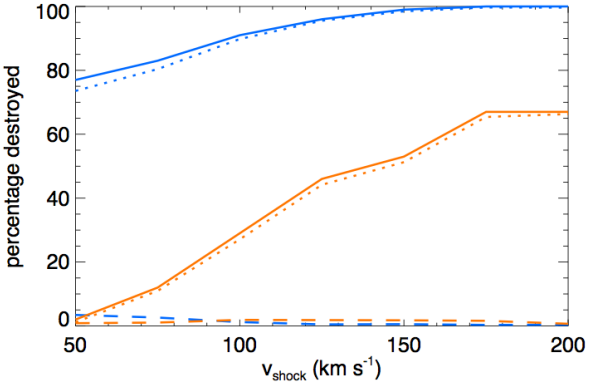

Figure 6.14: Dust destruction (percentage) for carbonaceous grains (blue line) and silicate grains (orange line) as a function of the shock velocity. Dotted and dashed lines, respectively, represent the sputtering and vaporization contributions to the destruction.

that have a large inertia and that are efficiently destroyed in shocks.

Table 6.4: Dust destruction (percentage) as a function of the shock velocity, $V_{\rm shock}$, for carbonaceous and silicate grains as estimated by JTH96 (Jones et al. 1996), SJ08 (Serra Díaz-Cano and Jones 2008) and by this study.

$V_{\rm shock}$ (km s^{-1})	50	75	100	125	150	175	200
carbonaceous grains							
JTH96	1	5	7	13	12	21	47
SJ08	4	21	31	56	58	81	100
this study	77	83	91	96	99	100	100
silicate grains							
JTH96	2	12	18	33	32	41	49
this study	2	12	29	46	53	67	67

6.4.3 Comparison with earlier results

The introduction of more detailed physics into the GRASH_EX version of the original code leads to a re-evaluation of the dust destruction by SN shocks. The modifications to the dust physics that we have made can be summarized as follows:

- an update of the grain charge scheme from McKee et al. (1987) to WD01,
- an update of the carbonaceous grain material from graphitic-type to a-C(:H) materials,

- a unification of inertial and thermal sputtering with the use of the skewed Maxwellian distribution.

In order to understand the relative importance of the different updates, we compare the destruction for our standard shock with and without the introduction of each of the new features and report the results obtained in Table 6.5. We notice that, while

Table 6.5: Dust destruction (percentage) for our standard 100 km s^{-1} shock, without and with the update of the [a]charge scheme (from McKee et al. (1987) to WD01), [b]the carbonaceous grain sputtering (from Tielens et al. 1994 to a-C(:H) sputtering), [c]the relative velocity distribution (from thermal and inertial sputtering to the skewed Maxwellian distribution).

	previous		updated	
	"graphitic"	silicate	a-C:H	silicate
charge scheme[a]	90	28	91	29
a-C(:H) sputtering[b]	5	28	91	29
distribution[c]	74	17	91	29

the change of the grain charge scheme little affects the results, updating the carbonaceous material and merging the thermal and inertial sputtering lead to increased dust destruction. In particular, we note that the lower density of the a-C(:H) particles with respect to graphitic-type materials makes them more susceptible to destructive processing. Finally, we point out that the displaced Maxwellian distribution better describes the physics of the interaction between gas ions and grains, with respect to the thermal/inertial approximation. We find that the inclusion of the more realistic physical treatment leads to the almost complete destruction of carbonaceous nanoparticles even in the case of a 50 km s^{-1} shock.

6.4.4 Dust lifetime

Following the approach by Dwek and Scalo (1980) and McKee (1989), the dust lifetime, $t_{\rm SNR}$, can be estimated as:

$$\frac{M_{\rm ISM}}{t_{\rm SNR}} = \frac{\int \epsilon(v_s) dM_s(v_s)}{\tau_{\rm SN}}, \tag{6.4.2}$$

where $M_{\rm ISM} \simeq 4.5 \times 10^9 M_\odot$ is the total (gas + dust) interstellar mass in our Galaxy, $\epsilon(v_s)$ is the efficiency of grain destruction, $M_s(v_s)$ is the mass of the gas shocked to at least v_s and $\tau_{\rm SN} = 125\,{\rm yr}$ is the effective interval between SNe. The estimate of the $\epsilon(v_s)$ strongly relies on both the assumed shock structure and the dust processing. On the other hand, $M_s(v_s)$ is based on the structure of the ISM and, more importantly, on the dynamical evolution model of a supernova explosion. Following Jones et al. (1994)

we assume SN remnant in the Sedov-Taylor stage and, as calculated by McKee (1989), we have

$$M_s(v_{s7}) = 6800 E_{51}/v_{s7}^2 \, M_\odot. \tag{6.4.3}$$

Then assuming, as per McKee and Ostriker (1977), a ratio of warm to hot interstellar medium filling factor of $f_w/f_h = 0.3/0.7 = 0.43$ and a mean SN energy of 10^{51} ergs we obtain

$$t_{\rm SNR} = \frac{9.7 \times 10^7}{\int \epsilon(v_{s7})/v_{s7}^3 dv_{s7}} \, \text{yr}. \tag{6.4.4}$$

We then use Eq. 4 from McKee (1989) to determine the fraction of the elements locked up in the surviving grains, $\delta_{\rm eq}$:

$$\delta_{\rm eq} = \frac{\delta_{\rm in}}{1 + \frac{t_{\rm in}}{t_{\rm SNR}} + (\alpha - 1)\frac{t_{\rm in}}{t_{\rm sf}}}, \tag{6.4.5}$$

where $t_{\rm in}$ is the timescale for the injection of dust into the ISM, $\delta_{\rm in}$ is the fraction of material injected in the ISM initially contained in the dust (we assume $\delta_{\rm in} = 0.9$), $t_{\rm sf}$ is the star formation timescale and α is a parameter introduced by Dwek and Scalo (1980): $\alpha > 1$ corresponds to a net dust destruction during star formation, $\alpha < 1$ corresponds to the case of dust formation in protostellar environment and $\alpha = 1$ is the case where dust is not destroyed nor formed but only incorporated into the newly formed star. We assume here $\alpha = 1$. We can approximate the carbonaceous destruction efficiency as:

$$\epsilon(v_{s7}) = \begin{cases} 0.66 + 0.23 v_{\rm s7} & \text{for } 0.5 < v_{s7} \leqslant 1.5 \\ 1 & \text{for } 1.5 < v_{s7} < 2.0 \end{cases}$$

and for silicate grains:

$$\epsilon(v_{s7}) = \begin{cases} 0.61 v_{\rm s7} - 0.31 & \text{for } 0.5 < v_{s7} \leqslant 1.25 \\ 0.11 + 0.28 v_{\rm s7} & \text{for } 1.25 < v_{s7} \leqslant 2 \end{cases}$$

Assuming the uncertainties estimated by Jones and Nuth (2011), this leads to a dust lifetime of:

$$t_{\rm SNR} = \begin{cases} (6.2 \pm 5.6) \times 10^7 \, \text{yr} & \text{for carbonaceous grains} \\ (3.1 \pm 2.7) \times 10^8 \, \text{yr} & \text{for silicate grains} \end{cases}$$

While the estimate for silicate grains is about the same as in the previous study by Jones et al. (1996), the estimate for carbonaceous grains is an order of magnitude shorter than in that study and a factor ~ 3 shorter than in the work by Serra Díaz-Cano and Jones (2008).

If we assume that $t_{\rm in} \sim (3 \pm 1.5) \times 10^9$ yr as estimated by different groups (Dwek and Scalo 1980, Gehrz 1989, Jones and Tielens 1994), the dust destruction timescale is

much shorter than the timescale for its injection into the ISM. The equilibrium fraction of elements locked in grains, in the absence of dust re-formation in the ISM, is then:

$$\delta_{\rm eq} = \begin{cases} 0.018 \pm 0.016 & \text{for carbonaceous grains} \\ 0.08 \pm 0.07 & \text{for silicate grains} \end{cases}$$

Comparing these values with typical values for the diffuse ISM (i.e. $\geq 50\%$ ($\geq 90\%$) of C (Si, Fe and Mg) atoms locked into grains), we see that our estimate is far from consistent with the observed values and we cannot avoid the conclusion that dust must be efficiently reformed in the ISM ($\alpha < 1$, see discussion in Section 6.5.5).

6.5 Discussion

The use of the Jones et al. (2013) dust model, with the majority of the carbonaceous dust mass in small particles, coupled with the detailed physics of a-C(:H) material processing in energetic regions (Serra Díaz-Cano and Jones 2008; Micelotta et al. 2010b,a; Bocchio et al. 2012, 2013b), leads to a very short carbon dust cycling time-scale in the ISM. Our modelling therefore predicts that the observed fraction of stardust material locked into carbonaceous grains in the ISM is essentially zero ($\delta_{\rm eq} = 0.018 \pm 0.016$) and that the a-C(:H) grain 'lifetime' is very short ($\approx [6.2 \pm 5.6] \times 10^7$ yr). Our carbonaceous dust lifetime estimation is almost three times shorter than the previous estimate by Serra Díaz-Cano and Jones (2008). This is due to the introduction of the molecular approach developed by Micelotta et al. (2010b), which leads to a high destruction rate for small grains. Furthermore, merging the inertial and thermal sputtering into a single process, leads to a lifetime three times shorter than that estimated by Micelotta et al. (2010b). This is because of the effects of the "high-temperature tail" in the skewed Maxwellian velocity distribution (see Fig. 6.4). The very large discrepancy (by a factor of about 50) between the derived carbonaceous dust lifetime and its formation timescale around evolved stars ($\simeq 3 \times 10^9$ yr) then implies that most of the carbonaceous dust in the ISM must have been re-formed there, most probably by the accretion of C (and H) atoms and small hydrocarbon species onto the more resilient silicate grains and that this must occur in dense regions of the ISM (Jones et al. 2013, 2014). Chemical vapour deposition (CVD) is a long-used process for hydrogenated amorphous carbon formation in the laboratory (e.g., Robertson 1986). Thus, and given that much of the silicate dust then survives in the ISM, there is then a viable mechanism for the re-formation of carbonaceous grain mantles via a CVD-type accretion process in the dense ISM.

On the other hand, the long coupling time between the gas and large silicate grains in a shock leads to high silicate destruction rates and we find that only a fraction of $\delta_{\rm eq} = 0.08 \pm 0.07$ of silicate stardust could be preserved in the ISM with a 'lifetime' of $\approx 3.1 \pm 2.7 \times 10^8$ yr, which is about an order of magnitude shorter than the injection timescale. However, as argued by Jones and Nuth (2011), the uncertainties on these calculations are of the order of the 100%. Moreover, despite the introduction of much new physics into the code, the exact nature of some of the physical processes is

still rather uncertain. In particular, in this section we will focus on the silicate core sputtering, the dynamics of the collision between large silicate grains and carbonaceous nanoparticles, the structure of the shock profile and the mass binning of the dust size distribution.

6.5.1 Silicate core sputtering

In this study, as per Jones et al. (1994, 1996), we model the silicate grain sputtering due to collisions with ions using the estimates by Tielens et al. (1994). However, more experimental data are now available and the sputtering yield for silicate grains can be estimated with more precision at low energies. The SRIM software (Ziegler et al. 1985) provides a means to calculate (to within 4% of the experimental values) the sputtering yield due to the interaction between ions and silicate target. In order to calculate the sputtering yield, the user must supply the following key parameters:

- the material density, ρ,
- the surface binding energy, $E_{\rm S}$, *i.e.* the energy that binds a surface atom to the lattice,
- the lattice binding energy, $E_{\rm B}$, *i.e.* the energy that binds an atom to a lattice site within the bulk, and,
- the displacement energy, $E_{\rm D}$, *i.e.* the energy needed to displace an atom within the lattice.

May et al. (2000) estimated these parameters for forsterite-type materials, i.e. $(Fe,Mg)_2SiO_4$. In particular, they used the heat of atomization as an estimate of the surface binding energy and performed calculations within the framework of the ionic model in order to quantify the lattice binding energy. However, while the surface and lattice binding energy are experimentally or theoretically rather well constrained, the value of the displacement energy is still uncertain. May et al. (2000) took the displacement energy of Mg and O atoms in MgO compounds as a guide ($E_{\rm D} = 52$ and 54 eV for Mg and O respectively) and assumed $E_{\rm D} = 50\,{\rm eV}$ for all the atoms in the silicate. However, the uncertainty on this parameter may be a factor of two and, for example, Wang et al. (1999) assumed a displacement energy of $E_{\rm D} \approx 25\,{\rm eV}$ for similar forsterite-type materials.

Experimental studies show that, under the effect of energetic ion irradiation, silicate grains become amorphous in structure (Demyk et al. 2001; Carrez et al. 2002) and so the displacement energy will be lower than for a crystalline structure. We therefore adopt a displacement energy of $E_{\rm D} = 25\,{\rm eV}$. Furthermore, since in an amorphous silicate, Fe and Mg atoms will tend have no preferred sites, we assume the same values for the lattice binding energy for both atoms ($E_{\rm B} \approx 1.9\,{\rm eV}$). We estimate the surface binding energy with the same approach as per May et al. (2000) and we assume the same silicate density as in the Jones et al. (2013) dust model. We show the assumed values in Table 6.6.

Table 6.6: Forsterite-type silicate physical properties. ρ is the material density, E_D, E_B and E_S are the displacement energy, the lattice binding energy and the surface binding energy, respectively.

material	element	ρ^a	E_D^b	E_B^c	E_S^c
forsterite-type	Si	2.5	25	4	6.8
	O		25	15.5	4.75
	Fe		25	1.9	6.47
	Mg		25	1.9	3.7

[a]We adopt the same density as per Jones et al. (2013).
[b]Wang et al. (1999).
[c]Adapted values from May et al. (2000).

We run SRIM for different impact angles and energies for H^+ and He^+ projectiles, simulating 10^6 collisions in each case. Assuming isotropic collisions, we calculate the average sputtering yield, for each target atom, at a given incident energy and integrate over all the impact angles:

$$Y_i(E) = \int_0^{\pi/2} d\theta Y_i(\theta, E) \sin(\theta), \tag{6.5.1}$$

where $Y(\theta, E)$ is the sputtering yield at a given angle, θ, and energy, E, for the i-th target atom. Then, averaging over all the different target atoms, the sputtering yield is given by

$$\overline{Y(E)} = \sum_i Y_i(E) w_i \,, \tag{6.5.2}$$

where $w_i = \frac{m_i}{\sum_j m_j}$ and m_i the i-th ion mass.

In Fig. 6.15 we compare the silicate sputtering yield as estimated by Tielens et al. (1994) and as calculated using SRIM for H^+ and He^+ impinging projectiles. We note that, the threshold energy is shifted to higher energies with respect to the Tielens et al. (1994). However, the SRIM results are sensitive to the assumed value of the displacement energy and a higher displacement energy (e.g. $E_D = 50\,\mathrm{eV}$ as estimated by May et al. 2000) will lead to a higher threshold energy and a lower sputtering yield over a large range of energies (Leroux 2007). In any case, these calculations seem to indicate that the estimates by Tielens et al. (1994) represent an upper limit and that the silicate destruction in shocks may be significantly lower.

Running GRASH_EX for the standard shock ($v_{\mathrm{shock}} = 100\,\mathrm{km\ s^{-1}}$) and replacing the Tielens et al. (1994) approach with the silicate sputtering yield derived using the SRIM simulations (with the assumed parameters in Table 6.6) we obtain a silicate destruction of 14%, which is almost half of the destruction obtained with the Tielens et al. (1994) yields. This result is even more dramatic if we assume a displacement energy of 50 eV: the silicate destruction in this case is only 6%.

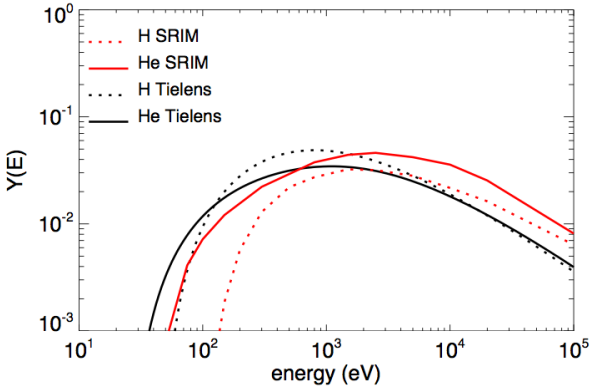

Figure 6.15: Silicate sputtering yield for incident H^+ (dotted lines) and He^+ (solid lines) as a function of the impinging energy. Tielens et al. (1994) estimates (black lines) and SRIM calculations (red lines) are shown. The sputtering yield for impinging He^+ ions are multiplied by their relative abundance with respect to hydrogen, i.e. $X_{\rm He} = 0.1$.

6.5.2 Shattering and vaporization

In Section 6.4 we showed that grain-grain collisions trigger the fragmentation of large grains leading to a broadening of the dust size distribution (see Fig. 6.10b). We have estimated the fraction of mass which is affected by shattering for different shock velocities and show the results in Fig. 6.16. We note that for carbonaceous grains the shattering is not very important ($\lesssim 10\%$ of the mass affected) while for silicate grains the affected mass peaks at a value of $\sim 35\%$ for a shock velocity of 100 km s^{-1} (i.e. where the betatron acceleration is most efficient). Since the size distribution is dominated by small carbonaceous grains and large silicate grains, grain-grain collisions mainly occur between these two populations. In our study the dynamics of small carbon grain impacts on silicates are treated using a 'hard sphere' approach (Jones et al. 1996). However, small a-C(:H) grains are low density, open structures and will therefore act as 'soft' impactors, rather than hard spheres, probably leading to a less efficient production of small silicate grains (Section 3.5.6).

In order to estimate the effects of reduced shattering by nano-particle impacts we run the 100 km s^{-1} shock ignoring the shattering process. Fig. 6.17 shows the post-shock size distribution in this case. Comparing the size distribution with and without the inclusion of the shattering process we note that shattering is the process responsible for the broadening of the size distribution. However, we note that the effect of the shattering process is to re-distribute the dust mass across the bins but that it does not lead to any net mass loss. On the other hand, the re-distribution of the dust mass leads to a second-order effect on the dust destruction. Ignoring the shattering process, the silicate grain destruction is slightly lower ($\sim 26\%$) than in the case where this process

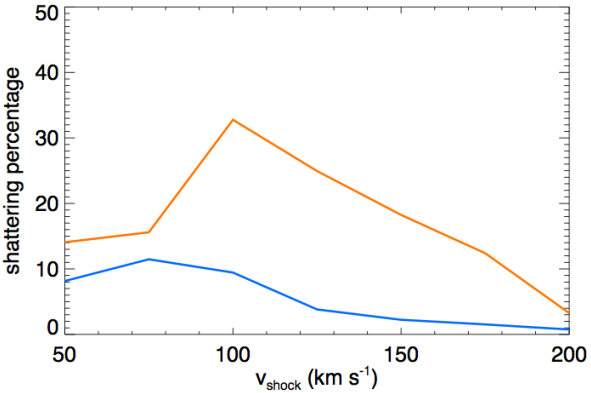

Figure 6.16: Percentage of the total dust mass affected by shattering in grain-grain collisions as a function of the shock velocity.

is included ($\sim$ 29%), while it does not lead to any change for carbonaceous grains. We also note that with shattering switched off the log-normal shape of the amorphous silicate size distribution is preserved and that the log-normal distribution of the large carbonaceous grains is also somewhat preserved.

6.5.3 Steady state shock vs. hydro-dynamical calculations

The approach that we have adopted here, as per Jones et al. (1994, 1996), is to assume steady state shocks propagating through the inter-cloud medium. However, full time-dependent hydro-dynamical modeling is really required to better evaluate dust processing in evolving SN remnants propagating through the ISM. Preliminary, hydro-dynamical studies indicate that the dust destruction effects could be reduced by about 20% (Slavin 2014). In that study, the dust destruction efficiency as a function of the shock velocity is very similar to our steady-state shock estimate but, on the contrary, the mass of gas shocked during a SN is strongly reduced when accounting for radiative cooling. Thus, physically-realistic studies of dust processing in SN shocks in the ISM strongly implies that our dust destruction estimates are rather upper limits.

6.5.4 Accuracy and reliability of the simulations

For all of the simulations we run we assume a pre-shock size distribution divided into 9 bins. However, in this way we could in principle introduce errors into the resulting dust SED and extinction compared to the case of a division of the size distribution into an infinite number of bins. We want to check whether a less accurate description of the size distribution can affect the dust emission and extinction. We divided the

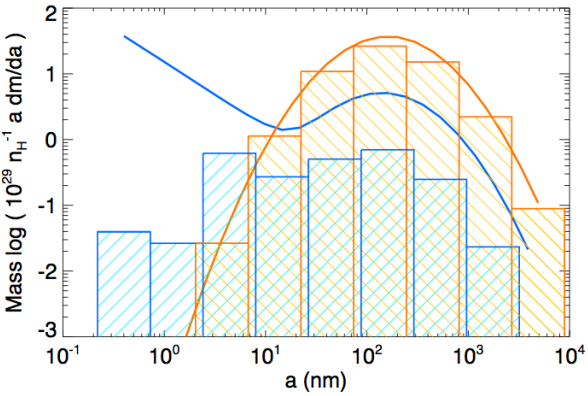

Figure 6.17: Size distribution for the case of 100 $\mathrm{km\,s^{-1}}$ with no shattering.

pre-shock size distribution into 9, 15 and 25 bins and we calculate with DustEM the emission and extinction in the three cases.

First of all we compare the IR emission for the fine binning with respect to a coarser one. We calculate the difference in intensity for each wavelength ($d_{n,m}$, with n and m the number of bins in the two cases) between the two cases and we normalize it to the intensity calculated with 25 bins:

$$\begin{aligned} d_{25,9} &= |I_{\nu,25} - I_{\nu,9}|/I_{\nu,25} \\ d_{25,15} &= |I_{\nu,25} - I_{\nu,15}|/I_{\nu,25}, \end{aligned} \tag{6.5.3}$$

where $I_{\nu,\mathrm{n}}$ is the dust emission calculated using n bins. The error that we introduce by dividing the size distribution into less than 25 bins can be as large as 100% of the emission. We then interpolate the coarser binning size distributions into 25 bins in order to mimic a finer grid and recalculate the difference in emission. The error we make, even assuming a grid of 9 bins (but interpolating to 25 bins), is never larger than $\sim 20\%$ ($d_{25,15} \lesssim 8\%$ interpolating to 25 bins) across the whole range of wavelengths. For our runs we can therefore use 9 bins and interpolate the resulting size distribution onto a 25 bin grid. This allows us to spend less computation time and to still produce reliable results.

We follow the same procedure for the extinction in the NIR-UV and IR bands. We define $d^{\mathrm{ext,UV}}_{\mathrm{n,m}}$ and $d^{\mathrm{ext,IR}}_{\mathrm{n,m}}$ the normalized difference between the extinction in the case of n and m bins in the NIR-UV and IR bands respectively. Also in this case the interpolation gives a good and reliable alternative to a finer grid ($d_{25,\mathrm{m}} \lesssim 1\%$, for $m = 9$ and 15, interpolation onto a 25 bin grid).

6.5.5 Consequences of the uncertainties

Using the silicate core sputtering estimates by Tielens et al. (1994), the lifetime of silicate grains is almost an order of magnitude shorter than the injection timescale. This leads us to the conclusion that, in order to have a fraction of heavy elements locked in grains comparable to the observed values, we need to allow for the re-formation of silicate grains in the ISM. However, as pointed out by Jones and Nuth (2011), silicate re-formation under the low density and temperature conditions of the ISM seems to be a rather problematic scenario. However, SiO and silicate grain formation at low temperatures ($T \lesssim 15\,\mathrm{K}$) has been observed in the laboratory using idealized neon matrix and helium droplet isolation techniques (Krasnokutski et al. 2014; Rouillé et al. 2014). The oligomerization of SiO molecules is barrierless and therefore could be an efficient mechanism for silicate formation in the low-temperature ISM (Rouillé et al. 2014).

SRIM calculations seem to indicate that the silicate sputtering rate might be significantly lower than estimated by Tielens et al. (1994) therefore leading to a much longer silicate grain lifetime ($t_{\mathrm{SNR}} \geqslant 6 \times 10^8\,\mathrm{yr}$), possibly of the same order as the injection timescale. This would then imply a totally different scenario for silicate grain evolution and therefore make the previously-assumed need to re-form silicate dust in the ISM no longer a requirement for new dust models.

6.6 Conclusions

In this study we have revisited the long-standing question of dust processing in interstellar shocks and the discrepancy with the dust injection time-scale. Updating the GRASH code presented by Jones et al. (1994, 1996) we have re-evaluated dust destruction in shocks with velocities between 50 and 200 km s^{-1}. In particular, we use the grain size distribution and material compositions of the Jones et al. (2013) dust model. Furthermore, we better model the dynamics of grains in the shock by updating the grain charge scheme with that of WD01 and by merging the inertial and thermal sputtering into a single process. Moreover, we have coupled the GRASH_EX code to the DustEM code in order to give the possibility to define any size distribution and to calculate the post-shock dust emission and extinction in shocked regions.

As a result of the new carbonaceous material and by putting most of the carbonaceous mass in the smallest grains, carbon dust is efficiently destroyed, even in a 50 km s^{-1} shock, which leads to a short carbon grain lifetime ($t_{\mathrm{SNR,c}} = [6.2 \pm 5.6] \times 10^7\,\mathrm{yr}$). Silicate grains are more resilient and large grains survive even in fast shocks. However, the calculated silicate grain lifetime, despite being longer than the carbonaceous grain lifetime is still short ($t_{\mathrm{SNR,s}} = [3.1 \pm 2.7] \times 10^8\,\mathrm{yr}$) compared to the dust injection timescale ($t_{\mathrm{in}} = 3 \times 10^9\,\mathrm{yr}$), leading to a predicted low fraction of elements locked in grains ($\delta_{\mathrm{eq,s}} = 0.08 \pm 0.07$).

The calculated fraction of elements locked in grains is not compatible with the observed values (i.e. $\geqslant 50\%$ for C and $\geqslant 90\%$ for Si, Fe and Mg). This implies that the

re-formation of grains in denser regions of the interstellar medium must be efficient. While, there seems to be viable mechanisms for the re-formation of carbonaceous grains from the gas phase under low temperature and pressure conditions (e.g. Dartois et al. 2005), silicate grains are seemingly hard to re-form in the dense ISM and must therefore be formed in AGB stars and preserved in interstellar shocks (Jones and Nuth 2011). This study is therefore not able to solve this long-standing conundrum. Although recent experiments (Krasnokutski et al. 2014; Rouillé et al. 2014) show that it may be possible to form silicates under ISM conditions.

However, it seems that the modelling of silicate sputtering together with hydrodynamical simulations of shock dynamics are absolutely critical to advance our understanding and will possibly give lower silicate sputtering resulting in a longer lifetime $t_{\rm SNR,s} \geqslant 6 \times 10^8$ yr. This could lead to a different scenario, making the assumed need to re-form the silicate dust in the ISM no longer such a stringent requirement. These features must therefore be explored more in detail in future studies.

Finally, in the recent Jones et al. (2013) dust model small carbonaceous grains and large silicate grains are the most abundant species, therefore a correct treatment of the interaction between them is necessary in order to have a better estimate of the fragmentation of the large silicate grains. Molecular dynamics simulations (e.g. Smith and Webb 1993) seem to indicate that this process would be much less effective than in the case of hard spheres collisions therefore leading to less mass in small silicate grains and reduced silicate emission in the MIR.

6.A Properties of the skewed Maxwellian distribution

The skewed Maxwellian distribution, $f_{\rm skM}$ (see Section 6.3.3), is a velocity probability distribution with integral normalized to unity. In order to prove this property, we integrate over relative velocities, $V_{\rm rel}$, from 0 km s^{-1} to $+\infty$ km s^{-1}.

$$\int_0^\infty f_{\rm skM} v dv = \sqrt{\frac{m}{2k_{\rm B}T_{\rm gas}\pi}} \int_0^\infty \frac{v}{V_{\rm drift}} \times \left[\exp\left(-\frac{m}{2k_{\rm B}T_{\rm gas}}(v - V_{\rm drift})^2\right) - \exp\left(-\frac{m}{2k_{\rm B}T_{\rm gas}}(v + V_{\rm drift})^2\right)\right] dv. \tag{6.A.1}$$

We split the two terms in brackets into two different integrals. In the first term we make the following change of variables $\sqrt{\frac{m}{2k_{\rm B}T_{\rm gas}}}(v - V_{\rm drift}) = x$, while in the second

term $\sqrt{\frac{m}{2k_{\rm B}T_{\rm gas}}}(v+V_{\rm drift})=x$. This leads to:

$$\begin{aligned}\int_0^\infty f_{\rm skM}v dv = &\sqrt{\frac{m}{2k_{\rm B}T_{\rm gas}\pi}}\frac{1}{V_{\rm drift}}\\ &\left[\int_0^\infty\left(x\sqrt{\frac{2k_{\rm B}T_{\rm gas}}{m}}+V_{\rm drift}\right)e^{-x^2}\sqrt{\frac{2k_{\rm B}T_{\rm gas}}{m}}dx+\right.\\ &\left.-\int_0^\infty\left(x\sqrt{\frac{2k_{\rm B}T_{\rm gas}}{m}}-V_{\rm drift}\right)e^{-x^2}\sqrt{\frac{2k_{\rm B}T_{\rm gas}}{m}}dx\right]\\ &=\sqrt{\frac{m}{2k_{\rm B}T_{\rm gas}\pi}}\frac{1}{V_{\rm drift}}\int_{-\infty}^\infty V_{\rm rel}\sqrt{\frac{2k_{\rm B}T_{\rm gas}}{m}}e^{-x^2}dx\\ &=1.\end{aligned}\tag{6.A.2}$$

We now demonstrate that the skewed Maxwellian distribution, under the approximation that the thermal motion of the gas ions is negligible with respect to their drift motion, tends to a Dirac delta probability. In this case we can assume that $T_{\rm gas}\to 0$ and that the relative velocity between a grain and the gas equals the drift velocity (i.e. $v\to V_{\rm drift}$). This then implies:

$$\frac{v}{V_{\rm drift}}\to 1\tag{6.A.3}$$

and

$$\exp\left(-\frac{m}{2k_{\rm B}T_{\rm gas}}(v+V_{\rm drift})^2\right)\to 0.\tag{6.A.4}$$

Making the following change of variables:

$$\sqrt{\frac{2k_{\rm B}T_{\rm gas}}{m}}=a,\tag{6.A.5}$$

the skewed Maxwellian distribution then results

$$f_{\rm skM}=\frac{1}{a\sqrt{\pi}}\exp\left(-\frac{x^2}{a^2}\right)\tag{6.A.6}$$

$$=\delta_a(x)\tag{6.A.7}$$

As desired, the skewed Maxwellian distribution in this case tends to a Dirac delta probability distribution, *i.e.* the case for the inertial sputtering described by Tielens et al. (1994), see Section 6.3.3.

Chapter 7

Ram pressure stripping dynamics

> Doing what you like is freedom. Like what you do is happiness.
>
> Frank Tyger

Contents

7.1 Introduction

THIS chapter focuses on "ram pressure stripping", an intriguing and fascinating phenomenon in galaxy clusters. In order to fully comprehend this mechanism and be able to interpret the observations of infalling galaxies in clusters we need to understand the interaction between the galaxy and the ICM as well as between the different galaxy components.

7.2 The mechanism of ram pressure stripping

Already during the 1950s, Spitzer and Baade (1951) observing galaxies in clusters such as the Coma or Corona clusters revealed interesting differences between cluster galaxies and their counterpart in the "field". They found that most of the galaxies in these clusters are S0 galaxies with no evidence for spiral arms or any sign of dust obscuration even if observed edge-on. In their study, Spitzer and Baade (1951), explained this characteristic nature of cluster galaxies as due to the frequent collisions between galaxies.

However, a better knowledge of clusters make this explanation rather unlikely and a more realistic mechanism able to account for the observed nature of cluster galaxies was proposed by Gunn and Gott (1972): "ram pressure stripping". According to the proposed mechanism, an infalling galaxy undergoes a ram pressure as it enters the denser ICM and is therefore stripped of (part of) its interstellar medium. The ram pressure, $P_{\rm RP}$, exerted by the ICM is expressed as (Gunn and Gott 1972):

$$P_{\rm RP} = \rho_{\rm ICM} v_{\rm gal}^2, \tag{7.2.1}$$

where $\rho_{\rm ICM}$ is the ICM density and $v_{\rm gal}$ the relative velocity between the infalling galaxy and the ICM. On the other hand, the ISM is held in the plane of the galaxy by a gravitational force per unit area, $P_{\rm g}$, of

$$P_{\rm g} = 2\pi G \sigma_{\rm s} \sigma_{\rm ISM}, \tag{7.2.2}$$

with $\sigma_{\rm s}$ and $\sigma_{\rm ISM}$ the stellar and ISM surface density, respectively. Assuming a galaxy with a total stellar mass of $M_{\rm s} = 10^{11}\,M_\odot$ and a radius of the disk of $r = 10\,{\rm kpc}$, the stellar surface density is then

$$\sigma_{\rm s} = \frac{M_{\rm s}}{\pi r^2} = 0.06\,{\rm g\,cm^{-2}}. \tag{7.2.3}$$

Furthermore, assuming a disk of thickness $d = 200\,{\rm pc}$ and a gas density of $n_{\rm H} = 1\,{\rm cm^{-3}}$, the ISM surface density can be estimated as

$$\sigma_{\rm ISM} = n_{\rm H}\, d\, m_{\rm H} = 10^{-3}\,{\rm g\,cm^{-2}}. \tag{7.2.4}$$

Therefore if we assume a galaxies moving with a RMS velocity of $\sim 1000\,{\rm km\ s^{-1}}$ then an ICM density $n_{\rm ICM} \gtrsim 10^{-3}\,{\rm cm^{-3}}$ is able to strip the interstellar matter from an

infalling galaxy. Therefore, especially in the central region of clusters, galaxies are effectively stripped of their interstellar matter. On the other hand, the stars are more tightly coupled to the galactic gravitational field and so the pressure exerted by the ICM wind is not sufficient to perturb the stellar distribution.

It is now well known that a galaxy Hubble type is correlated to the environment where the galaxy finds itself. In particular, the number of spiral galaxies passing from the "field" to the core of rich clusters has been observed to decrease from 80% to almost zero (e.g. Dressler 1980; Whitmore et al. 1993). Evidently, this effect is strongly related to the density of the environment and leads to morphological segregation. One of the possible explanations comes from the phenomenon of ram pressure stripping and is therefore important to understand it in detail.

Since these pioneering works many more observations are now available making it possible to better understand this phenomenon. In addition to this, during the last twenty years, the use of numerical simulations has become more and more important in astrophysics and has led to a better understanding of this effect.

7.3 Common properties of ram pressure stripped cluster galaxies

7.3.1 The atomic hydrogen deficiency

The extent of the atomic hydrogen distribution in normal, isolated galaxies is larger than their optical disk (stellar distribution). On the other hand, several radio observations of cluster galaxies show that the radius of the hydrogen disk is truncated and that the hydrogen content is lower than that in their isolated counterparts (e.g. Giovanelli and Haynes 1985; Warmels 1988; Cayatte et al. 1990; Bravo-Alfaro et al. 2000; Gavazzi et al. 2005). This is the primary effect of ram pressure stripping. The atomic gas, being loosely bound to the gravitational potential of the galaxy is therefore more easily stripped from the outskirts of a galaxy, where the effects of gravitation are weaker, resulting in a galaxy that is poor in atomic gas.

Following the method by Haynes and Giovanelli (1984) we can define the HI deficiency parameter, *Def*, as

$$Def = < \log_{10} M_{\rm HI}(D_{\rm opt}, T) > - \log_{10} M_{\rm HI}, \tag{7.3.1}$$

where $< \log_{10} M_{\rm HI}(D_{\rm opt}, T) >$ is the average mass of HI contained in an isolated galaxy of optical diameter $D_{\rm opt}$ and of type T, while $M_{\rm HI}$ is the HI mass in the considered galaxy.

Further evidence for this phenomenon was found in a statistical study by Solanes et al. (2001), who measured the HI - *Def* of galaxies in a sample of 18 nearby clusters and found that most of the galaxies within two Abell radii ($2\,R_{\rm A}$, with $R_{\rm A} = 2.14\,$Mpc) show an ISM affected by the ram pressure stripping and are highly HI deficient within the Abell radius. Moreover, more recent VLA observations of the Virgo cluster, show

several galaxies with one-sided long HI tails (Chung et al. 2007). In particular, all the tails point away from the massive galaxy M87, therefore suggesting that the effect is caused by ram pressure at the global cluster scale.

7.3.2 Dust stripping

As the ICM wind starts exerting pressure on the galactic ISM as the galaxy enters the cluster, the galactic atomic gas is instantaneously coupled to the wind through direct collisional processes, while dust grains, having more inertia will tend to couple smoothly during a longer time. We would therefore expect to see some difference in the behaviour of the dust and gas as a galaxy experiences an ICM wind.

Cortese et al. (2010b), using *Herschel* data, for the first time, showed the dust distribution of ram pressure stripped galaxies in the Virgo Cluster. HI deficient galaxies show dust distributions very similar to the HI distributions. In particular, the dust disks are truncated to smaller radii than the optical disk and dust distributions form tails with a very good spatial correlation with the atomic gas tails. However, there are cases where a galaxy presents an HI tail while the dust is mostly contained within the optical disk. There are currently no available observations that show dust further out than the gas distribution.

The fact that the dust is not stripped as easily as the atomic gas was shown by Cortese et al. (2012). By measuring the stellar, gas and dust masses of several Virgo cluster galaxies and comparing them to the values for "field" galaxies, they found that in clusters, the dust-to-stellar mass ratio is lower and the dust-to-HI mass is higher. This is clear evidence that the dust distribution is less affected by the ram pressure stripping than the atomic gas.

The Fornax cluster, is a smaller cluster than Virgo and is more relaxed. Virgo has a velocity dispersion which is ~ 4 times greater and an ICM ~ 2 times as dense as Fornax (Boselli and Gavazzi 2006; Chung et al. 2007). According to Eq. 7.2.1, the ram pressure exerted by the ICM wind is then ~ 32 times larger in Virgo than in Fornax, indicating that Fornax may be ~ 32 times less efficient than Virgo in removing a galaxy's ISM via ram pressure stripping. However, Fuller et al. (2014) found that Fornax cluster galaxies have very similar FIR properties to the galaxies in Virgo. This may suggest that the effect of the cluster is more subtle than previously thought.

7.3.3 Molecular gas removal

The molecular gas in a galaxy is found in much denser clouds than the atomic gas in the more diffuse ISM and is therefore expected to be more tightly bound to the galactic gravitational potential and less likely to be stripped. However, HI - *Def* galaxies show a lower molecular gas mass than "field" galaxies. A statistical study by Boselli et al. (2014), comparing the HI - *Def* and H_2 - *Def* of several galaxies in Virgo and in the field found that there is a weak correlation between the two quantities (see Fig. 7.1a), i.e. the H_2 - deficiency is slightly larger for HI - *Def* galaxies. Also, they found a

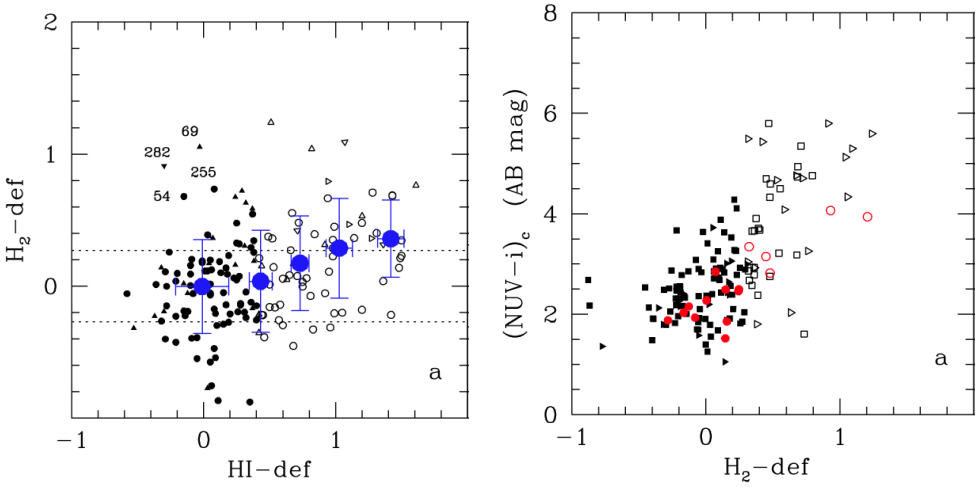

Figure 7.1: (a) H_2 - *Def* as a function of HI - *Def* for *Herschel* Reference Survey spiral galaxies. Circles indicate detected galaxies, triangles upper limits. Filled symbols indicate objects with a normal HI gas content (HI - *Def* $\leqslant 0.4$), open symbols HI - deficient objects (HI - *Def* > 0.4). The big blue filled dots indicate the mean values and the standard deviations. The horizontal dotted lines show the one-sigma dispersion of H_2 - deficiency parameter. (b) NUV - i as a function of H_2 - *Def* for the same sample of galaxies. Black squares indicate spiral galaxies whose molecular gas content has been determined using aperture corrections, red dots those objects with available CO integrated maps from Kuno et al. (2007). Filled symbols are for galaxies with H_2 - *Def* $\leqslant 0.3$, open symbols for objects with H_2 - *Def* > 0.3.

clear correlation between the NUV - i colour index (NUV band, ~ 227 nm and i band, ~ 806 nm), which is a reliable proxy for star formation activity, and the H_2 - deficiency parameter (see Fig. 7.1b). H_2 - *Def* galaxies show a less intense star formation activity. This tells us that, ram pressure stripping might be efficient at ablating or even stripping molecular gas from infalling galaxies and therefore quenching star formation.

7.4 Relevant observations of ram pressure stripped galaxies

From the general correlations mentioned in the previous section we have already learned much about the phenomenon of ram pressure stripping. However, to be able to fully understand this mechanism, we need to focus on observations of a few interesting sources. We selected here a sample of four galaxies which are particularly well suited

for our purposes:

- NGC 4330 (Virgo cluster)
- NGC 4402 (Virgo cluster)
- NGC 4522 (Virgo cluster)
- ESO 137-001 (Norma cluster)

In this section we focus on understanding of the dynamics of the molecular gas and dust in order to eventually model the processing of dust during such violent phenomena.

7.4.1 NGC 4330

This is a late-type, Sc galaxy in the Virgo Cluster. Its heliocentric velocity is 1569 km s^{-1}, exceeding the mean heliocentric velocity of the Virgo Cluster of ~ 470 km s^{-1} (Abramson et al. 2011), and is located at the projected distance of 2° (~ 600 kpc) away from the massive galaxy M87. Given the large relative velocity between the galaxy and the ICM and its vicinity to the centre of the cluster, this galaxy is expected to be undergoing heavy ram pressure stripping. Measurements of its atomic gas content, compared to equivalent galaxies in the field, result in a HI - *Def* of 0.8 (Chung et al. 2007).

Furthermore, this galaxy is almost edge-on (inclination angle of 84°), which makes this source particularly suitable for observations of the extra planar stripped gas. An HI tail is observed pointing away from M87, supporting the idea that NGC 4330 is falling towards M87 and has been stripped of its ISM because of the external pressure of the ICM (Abramson et al. 2011). Since the gas distribution is affected by the perturbation, while the stellar distribution is unperturbed, Abramson et al. (2011) ruled out the possibility of a gravitational encounter, which is supported by the relative distance and velocities of the nearby galaxies.

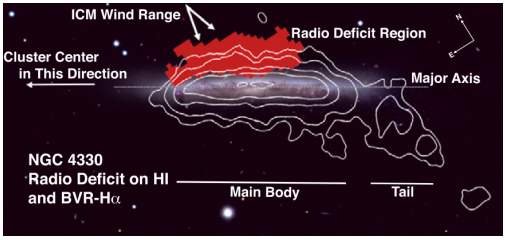

Figure 7.2: NGC 4330 radio deficit on HI and BVR - Hα observations (Abramson et al. 2011).

NGC 4330 shows interesting upwind and downwind features with respect to the main body of the galaxy (see Fig. 7.2). In the upwind region, the galaxy shows a local

radio continuum deficit, the strongest in the Virgo cluster sample observed by Murphy et al. (2009). This feature is believed to be a good tracer of ongoing ram pressure and is approximately coincident with the leading edge of the galaxy (Abramson et al. 2011).

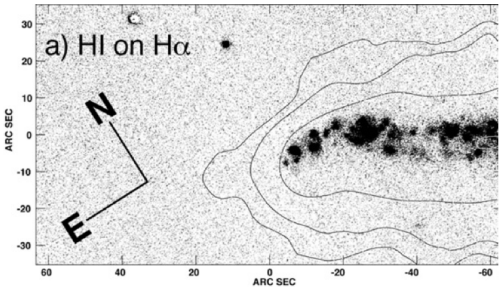

Figure 7.3: NGC 4330 HI on Hα, detail of the upturn (Abramson et al. 2011).

Furthermore, at its leading edge, to the north-east, NGC 4330 presents an important feature which Abramson et al. (2011) refer to as an "upturn" (see Fig. 7.3). In this region the Hα distribution is clearly shifted out of the galactic plane to a vertical extent of $\sim$ 13" ($\sim$1 kpc) from the optical major axis. This suggests that in the galactic plane star formation has been quenched because of the effects of ram pressure and that new stars are formed extra planar. Comparing the Hα observations with the B- and R-band images, Abramson et al. (2011) also deduced that the emission coming from the upwind direction is probably due to faint young stars while downwind the emission is dominated by redder stars suggesting that the upturn is the boundary beyond which the dust has been stripped away.

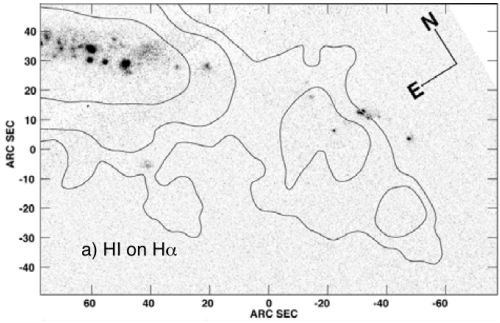

Figure 7.4: NGC 4330 HI on Hα, the trailing edge (Abramson et al. 2011).

The trailing edge of NGC 4330 (see Fig. 7.4) presents a 13 kpc long and 5 kpc wide HI tail (Chung et al. 2007). The Hα emission is clumpy and not continuous

between the main body of the galaxy and the tail while the FUV emission does not present any break. The lack of an extensive Hα distribution and a bright FUV emission suggest that there has been little star formation recently (~ 5 Myr ago, Abramson et al. 2011). However, from UV observations Abramson et al. (2011) inferred a burst of star formation in this region between ~ 10 and 200 Myr ago and that, in the meantime, conditions in the tail region became less suitable for star formation, probably because the HI gas has been swept away during the stripping process.

7.4.2 NGC 4522 and NGC 4402

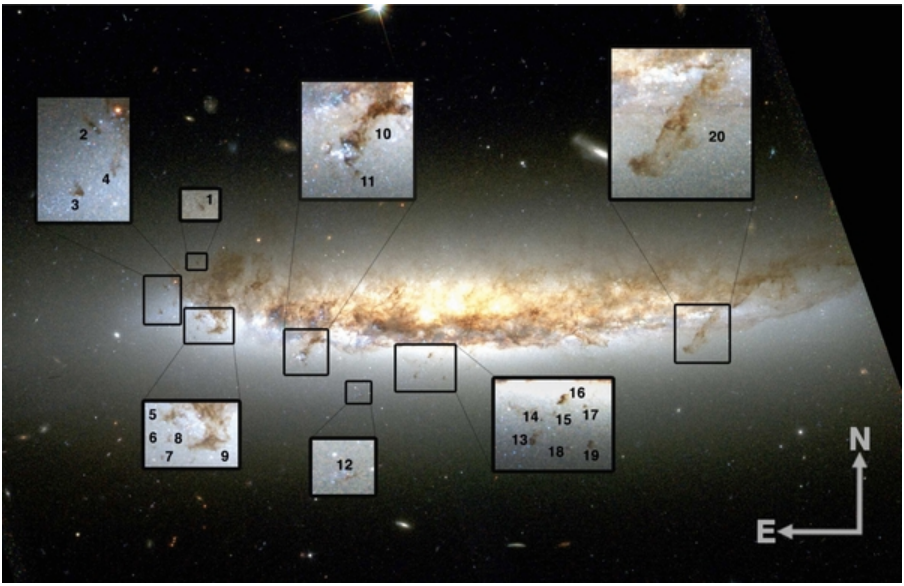

Figure 7.5: NGC 4402 as seen by *Hubble* Space Telescope (Abramson and Kenney 2014).

These are two interesting galaxies in the Virgo cluster, probably two of the best cases to study the interaction between the ISM of galaxies and the ICM. NGC 4522 and NGC 4402 are both highly-inclined (78° and 80°, respectively) and strongly HI - deficient. Both the galaxies show evidence for ongoing ram pressure stripping: they present truncated HI disks, one-sided extraplanar HI tails (Crowl et al. 2005; Kenney et al. 2004; Vollmer et al. 2004, 2010) and radially truncated star formation (Koopmann and Kenney 2004; Crowl et al. 2005). Furthermore, the leading edges of these galaxies show a radio continuum deficit, signature of the perturbation of the galactic magnetic field due to interaction with the ICM wind (Murphy et al. 2009).

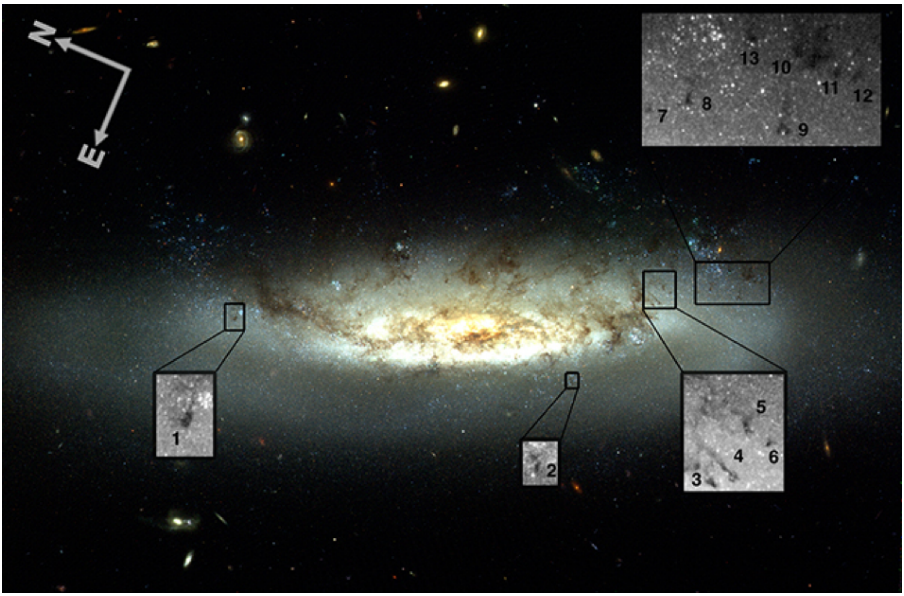

Figure 7.6: NGC 4522 as seen by *Hubble* Space Telescope (Abramson and Kenney 2014).

A recent study by Abramson and Kenney (2014) presents high-resolution images of these galaxies. The observations reveal the presence of decoupled dense clouds outside of the galactic planes. In Fig. 7.5 and 7.6 we show the observations of Abramson and Kenney. The zoomed regions highlight the largest dense clouds observed, which are clearly elongated in the same direction of the ICM wind. This is further evidence for ongoing ram pressure stripping, i.e., regions where decoupled dense gas are seen in the act of being stripped and ablated. These regions are called transition zone by Abramson and Kenney (2014).

In the transition zone, only $\sim 1-6\%$ of the original gas mass is observed and only $\sim 2-3\%$ of the star formation rate is measured. Furthermore, based on the star formation quenching time in the transition zone or beyond it, Abramson and Kenney (2014) deduce that the lifetime of the decoupled dense clouds is $\sim 150-200\,\mathrm{Myr}$ and estimate that the average stripping rate is $\sim 3-30\,\mathrm{pc\ Myr^{-1}}$ and $\sim 7.5-12.5\,\mathrm{pc\ Myr^{-1}}$ for NGC 4522 and NGC 4402, respectively. From these observations they were not able to conclude if the observed dense clouds are stripped from the galaxy or are formed downstream.

7.4.3 ESO 137-001 (=WKK 6176)

This is a barred spiral galaxy (see Fig. 7.7) in the Norma Cluster (Abell 3627). This galaxy is only ~ 180 kpc away from the cluster X-ray peak in projection and its radial velocity (i.e. the velocity along the line of sight) is very close to the average radial velocity of the cluster, suggesting that most of its motion is along the plane of the sky and making it a particularly interesting case to study ram pressure dynamics. However, since its velocity is mostly in the plane of the sky, it is difficult to estimate its relative velocity with respect to the ICM.

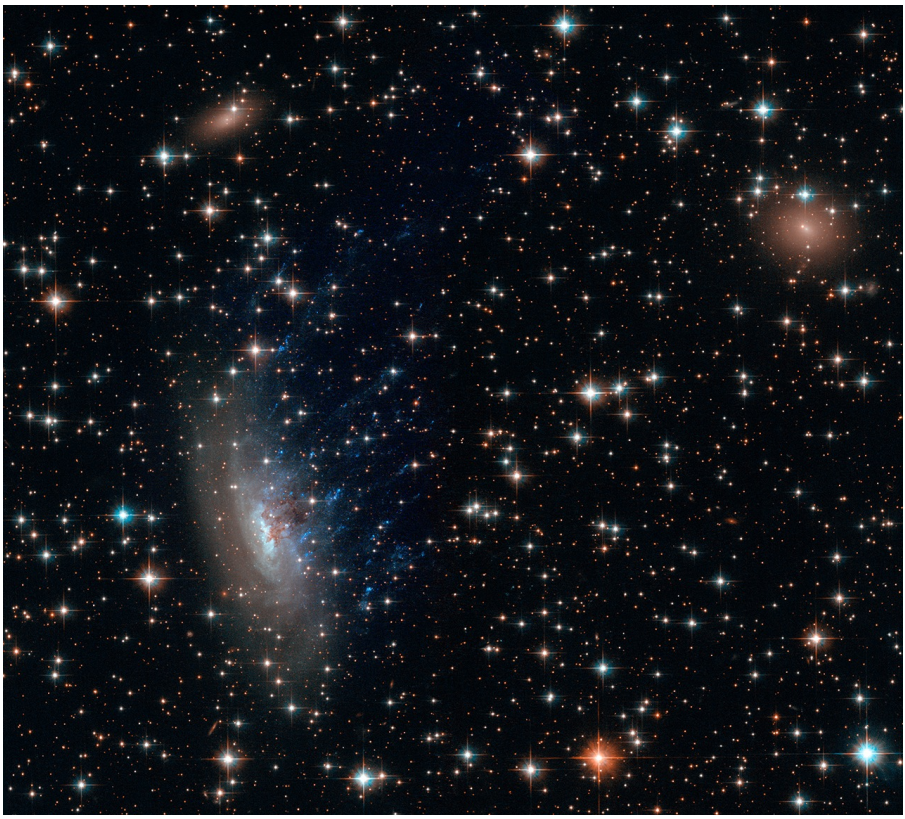

Figure 7.7: ESO 137-001 as observed by *Hubble* Space Telescope.

Chandra and *XMM-Newton* observations (Sun et al. 2006) and more recently deeper *Chandra* observations (Sun et al. 2010) revealed a remarkably long and bright X-ray tail associated with this galaxy. The tail is ~ 80 kpc long and has a length-to-width ratio of ~ 10. These observations leave no doubt about the ongoing phenomenon: the galaxy is being stripped by ram pressure. However, it should be noted that X-ray

emitting tails associated with ram pressure stripped galaxies are not common and may only be found in an extremely hot ICM such as in the Norma Cluster ($T = 6.5\,\mathrm{keV}$). Even in Virgo, where the ram pressure significantly affects infalling galaxies, no X-ray tail has yet been detected.

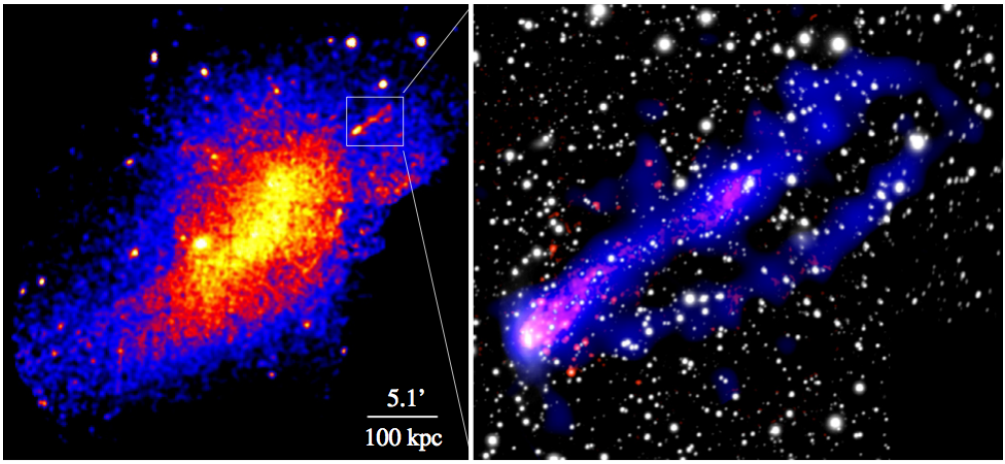

Figure 7.8: Left: XMM-Newton 0.5-2 keV mosaic of Abell 3627. Right: the composite X-ray/optical image of ESO 137-001's tail. The *Chandra* 0.6-2 keV image is in blue, while the net Hα emission (from the SOAR data; Sun et al. 2007) is in red. The white stellar image is SOAR Hα + continuum image. Sun et al. (2010).

Furthermore, Sun et al. (2010), using Gemini GMOS[1] spectroscopic observations, revealed at least 33 intracluster HII regions in the X-ray tail, confirming the Hα observations by Sun et al. (2007). This led them to the conclusion that the stripped material from a galaxy is able to form new stars in-situ downstream in the tail.

Finally, the recent *Chandra* observations of ESO 137-001 reveal the presence of a faint secondary tail associated with the main tail. This effect was totally unexpected and gives insight into the dynamics of ram pressure stripping, which can only be fully understood with the use of numerical simulations (see Section 7.5).

A few months later, Sivanandam et al. (2010) presented *Spitzer* IRAC and IRS observations of ESO 137-001. They discovered a warm (130 - 160 K) H_2 tail (see Fig. 7.9) associated with the X-ray emitting tail of the galaxy. The H_2 tail is at least 20 kpc long (this measurement is limited by the extension of the slit in their observation) and the H_2 mass has been estimated as $\sim 4 \times 10^7\,\mathrm{M}_\odot$.

[1]The Gemini Observatory consists of two 8.1-meter diameter, the Gemini South telescope on the summit of Cerro Pachon in Chile, and the Frederick C. Gillett Gemini North telescope on the summit of Mauna Kea on the island of Hawaii. The two Gemini Multi-Object Spectrographs (GMOS), one on each telescope, provide 0.36-0.94 μm long-slit and multi-slit spectroscopy and imaging.

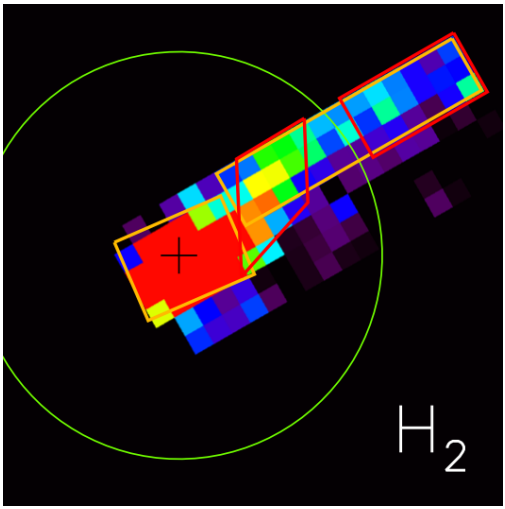

Figure 7.9: ESO 137-001 as observed by Spitzer (Sivanandam et al. 2010).

Assuming that the drift velocity of ESO 137-001 in the ICM is between ~ 900 and $1600\,\mathrm{km\,s^{-1}}$, Sivanandam et al. (2010) obtained an H_2 mass loss rate of $1.9{-}3.4\,M_{\odot}\mathrm{yr}^{-1}$ and derived a characteristic timescale for the total stripping of the ISM of $\sim 1\,\mathrm{Gyr}$, i.e. much shorter that the crossing time in this cluster, $\sim 5\,\mathrm{Gyr}$.

7.4.4 *Herschel* data of ESO 137-001

ESO 137-001 was observed with the *Herschel* Space Observatory using the PACS instrument at 70, 100 and 160 μm, and the SPIRE instrument at 250, 350 and 500 μm (see Table 7.1). Both instruments were used in photometry mode and set up to provide a uniform coverage over a field of view of about $5'$, with scans made along two orthogonal directions. We retrieved the data from the *Herschel* Science Archive and reduced them to produce new maps. Basic identification details of this dataset are given in Table 7.1.

Table 7.1: Observation details for the Herschel data of the galaxy ESO 137-001.

Observation ID	Instrument	Wavelengths	Program
1342230811	SPIRE	250/350/500	OT1_ssivanan_1
1342241663	PACS	70/160	OT1_ssivanan_1
1342241664	PACS	70/160	OT1_ssivanan_1
1342241665	PACS	100/160	OT1_ssivanan_1
1342241666	PACS	100/160	OT1_ssivanan_1

SPIRE maps were created with the standard script for the Small Map Observing mode, provided within the dedicated *Herschel* Interactive Processing Environment, HIPE v10 (Oct 2010); version 10.1 of the calibration tree was used. After extensive testing of the results, we decided to use the standard destriper provided within the script, removing DC offsets from the scans and avoiding scan turn-around regions.

For PACS, we used HIPE to reduce the data up to level 1, updating the calibration to release 48. Then, scans were projected onto a sky grid using the Scanamorphos v21 software (Roussel 2013), with standard settings for maps covering a small sky area[2].

The map pixel sizes were chosen to be $\sim 1/3$ of the FWHM at the various wavelengths, thus 1.5", 2", 3", 6", 8" and 12"/pixel at 70, 100, 160, 250, 350 and 500 μm, respectively. The assumed FWHM of the PACS-SPIRE beams and the flux accuracies are the same as those mentioned in Section 5.1.

The Norma cluster is at low Galactic latitude ($b \sim -7^\circ$) and in projection is very close to the Galactic bulge (only 35° away). Therefore the Herschel data is widely contaminated by the presence of the Galactic cirrus which makes the analysis of the dust in and around ESO 137-001 complicated. One way to distinguish between the infrared (IR) emission coming from the dust associated with the target galaxy and the cirrus emission is to make a dust equilibrium temperature map. Since the target galaxy is interacting with the ICM, the dust in both the main body and tail of the galaxy is expected to be rather warm ($T \gtrsim 20\,\mathrm{K}$), creating a contrast in the temperature map with the dust associated with the Milky Way ($T \sim 18 - 20\,\mathrm{K}$).

Temperature map

This section is part of a preliminary work by Bocchio et al. (2014, in prep.). In order to build the temperature map we use the 70 μm, 100 μm and 160 μm PACS data and the 250 μm SPIRE data. We decided not to use the 350 μm and 500 μm SPIRE data because the statistical noise is too high for these bands and it would not lead to a better estimate of the dust temperature but, on the other hand, would lead to a lower spatial resolution. We select a region of the sky of $\sim 5' \times 5'$ around ESO 137-001 and fit the data, on a pixel by pixel basis with a modified blackbody radiation:

$$I_\nu = \tau B_\nu(T)(\nu/\nu_0)^\beta, \tag{7.4.1}$$

where τ is the optical depth, $B_\nu(T)$ is the Planck blackbody emission for a given temperature T and β is the spectral index at the reference frequency $\nu_0 = 100\,\mu\mathrm{m}$.

First of all, we convolved all the maps to a common resolution (the beam size of the 250 μm SPIRE data, 17.6" / beam) and smoothed the images to a common pixel size (the pixel size of the 250 μm SPIRE data, 36 arcsec^2 / pixel). Then, for each band we calculated the average value of the background flux (calculated in a region that is not contaminated by any extended structure) and removed it from each pixel in the map.

[2]The author of this manuscript would like to thank S. Bianchi for having performed the PACS and SPIRE data reduction for this source.

The total error, $\sigma_{\rm TOT}$, on the flux in each pixel was estimated from the calibration errors ($\sigma_{\rm CAL}$) and statistical errors ($\sigma_{\rm STAT}$):

$$\sigma_{\rm TOT} = \sqrt{\sigma^2_{\rm CAL} + \sigma^2_{\rm STAT}}. \tag{7.4.2}$$

The statistical error is calculated as the standard deviation of the background flux, while the calibration error equals 20% of the flux in PACS data and 7% in SPIRE data.

Finally, we perform a fit (with the minimum χ^2 method) on a pixel by pixel basis using a modified blackbody to obtain the temperature map of the large grains. We set $\beta = 2.0$ as a fixed parameter, and we show in Fig. 7.10 the temperature map (north is up, west is right) for all the pixels with an uncertainty on the temperature of $\Delta T < 3\,$K. The black ellipse at the centre of the map represents the optical boundaries of ESO 137-001 (Woudt et al. 2008) while the small cross indicate its centre. The pixel size is 6" and since the galaxy is ~ 67.8 Mpc away from us, each pixel represents a size of $\sim 2\,$kpc.

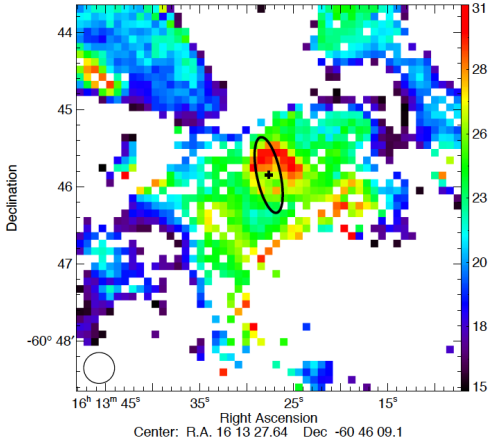

Figure 7.10: Temperature map in and around ESO 137-001 for all the pixels with $\Delta T < 3\,$K. We assumed a fixed $\beta = 2$. The ellipse at the centre of the image represents the optical image of the galaxy while the small black cross its centre.

We notice that the cirrus contamination in this region of the sky is considerable and that it is not easy to distinguish between the emission from the target galaxy or from the cirrus. In particular, the cirrus temperature in some regions is higher than expected (up to $\sim 25\,$K) but it does not seem to be associated with our target galaxy. However, since this observation is performed at low galactic latitude, this warm dust, not associated with ESO 137-001, might reside in central regions of the Milky Way where the stellar radiation is more intense. On the contrary, the dust associated with

our target galaxy is warmer ($T_{\rm ESO} \sim 25 - 30\,{\rm K}$). We note that we detect dust as far as $\sim 8\,{\rm kpc}$ from the galactic plane co-aligned with the observed X-ray and H_2 tails and further than that distance, the dust temperature and the IR flux abruptly decrease. The dusty disk is truncated with respect to the optical disk and we estimate that its radius is $\sim 7\,{\rm kpc}$.

7.4.5 Common features for ram pressure stripped galaxies

The increasing spatial resolution of recent observations has led to more and more information on the phenomenon of ram pressure stripping. Here we sum up the most evident common features of ram pressure stripped galaxies:

- maybe the most important parameter to judge the degree of stripping of a galaxy is the HI-def (Haynes and Giovanelli 1984). The atomic hydrogen gas is loosely bound to the gravitational potential well and is therefore the component of the ISM most affected by the ram pressure. This leads to a truncation of the HI disk (Cayatte et al. 1990; Bravo-Alfaro et al. 2000) and most of the time, to the formation of HI tails (e.g. Chung et al. 2007),

- interstellar dust is stripped together with the atomic gas (even if to a lesser degree), leading to a truncation of the dust disk and sometimes to dusty tails (Cortese et al. 2010b, 2012),

- during the ram pressure stripping dense clouds are decoupled from the stripped ISM and are ablated or stripped (Abramson and Kenney 2014; Boselli et al. 2014),

- a good tracer for ongoing ram pressure is the radio continuum deficiency at the leading edge of the galaxy. The interaction with the ICM wind is responsible for the perturbation of the galactic magnetic field and for a decrease in the radio continuum (Murphy et al. 2009),

- young stars can be formed downstream in the tail in the stripped ISM. However, this is not always the case as there are observations of ram pressure stripped galaxies with no ongoing star formation in the tail (Tonnesen and Bryan 2012 and references therein).

This evidence allows us to gain a better understanding of this phenomenon but there are still many open questions that only future observations, together with numerical simulations, may be able to answer. For our purposes maybe the two most important questions are:

- are molecular clouds stripped wholesale in the process or re-formed in the tail?

- what is the destruction timescale for dust during this process? How far in the ICM can we observe the stripped dust?

These two questions are closely related. If molecular clouds are stripped in the process then dust can be entrained together with dense clouds and therefore reach long distances from the galactic plane without being destroyed. On the other hand, if molecular clouds are only ablated by the ICM wind, and only stripped together with the diffuse atomic gas when their density is low, then the dust cannot be protected from the high velocity wind/shock and the hot ICM gas and it will be destroyed on short timescales.

However, as observed for example in ESO 137-001, the dust tail extends to $\sim 8\,\mathrm{kpc}$ from the galactic plane. This represents an intermediate distance between the extent of the molecular gas tail ($> 20\,\mathrm{kpc}$) and the characteristic spatial scale of shocks ($\lesssim 100\,\mathrm{pc}$).

7.5 Numerical simulations

During the last few years, numerical simulations have reached a certain sophistication and reliability in solving astrophysical problems and can therefore tell us much about the mechanisms involved in ram pressure stripping. There are essentially two kinds of numerical simulations: the Smoothed-Particle Hydrodynamics (SPH) and the Adaptive Mesh Refinement (AMR) approaches. Depending on the modelled astrophysical process, one might prefer one method to the other. Roughly speaking, SPH simulations are able to better describe hydrodynamic flows but tend to smear out shocks to a greater extent than AMR simulations. Furthermore, with AMR simulations we have a direct access to the thermodynamical parameter in a certain region (cell) and the extent of the simulation cell is refined in order to achieve the required accuracy.

As an example, Vollmer et al. (2012), using a SPH simulation, were able to qualitatively reproduce the dynamics of the HI and molecular distribution in the stripped Virgo galaxy NGC 4330. However, in the case of a larger ram pressure and ICM thermal pressure, such in the case of ESO 137-001, the discontinuities would be more important and SPH simulations would have more difficulty in reproducing the observations.

Tonnesen et al. (2011) using a AMR simulation, *Enzo* code, were able to reproduce quantitatively the luminosity of the X-ray tail of ESO 137-001 and the star formation in the tail (Tonnesen and Bryan 2012). They were thus able to successfully reproduce the multi-phase ISM of the stripped galaxy.

Finally, to add difficulty to an already complicated picture, magnetic fields seem to play a major role in the dynamics of this phenomenon. However, as Ruszkowski et al. (2014) showed, it is possible to include the effects of the magnetic field in AMR simulations (FLASH code), to reliably reproduce the shape of the stripped gaseous tails. In particular, they showed that the characteristic double tails observed in ESO 137-001 can be satisfactorily explained as ionised gas confined by the complicated shape of the magnetic field in the wake of the galaxy.

7.6 Can molecular gas be formed in the tail?

This section focuses on the dynamics of the molecular gas in ram pressure stripped galaxies. From observations we cannot conclude if molecular clouds are stripped from the ISM as a whole or if they are only ablated and then stripped when their density is low enough. Numerical simulations seem to indicate that the stripping of molecular clouds is not possible even in the case of high ram pressure and their ablation is the most likely scenario (e.g. Tonnesen and Bryan 2009, 2012).

What are then the mechanisms that can explain the presence of molecular gas in the tail of ram pressure stripping? We will explore three viable scenarios in the following and comment on each of them in turn.

7.6.1 Gas cooling and condensation

The AMR numerical simulations from Tonnesen and Bryan (2012) show that dense molecular clouds are not stripped wholesale from the galaxy but are rather ablated. However, once in the tail, the atomic gas cools and condenses under the ICM thermal pressure and forms molecular gas. This mechanism therefore triggers star formation in the tail. They conclude that the star formation in the tail is mostly regulated by the ICM pressure rather than the ram pressure itself.

7.6.2 H_2 formation on dust grains

This section is part of a preliminary work by Bocchio et al. (2014, in prep.). The formation of H_2 molecular gas is commonly believed to happen on the surface of dust grains. We compute the timescale necessary for the H_2 formation in the tail of ram pressure stripped galaxies and we show that, even in such a harsh environment, this represents a viable mechanism.

From results of the *Enzo* numerical simulation of ESO 137-001 Tonnesen et al. (2011) infer that the relative velocity between the galaxy and the surrounding ICM might be as high as $v_{\rm rel} \sim 1900$ km s^{-1}. The present time is estimated to be $t_{\rm pres} \sim 100$ Myr after the galaxy entered the cluster. In their simulations (at the present time) the tail of ESO 137-001 show (Fig. 2 in Tonnesen et al. 2011) an almost bimodal composition: part of the gas is cold and dense ($T_{\rm cold} \sim 10^3 - 10^4$ K, $n_{\rm H} \sim 1\,{\rm cm}^{-3}$) while the rest is hot and diffuse ($T_{\rm hot} \sim 10^7$ K, $n_{\rm H} \sim 10^{-2}\,{\rm cm}^{-3}$). In the simulation output (temperature and density for each simulation cell), in the first 4 - 5 kpc above the galactic plane, the volume fraction occupied by the cold atomic gas is about the 10%, while the 90% of the volume is occupied by the hot diffuse gas, but most of the gas mass is in atomic form[3].

If we assume that the gas-to-dust mass ratio is constant across the tail and inside the galaxy, we then have that almost all of the dust that is stripped is actually embedded

[3]The author of this manuscript would like to thank S. Tonnesen for having provided outputs from her simulations.

in the HI gas (Fig. 7.11) and entrained together with it therefore not undergoing any erosion (a similar mechanism is thought to happen around M 82; Micelotta et al. 2010a).

As the galaxy is invaded by the hot ICM wind, gas and the dust are progressively stripped out of the galaxy. At $t_{\rm pres}$ the z-velocity, parallel to ICM wind, of the majority of the clouds is $v_{\rm cloud} \sim 300\,{\rm km\ s^{-1}}$ (Tonnesen and Bryan 2010). It is likely that HI clouds are displaced wholesale and progressively accelerated to this velocity. Ignoring the gravitational force that hold the clouds to the galactic plane, the pressure exerted by the ICM wind is $P_{\rm ICM} = \rho_{\rm ICM} v_{\rm rel}^2$ and so the acceleration that a cloud of radius $r_{\rm cloud} = 10$ pc and mass $m_{\rm cloud} = {}^4\!/_3\,\pi \rho_{\rm cloud} r_{\rm cloud}^3$ undergoes is given by

$$a_{\rm cloud} = \frac{\rho_{\rm ICM} v_{\rm rel}^2 \pi r_{\rm cloud}^2}{m_{\rm cloud}}. \tag{7.6.1}$$

If we assume an ICM number density $n_{\rm H} = 10^{-3}\,{\rm cm^{-3}}$ and a cloud number density $n_{\rm H} = 1\,{\rm cm^{-3}}$, for a relative velocity between the galaxy and the ICM of $v_{\rm rel} = 1900\,{\rm km\ s^{-1}}$ we obtain $a_{\rm cloud} \sim 9 \times 10^{-7}\,{\rm cm\ s^{-2}}$. Therefore the coupling distance, $d_{\rm coupl}$, that travels such a cloud before reaching the velocity $v_{\rm cloud}$ is roughly given by:

$$\begin{aligned} d_{\rm coupl} &= \frac{1}{2}\frac{v_{\rm cloud}^2}{a_{\rm cloud}} \\ &\sim 200\,{\rm pc} \end{aligned} \tag{7.6.2}$$

We can assume that, a dust grain which was at rest in an HI cloud before the ram pressure takes over, will be at rest again rather soon after the acceleration is finished. This is a rough estimate of the coupling distance that does not take into account the gravitational force, which is function of the distance from the galactic plane. We therefore assume a more realistic coupling distance of $\sim 500\,{\rm pc}$, even in this case the coupling distance is very short with respect to the length of the observed tail. Starting from $\sim$ 500 pc above the galactic plane, the dust is coupled to the HI gas and H_2 molecules can be efficiently formed on the surfaces of grains.

The H_2 formation rate can be expressed as (e.g. Hollenbach and McKee 1979):

$$R_{\rm f}({\rm H_2}) = \pi a_{\rm gr}^2 \left(\frac{8 k_{\rm B} T}{\pi m_{\rm H}}\right)^{1/2} \times S(T) \times f \times \eta \quad [{\rm cm^3 s^{-1}}] \tag{7.6.3}$$

where $a_{\rm gr}$ is the grain radius, T is the HI gas temperature, $m_{\rm H}$ is the hydrogen mass, $S(T)$ is the temperature-dependent probability that an H atom sticks onto the grain surface, f is the probability that the incident H atom stays on the grain and migrates towards the other adsorbed H atom and η is the probability of recombination to form an H_2 molecule. The H_2 formation rate per unit volume is given by:

$$R({\rm H_2}) = R_{\rm f}({\rm H_2}) \times n_{\rm H} \times n_{\rm grain} \tag{7.6.4}$$

where $n_{\rm H}$ and $n_{\rm grain}$ are the number densities of hydrogen atoms and grains. Assuming an HI gas temperature and density $n_{\rm H} = 1\,{\rm cm}^{-3}$, $T_{\rm gas} = 5 \times 10^3\,{\rm K}$, following Hollenbach and McKee (1979) we estimate $S(T) \simeq 3 \times 10^{-3}$. We now assume a MRN size distribution for dust grains. The mean grain radius, $\bar{a}$, is then given by

$$\bar{a} = \frac{\int_{a_1}^{a_2} a\, a^{-3.5}\, da}{\int_{a_1}^{a_2} a^{-3.5}\, da} \sim 9\,{\rm nm} \tag{7.6.5}$$

where a_1 and a_2 are 5 and 250 nm, respectively. Then, if we assume that in ESO 137-001 the gas-to-dust mass ratio is the same as in our Galaxy ($m_{\rm dust}/m_{\rm H} = 0.0073$, Draine et al. 2007), a gas with density $n_{\rm H} = 1\,{\rm cm}^{-3}$ has an associated dust number density, $n_{\rm dust}$, obtained by

$$\frac{4/3\,\pi\rho\bar{a}^3 n_{\rm dust}}{m_{\rm H} n_{\rm H}} = \frac{m_{\rm dust}}{m_{\rm H}} = 0.0073 \tag{7.6.6}$$

and therefore $n_{\rm dust} \sim 1.75 \times 10^{-9}\,{\rm cm}^{-3}$. Then, the H_2 formation rate per unit volume $R({\rm H_2}) = 5 \times 10^{-18}\,{\rm cm}^{-3}{\rm s}^{-1}$ (we consider $f = \eta = 1$ for simplicity). Assuming a dust tail radius of $r \sim 7\,{\rm kpc}$ and a H_2 formation region $l \sim 4\,{\rm kpc}$ long, the volume where dust can efficiently form H_2 is

$$V = \pi r^2 l \sim 1.8 \times 10^{67}\,{\rm cm}^3. \tag{7.6.7}$$

Therefore we estimate that the total H_2 formation rate equals

$$R({\rm H_2}) \times V \sim 2.5 M_\odot/{\rm yr} \tag{7.6.8}$$

which is consistent with the estimate from *Spitzer* observations by Sivanandam et al. 2010 (1.9 - 3.4 $M_\odot$ yr^{-1}).

It should be noted that the observed X-ray emission has a uniform flux of $\sim 10^{-4}$ erg s^{-1} cm^2 (in the band 0.5 - 2 keV) and the H_2 cross-section is given by

$$\sigma_{H_2}(E) \sim \frac{45.6}{E({\rm keV})^{7/2}}\,{\rm barns}. \tag{7.6.9}$$

Therefore, even assuming X-ray photons of 0.5 keV, the timescale for the dissociation of H_2 molecules is $\sim 1\,{\rm Gyr}$, which is a timescale much longer than the ram pressure stripping timescale and H_2 molecules are formed efficiently without being immediately dissociated by X-ray radiation.

At about 4 - 5 kpc from the galactic plane the HI gas undergoes significant evaporation, so a large fraction of the dust is released into the hot and diffuse gas and H_2 formation is quenched. In a gas with $(T,\ n_{\rm H}) = (10^7\,{\rm K},\ 10^{-3}\,{\rm cm}^{-3})$ the estimated lifetime for a large carbonaceous grain of radius $a = 100\,{\rm nm}$ is $\sim 10^7\,{\rm yr}$ (Bocchio et al. 2012). Assuming a cloud velocity of $\gtrsim 300\,{\rm km\ s}^{-1}$ (Tonnesen et al. 2010), during this time dust would travel $\sim 3 - 4\,{\rm kpc}$ thus explaining the presence of dust in the tail as far as $\sim 8\,{\rm kpc}$ from the galactic plane.

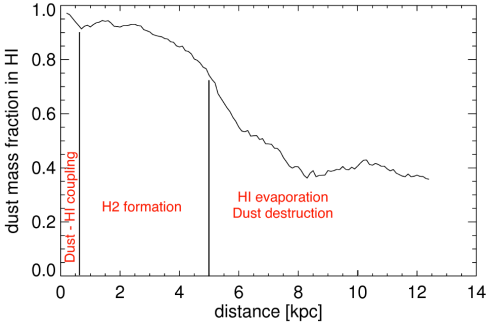

Figure 7.11: Dust mass in the HI gas as a function of the distance from the galactic plane. We show schematically the main processes in the different regions of the tail.

7.6.3 Magnetic field supported molecular clouds

All the hydrodynamical simulations performed by Tonnesen et al. (2011) do not include any effect of the magnetic field. However, there is evidence for magnetic fields both in spiral galaxies and in the ICM. As a galaxy move through the ICM, the ambient magnetic field is thought to wrap around the galaxy itself. Magnetic wrapping would lead to a magnetic energy ahead of the moving galaxy of a strength comparable to the ram pressure experienced by the galaxy (Dursi and Pfrommer 2008; Pfrommer and Dursi 2010). In this way magnetic fields would modify the process of stripping and may prevent Kelvin-Helmhotz instabilities.

It has been shown by Ruszkowski et al. (2014) that the inclusion of magnetic fields in hydrodynamical simulations leads to important effects during ram pressure stripping. Hydrodynamical simulations of ram pressure stripping show the formation of a clumpy tail downstream of the moving galaxy. The presence of a magnetic field leads to a big change in the shape of the tail which shows a rather filamentary structure (see Fig. 7.12). Furthermore, Ruszkowski et al. (2014) noticed an increase in the gas removal from the galaxy may be because the magnetic fields stretched along the tail are able to pull or at least not impede the stripping of gas. Finally, these magnetically supported filaments seem to reduce the thermal conduction between the tail and the ICM possibly leading to the formation of molecular clouds in the tail. Unfortunately using their setup it was not possible to reproduce specific observations.

In this scenario, the presence of a magnetically supported molecular tail would prevent dust destruction and would favor dust accretion. In this way it would be possible to explain the multi-phase composition of the tail and the presence of both a dusty and molecular tail behind ESO 137-001.

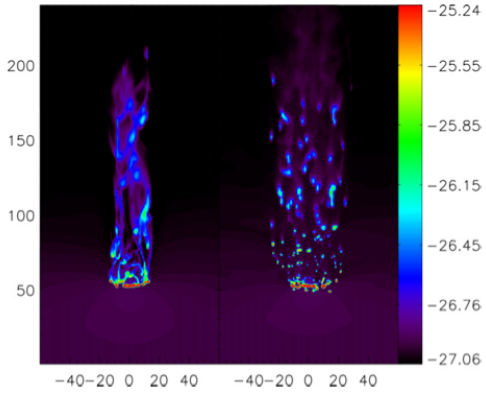

Figure 7.12: Gas density (in units of g cm^{-3}) projected along the line of sight (spatial dimensions are in pc). Left: MHD case. Right: non-magnetic case. Ruszkowski et al. (2014).

7.6.4 Summary and conclusions

Numerical simulations seem to indicate that, even in the case of high ram pressure, galactic molecular clouds are not stripped wholesale but rather undergo ablation (e.g. Tonnesen and Bryan 2009, 2012). We explored three possible mechanisms that can explain the presence of molecular gas in the tail of ram pressure stripped galaxies.

We proposed that during ram pressure, dust is entrained in atomic gas clouds stripped of the galactic ISM. In this cold and dense environment, dust grains undergo little destruction and can efficiently form H_2 molecules on their surface. Then, the atomic cloud, surrounded by the hot ICM evaporates and dust is exposed to the collisions of fast ions and electrons contained in this medium, therefore leading to the destruction of grains. In this harsh environment, small grains ($\lesssim 2$ nm) are destroyed on short timescales ($\lesssim 10^4$ yr) and only larger grains can survive for $\sim 10^7 - 10^8$ yr, thus explaining the observed IR emission in the tail up to ~ 8 kpc from the galactic plane. The amount of H_2 gas formed downstream on the surface of grains is sufficient to explain the observed long H_2 tail.

Furthermore, AMR numerical simulations from Tonnesen and Bryan (2012) show that, under the thermal pressure of the hot external ICM, the atomic gas in the tail cools and condenses possibly favoring the formation of H_2 gas.

Finally, the inclusion of magnetic fields in hydrodynamical simulations leads to important consequences to the modelling of ram pressure stripping (Ruszkowski et al. 2014). In particular, this leads to the formation of magnetically supported filaments which seem to reduce the thermal conduction between the tail and the ICM.

Most likely, all these three mechanisms are at play during ram pressure stripping, therefore possibly explaining the survival of dust and the formation of molecular gas

even in such a harsh environment. The use of numerical simulations gives us the possibility to shed some light on this phenomenon and therefore help us to better understand the evolution of cluster galaxies.

Chapter 8

Conclusions and perspectives

> Focus on the journey, not the destination. Joy is found not in finishing an activity but in doing it.
>
> Greg Anderson

8.1 Conclusions

VIOLENT phenomena such as galaxy-galaxy interactions or ram pressure stripping are responsible for the mixing between the galactic ISM and the ICM therefore leading to the injection of dust in the ICM and contributing to the metal enrichment of the medium itself. However, the ICM is a hot coronal-type gas and therefore represents an extreme environment for dust grains. The main questions that I asked myself during my PhD study are:

- what is the lifetime of dust grains in such a hot gas?
- What is the main source of dust heating?
- Can dust be detected by modern IR telescopes in the ICM?

Answering these questions is not an easy task and a complete solution to the problem will be given only with the support from the three pillars of astrophysics: modelling, observations and numerical simulations (see Fig. 8.1).

During the first part of my PhD study I focused my attention on the basic principles that govern the interaction between energetic ions and electrons and dust grains. A particle, hitting the surface of a grain, transfers a fraction of its initial energy and momentum to the grain itself. As a consequence the grain can undergo erosion or

can relax through photon emission. These two processes are coupled and cannot be considered separately.

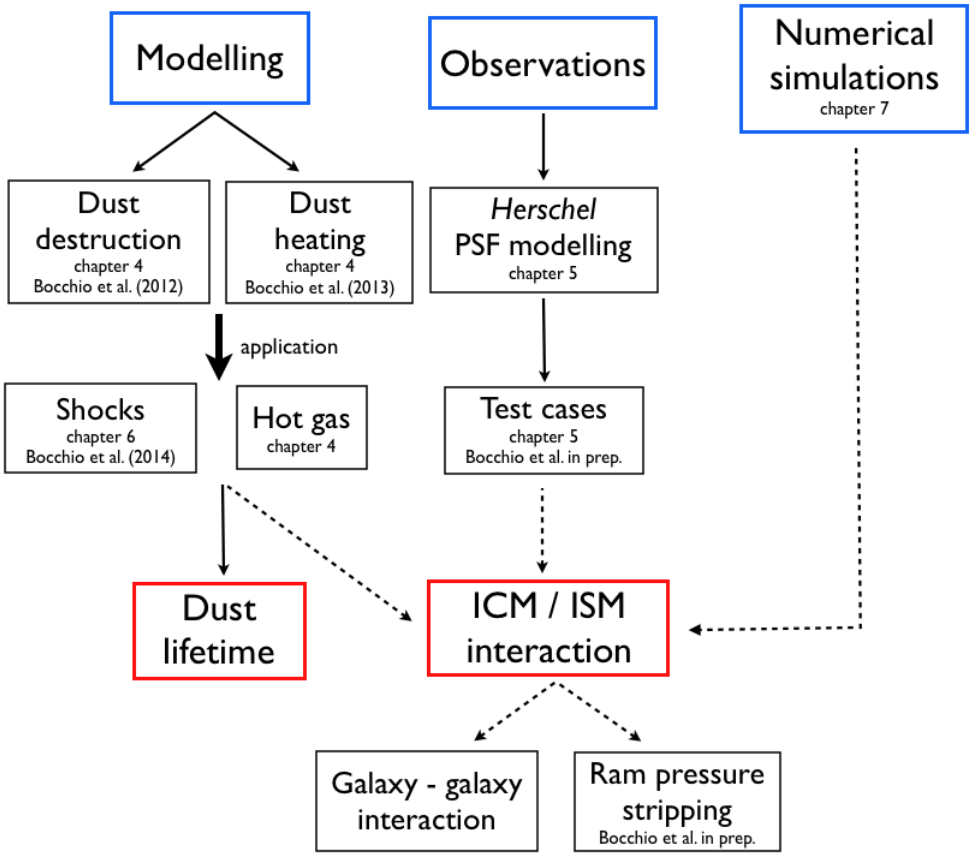

Figure 8.1: Flowchart of the different works and projects performed during my PhD study. Solid lines represent advanced or ongoing works, while dashed lines preliminary works or perspectives. Blue and red rectangles indicate the main methods and goals respectively.

In a first work (Chapter 4, Bocchio et al. 2012), based on previous studies (Tielens et al. 1994; Micelotta et al. 2010a,b) we estimated the destruction rate of carbonaceous grains ranging from μm size down to the molecular domain (sub-nm size) in a hot gas at different temperatures. In particular, we found that in a hot gas ($T_{\rm gas} \sim 10^5 - 10^7$ K) the erosion rate of nm size grains estimated with the classical approach by Tielens et al. (1994) is similar within a factor two to the dissociation rate of a PAH with the

same number of carbon atoms predicted by Micelotta et al. (2010a,b). Furthermore, we found that the lifetime of a 100 nm carbonaceous grain in a typical hot coronal-type gas ($T_{\rm gas} = 10^7\,{\rm K}$, $n_{\rm H} = 10^{-3}\,{\rm cm}^{-3}$) is $\sim 10^7\,{\rm yr}$, about one order of magnitude lower than previous estimates (Draine and Salpeter 1979a; Jones 2004).

Energetic electrons dominate the dissociation of small PAH-like particles but colliding with large grains are not able to efficiently erode them. In this case, most of the energy of an impinging electron is transferred to the grain leading to an increase of the grain temperature, a process known as electron collisional heating. Based on previous studies (Dwek 1986, 1987; Micelotta et al. 2010a,b) we calculated the fraction of the energy of the impinging electrons that is deposited into the grain and that subsequently leads to dust temperature evolution (Chapter 4, Bocchio et al. 2013b). Then, considering both electron collisional heating and destruction, using the DustEM code, we predicted the spectral energy distribution that we would expect observing dust embedded in a hot gas[1]. We note that under these conditions, the dust SED would present a drop in the MIR bands due to rapid destruction of the small grains. Furthermore, because of the extra source of heating and enhanced dust temperature, the peak position of the FIR emission is observed shifted to shorter wavelengths with respect to the standard dust SED in diffuse clouds.

In order to test these models we compared the expected dust SED in a hot gas with observations of NGC 4438, a perturbed galaxy in the Virgo cluster (Chapter 5, Bocchio et al. 2014 in prep.). In the case of galaxy-galaxy collisions, the mixing between the ISM and the hot IGM / ICM occurs and, at the interface between these two media, dust is mainly heated by collisions with the fast electrons in the gas. However, as predicted by dust destruction models (Tielens et al. 1994; Micelotta et al. 2010a,b; Bocchio et al. 2012) the lifetime of dust in such a harsh environment is rather short ($\lesssim 10^3\,{\rm yr}$ for a 1 nm carbonaceous grain in a hot gas with $T_{\rm gas} = 10^7\,{\rm K}$ and $n_{\rm H} = 10^{-3}\,{\rm cm}^{-3}$). This process then confines the dust to a thin interface region and only with the extremely good spatial resolution of the *Herschel* Space Observatory we are now able to detect this phenomenon. In order to perform a pixel by pixel multi wavelength study we then need to convolve all the images to the same resolution, carefully taking into account the PSF shape of all the instruments so as not to create any artifacts in the final images. This is not an easy operation and represents an ongoing work. However, already from preliminary results we clearly see that, to determine the "effective" PSF of the instruments, we need to take into account the difference in the spectrum of the observed source with respect to the astronomical object used for the PSF characterization.

Furthermore, we applied our updated dust destruction modelling to the case of dust processing in supernova-triggered interstellar shocks (Chapter 6, Bocchio et al. 2014). Jones et al. (1994, 1996), assuming an MRN-like dust size distribution estimated the dust processing in shocks of different velocities including thermal and inertial sputtering due to ion/atom - grain interactions and vaporization and shattering upon grain-grain collisions. We updated the code (now called GRASH_EX) described in their work using

[1]The author of this manuscript incorporated electron collisional heating into the IAS working version of DustEM and this will subsequently be made public in a near future DustEM update release.

the recent dust model proposed by Jones et al. (2013), re-evaluated the dust processing according to the materials used in this new model, and coupled the GRASH_EX code to the DustEM code in order to calculate the dust emission in post-shock regions. We found that carbonaceous grains are much more efficiently destroyed than previously estimated by Jones et al. (1996) and Serra Díaz-Cano and Jones (2008) while silicate grains are only slightly more eroded than estimated by Jones et al. (1996). Then, following the method described by Dwek and Scalo (1980) and McKee (1989), in the framework of the three-phase model by McKee and Ostriker (1977), we calculated the dust lifetime in our Galaxy. Our updated calculations lead to a lifetime of $(6.2 \pm 5.6) \times 10^7$ yr and $(3.1 \pm 2.7) \times 10^8$ yr for carbonaceous and silicate grains, respectively. While the estimate for silicate grains is about the same as in the previous study by Jones et al. (1996), the estimate for carbonaceous grains is an order of magnitude shorter than in that study. The dust lifetime is then shorter than the dust injection timescale ($\sim 3 \times 10^9$ yr, Dwek and Scalo 1980; Gehrz 1989; Jones and Tielens 1994) and we need to include grain re-formation in dense regions in the ISM in order to explain the observed fraction of elements locked up in grains in the diffuse ISM. While, there seems to be viable mechanisms for the re-formation of carbonaceous grains from the gas phase under low temperature and pressure conditions (e.g. Dartois et al. 2005), silicate grains are seemingly hard to re-form in the dense ISM and must therefore be formed in AGB stars and preserved in interstellar shocks (Jones and Nuth 2011). This study is therefore not able to solve this long-standing conundrum. However, it seems that the modelling of silicate sputtering together with hydrodynamical simulations of shock dynamics are absolutely critical to advance our understanding and will possibly give lower silicate sputtering resulting in a longer lifetime $t_{\rm SNR,s} > 6 \times 10^8$ yr. This could lead to a different scenario, making the assumed need to re-form the silicate dust in the ISM no longer such a stringent requirement. These features must therefore be explored more in detail in future studies.

Finally, using available multi-wavelength observations and numerical simulations of ram pressure stripped galaxies we were able to retrieve information on this phenomenon (Chapter 7). As a galaxy enters the cluster environment, the ICM wind exerts pressure on the ISM and, the atomic hydrogen, being loosely bound to the gravitational potential well, is the component of the ISM most affected by the ram pressure. This leads to a truncation of the HI disk (Cayatte et al. 1990; Bravo-Alfaro et al. 2000) and most of the time, to the formation of HI tails (e.g. Chung et al. 2007). Interstellar dust is stripped together with the atomic gas (even if to a lesser degree), leading to a truncation of the dust disk and sometimes to dusty tails (Cortese et al. 2010b, 2012). During the ram pressure stripping dense clouds are decoupled from the stripped ISM and are ablated or stripped (Abramson and Kenney (2014); Boselli et al. (2014)). We focused then on observations of the well-known galaxy ESO 137-001, an in falling galaxy in the Norma cluster. This galaxy presents a ~ 80 kpc long X-ray emitting tail, a > 20 kpc long H_2 tail and a ~ 8 kpc long dusty tail. The main questions I asked myself on this subject are:

- what is the origin of the molecular gas detected in the tail of ram pressure stripped

galaxies?

- How long dust can survive in the tail?

A first possible mechanism to explain the presence of molecular gas in the tail of ram pressure stripped galaxies was found by Tonnesen and Bryan (2012). AMR numerical simulations in that study show that molecular clouds are not stripped wholesale, but rather ablated and transformed to atomic gas. However, once in the tail, the atomic gas cools and condenses under the ICM thermal pressure and forms molecular gas.

We proposed a second mechanism. During ram pressure stripping, dust is entrained in atomic gas clouds stripped of the galactic ISM. Dust grains in this cold environment undergo little destruction and can efficiently form H_2 molecules on their surface. This mechanism can therefore explain at the same time the observation of dust emission in the tail up to $\sim 8\,\mathrm{kpc}$ from the galactic plane and the presence of a long molecular gas tail.

A third mechanism was found by Ruszkowski et al. (2014). The inclusion of magnetic fields in hydrodynamical simulations leads to important effects during ram pressure stripping. In that work they show that the structure of the tail is more filamentary than that in simulations without the inclusion of magnetic fields. As a consequence, these magnetically supported filaments seem to reduce the thermal conduction between the tail and the ICM possibly leading to the formation of molecular gas in the tail, therefore explaining the radio observations.

8.2 Perspective

8.2.1 PSF modelling and convolution

We have shown that, in order to perform studies on a pixel by pixel basis using the *Herschel* PACS and SPIRE data a good knowledge of the instrument's PSF is required. PACS and SPIRE PSFs present asymmetric features and approximating them with 2D Gaussian functions introduces significant errors. Furthermore, the spectrum of the astronomical objects used to measure the PSFs is generally not the same of that of the observed source, leading to an erroneous estimate of the width of the PSF. The study that we are performing on the *Haerschel* PACS and SPIRE PSFs is therefore going to be essential to calculate the convolution kernels to smooth all the images to the same resolution. Finally, at this first stage, we have been calculating the convolution kernels using the method described by Aniano et al. (2011). This implies the radialization of the initial PSFs used in the routine, neglecting all the asymmetric features. We planned therefore to use a Bayesian method, an approach which does not imply the radialization of the PSFs and account for asymmetric features correctly.

8.2.2 MHD numerical simulations

During my PhD study we developed the basic tools to estimate the dust destruction and heating in a hot gas and interstellar shocks. These models will be key to understanding the processing of dust during the phenomenon of ram pressure stripping. However, in order to simulate the dynamics of the process and therefore the physical properties of the gas along the tail of ram pressure stripping galaxies we need to make use of numerical simulations. AMR numerical simulations (e.g. Tonnesen et al. 2011; Tonnesen and Bryan 2012) are able to reproduce the main features observed in cluster galaxies. However, to really understand the formation mechanism of the molecular gas and the survival of dust in the tail a magnetohydrodynamical simulation of ram pressure stripped galaxies would give a more realistic simulation of the thermodynamics of the gas in the tail.

8.3 Papers related to this PhD study

Here is a list of the papers I have been working on during my PhD study and I am still working on:

- **M. Bocchio**, E. R. Micelotta, A.-L. Gautier, A. P. Jones, Small hydrocarbon particle erosion in a hot gas. A comparative study, *A&A*, 2012
- **M. Bocchio**, A. P. Jones, L. Verstraete, E. M. Xilouris, E. R. Micelotta, S. Bianchi, Dust heating. Photon absorption versus electron collision, *A&A*, 2013
- A. P. Jones, L. Fanciullo, M. Köhler, L. Verstraete, V. Guillet, **M. Bocchio**, N. Ysard, The evolution of amorphous hydrocarbons in the ISM: dust modelling from a new vantage point, *A&A*, 2013
- **M. Bocchio**, A. P. Jones, A. Abergel, Dust collisional heating and small grain destruction in NGC 4438, In *"The Life Cycle of Dust in the Universe" Conf. Proceedings*, 2013
- **M. Bocchio**, A. P. Jones, Dust Lifetime Re-evaluation in the Light of a New Dust Model, In *"The Life Cycle of Dust in the Universe" Conf. Proceedings*, 2013
- E. Micelotta, A. P. Jones, **M. Bocchio**, J. Cami, E. Peeters and J. Bernard-Salas, The Circle of Dust: From Nanoparticles to Macromolecules and Beyond, In *"The Life Cycle of Dust in the Universe" Conf. Proceedings*, 2013
- **M. Bocchio**, A. P. Jones, J. D. Slavin, A re-evaluation of dust processing in supernova shock waves, *A&A*, 2014
- **M. Bocchio**, A. P. Jones, A. Abergel, Dust collisional heating and small grain destruction in NGC 4438, *in preparation*, 2014

- **M. Bocchio**, A. P. Jones, G. Pineau des Forêts, Molecular gas in a hot ram pressure stripped tail?, *in preparation*, 2014
- A. P. Jones, N. Ysard, M. Köhler, L. Fanciullo, **M. Bocchio**, L. Verstraete, V. Guillet, The cycling of carbon into and out of dust, *Faraday discussions*, 2014, in press
- A. Rémy-Ruyer, S. C. Madden, F. Galliano, M. Galametz, T. T. Takeuchi, R. S. Asano, S. Zhukovska, V. Lebouteiller, D. Cormier, A. P. Jones, **M. Bocchio**, M. Baes, G. J. Bendo, M .Boquien, A. Boselli, I. de Looze, V. Doublier-Pritchard, T. M. Hugues, O. Ł. Karczewski, L. Spinoglio, Gas-to-dust mass ratios in local galaxies over a 2 dex metallicity range, *A&A*, 2014
- C. Fuller, J. I. Davies, R. Auld, M. W. L. Smith, M. Baes, S. Bianchi, **M. Bocchio**, A. Boselli, M. Clemens, T. A. Davis, I. De Looze, S. di Serego Alighieri, M. Grossi, T. M. Hughes, S. Viaene, P. Serra, The Herschel Fornax Cluster Survey II: FIR properties of optically selected Fornax cluster galaxies, *MNRAS*, 2014

Bibliography

A. Abramson and J. D. P. Kenney. Hubble Space Telescope Imaging of Decoupled Dust Clouds in the Ram Pressure Stripped Virgo Spirals NGC 4402 and NGC 4522. AJ, 147:63, March 2014. doi: 10.1088/0004-6256/147/3/63.

A. Abramson, J. D. P. Kenney, H. H. Crowl, A. Chung, J. H. van Gorkom, B. Vollmer, and D. Schiminovich. Caught in the Act: Strong, Active Ram Pressure Stripping in Virgo Cluster Spiral NGC 4330. AJ, 141:164, May 2011. doi: 10.1088/0004-6256/141/5/164.

A. J. Adamson, D. C. B. Whittet, A. Chrysostomou, J. H. Hough, D. K. Aitken, G. S. Wright, and P. F. Roche. Spectropolarimetric Constraints on the Nature of the 3.4 Micron Absorber in the Interstellar Medium. ApJ, 512:224–229, February 1999. doi: 10.1086/306766.

P. B. Alton, S. Bianchi, R. J. Rand, E. M. Xilouris, J. I. Davies, and M. Trewhella. Deep Submillimeter Images of NGC 891-Cold Dust at Larger Galactic Radii. ApJ, 507:L125–L129, November 1998. doi: 10.1086/311692.

H. H. Andersen and H. L. Bay. *Sputtering yield measurements*, page 145. 1981. doi: 10.1007/3540105212_9.

G. Aniano. private communication, 2013.

G. Aniano, B. T. Draine, K. D. Gordon, and K. Sandstrom. Common-Resolution Convolution Kernels for Space- and Ground-Based Telescopes. PASP, 123:1218–1236, October 2011. doi: 10.1086/662219.

H. Arab, A. Abergel, E. Habart, J. Bernard-Salas, H. Ayasso, K. Dassas, P. G. Martin, and G. J. White. Evolution of dust in the Orion Bar with Herschel. I. Radiative transfer modelling. A&A, 541:A19, May 2012. doi: 10.1051/0004-6361/201118537.

Richard G. Arendt, E. Dwek, G. Kober, J. Rho, and U. Hwang. Interstellar and ejecta dust in the cas a supernova remnant. *arXiv:1403.3008 [astro-ph.GA]*, 2014.

M. J. Barlow. The destruction and growth of dust grains in interstellar space. I - Destruction by sputtering. MNRAS, 183:367–395, May 1978a.

M. J. Barlow. The destruction and growth of dust grains in interstellar space - II. Destruction by grain surface reactions, grain-grain collisions and photodesorption. MNRAS, 183:397–416, May 1978b.

E. E. Barnard. On a nebulous groundwork in the constellation Taurus. ApJ, 25: 218–225, April 1907. doi: 10.1086/141434.

E. E. Barnard. On a great nebulous region and the question of absorbing matter in space and the transparency of the nebulae. ApJ, 31:8–14, January 1910. doi: 10.1086/141719.

G. Bendo. private communication, 2013.

G. J. Bendo, A. Boselli, A. Dariush, M. Pohlen, H. Roussel, M. Sauvage, M. W. L. Smith, C. D. Wilson, M. Baes, A. Cooray, D. L. Clements, L. Cortese, K. Foyle, M. Galametz, H. L. Gomez, V. Lebouteiller, N. Lu, S. C. Madden, E. Mentuch, B. O'Halloran, M. J. Page, A. Remy, B. Schulz, and L. Spinoglio. Investigations of dust heating in M81, M83 and NGC 2403 with the Herschel Space Observatory. MNRAS, 419:1833–1859, January 2012a. doi: 10.1111/j.1365-2966.2011.19735.x.

G. J. Bendo, F. Galliano, and S. C. Madden. MIPS 24-160 μm photometry for the Herschel-SPIRE Local Galaxies Guaranteed Time Programs. MNRAS, 423:197–212, June 2012b. doi: 10.1111/j.1365-2966.2012.20784.x.

M. J. Berger and S. M. Seltzer. Tables of Energy Losses and Ranges of Electrons and Positrons. NASA SP-3012. *NASA Special Publication*, 3012, 1964.

S. Bianchi. Dust extinction and emission in a clumpy galactic disk. An application of the radiative transfer code TRADING. A&A, 490:461–475, October 2008. doi: 10.1051/0004-6361:200810027.

S. Bianchi and E. M. Xilouris. The extent of dust in NGC 891 from Herschel/SPIRE images. A&A, 531:L11, July 2011. doi: 10.1051/0004-6361/201116772.

M. Bocchio and A. P. Jones. Dust Lifetime Re-evaluation in the Light of a New Dust Model. In *"The Life Cycle of Dust in the Universe" Conf. Proceedings, http://pos.sissa.it/archive/conferences/207/028/LCDU2013_028.pdf*, 2013.

M. Bocchio, E. R. Micelotta, A.-L. Gautier, and A. P. Jones. Small hydrocarbon particle erosion in a hot gas. A comparative study. A&A, 545:A124, September 2012. doi: 10.1051/0004-6361/201219705.

M. Bocchio, A. P. Jones, and A. Abergel. Dust collisional heating and small grain destruction in NGC 4438. In *"The Life Cycle of Dust in the Universe" Conf. Proceedings, http://pos.sissa.it/archive/conferences/207/071/LCDU2013_071.pdf*, 2013a.

M. Bocchio, A. P. Jones, L. Verstraete, E. M. Xilouris, E. R. Micelotta, and S. Bianchi. Dust heating. Photon absorption versus electron collisions. A&A, 556:A6, August 2013b. doi: 10.1051/0004-6361/201321054.

M. Bocchio, A. P. Jones, and J. D. Slavin. A re-evaluation of dust processing in supernova shock waves. A&A, 2014.

M. Bocchio, A. P. Jones, and G. Pineau des Forêts. Molecular gas in a hot ram pressure stripped tail? A&A, 2014, in prep.

J. Bohdansky. Important sputtering yield data for tokamaks: A comparison of measurements and estimates. *Journal of Nuclear Materials*, 93:44–60, October 1980. doi: 10.1016/0022-3115(80)90302-5.

J. Bohdansky. A universal relation for the sputtering yield of monatomic solids at normal ion incidence. *Nuclear Instruments and Methods in Physics Research B*, 2: 587–591, March 1984. doi: 10.1016/0168-583X(84)90271-4.

J. Bohdansky, J. Roth, and H. L. Bay. An analytical formula and important parameters for low-energy ion sputtering. *Journal of Applied Physics*, 51:2861–2865, May 1980. doi: 10.1063/1.327954.

F. Bohren, C. and D. R. Huffman. *Absorption and Scattering of Light by Small Particles*. Wiley, 1998.

A. Boselli and G. Gavazzi. Environmental Effects on Late-Type Galaxies in Nearby Clusters. PASP, 118:517–559, April 2006. doi: 10.1086/500691.

A. Boselli, S. Boissier, L. Cortese, A. Gil de Paz, V. Buat, J. Iglesias-Paramo, B. F. Madore, T. Barlow, L. Bianchi, Y.-I. Byun, J. Donas, K. Forster, P. G. Friedman, T. M. Heckman, P. Jelinsky, Y.-W. Lee, R. Malina, D. C. Martin, B. Milliard, P. Morrissey, S. Neff, R. M. Rich, D. Schiminovich, M. Seibert, O. Siegmund, T. Small, A. S. Szalay, B. Welsh, and T. K. Wyder. GALEX Ultraviolet Observations of the Interacting Galaxy NGC 4438 in the Virgo Cluster. ApJ, 623:L13–L16, April 2005. doi: 10.1086/429377.

A. Boselli, L. Ciesla, L. Cortese, V. Buat, M. Boquien, G. J. Bendo, S. Boissier, S. Eales, G. Gavazzi, T. M. Hughes, M. Pohlen, M. W. L. Smith, M. Baes, S. Bianchi, D. L. Clements, A. Cooray, J. Davies, W. Gear, S. Madden, L. Magrini, P. Panuzzo, A. Remy, L. Spinoglio, and S. Zibetti. Far-infrared colours of nearby late-type galaxies in the Herschel Reference Survey. A&A, 540:A54, April 2012. doi: 10.1051/0004-6361/201118602.

A. Boselli, L. Cortese, M. Boquien, S. Boissier, B. Catinella, G. Gavazzi, C. Lagos, and A. Saintonge. Cold gas properties of the Herschel Reference Survey. III. Molecular gas stripping in cluster galaxies. A&A, 564:A67, April 2014. doi: 10.1051/0004-6361/201322313.

O. Boulade, M. Sauvage, B. Altieri, J. Blommaert, P. Gallais, S. Guest, L. Metcalfe, K. Okumura, S. Ott, D. Tran, and L. Vigroux. NGC 5195 - a look into the hot dusty ISM of an interacting SB0 galaxy with ISOCAM. A&A, 315:L85–L88, November 1996.

F. Boulanger, A. Abergel, J.-P. Bernard, W. B. Burton, F.-X. Desert, D. Hartmann, G. Lagache, and J.-L. Puget. The dust/gas correlation at high Galactic latitude. A&A, 312:256–262, August 1996.

H. Bravo-Alfaro, V. Cayatte, J. H. van Gorkom, and C. Balkowski. VLA H I Imaging of the Brightest Spiral Galaxies in Coma. AJ, 119:580–592, February 2000. doi: 10.1086/301194.

M. Cappi, M. Persic, L. Bassani, A. Franceschini, L. K. Hunt, S. Molendi, E. Palazzi, G. G. C. Palumbo, Y. Rephaeli, and P. Salucci. Diffuse thermal emission from very hot gas in starburst galaxies. A&A, 350:777–790, October 1999.

J. A. Cardelli, G. C. Clayton, and J. S. Mathis. The relationship between infrared, optical, and ultraviolet extinction. ApJ, 345:245–256, October 1989. doi: 10.1086/167900.

J. A. Cardelli, D. M. Meyer, M. Jura, and B. D. Savage. The Abundance of Interstellar Carbon. ApJ, 467:334, August 1996. doi: 10.1086/177608.

P. Carrez, K. Demyk, P. Cordier, L. Gengembre, J. Grimblot, L. D'Hendecourt, A. P. Jones, and H. Leroux. Low-energy helium ion irradiation-induced amorphization and chemical changes in olivine: Insights for silicate dust evolution in the interstellar medium. *Meteoritics and Planetary Science*, 37:1599–1614, November 2002. doi: 10.1111/j.1945-5100.2002.tb00814.x.

V. Cayatte, J. H. van Gorkom, C. Balkowski, and C. Kotanyi. VLA observations of neutral hydrogen in Virgo Cluster galaxies. I - The Atlas. AJ, 100:604–634, September 1990. doi: 10.1086/115545.

J. E. Chiar, A. J. Adamson, D. C. B. Whittet, A. Chrysostomou, J. H. Hough, T. H. Kerr, R. E. Mason, P. F. Roche, and G. Wright. Spectropolarimetry of the 3.4 μm Feature in the Diffuse ISM toward the Galactic Center Quintuplet Cluster. ApJ, 651:268–271, November 2006. doi: 10.1086/507462.

J. E. Chiar, A. G. G. M. Tielens, A. J. Adamson, and A. Ricca. The Structure, Origin, and Evolution of Interstellar Hydrocarbon Grains. ApJ, 770:78, June 2013. doi: 10.1088/0004-637X/770/1/78.

J. H. Christensen. Inclination Effects on Galaxy Photometry Using Finite Apertures. MNRAS, 246:535, October 1990.

A. Chung, J. H. van Gorkom, J. D. P. Kenney, and B. Vollmer. Virgo Galaxies with Long One-sided H I Tails. ApJ, 659:L115–L119, April 2007. doi: 10.1086/518034.

L. Ciesla, A. Boselli, M. W. L. Smith, G. J. Bendo, L. Cortese, S. Eales, S. Bianchi, M. Boquien, V. Buat, J. Davies, M. Pohlen, S. Zibetti, M. Baes, A. Cooray, I. de Looze, S. di Serego Alighieri, M. Galametz, H. L. Gomez, V. Lebouteiller, S. C. Madden, C. Pappalardo, A. Remy, L. Spinoglio, M. Vaccari, R. Auld, and D. L. Clements. Submillimetre photometry of 323 nearby galaxies from the Herschel Reference Survey. A&A, 543:A161, July 2012. doi: 10.1051/0004-6361/201219216.

F. Combes, C. Dupraz, F. Casoli, and L. Pagani. CO emission in NGC 4438 - A case for tidal stripping? A&A, 203:L9–L12, September 1988.

M. Compiègne, L. Verstraete, A. Jones, J.-P. Bernard, F. Boulanger, N. Flagey, J. Le Bourlot, D. Paradis, and N. Ysard. The global dust SED: tracing the nature and evolution of dust with DustEM. A&A, 525:A103, January 2011. doi: 10.1051/0004-6361/201015292.

L. Cortese, G. J. Bendo, A. Boselli, J. I. Davies, H. L. Gomez, M. Pohlen, R. Auld, M. Baes, J. J. Bock, M. Bradford, V. Buat, N. Castro-Rodriguez, P. Chanial, S. Charlot, L. Ciesla, D. L. Clements, A. Cooray, D. Cormier, E. Dwek, S. A. Eales, D. Elbaz, M. Galametz, F. Galliano, W. K. Gear, J. Glenn, M. Griffin, S. Hony, K. G. Isaak, L. R. Levenson, N. Lu, S. Madden, B. O'Halloran, K. Okumura, S. Oliver, M. J. Page, P. Panuzzo, A. Papageorgiou, T. J. Parkin, I. Perez-Fournon, N. Rangwala, E. E. Rigby, H. Roussel, A. Rykala, N. Sacchi, M. Sauvage, B. Schulz, M. R. P. Schirm, M. W. L. Smith, L. Spinoglio, J. A. Stevens, S. Srinivasan, M. Symeonidis, M. Trichas, M. Vaccari, L. Vigroux, C. D. Wilson, H. Wozniak, G. S. Wright, and W. W. Zeilinger. Herschel-SPIRE observations of the disturbed galaxy NGC 4438. A&A, 518:L63, July 2010a. doi: 10.1051/0004-6361/201014547.

L. Cortese, J. I. Davies, M. Pohlen, M. Baes, G. J. Bendo, S. Bianchi, A. Boselli, I. de Looze, J. Fritz, J. Verstappen, D. J. Bomans, M. Clemens, E. Corbelli, A. Dariush, S. di Serego Alighieri, D. Fadda, D. A. Garcia-Appadoo, G. Gavazzi, C. Giovanardi, M. Grossi, T. M. Hughes, L. K. Hunt, A. P. Jones, S. Madden, D. Pierini, S. Sabatini, M. W. L. Smith, C. Vlahakis, E. M. Xilouris, and S. Zibetti. The Herschel Virgo Cluster Survey . II. Truncated dust disks in H I-deficient spirals. A&A, 518:L49, July 2010b. doi: 10.1051/0004-6361/201014550.

L. Cortese, L. Ciesla, A. Boselli, S. Bianchi, H. Gomez, M. W. L. Smith, G. J. Bendo, S. Eales, M. Pohlen, M. Baes, E. Corbelli, J. I. Davies, T. M. Hughes, L. K. Hunt, S. C. Madden, D. Pierini, S. di Serego Alighieri, S. Zibetti, M. Boquien, D. L. Clements, A. Cooray, M. Galametz, L. Magrini, C. Pappalardo, L. Spinoglio, and C. Vlahakis. The dust scaling relations of the Herschel Reference Survey. A&A, 540: A52, April 2012. doi: 10.1051/0004-6361/201118499.

L. L. Cowie. Refractory grain destruction in low-velocity shocks. ApJ, 225:887–892, November 1978. doi: 10.1086/156553.

D. P. Cox. The Three-Phase Interstellar Medium Revisited. ARA&A, 43:337–385, September 2005. doi: 10.1146/annurev.astro.43.072103.150615.

D. P. Cox and B. W. Smith. Large-Scale Effects of Supernova Remnants on the Galaxy: Generation and Maintenance of a Hot Network of Tunnels. ApJ, 189:L105, May 1974. doi: 10.1086/181476.

S. K. Croft. Cratering flow fields - Implications for the excavation and transient expansion stages of crater formation. In S. A. Bedini, editor, *Lunar and Planetary Science Conference Proceedings*, volume 11 of *Lunar and Planetary Science Conference Proceedings*, pages 2347–2378, 1980.

H. H. Crowl, J. D. P. Kenney, J. H. van Gorkom, and B. Vollmer. Dense Cloud Ablation and Ram Pressure Stripping of the Virgo Spiral NGC 4402. AJ, 130:65–72, July 2005. doi: 10.1086/430526.

E. Dartois, G. M. Muñoz Caro, D. Deboffle, G. Montagnac, and L. D'Hendecourt. Ultraviolet photoproduction of ISM dust. Laboratory characterisation and astrophysical relevance. A&A, 432:895–908, March 2005. doi: 10.1051/0004-6361:20042094.

K. M. Dasyra, E. M. Xilouris, A. Misiriotis, and N. D. Kylafis. Is the Galactic submillimeter dust emissivity underestimated? A&A, 437:447–456, July 2005. doi: 10.1051/0004-6361:20042442.

J. I. Davies, M. Baes, G. J. Bendo, S. Bianchi, D. J. Bomans, A. Boselli, M. Clemens, E. Corbelli, L. Cortese, A. Dariush, I. de Looze, S. di Serego Alighieri, D. Fadda, J. Fritz, D. A. Garcia-Appadoo, G. Gavazzi, C. Giovanardi, M. Grossi, T. M. Hughes, L. K. Hunt, A. P. Jones, S. Madden, D. Pierini, M. Pohlen, S. Sabatini, M. W. L. Smith, J. Verstappen, C. Vlahakis, E. M. Xilouris, and S. Zibetti. The Herschel Virgo Cluster Survey. I. Luminosity function. A&A, 518:L48, July 2010. doi: 10.1051/0004-6361/201014571.

A. de Oliveira-Costa, A. Kogut, M. J. Devlin, C. B. Netterfield, L. A. Page, and E. J. Wollack. Galactic Microwave Emission at Degree Angular Scales. ApJ, 482:L17–L20, June 1997. doi: 10.1086/310684.

K. Demyk, P. Carrez, H. Leroux, P. Cordier, A. P. Jones, J. Borg, E. Quirico, P. I. Raynal, and L. d'Hendecourt. Structural and chemical alteration of crystalline olivine under low energy He^+ irradiation. A&A, 368:L38–L41, March 2001. doi: 10.1051/0004-6361:20010208.

F. X. Désert, F. Boulanger, and S. N. Shore. Grain temperature fluctuations - A key to infrared spectra. A&A, 160:295–300, May 1986.

F.-X. Desert, F. Boulanger, and J. L. Puget. Interstellar dust models for extinction and emission. A&A, 237:215–236, October 1990.

J. K. Dienes and J. M. Walsh. *High-Velocity Impact Phenomenae*. Kinslow, R., 1970.

C. L. Dobbs, C. Theis, J. E. Pringle, and M. R. Bate. Simulations of the grand design galaxy M51: a case study for analysing tidally induced spiral structure. MNRAS, 403:625–645, April 2010. doi: 10.1111/j.1365-2966.2009.16161.x.

B. T. Draine. Photoelectric heating of interstellar gas. ApJS, 36:595–619, April 1978. doi: 10.1086/190513.

B. T. Draine. Infrared emission from dust in shocked gas. ApJ, 245:880–890, May 1981. doi: 10.1086/158864.

B. T. Draine. *Physics of the Interstellar and Intergalactic Medium*. 2011.

B. T. Draine and N. Anderson. Temperature fluctuations and infrared emission from interstellar grains. ApJ, 292:494–499, May 1985. doi: 10.1086/163181.

B. T. Draine and A. Lazarian. Diffuse Galactic Emission from Spinning Dust Grains. ApJ, 494:L19, February 1998. doi: 10.1086/311167.

B. T. Draine and H. M. Lee. Optical properties of interstellar graphite and silicate grains. ApJ, 285:89–108, October 1984. doi: 10.1086/162480.

B. T. Draine and A. Li. Infrared Emission from Interstellar Dust. IV. The Silicate-Graphite-PAH Model in the Post-Spitzer Era. ApJ, 657:810–837, March 2007. doi: 10.1086/511055.

B. T. Draine and E. E. Salpeter. On the physics of dust grains in hot gas. ApJ, 231: 77–94, July 1979a. doi: 10.1086/157165.

B. T. Draine and E. E. Salpeter. Destruction mechanisms for interstellar dust. ApJ, 231:438–455, July 1979b. doi: 10.1086/157206.

B. T. Draine and B. Sutin. Collisional charging of interstellar grains. ApJ, 320:803–817, September 1987. doi: 10.1086/165596.

B. T. Draine, D. A. Dale, G. Bendo, K. D. Gordon, J. D. T. Smith, L. Armus, C. W. Engelbracht, G. Helou, R. C. Kennicutt, Jr., A. Li, H. Roussel, F. Walter, D. Calzetti, J. Moustakas, E. J. Murphy, G. H. Rieke, C. Bot, D. J. Hollenbach, K. Sheth, and H. I. Teplitz. Dust Masses, PAH Abundances, and Starlight Intensities in the SINGS Galaxy Sample. ApJ, 663:866–894, July 2007. doi: 10.1086/518306.

A. Dressler. Galaxy morphology in rich clusters - Implications for the formation and evolution of galaxies. ApJ, 236:351–365, March 1980. doi: 10.1086/157753.

W. W. Duley and D. A. Williams. The infrared spectrum of interstellar dust - Surface functional groups on carbon. MNRAS, 196:269–274, July 1981.

L. J. Dursi and C. Pfrommer. Draping of Cluster Magnetic Fields over Bullets and Bubbles-Morphology and Dynamic Effects. ApJ, 677:993–1018, April 2008. doi: 10.1086/529371.

E. Dwek. Temperature fluctuations and infrared emission from dust particles in a hot gas. ApJ, 302:363–370, March 1986. doi: 10.1086/163995.

E. Dwek. The infrared diagnostic of a dusty plasma with applications to supernova remnants. ApJ, 322:812–821, November 1987. doi: 10.1086/165774.

E. Dwek and J. M. Scalo. The evolution of refractory interstellar grains in the solar neighborhood. ApJ, 239:193–211, July 1980. doi: 10.1086/158100.

M. Ehle, W. Pietsch, and R. Beck. ROSAT high-resolution X-ray observations of the galaxies M 51 and NGC 5195. A&A, 295:289–301, March 1995.

A. Einstein. Über einen die Erzeugung und Verwandlung des Lichtes betreffenden heuristischen Gesichtspunkt. *Annalen der Physik*, 322:132–148, 1905. doi: 10.1002/andp.19053220607.

K. M. Ferriere. The hot gas filling factor in the vicinity of the Sun. ApJ, 441:281–299, March 1995. doi: 10.1086/175355.

M. Fioc and B. Rocca-Volmerange. PEGASE: a UV to NIR spectral evolution model of galaxies. Application to the calibration of bright galaxy counts. A&A, 326:950–962, October 1997.

E. L. Fitzpatrick and D. Massa. An Analysis of the Shapes of Interstellar Extinction Curves. V. The IR-through-UV Curve Morphology. ApJ, 663:320–341, July 2007. doi: 10.1086/518158.

C. Fuller, J. I. Davies, R. Auld, M. W. L. Smith, M. Baes, S. Bianchi, M. Bocchio, A. Boselli, M. Clemens, T. A. Davis, I. De Looze, S. di Serego Alighieri, M. Grossi, T. M. Hughes, S. Viaene, and P. Serra. The Herschel Fornax Cluster Survey II: FIR properties of optically selected Fornax cluster galaxies. MNRAS, 440:1571–1589, May 2014. doi: 10.1093/mnras/stu369.

G. Gavazzi, A. Boselli, W. van Driel, and K. O'Neil. Completing H I observations of galaxies in the Virgo cluster. A&A, 429:439–447, January 2005. doi: 10.1051/0004-6361:20041678.

R. Gehrz. Sources of Stardust in the Galaxy. In L. J. Allamandola and A. G. G. M. Tielens, editors, *Interstellar Dust*, volume 135 of *IAU Symposium*, page 445, 1989.

E. L. Gibb, D. C. B. Whittet, A. C. A. Boogert, and A. G. G. M. Tielens. Interstellar Ice: The Infrared Space Observatory Legacy. ApJS, 151:35–73, March 2004. doi: 10.1086/381182.

F. C. Gillett, F. J. Low, and W. A. Stein. Infrared Observations of the Planetary Nebula NGC 7027. ApJ, 149:L97, September 1967. doi: 10.1086/180066.

F. C. Gillett, W. J. Forrest, and K. M. Merrill. 8 - 13-micron spectra of NGC 7027, BD +30 3639, and NGC 6572. ApJ, 183:87–93, July 1973. doi: 10.1086/152211.

R. Giovanelli and M. P. Haynes. Gas deficiency in cluster galaxies - A comparison of nine clusters. ApJ, 292:404–425, May 1985. doi: 10.1086/163170.

R. Gomer. *Field Emission and Field Ionization*. Cambridge: Harvard University Press, 1961.

M. D. Gray and M. G. Edmunds. Modification of dust-grain structure by sputtering. MNRAS, 349:491–502, April 2004. doi: 10.1111/j.1365-2966.2004.07502.x.

Y. A. Gruzdkov, K. Watanabe, K. Sawabe, and Y. Matsumoto. Photochemical C#58872H bond activation of methane on a Pt(111) surface. *Chemical Physics Letters*, 227:243–247, September 1994. doi: 10.1016/0009-2614(94)00849-3.

V. Guillet. *Evolution des poussières dans les chocs*, phd thesis, 2008.

J. E. Gunn and J. R. Gott, III. On the Infall of Matter Into Clusters of Galaxies and Some Effects on Their Evolution. ApJ, 176:1, August 1972. doi: 10.1086/151605.

A. A. Haasz, J. W. Davis, and C. H. Wu. Angle of incidence dependence of light ion physical sputtering of carbon. *Journal of Nuclear Materials*, 162:915–919, April 1989. doi: 10.1016/0022-3115(89)90385-1.

M. P. Haynes and R. Giovanelli. Neutral hydrogen in isolated galaxies. IV - Results for the Arecibo sample. AJ, 89:758–800, June 1984. doi: 10.1086/113573.

B. Hellyer. The fragmentation of the asteroids. MNRAS, 148:383, 1970.

T. Henning, V. B. Il'In, N. A. Krivova, B. Michel, and N. V. Voshchinnikov. WWW database of optical constants for astronomy. A&AS, 136:405–406, April 1999. doi: 10.1051/aas:1999222.

R. C. Henry. The Local Interstellar Ultraviolet Radiation Field. ApJ, 570:697–707, May 2002. doi: 10.1086/339623.

D. Hollenbach and C. F. McKee. Molecule formation and infrared emission in fast interstellar shocks. I Physical processes. ApJS, 41:555–592, November 1979. doi: 10.1086/190631.

P. Hoppe, J. Leitner, B. S. Meyer, L.-S. The, M. Lugaro, and S. Amari. An Unusual Presolar Silicon Carbide Grain from a Supernova: Implications for the Production of Silicon-29 in Type II Supernovae. ApJ, 691:L20–L23, January 2009. doi: 10.1088/0004-637X/691/1/L20.

P. Hoppe, J. Leitner, E. Gröner, K. K. Marhas, B. S. Meyer, and S. Amari. NanoSIMS Studies of Small Presolar SiC Grains: New Insights into Supernova Nucleosynthesis, Chemistry, and Dust Formation. ApJ, 719:1370–1384, August 2010. doi: 10.1088/0004-637X/719/2/1370.

K. Hornung and K. W. Michel. Equation-of-State Data of Solids from Shock Vaporization. J. Chem. Phys., 56:2072–2078, March 1972. doi: 10.1063/1.1677500.

A. Hota, D. J. Saikia, and J. A. Irwin. NGC 4438 and its environment at radio wavelengths. MNRAS, 380:1009–1022, September 2007. doi: 10.1111/j.1365-2966.2007.12114.x.

S. Iida, T. Ohtaki, and T. Seki. Optical effects in amorphous semiconductors. In *AIP Conf. Proceedings No. 120, eds. Taylor, P. C. and Bishop, S. G., AIP, New York*, 1985.

H. Iskef, J. W. Cunningham, and D. E. Watt. Projected ranges and effective stopping powers of electrons with energy between 20 eV and 10 keV. *Physics in Medicine and Biology*, 28:535–545, May 1983. doi: 10.1088/0031-9155/28/5/007.

E. B. Jenkins. A Unified Representation of Gas-Phase Element Depletions in the Interstellar Medium. ApJ, 700:1299–1348, August 2009. doi: 10.1088/0004-637X/700/2/1299.

H. W. Jochims, E. Ruhl, H. Baumgartel, S. Tobita, and S. Leach. Size effects on dissociation rates of polycyclic aromatic hydrocarbon cations: Laboratory studies and astophysical implications. ApJ, 420:307–317, January 1994. doi: 10.1086/173560.

A. P. Jones. Dust Destruction Processes. In A. N. Witt, G. C. Clayton, and B. T. Draine, editors, *Astrophysics of Dust*, volume 309 of *Astronomical Society of the Pacific Conference Series*, page 347, May 2004.

A. P. Jones. Variations on a theme - the evolution of hydrocarbon solids. I. Compositional and spectral modelling - the eRCN and DG models. A&A, 540:A1, April 2012a. doi: 10.1051/0004-6361/201117623.

A. P. Jones. Variations on a theme - the evolution of hydrocarbon solids. II. Optical property modelling - the optEC$_{(s)}$ model. A&A, 540:A2, April 2012b. doi: 10.1051/0004-6361/201117624.

A. P. Jones. Variations on a theme - the evolution of hydrocarbon solids. III. Size-dependent properties - the optEC$_{(s)}$(a) model. A&A, 542:A98, June 2012c. doi: 10.1051/0004-6361/201118483.

A. P. Jones. Variations on a theme - the evolution of hydrocarbon solids (Corrigendum). II. Optical property modelling - the optEC$_{(s)}$ model. A&A, 545:C2, September 2012d. doi: 10.1051/0004-6361/201117624e.

A. P. Jones. Variations on a theme - the evolution of hydrocarbon solids (Corrigendum). III. Size-dependent properties - the optEC$_{(s)}$(a) model. A&A, 545:C3, September 2012e. doi: 10.1051/0004-6361/201118483e.

A. P. Jones. Heteroatom-doped hydrogenated amorphous carbons, a-C:H:X. "Volatile" silicon, sulphur and nitrogen depletion, blue photoluminescence, diffuse interstellar bands and ferro-magnetic carbon grain connections. A&A, 555:A39, July 2013. doi: 10.1051/0004-6361/201321687.

A. P. Jones and J. A. Nuth. Dust destruction in the ISM: a re-evaluation of dust lifetimes. A&A, 530:A44, June 2011. doi: 10.1051/0004-6361/201014440.

A. P. Jones and A. G. G. M. Tielens. The formation of small grains in shocks in the ISM. In A. G. G. M. Tielens, editor, *The Diffuse Interstellar Bands*, pages 79–83, May 1994.

A. P. Jones, A. G. G. M. Tielens, D. J. Hollenbach, and C. F. McKee. Grain destruction in shocks in the interstellar medium. ApJ, 433:797–810, October 1994. doi: 10.1086/174689.

A. P. Jones, A. G. G. M. Tielens, and D. J. Hollenbach. Grain Shattering in Shocks: The Interstellar Grain Size Distribution. ApJ, 469:740, October 1996. doi: 10.1086/177823.

A. P. Jones, L. Fanciullo, M. Köhler, L. Verstraete, V. Guillet, M. Bocchio, and N. Ysard. The evolution of amorphous hydrocarbons in the ISM: dust modelling from a new vantage point. A&A, 558:A62, October 2013. doi: 10.1051/0004-6361/201321686.

A. P. Jones, N. Ysard, M. Köhler, L. Fanciullo, M. Bocchio, E. R. Micelotta, L. Verstraete, and V. Guillet. The cycling of carbon into and out of dust. *Faraday discussions, in press*, art. A62, 2014. doi: 10.1051/0004-6361/201321686.

D. C. Joy. *Scanning*, 17:270, 1995.

S. Jurac, R. E. Johnson, and B. Donn. Monte Carlo Calculations of the Sputtering of Grains: Enhanced Sputtering of Small Grains. ApJ, 503:247, August 1998. doi: 10.1086/305994.

S. Kassavetis, P. Patsalas, S. Logothetidis, J. Robertson, and S. Kennou. Dispersion relations and optical properties of amorphous carbons. *Diamond and Related Materials*, 16:1813–1822, October 2007. doi: 10.1016/j.diamond.2007.08.027.

J. D. P. Kenney, V. C. Rubin, P. Planesas, and J. S. Young. Gas filaments in the collisional debris of NGC 4438. ApJ, 438:135–154, January 1995. doi: 10.1086/175060.

J. D. P. Kenney, J. H. van Gorkom, and B. Vollmer. VLA H I Observations of Gas Stripping in the Virgo Cluster Spiral NGC 4522. AJ, 127:3361–3374, June 2004. doi: 10.1086/420805.

J. D. P. Kenney, T. Tal, H. H. Crowl, J. Feldmeier, and G. H. Jacoby. A Spectacular Hα Complex in Virgo: Evidence for a Collision between M86 and NGC 4438 and Implications for the Collisional ISM Heating of Ellipticals. ApJ, 687:L69–L74, November 2008. doi: 10.1086/593300.

S.-H. Kim, P. G. Martin, and P. D. Hendry. The size distribution of interstellar dust particles as determined from extinction. ApJ, 422:164–175, February 1994. doi: 10.1086/173714.

A. Kogut, A. J. Banday, C. L. Bennett, K. M. Gorski, G. Hinshaw, G. F. Smoot, and E. I. Wright. Microwave Emission at High Galactic Latitudes in the Four-Year DMR Sky Maps. ApJ, 464:L5, June 1996. doi: 10.1086/310072.

M. Köhler, A. Jones, and N. Ysard. A hidden reservoir of Fe/FeS in interstellar silicates? A&A, 565:L9, May 2014. doi: 10.1051/0004-6361/201423985.

K. Kohno, T. Tosaki, S. Matsushita, B. Vila-Vilaó, T. Shibatsuka, and R. Kawabe. Diffuse and Gravitationally Stable Molecular Gas in the Post-Starburst Galaxy NGC 5195. PASJ, 54:541–553, August 2002. doi: 10.1093/pasj/54.4.541.

R. A. Koopmann and J. D. P. Kenney. Hα Morphologies and Environmental Effects in Virgo Cluster Spiral Galaxies. ApJ, 613:866–885, October 2004. doi: 10.1086/423191.

S. A. Krasnokutski, G. Rouillé, C. Jäger, F. Huisken, S. Zhukovska, and T. Henning. Formation of Silicon Oxide Grains at Low Temperature. ApJ, 782:15, February 2014. doi: 10.1088/0004-637X/782/1/15.

K. S. Krishna Swamy and C. R. O'dell. Thermal Emission by Particles in NGC 7027. ApJ, 151:L61, February 1968. doi: 10.1086/180142.

N. Kuno, N. Sato, H. Nakanishi, A. Hirota, T. Tosaki, Y. Shioya, K. Sorai, N. Nakai, K. Nishiyama, and B. Vila-Vilaró. Nobeyama CO Atlas of Nearby Spiral Galaxies: Distribution of Molecular Gas in Barred and Nonbarred Spiral Galaxies. PASJ, 59: 117–166, February 2007. doi: 10.1093/pasj/59.1.117.

L. A. Lebofsky, M. V. Sykes, E. F. Tedesco, G. J. Veeder, D. L. Matson, R. H. Brown, J. C. Gradie, M. A. Feierberg, and R. J. Rudy. A refined 'standard' thermal model for asteroids based on observations of 1 Ceres and 2 Pallas. , 68:239–251, November 1986. doi: 10.1016/0019-1035(86)90021-7.

J. H. Lee, N. Hwang, and M. G. Lee. H II Region Luminosity Function of the Interacting Galaxy M51. ApJ, 735:75, July 2011. doi: 10.1088/0004-637X/735/2/75.

A. Leger and L. D'Hendecourt. Identification of Polycyclic Aromatic Hydrocarbons. In M. S. Vardya and S. P. Tarafdar, editors, *Astrochemistry*, volume 120 of *IAU Symposium*, page 557, 1987.

A. Leger and J. L. Puget. Identification of the 'unidentified' IR emission features of interstellar dust? A&A, 137:L5–L8, August 1984.

E. M. Leitch, A. C. S. Readhead, T. J. Pearson, and S. T. Myers. An Anomalous Component of Galactic Emission. ApJ, 486:L23–L26, September 1997. doi: 10.1086/310823.

H. Leroux. private communication, 2007.

R. S. Lewis, E. Anders, and B. T. Draine. Properties, detectability and origin of interstellar diamonds in meteorites. Nature, 339:117–121, May 1989. doi: 10.1038/339117a0.

A. Li and B. T. Draine. Infrared Emission from Interstellar Dust. II. The Diffuse Interstellar Medium. ApJ, 554:778–802, June 2001. doi: 10.1086/323147.

A. Li and J. M. Greenberg. Mid-Infrared Spectropolarimetric Constraints on the Core-Mantle Interstellar Dust Model. ApJ, 577:789–794, October 2002. doi: 10.1086/342222.

J.-T. Li and Q. D. Wang. Chandra survey of nearby highly inclined disc galaxies - I. X-ray measurements of galactic coronae. MNRAS, 428:2085–2108, January 2013a. doi: 10.1093/mnras/sts183.

J.-T. Li and Q. D. Wang. Chandra Survey of Nearby Highly Inclined Disc Galaxies - II: Correlation Analysis of Galactic Coronal Properties. *ArXiv e-prints*, August 2013b.

K. Lodders. They Came from the Deep in the Supernova: The Origin of TiC and Metal Subgrains in Presolar Graphite Grains. ApJ, 647:L37–L40, August 2006. doi: 10.1086/507181.

M. E. Machacek, C. Jones, and W. R. Forman. Chandra Observations of NGC 4438: An Environmentally Damaged Galaxy in the Virgo Cluster. ApJ, 610:183–200, July 2004. doi: 10.1086/421448.

J. S. Mathis. Interstellar dust and extinction. ARA&A, 28:37–70, 1990. doi: 10.1146/annurev.aa.28.090190.000345.

J. S. Mathis, W. Rumpl, and K. H. Nordsieck. The size distribution of interstellar grains. ApJ, 217:425–433, October 1977. doi: 10.1086/155591.

J. S. Mathis, P. G. Mezger, and N. Panagia. Interstellar radiation field and dust temperatures in the diffuse interstellar matter and in giant molecular clouds. A&A, 128:212–229, November 1983.

N. Matsunami. *Energy dependence of sputtering yields of monatomic solids.* 1980.

M. Matsuura, E. Dwek, M. Meixner, M. Otsuka, B. Babler, M. J. Barlow, J. Roman-Duval, C. Engelbracht, K. Sandstrom, M. Lakićević, J. T. van Loon, G. Sonneborn, G. C. Clayton, K. S. Long, P. Lundqvist, T. Nozawa, K. D. Gordon, S. Hony, P. Panuzzo, K. Okumura, K. A. Misselt, E. Montiel, and M. Sauvage. Herschel Detects a Massive Dust Reservoir in Supernova 1987A. *Science*, 333:1258–, September 2011. doi: 10.1126/science.1205983.

P. W. May, G. Pineau des Forêts, D. R. Flower, D. Field, N. L. Allan, and J. A. Purton. Sputtering of grains in C-type shocks. MNRAS, 318:809–816, November 2000. doi: 10.1046/j.1365-8711.2000.03796.x.

C. McKee. Dust Destruction in the Interstellar Medium. In L. J. Allamandola and A. G. G. M. Tielens, editors, *Interstellar Dust*, volume 135 of *IAU Symposium*, page 431, 1989.

C. F. McKee and D. J. Hollenbach. Interstellar shock waves. ARA&A, 18:219–262, 1980. doi: 10.1146/annurev.aa.18.090180.001251.

C. F. McKee and J. P. Ostriker. A theory of the interstellar medium - Three components regulated by supernova explosions in an inhomogeneous substrate. ApJ, 218:148–169, November 1977. doi: 10.1086/155667.

C. F. McKee, D. J. Hollenbach, G. C. Seab, and A. G. G. M. Tielens. The structure of the time-dependent interstellar shocks and grain destruction in the interstellar medium. ApJ, 318:674–701, July 1987. doi: 10.1086/165403.

R. G. McQueen, S. P. Marsh, J W. Taylor, J. N. Fritz, and W. J. Carter. *High-Velocity Impact Phenomenae.* ed. R. Kinslow (New York: Academic), 1970.

V. Mennella. Activation Energy of CH Bond Formation in Carbon Grains Irradiated with Hydrogen Atoms. ApJ, 647:L49–L52, August 2006. doi: 10.1086/507296.

V. Mennella. Activation of the 3.47 μm Band by H Atom Irradiation of Carbon Grains Covered with a Water Ice Layer at 12 K. ApJ, 682:L101–L104, August 2008. doi: 10.1086/591051.

V. Mennella. H Atom Irradiation of Carbon Grains under Simulated Dense Interstellar Medium Conditions: The Evolution of Organics from Diffuse Interstellar Clouds to the Solar System. ApJ, 718:867–875, August 2010. doi: 10.1088/0004-637X/718/2/867.

V. Mennella, L. Colangeli, and E. Bussoletti. The absorption coefficient of cosmic carbon analogue grains in the wavelength range 20 - 2000 microns. A&A, 295:165–170, March 1995.

V. Mennella, G. M. Muñoz Caro, R. Ruiterkamp, W. A. Schutte, J. M. Greenberg, J. R. Brucato, and L. Colangeli. UV photodestruction of CH bonds and the evolution of the 3.4 mu m feature carrier. II. The case of hydrogenated carbon grains. A&A, 367: 355–361, February 2001. doi: 10.1051/0004-6361:20000340.

V. Mennella, J. R. Brucato, L. Colangeli, and P. Palumbo. CH Bond Formation in Carbon Grains by Exposure to Atomic Hydrogen: The Evolution of the Carrier of the Interstellar 3.4 Micron Band. ApJ, 569:531–540, April 2002. doi: 10.1086/339229.

E. Mentuch Cooper, C. D. Wilson, K. Foyle, G. Bendo, J. Koda, M. Baes, M. Boquien, A. Boselli, L. Ciesla, A. Cooray, S. Eales, M. Galametz, V. Lebouteiller, T. Parkin, H. Roussel, M. Sauvage, L. Spinoglio, and M. W. L. Smith. Spatially Resolved Stellar, Dust, and Gas Properties of the Post-interacting Whirlpool Galaxy System. ApJ, 755:165, August 2012. doi: 10.1088/0004-637X/755/2/165.

P. G. Mezger, J. S. Mathis, and N. Panagia. The origin of the diffuse galactic far infrared and sub-millimeter emission. A&A, 105:372–388, January 1982.

E. R. Micelotta, A. P. Jones, and A. G. G. M. Tielens. Polycyclic aromatic hydrocarbon processing in interstellar shocks. A&A, 510:A36, February 2010a. doi: 10.1051/0004-6361/200911682.

E. R. Micelotta, A. P. Jones, and A. G. G. M. Tielens. Polycyclic aromatic hydrocarbon processing in a hot gas. A&A, 510:A37, February 2010b. doi: 10.1051/0004-6361/200911683.

E. R. Micelotta, A. P. Jones, J. Cami, E. Peeters, J. Bernard-Salas, and G. Fanchini. The Formation of Cosmic Fullerenes from Arophatic Clusters. ApJ, 761:35, December 2012. doi: 10.1088/0004-637X/761/1/35.

E. R. Micelotta, A. P. Jones, M. Bocchio, J. Cami, E. Peeters, and J. Bernard-Salas. The Circle of Dust: From Nanoparticles to Macromolecules and Beyond. In *"The Life Cycle of Dust in the Universe" Conf. Proceedings, http://pos.sissa.it/archive/conferences/207/125/LCDU2013_125.pdf*, 2013.

A. Misiriotis, I. E. Papadakis, N. D. Kylafis, and J. Papamastorakis. Dust masses and star formation in bright IRAS galaxies. Application of a physical model for the interpretation of FIR observations. A&A, 417:39–50, April 2004. doi: 10.1051/0004-6361:20035602.

A. Misiriotis, E. M. Xilouris, J. Papamastorakis, P. Boumis, and C. D. Goudis. The distribution of the ISM in the Milky Way. A three-dimensional large-scale model. A&A, 459:113–123, November 2006. doi: 10.1051/0004-6361:20054618.

H. Mizuno, W. J. Markiewicz, and H. J. Voelk. Grain growth in turbulent protoplanetary accretion disks. A&A, 195:183–192, April 1988.

R. Moreno. PhD thesis, Université Paris VI, 1998.

R. Moreno. Neptune and Uranus planetary brightness temperature tabulation, 2010. URL `ftp://ftp.sciops.esa.int/pub/hsc-calibration`.

D. C. Morton. Atomic Data for Resonance Absorption Lines. III. Wavelengths Longward of the Lyman Limit for the Elements Hydrogen to Gallium. ApJS, 149:205–238, November 2003. doi: 10.1086/377639.

J. Moustakas, R. C. Kennicutt, Jr., C. A. Tremonti, D. A. Dale, J.-D. T. Smith, and D. Calzetti. Optical Spectroscopy and Nebular Oxygen Abundances of the Spitzer/SINGS Galaxies. ApJS, 190:233, October 2010. doi: 10.1088/0067-0049/190/2/233.

G. M. Muñoz Caro, R. Ruiterkamp, W. A. Schutte, J. M. Greenberg, and V. Mennella. UV photodestruction of CH bonds and the evolution of the 3.4 mu m feature carrier. I. The case of aliphatic and aromatic molecular species. A&A, 367:347–354, February 2001. doi: 10.1051/0004-6361:20000341.

E. W. Muller and T. T. Tsong. *Field Ion Microscopy.* American Elsevier, 1969.

E. J. Murphy, J. D. P. Kenney, G. Helou, A. Chung, and J. H. Howell. Environmental Effects in Clusters: Modified Far-Infrared-Radio Relations within Virgo Cluster Galaxies. ApJ, 694:1435–1451, April 2009. doi: 10.1088/0004-637X/694/2/1435.

Y. Nakagawa, K. Nakazawa, and C. Hayashi. Growth and sedimentation of dust grains in the primordial solar nebula. , 45:517–528, March 1981. doi: 10.1016/0019-1035(81)90018-X.

N. Nesvadba. 2014, in prep. A&A, 2014.

C. Norman and J. Silk. Clumpy molecular clouds - A dynamic model self-consistently regulated by T Tauri star formation. ApJ, 238:158–174, May 1980. doi: 10.1086/157969.

A. Omont. Physics and chemistry of interstellar polycyclic aromatic molecules. A&A, 164:159–178, August 1986.

J. H. Oort and H. C. van de Hulst. Gas and smoke in interstellar space. Bull. Astron. Inst. Netherlands, 10:187, November 1946.

J. P. Ostriker and C. F. McKee. Astrophysical blastwaves. *Reviews of Modern Physics*, 60:1–68, 1988. doi: 10.1103/RevModPhys.60.1.

R. Paladini, H. Linz, B. Altieri, and B. Ali. PACS technical note, 2012. URL `https://nhscdmz2.ipac.caltech.edu/pacs/docs/Photometer/PICC-NHSC-TR-034.pdf`.

V. S. Parvathi, U. J. Sofia, J. Murthy, and B. R. S. Babu. Probing the Role of Carbon in Ultraviolet Extinction along Galactic Sight Lines. ApJ, 760:36, November 2012. doi: 10.1088/0004-637X/760/1/36.

C. Pfrommer and L. J. Dursi. Detecting the orientation of magnetic fields in galaxy clusters. *Nature Physics*, 6:520–526, July 2010. doi: 10.1038/nphys1657.

W. Pietsch, A. Vogler, U. Klein, and H. Zinnecker. X-ray observations of the starburst galaxy NGC 253 — II. Extended emission from hot gas in the nuclear area, disk, and halo. A&A, 360:24–48, August 2000.

P. Pilleri, S. Treviño-Morales, A. Fuente, C. Joblin, J. Cernicharo, M. Gerin, S. Viti, O. Berné, J. R. Goicoechea, J. Pety, M. Gonzalez-García, J. Montillaud, V. Ossenkopf, C. Kramer, S. García-Burillo, F. Le Petit, and J. Le Bourlot. Spatial distribution of small hydrocarbons in the neighborhood of the ultra compact HII region Monoceros R2. A&A, 554:A87, June 2013. doi: 10.1051/0004-6361/201220795.

C. C. Popescu, A. Misiriotis, N. D. Kylafis, R. J. Tuffs, and J. Fischera. Modelling the spectral energy distribution of galaxies. I. Radiation fields and grain heating in the edge-on spiral NGC 891. A&A, 362:138–150, October 2000.

P. Predehl and J. H. M. M. Schmitt. X-raying the interstellar medium: ROSAT observations of dust scattering halos. A&A, 293:889–905, January 1995.

J. Quintanilla and S. Torquato. Clustering properties of d-dimensional overlapping spheres. Phys. Rev. E, 54:5331–5339, November 1996. doi: 10.1103/PhysRevE.54.5331.

W. J. Rae. *High-Velocity Impact Phenomenae*. Kinslow, R., 1970.

J. Raymond. private communication, 1992.

J. C. Raymond, D. P. Cox, and B. W. Smith. Radiative cooling of a low-density plasma. ApJ, 204:290–292, February 1976. doi: 10.1086/154170.

A. Rémy-Ruyer, S. C. Madden, F. Galliano, M. Galametz, T. T. Takeuchi, R. S. Asano, S. Zhukovska, V. Lebouteiller, D. Cormier, A. Jones, M. Bocchio, M. Baes, G. J. Bendo, M. Boquien, A. Boselli, I. DeLooze, V. Doublier-Pritchard, T. Hughes, O. Ł. Karczewski, and L. Spinoglio. Gas-to-dust mass ratios in local galaxies over a 2 dex metallicity range. A&A, 563:A31, March 2014. doi: 10.1051/0004-6361/201322803.

J. Robertson. Amorphous carbon. *Advances in Physics*, 35:317–374, November 1986. doi: 10.1080/00018738600101911.

G. Rouillé, C. Jäger, S. A. Krasnokutski, M. Krebsz, and T. Henning. Cold condensation of dust in the ism. *Faraday discussions, accepted*, 2014.

F. Rouleau and P. G. Martin. Shape and clustering effects on the optical properties of amorphous carbon. ApJ, 377:526–540, August 1991. doi: 10.1086/170382.

H. Roussel. Scanamorphos: A Map-making Software for Herschel and Similar Scanning Bolometer Arrays. PASP, 125:1126–1163, September 2013. doi: 10.1086/673310.

P. M. Routly and L. Spitzer, Jr. A Comparison of the Components in Interstellar Sodium and Calcium. ApJ, 115:227, March 1952. doi: 10.1086/145535.

M. Ruszkowski, M. Brüggen, D. Lee, and M.-S. Shin. Impact of Magnetic Fields on Ram Pressure Stripping in Disk Galaxies. ApJ, 784:75, March 2014. doi: 10.1088/0004-637X/784/1/75.

E. V. Ryan-Weber, R. L. Webster, and L. Staveley-Smith. The column density distribution function at z= 0 from HI selected galaxies. MNRAS, 343:1195–1206, August 2003. doi: 10.1046/j.1365-8711.2003.06754.x.

H. Salo and E. Laurikainen. N-body model for M51 - I. Multiple encounter versus single passage? MNRAS, 319:377–392, December 2000. doi: 10.1046/j.1365-8711.2000.03650.x.

D. J. Schlegel, D. P. Finkbeiner, and M. Davis. Maps of Dust Infrared Emission for Use in Estimation of Reddening and Cosmic Microwave Background Radiation Foregrounds. ApJ, 500:525–553, June 1998. doi: 10.1086/305772.

C. G. Seab. Grain destruction, formation, and evolution. In D. J. Hollenbach and H. A. Thronson, Jr., editors, *Interstellar Processes*, volume 134 of *Astrophysics and Space Science Library*, pages 491–512, 1987.

C. G. Seab and J. M. Shull. Shock processing of interstellar grains. ApJ, 275:652–660, December 1983. doi: 10.1086/161563.

L. I. Sedov. Similarity and Dimentional Methods in Mechanics. *New York: Academic*, 1969.

L. Serra Díaz-Cano and A. P. Jones. Carbonaceous dust in interstellar shock waves: hydrogenated amorphous carbon (a-C:H) vs. graphite. A&A, 492:127–133, December 2008. doi: 10.1051/0004-6361:200810622.

J. M. Shull. Disruption and sputtering of grains in intermediate-velocity interstellar clouds. ApJ, 226:858–862, December 1978. doi: 10.1086/156666.

J. M. Shull and B. T. Draine. The physics of interstellar shock waves. In D. J. Hollenbach and H. A. Thronson, Jr., editors, *Interstellar Processes*, volume 134 of *Astrophysics and Space Science Library*, pages 283–319, 1987.

R. Siebenmorgen, N. V. Voshchinnikov, and S. Bagnulo. Dust in the diffuse interstellar medium. Extinction, emission, linear and circular polarisation. A&A, 561:A82, January 2014. doi: 10.1051/0004-6361/201321716.

P. Sigmund. *Sputtering by ion bombardment theoretical concepts*, page 9. 1981. doi: 10.1007/3540105212_7.

S. Sivanandam, M. J. Rieke, and G. H. Rieke. A Warm Molecular Hydrogen Tail due to Ram-pressure Stripping of a Cluster Galaxy. ApJ, 717:147–162, July 2010. doi: 10.1088/0004-637X/717/1/147.

J. D. Slavin. in prep. *in prep.*, 2014.

F. W. Smith. Optical constants of a hydrogenated amorphous carbon film. *Journal of Applied Physics*, 55:764–771, February 1984. doi: 10.1063/1.333135.

R. Smith and R. P. Webb. Energetic fullerene interactions with a graphite surface. *Royal Society of London Proceedings Series A*, 441:495–499, June 1993. doi: 10.1098/rspa.1993.0075.

T. P. Snow and A. N. Witt. Interstellar Depletions Updated: Where All the Atoms Went. ApJ, 468:L65, September 1996. doi: 10.1086/310225.

U. J. Sofia and V. S. Parvathi. Carbon Abundances in Interstellar Gas and Dust. In T. Henning, E. Grün, and J. Steinacker, editors, *Cosmic Dust - Near and Far*, volume 414 of *Astronomical Society of the Pacific Conference Series*, page 236, December 2009.

U. J. Sofia, V. S. Parvathi, B. R. S. Babu, and J. Murthy. Determining Interstellar Carbon Abundances from Strong-line Transitions. AJ, 141:22, January 2011. doi: 10.1088/0004-6256/141/1/22.

J. M. Solanes, A. Manrique, C. García-Gómez, G. González-Casado, R. Giovanelli, and M. P. Haynes. The H I Content of Spirals. II. Gas Deficiency in Cluster Galaxies. ApJ, 548:97–113, February 2001. doi: 10.1086/318672.

L. Spitzer, Jr. and W. Baade. Stellar Populations and Collisions of Galaxies. ApJ, 113:413, March 1951. doi: 10.1086/145406.

T. P. Stecher. Interstellar Ectinction in the Ultraviolet. ApJ, 142:1683, November 1965. doi: 10.1086/148462.

T. P. Stecher. Interstellar Extinction in the Ultraviolet. II. ApJ, 157:L125, August 1969. doi: 10.1086/180400.

M. Sun, C. Jones, W. Forman, P. E. J. Nulsen, M. Donahue, and G. M. Voit. A 70 Kiloparsec X-Ray Tail in the Cluster A3627. ApJ, 637:L81–L84, February 2006. doi: 10.1086/500590.

M. Sun, M. Donahue, and G. M. Voit. Hα Tail, Intracluster H II Regions, and Star Formation: ESO 137-001 in Abell 3627. ApJ, 671:190–202, December 2007. doi: 10.1086/522690.

M. Sun, M. Donahue, E. Roediger, P. E. J. Nulsen, G. M. Voit, C. Sarazin, W. Forman, and C. Jones. Spectacular X-ray Tails, Intracluster Star Formation, and ULXs in A3627. ApJ, 708:946–964, January 2010. doi: 10.1088/0004-637X/708/2/946.

G. Taylor. The Formation of a Blast Wave by a Very Intense Explosion. II. The Atomic Explosion of 1945. *Royal Society of London Proceedings Series A*, 201:175–186, March 1950. doi: 10.1098/rspa.1950.0050.

H. A. Thronson, Jr., H. Rubin, and A. Ksir. Where galaxies collide. II - NGC 5195, the M51 system and the luminosity function of H II regions. MNRAS, 252:550–557, October 1991.

A. G. G. M. Tielens. *The Physics and Chemistry of the Interstellar Medium*. August 2010.

A. G. G. M. Tielens, C. F. McKee, C. G. Seab, and D. J. Hollenbach. The physics of grain-grain collisions and gas-grain sputtering in interstellar shocks. ApJ, 431: 321–340, August 1994. doi: 10.1086/174488.

N. A. Tikhonov, O. A. Galazutdinova, and E. N. Tikhonov. Stellar content of the interacting galaxies of the M51 system. *Astronomy Letters*, 35:599–608, September 2009. doi: 10.1134/S1063773709090035.

S. Tonnesen and G. L. Bryan. Gas Stripping in Simulated Galaxies with a Multiphase Interstellar Medium. ApJ, 694:789–804, April 2009. doi: 10.1088/0004-637X/694/2/789.

S. Tonnesen and G. L. Bryan. The Tail of the Stripped Gas that Cooled: H I, Hα, and X-ray Observational Signatures of Ram Pressure Stripping. ApJ, 709:1203, February 2010. doi: 10.1088/0004-637X/709/2/1203.

S. Tonnesen and G. L. Bryan. Star formation in ram pressure stripped galactic tails. MNRAS, 422:1609–1624, May 2012. doi: 10.1111/j.1365-2966.2012.20737.x.

S. Tonnesen, G. L. Bryan, and R. Chen. How to Light it Up: Simulating Ram-pressure Stripped X-ray Bright Tails. ApJ, 731:98, April 2011. doi: 10.1088/0004-637X/731/2/98.

R. J. Trumpler. Absorption of Light in the Galactic System. PASP, 42:214, August 1930. doi: 10.1086/124039.

D. Tschöke, G. Hensler, and D. J. Bomans. Hot Gas in Starburst Galaxies - X-rays from NGC 2903 and NGC 4569. *Astrophysics and Space Science Supplement*, 277: 119–119, 2001. doi: 10.1023/A:1012781122404.

B. Vollmer, R. Beck, J. D. P. Kenney, and J. H. van Gorkom. Radio Continuum Observations of the Virgo Cluster Spiral NGC 4522: The Signature of Ram Pressure. AJ, 127:3375–3381, June 2004. doi: 10.1086/420802.

B. Vollmer, J. Braine, F. Combes, and Y. Sofue. New CO observations and simulations of the NGC 4438/NGC 4435 system. Interaction diagnostics of the Virgo cluster galaxy NGC 4438. A&A, 441:473–489, October 2005. doi: 10.1051/0004-6361:20041389.

B. Vollmer, M. Soida, A. Chung, L. Chemin, J. Braine, A. Boselli, and R. Beck. Ram pressure stripping of the multiphase ISM in the Virgo cluster spiral galaxy NGC 4438. A&A, 496:669–675, March 2009. doi: 10.1051/0004-6361/200811140.

B. Vollmer, M. Soida, A. Chung, R. Beck, M. Urbanik, K. T. Chyży, K. Otmianowska-Mazur, and J. H. van Gorkom. The influence of the cluster environment on the large-scale radio continuum emission of 8 Virgo cluster spirals. A&A, 512:A36, March 2010. doi: 10.1051/0004-6361/200913591.

B. Vollmer, M. Soida, J. Braine, A. Abramson, R. Beck, A. Chung, H. H. Crowl, J. D. P. Kenney, and J. H. van Gorkom. Ram pressure stripping of the multiphase ISM and star formation in the Virgo spiral galaxy NGC 4330. A&A, 537:A143, January 2012. doi: 10.1051/0004-6361/201117680.

R. H. Warmels. The HI properties of spiral galaxies in the Virgo Cluster. III - The HI surface density distribution in 36 galaxies. A&AS, 72:427–447, March 1988.

E. Waxman and B. T. Draine. Dust Sublimation by Gamma-ray Bursts and Its Implications. ApJ, 537:796–802, July 2000. doi: 10.1086/309053.

J. C. Weingartner and B. T. Draine. Photoelectric Emission from Interstellar Dust: Grain Charging and Gas Heating. ApJS, 134:263–281, June 2001. doi: 10.1086/320852.

J. C. Weingartner, B. T. Draine, and D. K. Barr. Photoelectric Emission from Dust Grains Exposed to Extreme Ultraviolet and X-Ray Radiation. ApJ, 645:1188–1197, July 2006. doi: 10.1086/504420.

A. R. Welch and D. L. Judge. Absolute Specific Photodissociation Cross Sections of CH_4 in the Extreme Ultraviolet. J. Chem. Phys., 57:286–290, July 1972. doi: 10.1063/1.1677958.

D. E. Welty, E. B. Jenkins, J. C. Raymond, C. Mallouris, and D. G. York. Intermediate- and High-Velocity Ionized Gas toward ζ Orionis. ApJ, 579:304–326, November 2002. doi: 10.1086/342755.

B. C. Whitmore, D. M. Gilmore, and C. Jones. What determines the morphological fractions in clusters of galaxies? ApJ, 407:489–509, April 1993. doi: 10.1086/172531.

L. Woltjer. Supernova Remnants. ARA&A, 10:129, 1972. doi: 10.1146/annurev.aa.10.090172.001021.

N. J. Woolf. Infrared Emission from Planetary Nebulae. ApJ, 157:L37, July 1969. doi: 10.1086/180379.

P. A. Woudt, R. C. Kraan-Korteweg, J. Lucey, A. P. Fairall, and S. A. W. Moore. The Norma cluster (ACO 3627) - I. A dynamical analysis of the most massive cluster in the Great Attractor. MNRAS, 383:445–457, January 2008. doi: 10.1111/j.1365-2966.2007.12571.x.

E. M. Xilouris, Y. I. Byun, N. D. Kylafis, E. V. Paleologou, and J. Papamastorakis. Are spiral galaxies optically thin or thick? A&A, 344:868–878, April 1999.

Y. Yamamura, N. Matsunami, and N. Itoh. *Radiation Effects*, 71(65), 1983.

Y. B. Zeldovich and Y. P. Raizer. *Elements of gasdynamics and the classical theory of shock waves*. 1966.

J. F. Ziegler and J. P. Biersack. *The Stopping and Range of Ions in Matter*, page 93. 1985. doi: 10.1007/978-1-4615-8103-1_3.

J. F. Ziegler, J. P. Biersack, and U. Littmark. Stopping and range of ions in matter, version 2013, www.srim.org, 1985.

V. Zubko, E. Dwek, and R. G. Arendt. Interstellar Dust Models Consistent with Extinction, Emission, and Abundance Constraints. ApJS, 152:211–249, June 2004. doi: 10.1086/382351.

V. G. Zubko, J. Krełowski, and W. Wegner. The size distribution of dust grains in single clouds. I. The analysis of extinction using multicomponent mixtures of bare spherical grains. MNRAS, 283:577–588, December 1996.

V. G. Zubko, J. Krelowski, and W. Wegner. The size distribution of dust grains in single clouds. II - The analysis of extinction using inhomogeneous grains. MNRAS, 294:548, March 1998. doi: 10.1046/j.1365-8711.1998.01048.x.